January 2010

# Synthesis and investigation of UV-cured, complex amphiphilic polymer films for use in anti-biofouling applications

Jeremy Bartels
*Washington University in St. Louis*

WASHINGTON UNIVERSITY IN ST. LOUIS

Department of Chemistry

Dissertation Examination Committee:
Prof. Karen L. Wooley, Chairperson
Prof. Kevin D. Moeller, co-chair
Prof. Jacob Schaefer
Prof. Garland R. Marshall
Prof. Donald L. Elbert
Prof. Joshua A. Maurer

# Synthesis and investigation of UV-cured, complex amphiphilic polymer films for use in anti-biofouling applications

by

Jeremy W. Bartels

A dissertation presented to the
Graduate School of Arts and Sciences
of Washington University in
partial fulfillment of the
requirements for the degree
of Doctor of Philosophy

May 2010

Saint Louis, Missouri

# ABSTRACT OF THE DISSERTATION

Synthesis and investigation of UV-cured, complex amphiphilic polymer films for use in anti-biofouling applications

by

Jeremy Wayne Bartels

Doctor of Philosophy in Chemistry

Washington University in Saint Louis, 2010

Professor Karen L. Wooley, Chairperson

The overall emphasis of this dissertation research included the development of novel amphiphilic anti-fouling coatings having complex surface topography and compositional heterogeneity and a fundamental investigation of their properties. These films were cultivated as non-fluorinated or non-fluorinated/non-PEGylated analogs to the hyperbranched fluoropolymer-poly(ethylene glycol) (HBFP-PEG) film system. The coating compositions consisted of the mixing and crosslinking of either two disparate polymers or a complex amphiphilic block copolymer with crosslinking agents. A variety of crosslinking methods was analyzed, including vulcanization and UV-promoted thiol-ene reactions. The coatings were analyzed using a variety of advanced methods, including thermomechanical techniques, tensile testing and surface analysis.

A combinatorial series of UV-promoted, thiol-ene generated amphiphilic films was prepared by the crosslinking of varying wt% of 4-armed poly(ethylene glycol) (PEG) tetrathiol and equivalents of pentaerythritol tetrakis(3-mercaptopropionate) (PETMP) with alkene-modified Boltorn polyesters. The Boltorn-alkene components were prepared through the

esterification between commercially available Boltorn H30™ and 3-butenoic acid. The thermomechanical attributes of the films were analyzed, showing an increase in $T_g$ with an increase in PEG wt%, regardless of PETMP concentration. The films were then studied for their bulk mechanical properties in both dry and wet state. The nanoscopic surface features were probed using atomic force microscopy and contact angle analysis. Additionally, a series of coatings were prepared at a low PETMP concentration with varying PEG wt% (0-35 wt%), where they were tested for anti-biofouling character and fouling release ability against *Ulva* marine algae. The films have a vastly decreased spore settlement and growth when compared to commercial PDMS coatings.

A non-fluorinated, non-PEGylated analog of the HBFP-PEG system was synthesized using RAFT copolymerization. It was hypothesized that the non-ionic polar polymer, poly(*N*-vinylpyrrolidinone) (PNVP), would work as a more durable replacement for the hydrophilic PEG of the original system and that the hydrophobic polymer polyisoprene (PIp) could be used as a low surface energy, potentially multi-crosslinkable analog of HBFP. Vulcanization crosslinking methods were employed during polymer phase segregation, driven by differences in composition and macromolecular topology. The new design differs not only in the chemical compositions (PIp for HBFP and PNVP for PEG), but also in the macromolecular architecture. The complex films were analyzed using a variety of advanced surface analysis, including XPS, IRIR imaging, and XPS.

A similar block copolymer system was investigated, PEO-*b*-PIp, as an additional analog to HBFP-PEG. Two RAFT-capable PEO macro-CTAs, 2 and 5 kDa, were prepared and used for the polymerization of isoprene which yielded well-defined block copolymers of varied lengths and compositions. Mathematical deconvolution of the GPC chromatograms allowed for the

estimation of the blocking efficiency, about 50% for the 5 kDa PEO macro-CTA and 64% for the 2 kDa CTA. Self assembly of the block copolymers in both water and decane was investigated and the resulting regular and inverse assemblies, respectively, were analyzed with DLS, AFM, and TEM to ascertain their dimensions and properties. Assembly of PEO-*b*-PIp block copolymers in aqueous solution resulted in well-defined micelles of varying sizes while the assembly in hydrophobic, organic solvent resulted in the formation of different morphologies including large aggregates and well-defined cylindrical and spherical structures. Additional investigation into the potential anti-fouling ability was performed using fluorescently-tagged biomolecule adsorption assays.

During the studies of these analogs, several discoveries were made with the original HBFP-PEG system on which the dissertation author is listed as co-author. Since the work was performed in conjunction with the dissertation author and is pertinent to the dissertation, the work is included in the Appendices. Nanocompositing materials, specifically carbon nanotubes and nanoscopic silica, were either physically mixed or engineered to be phase-specific for either the HBFP domain or the PEG domain. The nanocomposited HBFP-PEG materials were then subjected to a variety of mechanical tests in order to see how the compositing agents effected modulus in either dry or wet environments. Additional advanced investigations into the unique mechanical properties of HBFP-PEG were performed using solid-state NMR. At varying wt% PEG, the wetted film acts as either a structurally-reinforced material (sub-45 wt%) or as a mechanically-weakened hydrogel (>55 wt%). The mechanism of the structural reinforcing was probed using a variety of advanced solid state NMR techniques, providing information into the unique mechanical properties of the HBFP-PEG material.

For Jenny and Logan

# ACKNOWLEDGEMENTS

"There are these two young fish swimming along and they happen to meet an older fish swimming the other way, who nods at them and says "Morning, boys. How's the water?" And the two young fish swim on for a bit, and then eventually one of them looks over at the other and goes "What the hell is water?""

-David Foster Wallace

I'm finally done with school! My life has changed over the last five years in ways that I can't even begin to explain, but I'll attempt to do so brief, yet ever so colloquial, manner. First off, I would like to acknowledge Prof. Gary Beall for sitting me down in his office during the first year of my master's research and telling me that I shouldn't stop at a masters. I had never considered getting my PhD before, but that conversation struck me in a powerful way. Luckily for all parties involved, Prof. Beall was a former resident of Saint Louis, and recommended this one particular school that I had never heard of for grad school, Washington University, St Louis, which I applied to along with 4 other schools. While at WashU, I happened to schedule a meeting with Professor Karen Wooley. From then on, I knew I wanted to go to WashU, and I wanted to work for Karen Wooley. Karen literally changed the game for me. I wish to thank her for her mentorship over the last 5 years, and for never letting "just enough" pass. Her insistence on quality of data and strong work ethic has instilled in me principles that I will apply for the rest of my life. I also wish to thank her for the many opportunities I have had since working with her. She also had the courage and strength to believe in me, even though I literally started my

work for her with a "bang," when I blew up one of her lab hoods *one week* after starting research. (Just for the record, it turned out a faulty hot plate was to ultimately to blame).

I also wish to thank my committee members, Prof. Kevin Moeller and Prof. Jacob Schaefer. In a rare twist of events, I managed to complete my PhD career under their guidance while simultaneously *publishing* with both of them. Thank you for serving on my committee and offering your many suggestions over the years. In addition, I would like to dedicate Chapter 4 (PEO-*b*-PIp work) to Professor Moeller, as he suggested this work during one of my committee meetings several years ago.

As many people know, or soon figure out upon starting their studies, PhD research is never a solo project. I would like to thank my many collaborators, co-authors and friends over the last few years, in no particular order: Professor Michael Mackay and his current and former members David Bohnsack, Erica Tseng, and Jon Seppala. Jinqi Xu for his amazing guidance at the beginning of my tenure at the Wooley lab. Kenya and Eric for their help and strategies with HBFP systems. Andreas Nyström, who acted as a model for me during my "middle years;" I can only hope that I become half the scientist he is. Professor Schaefer and Ryutaro for their NMR investigations into the HBFP-PEG system. Professor Moeller and Libo for their collaboration. Professor Marek Urban and Biswajit Ghosh for their IRIRI investigations of my coating formulations. Professor Mike Greenlief for his help with obtaining XPS and interpreting the results. Undergrad assistant Peter Billings, who worked with me and performed awesome (2 papers!) in such a short time. Solène Cauët for her incredible knowledge of GPC, which helped take an already interesting paper into a fantastic one. Professor Darrin Pochan and Jiahua Zhu for their experiments and insights into polymer micelles. Christopher Fidge, Phil Imbesi and Jun Ma for their help with the thiol-ene/UV coating experiments. Tony Clare and Nick Aldred,

Lenora and Dean Wendt, John Finlay and Jim and Maureen Callow for their tireless efforts in testing my many coatings. Finally, here's to my many friends: Rhiannon, for being my "lab husband," or is the other way around? Melissae and Laura for their friendship over the years. Dave, Brooke and Shrini for being great friends and role models. Yali for being an evil cohort. Guorong for shooting the breeze and for the intense scientific discussions. Lily and Nam for being amazing friends over the last few years. Ke for being a great friend and for giving me the great images that appear throughout this work, as well as tips on dissertation writing. Eileen for the great chats and for helping with the fish. And the rest of the Wooley Lab, Zhou, Jenn, Ang, Sandani, Ritu, Chao, Shiyi and Chong.

I wish to thank my incredible family for their love and support during my time here. Thank you to the in-laws Mike and Cindy for their love and humor in helping me get through the PhD years. A huge thank you to my parents, Petey and Sharon, for fostering my interest in science that I had as a young boy into the man I am today. I know you're both surprised I didn't end up as either a paleontologist or an astronomer, but I think that a "chemist" is a good compromise. Thank you to my sister, Jennifer, for your support and, amazingly, for *coming* to WashU and for always being there for the last 4 years. Finally, thank you to my wife Jenny for going on this incredible journey with me. Just think, since we've come here, we've gotten engaged, married, crossed the oceans and back, and brought a new life into this world. You kept me sane while I was buried in my studies or struggling at work. I can't wait to see where our journey takes us. Logan, although you didn't know it at the time, you helped me wrap things up at the very end.

"This is water."

*(Individual funding acknowledgements are included in the respective chapters)*

# TABLE OF CONTENTS

## LIST OF FIGURES

**Chapter 1**



**Chapter 2**

## LIST OF SCHEMES

**Appendix 1**

## LIST OF TABLES

**Appendix 2**

## GLOSSARY OF TERMS AND ABBREVIATIONS

| | |
|---|---|
| **ACVA** | Azobiscyanovaleric acid |
| **AFM** | Atomic force microscopy |
| **ATRP** | Atom transfer radical polymerization |
| **CNT** | Carbon nanotube |
| **CRP** | Controlled radical polymerization |
| **CP** | Cross-polarization |
| **CTA** | Chain transfer agent |
| **DACM** | *N*-(7-dimethylamino-4-methylcoumarin-3-yl) maleimide |
| **DDMAT** | *S*-1-dodecyl-*S*'-(α,α'-dimethyl-α"-acetic acid)trithiocarbonate |
| **DIPEA** | *N*,*N*-diisopropylethylamine |
| **DLS** | Dynamic light scattering |
| **DPTS** | 4-(Dimethylamino)pyridinium 4-toluenesulfonate |
| **DSC** | Differential scanning calorimetry |
| **EDCI** | 1-[Dimethylamino)propyl]-3-ethylcarbodiimide methiodide |
| **EPR** | Electron paramagnetic resonance |
| **GPC** | Gel permeation chromatography |
| **HBFP** | Hyperbranched fluoropolymer |
| **HOBt** | Hydroxybenzotriazole monohydrate |
| **IRIRI** | Internal reflectance infrared imaging |
| **MHz** | Megahertz |
| **MPA** | 2,2-bis(hydroxymethyl) propionate |

| | |
|---|---|
| **MWCO** | Molecular weight cut-off |
| **NMRP** | Nitroxide-mediated radical polymerization |
| **RAFT** | Reversible addition-fragmentation chain transfer |
| **PAA** | Poly(acrylic acid) |
| **PCL** | Poly(ε-caprolactone) |
| **PDI** | Polydispersity index |
| **PDMS** | Polydimethylsiloxane |
| **PEG** | Poly(ethylene glycol) |
| **PEO** | Poly(ethylene oxide) |
| **PETMP** | Pentaerythritol tetrakis(3-mercaptopropionate) |
| **PIp** | Polyisoprene |
| **PNVP** | Poly(*N*-vinylpyrrolidinone) |
| **PS** | Polystyrene |
| **PTFE** | Poly(tetrafluoroethylene) |
| **RMS** | Root mean square |
| **SANS** | Small angle neutron scattering |
| **SWNT** | Single-walled carbon nanotube |
| **TEM** | Transmission electron microscopy |
| **TBT** | Tributyltin |
| **TFA** | Trifluoroacetic acid |
| **TGA** | Thermogravimetric analysis |
| **UV** | Ultraviolet |
| **XPS** | X-ray photoelectron spectroscopy |

# Chapter 1

## Introduction

The biofouling of ships and other marine structures has been an ever since mankind built the first boats to sail the oceans. This global nuisance is responsible for >$5.7 billion dollars per year in lost revenue for cargo and other ships due to the increased drag and related fuel costs.(1) Historical accounts of biofouling date as far back as the Carthaginians and Phoenicians, who were reported to have used tar and pitch on their sea-going vessels, both for water-proofing and anti-fouling purposes.(2) The first written account of fouling comes from the *Deipnosophistae*,(3) wherein the Greek rhetorician and grammarian Athenaeus described the anti-fouling efforts taken in the construction of the great ship of Hiero I, which was coated with sheets of lead. An account in 1627by Captain John Smith,(4) titled "*The Generall Historie of Virginia, New England and the Summer Isles, together with the True Travels, Adventures, and Observations, and a Sea Grammar*," there is a description of the process of "graving," where "a white mixture of Tallow, Sope [sic] and Brimstone; or Train-oile, Rosin, and Brimstone boiled together, is the best to preserve her calking [sic] and make her glib or slippery to passe [sic] the water; and when it is decayed by weeds, or Barnacles, which is a *Barnacles, or* kinde [sic] of fish like a long red worme [sic], will eat thorow [sic] all the Plankes if she be not sheathed, which is as casing the Hull under water with Tar, and Haire [sic], close covered over with thin boords [sic] fast nailed to the Hull, which though the Worme pierce, shee [sic] cannot endure the Tar." Christopher Columbus was

reported to have used “tallow and pitch” to aid with preventing barnacles or fouling worms from growing on sea-faring vessels.(5) The first patent for an anti-fouling coating was awarded to William Beale in 1625 (British patent), based on a mixture of iron powder, cement and a mineral compound that was probably copper arsenide or copper sulfide. Pitch and tar were primarily used up until the 18$^{th}$ century, however various agencies, including the British Navy, started using lead sheathing. Copper sheathing was first suggested in 1708 by Charles Perry, however it was rejected initially and not applied until decades later due to the high cost of implementation.(6) Copper sheathing turned out to be highly successful, as it acts in two primary modes: 1) The formation of a slightly soluble, extremely smooth surface coating which washes away slowly over time, taking built up marine fauna with it, and 2) The formation of toxic copper(II) species which actively prevents fouling accumulation.(7) From the mid 1770s up until the 1890s, the British Royal Navy prepared copper sheathing over iron framing(8) Ironically, the copper sheathing performed so well that little innovation occurred. Few patents or new inventions surfaced until the late 1800s when steel, which is structurally strong but galvanically corrodes in a marine environment, became the building material of choice for ship building.

The use of sheathing went out of practice when anti-fouling paints were developed in the late 19$^{th}$ century. In 1863, the first American patent for an antifouling paint for ships' hulls was issued to J.G. Tarr and A.H. Wonson(9) for a “copper oxide, tar and benzene mixture,” which claimed that a ship painted with this composition could have protection against growth of barnacle shells and seaweeds "for a period of twelve months, while another vessel painted in the common manner and employed in the same

trade became so foul in six weeks as to require scraping." Unfortunately, many of the patented compositions for anti-fouling paints in this period were fraudulent, containing everything from kitchen salt to bat guano.(10) Moreover, some coating formulations contained toxic metal salts of copper, arsenic or mercury, and typically used tar or pitch as the base, which would coat unevenly and be vulnerable to flaking or mechanical removal.(6) The use of a less toxic active ingredient and more permanent base coating would not be developed until the late 20$^{th}$ century. Initial investigations into stronger base coatings came in the form of rosin-based formulations, such as "Italian Moravian" and "McInness'" so-called "hot plastic paints," which were mixtures of copper salts and rosin, which would last up to 9 months in marine waters. The use of rosin- or tar-based paints was soon abandoned for shellac-based compositions, such as Norfolk shellac-type paint, developed in 1906,(11) or related "cold plastic paints" which used solvent evaporation to form even coatings. By the late 1920s, anti-fouling paint technology was at an adaquately advanced stage that formulations could keep ships out of dry dock for up to 18 months.(12) It was around this time that the modes of fouling accumulation were elucidated, as were the mechanisms of fouling prevention and toxicity of chemical components to marine organisms.(13, 14) This knowledge allowed for the development of more advanced coating compositions, such as leaching or ablative coatings.(15)

In 1971, a British patent revolutionized maritime fouling research.(16) Milne and Hails developed a "self-polishing copolymer" composition containing a potent new biocide, tributyltin, TBT, in the form of a metal acrylate, which allowed ships to go up to five years before needing dry dock. This astonishing find, dubbed by many as the end-goal in fouling research, now shifted new exploration into improving ship speed or

controlling/improving ablation rates rather than focusing on novel anti-fouling or biocidal components.(17) The era of TBT was short-lived, however, when many shocking discoveries came forward about the effects of the biocide on marine life in the mid-90s,(18) a finding which prompted outcries and global protests. TBT is now considered to be "one of the most toxic compounds ever deliberately introduced to a marine environment by mankind."(2, 19) It was found that extremely low concentrations of tributyltin can cause defective shell growth in the oyster *Crassostrea gigas* (at a concentration of >20 ng/L) and development of male characteristics in female genitalia (imposex behavior) in the dog whelk *Nucella lapillus* at 1 ng/L.(18, 20) Unfortunately, the toxicity was not just limited to marine anthropods. Recent studies have shown that wild, dead sea otters and stranded bottlenose dolphins can possess extremely high levels of tributyltin in their livers.(21) TBT also tends to bioaccumulate up to higher ranking predators, including commercially fished tuna.(22) There have even been reports of TBT effecting large aquatic mammals, where a link between TBT concentration and hearing loss in whales was recently discovered.(23) High levels were also discovered in the corpses of killer whales who were intentionally stranding themselves.(24) A draft Assembly Resolution prepared by the Marine Environmental Protection Committee (MEPC) of the International Maritime Organization (IMO) proposed a global ban on the use of organotin compounds in antifouling paints at the 21st regular session in November 1999, effective 2008. Unfortunately, due to the long persistence time of TBT in marine silt and water (half-life ranging from several days in water near the surface, to several weeks in aerobic soils and several years in anaerobic solids),(25, 26) it is continuing to effect marine life to this day and is expected to do so for several decades.(27, 28)

Recent development of modern copper-based self-polishing (see Figure 1.1 for a schematic of a self-polishing coating) or leaching (see Figure 1.2 for a schematic of a biocide-leaching coating) coatings, generally produced from acrylic or methacrylic

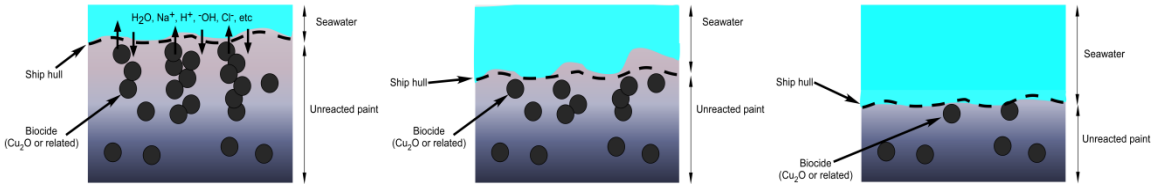


**Figure 1.1**. Ablative, or "self-polishing," coating deteriorating and releasing biocide load as a function of time from initial stage (left) to intermediate stage (middle) and final stage (right).

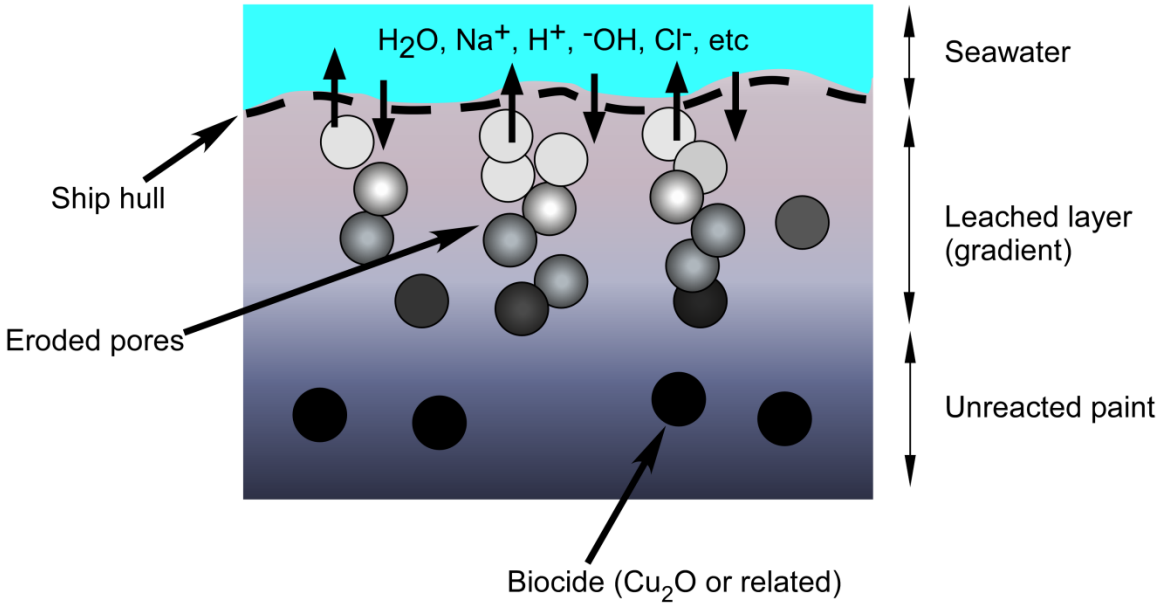


**Figure 1.2**. Biocide-leaching coating.

polymer formulations, show promise in that they are much less toxic than TBT, and can provide long times between dry dock. The state-of-the-art success and research of copper-based ablative formulations, which generally contain $Cu_2O$, CuSCN or metallic

copper, may be useful for modern commercial and military applications, however a few countries, including Scandinavia, and even a few states like California have started monitoring and limiting docking of copper-painted ships in their harbors.(25, 26) Many experts, both academic and military, believe it is only a matter of time before these copper-based formulations will be banned internationally just as TBT was,(17) which shifts the modern research focus into non-metal/non-biocide formulations.

Understandably, modern anti-fouling research is now largely based on non-metal based coatings, either of the "non-fouling" (see Figure 1.3) or "fouling release" (see

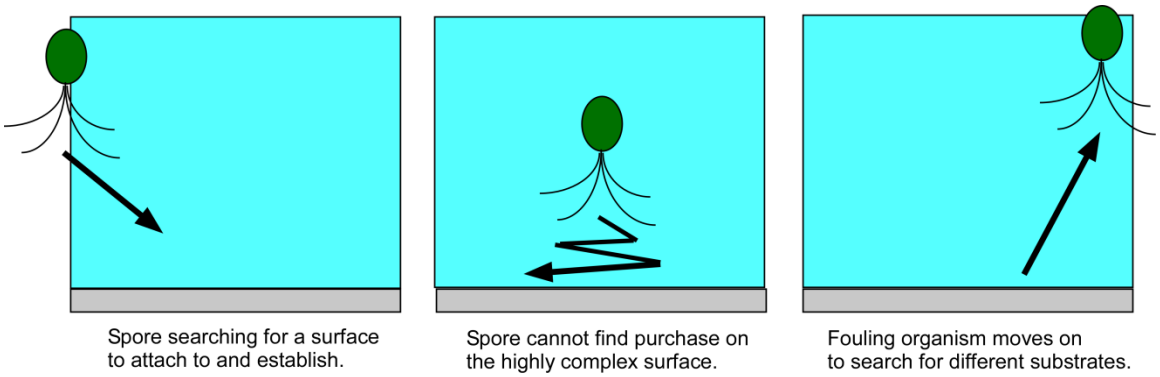


**Figure 1.3**. Schematic representation of a non-fouling coating with an algae spore acting as the fouling organism.

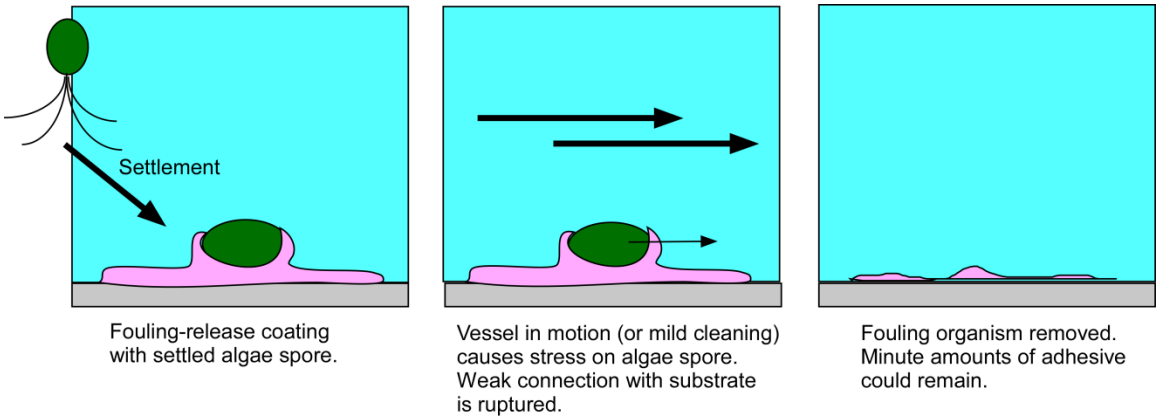


**Figure 1.4**. Schematic representation of a fouling release coating with an algae spore acting as the fouling organism.

Figure 1.4) categories. However, it should be noted, that there is ongoing research regarding environmentally-benign biocide formulations (Figure 1.5).(29) Non-fouling coatings, by definition, prevent the initial fouling of marine organisms, and therefore, ultimate build up of a fouling community, through a variety of mechanisms. Fouling release coatings are readily fouled, but retain special chemical and mechanical properties

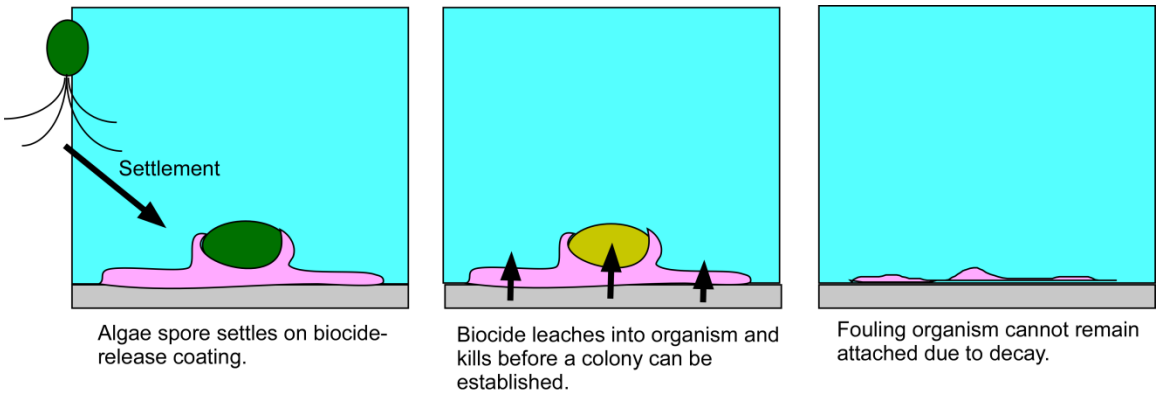


**Figure 1.5**. Schematic representation of a biocide-release coating with an algae spore acting as the fouling organism.

which allow weak attachments with fouling organisms.(30-32) Therefore, outside forces, from drag or mechanical cleaning, can easily release the weakly-bound fouling organisms.(33)

The mechanisms for fouling, which are still largely unknown and are not only species-dependent but surface-dependent, are only beginning to be understood on a molecular level. Modern research into fouling biology has shown that a mixture of excreted extracellular polymers, including polysaccharides, lipopolysaccharides, proteins and nucleic acids, form a kind of biological "cement" which allows organisms to adhere to surfaces.(34) Knowledge of this how adhesive sticks to surfaces in addition to the chemical make-up and crosslinking mechanisms is extremely useful in the generation of

anti-fouling coatings. Research into non-toxic fouling release or anti-fouling coatings has demonstrated that there are a wide array of characteristics that influence anti-biofouling ability. Fouling organisms tend to stick more readily to hydrophobic surfaces, including Teflon™, rather than hydrophilic surfaces.(35-37) Properties such as surface roughness,(38-40) topography,(41) free energy,(42, 43) polymer composition,(44-46) and the mechanical properties of the bulk substrate(47) all play large roles in inhibiting or promoting adhesion of biomacromolecules and, thereby, whole organisms, onto substrates.(48) An interesting switching behavior between hydrophobicity and hydrophilicity can be generated for responsive nanocomposite surfaces.(49) Surfaces made from amphiphilic crosslinked networks of poly(ethylene glycol) (PEG) and hyperbranched fluoropolymers(50-54) or linear block fluorocopolymers containing PEG-based segments,(44, 45, 55-57) have demonstrated excellent anti-fouling ability. Polymers composed of polydimethylsiloxane (PDMS),(17, 47, 58) hybrid xerogels,(59, 60) and zwitterionic block copolymers(61-66) undergo self-cleaning in water. Interestingly, lithographically micropatterned PDMS surfaces further inhibit fouling organisms from attaching to surfaces,(40, 67) indicating that surface features are as important as composition in developing anti-biofouling coatings. The major theme in these discoveries has been that high degrees of complexity are needed to combat the various mechanisms that fouling organisms rely upon for adhesion to substrates.

Previous work in our lab has shown that hyperbranched fluoropolymers crosslinked with polyethylene glycol (HBFP-PEG, see Figure 1.6 for 1$^{st}$ generation) form

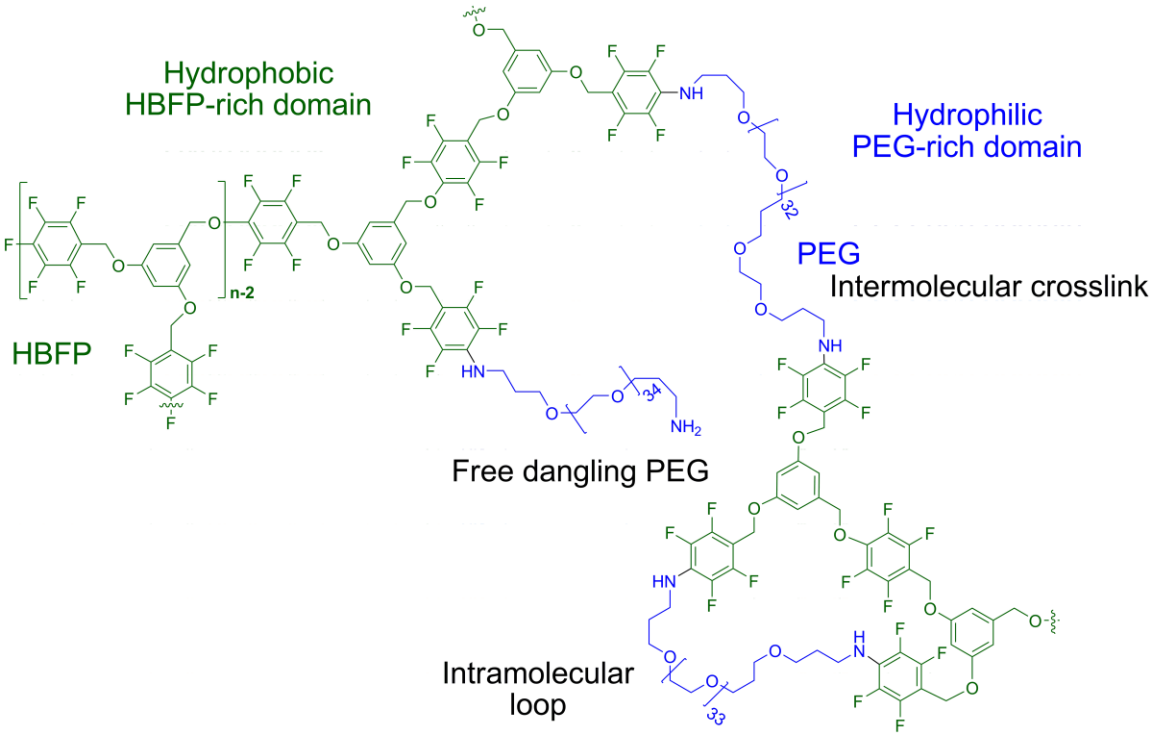


**Figure 1.6**. HBFP-PEG 1st generation network showing the variety of domains and crosslinks.

phase-segregated domains on the nano- and microscales.(50-54) The formation of an amphiphilically-, morphologically- and topographically-complex surface environment as a result of the phase segregation is believed to be responsible for inhibiting biomacromolecule adsorption and adhesion of *Ulva* algae spores.(17, 68, 69) The HBFP-PEG system also possesses interesting mechanical(70, 71) and host-guest properties.(72) Despite HBFP-PEG's excellent ability to resist adhesion, the fluorinated polymer domain is relatively expensive, difficult to produce and has unknown toxicity or bioaccumulation data. These unfortunate factors are true of all fluoropolymers currently being researched in this area. The primary research conducted in this dissertation, therefore, has been the 1) duplication of the successes of the amphiphilic HBFP-PEG coating system using new polymer compositions, 2) exploration of rapid crosslinking methods, such as those

provided by UV curing, 3) expanding the types of materials that can achieve similar degrees of surface complexities, and 4) doing so by using common, commercially-available components.

Strategies into the development of analogs to the HBFP-PEG system were analyzed using a variety of different methods. These novel coating analogs were designed and synthesized in order to exhibit similar surface topography and compositional heterogeneity to the original HBFP-PEG films, and provide similar anti-biofouling behavior. For example, in **Chapter 2**, a combinatorial series of thiol-ene generated amphiphilic films were prepared by the crosslinking of varying wt% of 4-armed poly(ethylene glycol) tetrathiol and equivalents of pentaerythritol tetrakis(3-mercaptopropionate) (PETMP) with alkene-modified Boltorn polyesters. The Boltorn-alkene components were prepared through the esterification between commercially available Boltorn H30™ and 3-butenoic acid. The thermomechanical attributes of the films were analyzed, showing an increase in $T_g$ with an increase in PEG wt%, regardless of PETMP concentration. The films were then studied for their bulk mechanical properties in both the dry and wet state, where it was found that Young's modulus is the highest at 0.75 eq SH/ene. Young's modulus did reduce slightly when wetted at constant PEG or constant PETMP, however ultimate tensile strength increased at constant PETMP concentration. The nanoscopic surface features were investigated using atomic force microscopy and contact angle analysis, where it was observed that the surface of the amphiphilic films increased in nanoscopic roughness with increasing PEG wt%. A series of coatings were then prepared at a low constant PETMP concentration with varying PEG wt% (0-35 wt%) and they were tested for anti-biofouling character and fouling release

ability against *Ulva* marine algae, where the films have a vastly decreased spore settlement and growth when compared to commercial PDMS coatings.

In **Chapter 3**, the synthesis of a non-fluorinated, non-PEGylated analog of the HBFP-PEG system was performed. It was hypothesized that the non-ionic polar polymer, poly(*N*-vinylpyrrolidinone) (PNVP), would work as a durable replacement for the hydrophilic PEG of the original system and that the hydrophobic polymer polyisoprene (PIp) could be used as a low surface energy, potentially multi-crosslinkable analog of HBFP. In the HBFP-PEG system, two homopolymers were blended together and crosslinked using vulcanization methods during their phase segregation, driven by differences in composition and macromolecular topology. The highly branched architecture of the HBFP, which provided large numbers of chemically reactive chain ends, allowed for rapid, kinetic trapping of the phase segregation events before equilibrium was reached. The new design differs not only in the chemical compositions (PIp for HBFP and PNVP for PEG), but also in the macromolecular architecture. Rather than working with two homopolymers, we chose to employ a block copolymer, which restricts the degree of phase segregation by covalently pre-attaching the incompatible hydrophobic and hydrophilic polymer chains prior to crosslinking.

In **Chapter 4**, a similar block copolymer system, PEO-*b*-PIp, was investigated. Two RAFT-capable PEO macro-CTAs, 2 and 5 kDa, were prepared and used for the polymerization of isoprene which yielded well-defined block copolymers of varied lengths and compositions. GPC analysis of the PEO macro-CTAs and block copolymers showed remaining unreacted PEO macro-CTA. Mathematical deconvolution of the GPC chromatograms allowed for the estimation of the blocking efficiency, about 50% for the 5

kDa PEO macro-CTA and 64% for the 2 kDa CTA. Self assembly of the block copolymers in both water and decane was investigated and the resulting micellar and inverse micellar assemblies, respectively, were analyzed with DLS, AFM, and TEM to ascertain their dimensions and properties. Assembly of PEO-*b*-PIp block copolymers in aqueous solution resulted in well-defined micelles of varying sizes while the assembly in hydrophobic, organic solvent resulted in the formation of different morphologies including large aggregates and well-defined cylindrical and spherical structures. Additional investigation into the thiol-ene based crosslinking of PEO-*b*-PIp films and their potential anti-fouling ability was performed using fluorescently-tagged biomolecule adsorption assays.

During the studies of these analogs, several discoveries were made with the original HBFP-PEG system on which the dissertation author is listed as co-author. Since the work was performed in conjunction with the dissertation author and is pertinent to the dissertation, the work is included in the Appendices. In **Appendix 1**, nanocompositing materials, specifically carbon nanotubes and nanoscopic silica, were either physically mixed or engineered to be phase-specific for either the HBFP domain or the PEG domain. The nanocomposited HBFP-PEG materials were then subjected to a variety of mechanical tests in order to see how the compositing agents effected modulus in either dry or wet environments. Additional advanced investigations into the unique mechanical properties of HBFP-PEG were performed using solid-state NMR, as can be observed in **Appendix 2**. At varying wt% PEG, the wetted film acts as either a structurally-reinforced material (sub-45 wt%) or as a mechanically-weakened hydrogel (>55 wt%). The mechanism of the structural reinforcing was probed using a variety of advanced solid

state NMR techniques, providing information into the unique mechanical properties of the HBFP-PEG material.

**References**

(1) Rouhi, A. M. (1998) The squeeze on tributyltins. *Chemical and Engineering News 76*(14), 41-42.

(2) Howell, D.; Behrends, B. (2010) Consequences of anti-fouling coatings - The chemist's perspective. In *Biofouling*, Dürr, S.; Thomason, J. C., Eds. Wiley-Blackwell: Oxford, pp 226-242.

(3) Athenaeus *The Deipnosophists, or, Banquet of the Learned of Athenæus*. Vol. 1, Book V, Chapter 40.

(4) The Generall Historie of Virginia, New England and the Summer Isles, together with the True Travels, Adventures, and Observations, and a Sea Grammar. In *The Travels of Captaine John Smith*, MacLehose, J., Ed. MacMillan: Glasgow, 1907; Vol. II, p 235.

(5) Morison, S. E. (1942) *Admiral of the Ocean Sea - A Life of Christopher Columbus*. Little, Brown and Co: Camden, NJ.

(6) WHOI (1952) *Marine fouling and its prevention; prepared for Bureau of Ships, Navy Dept.* Woods Hole Oceanographic Institution.

(7) Howell, D.; Behrends, B. (2006) A methodology for evaluating biocide release rate, surface roughness and leach layer formation in a TBT-free, self-polishing antifouling coating. *Biofouling 22*(5), 303-315.

(8) Lavery, B. (2000) *The Arming and Fitting of English Ships of War 1600-1815*.

(9) Tarr, J. G.; Wonson, A. H. Paint for ships' bottoms. (1863).

(10) Mallet, R. (1872) On the Corrosion and Fouling of Iron Ships. *Trans. Inst. Nav. Arch. 13*, 90-162.

(11) Wehmhoff, B. L.; Jordan, A. M.; Knight, H. C. (1929) Hot Plastic Ship Bottom Paints. *Chem. Warfare Service 15*, 675-680.

(12) Ingram, H. A. (1944) Research in the Bureau of Ships. *J. Appl. Phys. 15*, 215-220.

(13) Bray, A. W., Report on the toxic action of certain chemical compounds on marine organisms. **1919**; p 27. (Privately published).

(14) Visscher, J. (1927) Nature and extent of fouling of ships' bottoms. *Bull. Bur. Fish 43*, 193-252.

(15) Ketchum, B. H.; Ferry, J. D.; Redfield, A. C.; Burns, A. E. (1945) Evaluation of antifouling paints by leaching rate determinations. *Ind. and Eng. Chem., Int. Ed. 37*, 456-460.

(16) Milne, A.; Hails, G. British Patent. 1,457,590, (1971).

(17) Anderson, C.; Atlar, M.; Callow, M. E.; Candries, M.; Milne, A.; Townsin, R. L. (2003) The development of foul-release coatings for seagoing vessels. *Journal of Marine Design and Operations* (B4), 11-23.

(18) Swain, G. (1998) *Proceedings of the Internation Symposium on Sea Water Drag Reduction*. The Naval Undersea Warfare Center: Newport, p 155-161.

(19) Goldberg, E. (1986) TBT as an environmental dilemma. *Environment 28*(8), 42-44.

(20) Artham, T.; Sudhakar, M.; Venkatesan, R.; Madhavan Nair, C.; Murty, K. V. G. K.; Doble, M. (2009) Biofouling and stability of synthetic polymers in sea water. *International Biodeterioration & Biodegradation 63*(7), 884-890.

(21) Murata, S.; Takahashi, S.; Agusa, T.; Thomas. N.J.; Kannan, K.; Tanabe, S. (2008) Contamination status and accumulation profiles of organotins in sea otters (Enhydra lutris) found dead along the coasts of California, Washington, Alaska (USA), and Kamchatka (Russia). *Mar. Pollut. Bull. 56*(4), 641-649.

(22) Ueno, D.; Inoue, S.; Takahashi, S. (2006) Global pollution monitoring of butyltin compounds using skipjack tuna as a bioindicator. *Environ. Poll. 127*(1), 1.

(23) Santos-Sacchi, J.; Song, L.; Zheng, J.; Nuttall, A. L. (2006) Control of Mammalian Cochlear Amplification by Chloride Anions. *J. Neurosci. 26*(15), 3992-3998.

(24) Kajiwara, N.; Kunisue, T.; Kamikawa, S.; Ochi, Y.; Yano, S.; Tanabe, S. (2006) Organohalogen and organotin compounds in killer whales mass-stranded in the Shiretoko Peninsula, Hokkaido, Japan. *Mar. Pollut. Bull. 52*(9), 1066-1097.

(25) Batley, G. (1996) The distribution and fate of tributyltin in the marine environment. In *Tributyltin: Case Study of an Environmental Contaminant*, de Mora, S. J., Ed. Cambridge University Press: Cambridge, pp 139-166.

(26) Maguire, R. J. (1996) The occurrence, fate and toxicity of tributyltin and its degradation products in fresh water environments. In *Tributyltin: Case Study of an Environmental Contaminant*, de Mora, S. J., Ed. Cambridge University Press: Cambridge, pp 94-138.

(27) Alzieu, C. (1998) Tributyltin: case study of a chronic contaminant in the coastal environment. *Ocean Coastal Manage. 40*(1), 23-36.

(28) Rudel, H. (2003) Case study: bioavailability of tin and tin compounds. *Ecotox. Environ. Safe. 56*(1), 180-189.

(29) Angarano, M.-B.; McMahon, R. F.; Schetz, J. A. J. (2009) Cannabinoids as inhibitors of zebra mussel (Dreissena polymorpha) byssal attachment: A potentially green antifouling technology. . *Biofouling 25*, 127-138.

(30) Beigbeder, A.; Degee, P.; Conlan, S. L.; Mutton, R. J.; Clare, A. S.; Pettitt, M. E.; Callow, M. E.; Callow, J. A.; Dubois, P. (2008) Preparation and characterisation of

silicone-based coatings filled with carbon nanotubes and natural sepiolite and their application as marine fouling-release coatings. *Biofouling 24*, 291-302.

(31) Majumdar, P.; Lee, E.; Patel, N.; Ward, K.; Stafslien, S. J.; Daniels, J.; Boudjouk, P.; Callow, M. E.; Callow, J. A.; Thompson, S. E. M. (2008) Combinatorial materials research applied to the development of new surface coatings IX: An investigation of novel anti-fouling/fouling-release coatings containing quaternary ammonium salt groups. *Biofouling 24*, 185-200.

(32) Marabotti, I.; Morelli, A.; Orsini, L. M.; Martinelli, E.; Galli, G.; Chiellini, E.; Lien, E. M.; Pettitt, M. E.; Callow, J. A.; Conlan, S. L.; Mutton, R. J.; Clare, A. S.; Kocijan, A.; Donik, C.; Jenko, M. (2009) Fluorinated/siloxane copolymer blends for fouling release: Chemical characteristion and biological evaluation with algae and barnacles. *Biofouling 25*, 481-493.

(33) Kim, J.; Nyren-Erikson, E.; Stafslien, S.; Daniels, J.; Bahr, J.; Chisholm, B. J. (2008) Release characteristics of reattached barnacles to non-toxic silicone coatings. *Biofouling 24*, 313-319.

(34) Flemming, H.-C.; Wingender, J.; Griebe, T.; Mayer, C. (2001) Physico-chemical properties of biofilms. In *Biofilms: Recent advances in their study and control*, Evans, L. V., Ed. Harwood Academic Publishers: Amsterdam, pp 19-34.

(35) Dobretsov, S. (2010) Marine Biofilms. In *Biofouling*, Dürr, S.; Thomason, J. C., Eds. Wiley-Blackwell: Oxford, pp 123-136.

(36) Fletcher, M.; Loeb, G. (1979) Influence of substratum characteristics on the attachment of marine psuedomonas to solid surfaces. *Applied Environmental Microbiology 29*, 107-118.

(37) Railkin, A. I. (2004) *Marine Biofouling: Colonization Processes and Defenses*. CRC Press: Boca Raton.

(38) Chambers, L. D.; Stokes, K. R.; Walsh, F. C.; Wood, R. J. K. (2006) Modern approaches to marine antifouling coatings. *Surf. Coat. Technol. 201*(6), 3642-3652.

(39) Hovgaard, M. B.; Rechendorff, K.; Chevallier, J.; Foss, M.; Besenbacher, F. (2008) Fibronectin adsorption on tantalum: The influence of nanoroughness. *J. Phys. Chem. B 112*(28), 8241-8249.

(40) Schumacher, J. F.; Long, C. J.; Callow, M. E.; Finlay, J. A.; Callow, J. A.; Brennan, A. B. (2008) Engineered nanoforce gradients for inhibition of settlement (attachment) of swimming algal spores. *Langmuir 24*(9), 4931-4937.

(41) Genzer, J.; Efimenko, K. (2006) Recent developments in superhydrophobic surfaces and their relevance to marine fouling: A review. *Biofouling 22*(5), 339-360.

(42) Callow, J. A.; Callow, M. E.; Ista, L. K.; Lopez, G.; Chaudhury, M. K. (2005) The influence of surface energy on the wetting behaviour of the spore adhesive of the marine alga Ulva linza (synonym Enteromorpha linza). *J. R. Soc. Interface 2*(4), 319-325.

(43) Schmidt, D. L.; Brady, R. F.; Lam, K.; Schmidt, D. C.; Chaudhury, M. K. (2004) Contact angle hysteresis, adhesion, and marine biofouling. *Langmuir 20*(7), 2830-2836.

(44) Krishnan, S.; Wang, N.; Ober, C. K.; Finlay, J. A.; Callow, M. E.; Callow, J. A.; Hexemer, A.; Sohn, K. E.; Kramer, E. J.; Fischer, D. A. (2006) Comparison of the fouling release properties of hydrophobic fluorinated and hydrophilic PEGylated block copolymer surfaces: Attachment strength of the diatom Navicula and the green alga Ulva. *Biomacromolecules 7*(5), 1449-1462.

(45) Krishnan, S.; Ayothi, R.; Hexemer, A.; Finlay, J. A.; Sohn, K. E.; Perry, R.; Ober, C. K.; Kramer, E. J.; Callow, M. E.; Callow, J. A.; Fischer, D. A. (2006) Anti-biofouling properties of comblike block copolymers with amphiphilic side chains. *Langmuir 22*(11), 5075-5086.

(46) Ma, H. W.; Hyun, J. H.; Stiller, P.; Chilkoti, A. (2004) "Non-fouling" oligo(ethylene glycol)-functionalized polymer brushes synthesized by surface-initiated atom transfer radical polymerization. *Adv. Mater. 16*(4), 338-+.

(47) Wendt, D. E.; Kowalke, G. L.; Kim, J.; Singer, I. L. (2006) Factors that influence elastomeric coating performance: the effect of coating thickness on basal plate morphology, growth and critical removal stress of the barnacle Balanus amphitrite. *Biofouling 22*(1), 1-9.

(48) Aldred, N.; Clare, A. S. (2008) The adhesive strategies of cyprids and development of barnacle-resistant marine coatings. *Biofouling 24*(5), 351-363.

(49) Liao, K.-S.; Fu, H.; Wan, A.; Batteas, J. D.; Bergbreiter, D. E. (2009) Designing surfaces with wettability that varies in response to solute identity and concentration. *Langmuir 25*, 26-28.

(50) Bartels, J. W.; Cheng, C.; Powell, K. T.; Xu, J. Q.; Wooley, K. L. (2007) Hyperbranched fluoropolymers and their hybridization into complex amphiphilic crosslinked copolymer networks. *Macromol. Chem. Phys. 208*(15), 1676-1687.

(51) Gan, D. J.; Mueller, A.; Wooley, K. L. (2003) Amphiphilic and hydronhobic surface patterns generated from hyperbranched fluoropolymer/linear polymer networks: Minimally adhesive coatings via the crosslinking of hyperbranched fluoropolymers. *J. Polym. Sci., Part A: Polym. Chem. 41*(22), 3531-3540.

(52) Gudipati, C. S.; Finlay, J. A.; Callow, J. A.; Callow, M. E.; Wooley, K. L. (2005) The antifouling and fouling-release perfomance of hyperbranched fluoropolymer (HBFP)-poly(ethylene glycol) (PEG) composite coatings evaluated by adsorption of biomacromolecules and the green fouling alga Ulva. *Langmuir 21*(7), 3044-3053.

(53) Gudipati, C. S.; Greenlief, C. M.; Johnson, J. A.; Prayongpan, P.; Wooley, K. L. (2004) Hyperbranched fluoropolymer and linear poly(ethylene glycol) based Amphiphilic crosslinked networks as efficient antifouling coatings: An insight into the surface compositions, topographies, and morphologies. *J. Polym. Sci., Part A: Polym. Chem. 42*(24), 6193-6208.

(54) Powell, K. T.; Cheng, C.; Wooley, K. L.; Singh, A.; Urban, M. W. (2006) Complex amphiphilic networks derived from diamine-terminated poly(ethylene glycol) and benzylic chloride-functionalized hyperbranched fluoropolymers. *J. Polym. Sci., Part A: Polym. Chem. 44*(16), 4782-4794.

(55) Nguyen, T. L. U.; Eagles, K.; Davis, T. P.; Barner-Kowollik, C.; Stenzel, M. H. (2006) Investigation of the influence of the architectures of poly(vinyl pyrrolidone) polymers made via the reversible addition-fragmentation chain transfer/macromolecular design via the interchange of xanthates mechanism on the stabilization of suspension polymerizations. *J. Polym. Sci., Part A: Polym. Chem. 44*(15), 4372-4383.

(56) Yarbrough, J. C.; Rolland, J. P.; DeSimone, J. M.; Callow, M. E.; Finlay, J. A.; Callow, J. A. (2006) Contact angle analysis, surface dynamics, and biofouling characteristics of cross-linkable, random perfluoropolyether-based graft terpolymers. *Macromolecules 39*(7), 2521-2528.

(57) Youngblood, J. P.; Andruzzi, L.; Ober, C. K.; Hexemer, A.; Kramer, E. J.; Callow, J. A.; Finlay, J. A.; Callow, M. E. (2003) Coatings based on side-chain ether-linked poly(ethylene glycol) and fluorocarbon polymers for the control of marine biofouling. *Biofouling 19*, 91-98.

(58) Hoipkemeier-Wilson, L.; Schumacher, J.; Carman, M.; Gibson, A.; Feinberg, A.; Callow, M.; Finlay, J.; Callow, J.; Brennan, A. (2004) Antifouling potential of lubricious, micro-engineered, PDMS elastomers against zoospores of the green fouling alga Ulva (Enteromorpha). *Biofouling 20*(1), 53-63.

(59) Tang, Y.; Finlay, J. A.; Kowalke, G. L.; Meyer, A. E.; Bright, F. V.; Callow, M. E.; Callow, J. A.; Wendt, D. E.; Detty, M. R. (2005) Hybrid xerogel films as novel coatings for antifouling and fouling release. *Biofouling 21*(1), 59-71.

(60) McMaster, D.; Bennett, S.; Tang, Y.; Finlay, J.; Kowalke, G.; Nedved, B.; Bright, F.; Callow, M.; Callow, J.; Wendt, D.; Hadfield, M.; Detty, M. (2009) Antifouling character of 'active' hybrid xerogel coatings with sequestered catalysts for the activation of hydrogen peroxide. *Biofouling 25*(1), 21-33.

(61) Zhang, Z.; Chao, T.; Chen, S. F.; Jiang, S. Y. (2006) Superlow fouling sulfobetaine and carboxybetaine polymers on glass slides. *Langmuir 22*(24), 10072-10077.

(62) Zhang, Z.; Chen, S. F.; Chang, Y.; Jiang, S. Y. (2006) Surface grafted sulfobetaine polymers via atom transfer radical polymerization as superlow fouling coatings. *Journal of Physical Chemistry B 110*(22), 10799-10804.

(63) Cheng, G.; Zhang, Z.; Chen, S. F.; Bryers, J. D.; Jiang, S. Y. (2007) Inhibition of bacterial adhesion and biofilm formation on zwitterionic surfaces. *Biomaterials 28*(29), 4192-4199.

(64) Li, G. Z.; Xue, H.; Gao, C. L.; Zhang, F. B.; Jiang, S. Y. (2010) Nonfouling Polyampholytes from an Ion-Pair Comonomer with Biomimetic Adhesive Groups. *Macromolecules 43*(1), 14-16.

(65) Yang, W.; Zhang, L.; Wang, S. L.; White, A. D.; Jiang, S. Y. (2009) Functionalizable and ultra stable nanoparticles coated with zwitterionic poly(carboxybetaine) in undiluted blood serum. *Biomaterials 30*(29), 5617-5621.

(66) Zhang, Z.; Finlay, J. A.; Wang, L. F.; Gao, Y.; Callow, J. A.; Callow, M. E.; Jiang, S. Y. (2009) Polysulfobetaine-Grafted Surfaces as Environmentally Benign Ultralow Fouling Marine Coatings. *Langmuir 25*(23), 13516-13521.

(67) Carman, M. L.; Estes, T. G.; Feinberg, A. W.; Schumacher, J. F.; Wilkerson, W.; Wilson, L. H.; Callow, M. E.; Callow, J. A.; Brennan, A. B. (2006) Engineered antifouling microtopographies - correlating wettability with cell attachment. *Biofouling 22*(1), 11-21.

(68) von Byern, J.; Klepal, W. (2006) Adhesive mechanisms in cephalopods: A review. *Biofouling 22*(5), 329-338.

(69) Wiegemann, M. (2005) Adhesion in blue mussels (Mytilus edulis) and barnacles (genus Balanus): Mechanisms and technical applications. *Aquat. Sci. 67*(2), 166-176.

(70) Xu, J.; Bohnsack, D. A.; Mackay, M. E.; Wooley, K. L. (2007) Unusual mechanical performance of amphiphilic crosslinked polymer networks. *J. Am. Chem. Soc. 129*(3), 506-507.

(71) Xu, J.; Bartels, J. W.; Bohnsack, D. A.; Tseng, T.-C.; Mackay, M. E.; Wooley, K. L. (2008) Hierarchical Inorganic-Organic Nanocomposites Possessing Amphiphilic and

Morphological Complexities: Influence of Nanofiller Dispersion on Mechanical Performance. *Adv. Funct. Mater. 18*(18), 2733-2744.

(72) Brown, G. O.; Bergquist, C.; Ferm, P.; Wooley, K. L. (2005) Unusual, promoted release of guests from amphiphilic cross-linked polymer networks. *J. Am. Chem. Soc. 127*(32), 11238-11239.

# Chapter 2

## Anti-fouling PEGylated thiol-ene crosslinked networks

[Portions of this work have been submitted for publication as Jeremy W. Bartels, Phillip M. Imbesi, John A. Finlay, Christopher Fidge, Jun Ma, Jonathan E. Seppala, Andreas M. Nyström, Michael E. Mackay, John A. Callow, Maureen E. Callow and Karen L. Wooley to *ACS Applied Materials and Interfaces*, **2010**]

### Abstract

A combinatorial series of thiol-ene generated amphiphilic films were prepared by crosslinking alkene-modified Boltorn polyesters with varying wt% of 4-armed poly(ethylene glycol) (PEG) tetrathiol and varying equivalents of pentaerythritol tetrakis(3-mercaptopropionate) (PETMP). The Boltorn-alkene components were prepared through the esterification of commercially available Boltorn H30™ with 3-butenoic acid. The subsequent crosslinking of the films was monitored using IR spectroscopy, where it was found that near-complete consumption of both thiol and alkene occurs around 0.75 eq alkene/SH. The thermomechanical attributes of the films were analyzed, showing an increase in $T_g$ with an increase in 4-armed PEG-tetrathiol wt%, regardless of PETMP concentration. The bulk mechanical properties in both dry and wet state were studied, where it was found that Young's modulus was the highest at

0.75 eq SH/ene. The Young's modulus was slightly lower for wet films at constant PEG or constant PETMP, however, ultimate tensile strength increased when PETMP was constant and the PEG concentration was increased. The nanoscopic surface features were probed using Atomic Force Microscopy (AFM), where it was observed that the surface of the amphiphilic films became more nanoscopically rough with increasing PEG wt%. A series of coatings were then prepared at a low PETMP concentration with varying PEG wt% (0-35 wt%) and tested for anti-fouling and fouling-release activity against the marine alga *Ulva.* Spore settlement densities were lower on these films compared to that on standards of polydimethylsiloxane and glass.

## Introduction

Over the past decade, there has been increased effort to devise non-biocidal anti-fouling and fouling-release coatings that inhibit adhesion and/or promote detachment of marine fouling organisms on the hulls of ships and underwater structures. Biocidal metal based paints, such as those containing tributylytin (TBT), which are banned from maritime application, or copper oxide formulations, which are currently in use, have been shown to be detrimental to many marine organisms.(1, 2) While modern efforts toward non-toxic, anti-fouling coatings have focused primarily on fluoropolymers(3-6) and silicone elastomers,(7-10) it should be noted that there is a strong interest in novel formulations involving xerogels,(11) zwitterionic polymer coatings,(12-14) and PEGylated polymer compositions(3-6, 15, 16). While formulation and chemistry of the substrate plays a vital role, additional studies have established that surface and bulk properties, including surface free energy,(17) mechanical properties/modulus,(18) wettability,(19) and roughness,(19-21) have a profound impact on both nano- and microscales. It is anticipated that a combination of these factors, giving the polymer film a high degree of complexity, are needed to combat the various mechanisms that are used by fouling organisms for settlement and adhesion to substrates.

Novel polymer coatings developed by thiol-ene UV photopolymerization methods have many attractive properties which can provide high extents of complexity, giving potential promise for anti-fouling applications. The thiol-ene technique, used industrially since the 1970's,(22, 23) has recently demonstrated its importance(24) where it was employed as a "click" method between small molecules and larger macromolecules such as polymers(25) and proteins.(26) This approach has also been used to build complex

nanostructures such as dendrimers(27) and star polymers.(28) The thiol-ene process is also attractive for making bulk films because it is insensitive to oxygen,(29) gives low shrinkage,(30) imparts high thermo-stability, and proceeds to relatively high conversion, all while crosslinking at a rate that is as rapid as traditional UV-crosslinking.(31-33) The thioether bonds in the crosslinked network lend interesting mechanical properties and provide chemical insensitivity to the final products.(31) Bulk thiol-ene crosslinking has been used for nanoimprint lithography,(34, 35) inks,(36) adhesives(37) and biomaterials.(16, 38) While traditional UV photocured films have several examples in modern anti-fouling literature,(39, 40) at the time of publishing, there are no known thiol-ene generated coatings that have been tested for marine anti-fouling performance.(41)

Selection of appropriate components is key when constructing an advanced thiol-ene coating. Traditionally, thiol-ene coatings are prepared by crosslinking multi-thiol and multi-ene mixtures, comprised of small molecules, or a combination of small molecules and macromolecules.(31) Modern compositions utilizing the branching monomer 2,2-bis(hydroxymethyl) propionate (Bis-MPA) can readily create highly branched and functionalized polyesters, such as dendritic Boltorn™ polyols, which have special rheological and mechanical properties.(32) The Boltorn polyols, or dendronized versions of poly(bis-MPA), contain a large number of hydroxyl groups, which can be readily esterified to form either thiol-functionalized(42, 43) or alkene-functionalized(44) macromolecules. Bis-MPA can be grown divergently up to several generations from a variety of cores,(45, 46) specialized molecules,(47) and even from polymer backbones,(47-50). Functionalized Boltorn macromolecules have been used in targeted drug delivery,(51, 52) packaging of Paclitaxel(53, 54) and Doxorubicin,(55) and vesicle preparation.(49) Boltorn polymers have been used extensively in thiol-ene based

coatings,(43, 56, 57) where they provide unique mechanical properties including narrow $T_g$'s,(58) and thermal stability.(56) Fluorinated Boltorn thiol-ene coatings have also been investigated,(59) in addition to coatings containing organoclay nanocomposites for improved strength.(44)

Previous investigations by our laboratory into coatings comprised of hyperbranched fluoropolymers crosslinked with poly(ethylene glycol), (HBFP-PEG), led into examination of alternative coatings prepared by thiol-ene crosslinking of a highly branched, alkenylated Boltorn H30 polymer with thiol-modified PEG, in the presence of a small molecule crosslinker to assist with mechanical properties. The interest in duplicating the success of HBFP-PEG comes from the wide range of unique properties of the coatings, including anti-fouling properties,(3, 4, 60) uncommon mechanical behavior,(61, 62) and interesting host-guest interactions with small organic molecules.(63) The HBFP-PEG mode of action for biofouling prevention is believed to be a combination of complex surface topographies, morphologies, and compositions over nano- and microscopic dimensions. These coatings are not without fault, as they come from expensive reagents, are difficult to synthesize, lack optical translucence and take long periods of time to adequately crosslink. Therefore, exploration into thiol-ene based alternatives was conducted to develop highly PEGylated coatings with affordable, commercially available precursors, that utilize "click" methods, which yield films of high degrees of optical transparency, and that can rapidly crosslink, without compromising the tensile strength and surface complexity observed in the HBFP-PEG films. In this work, the Boltorn H30 polyol was per-enylated using simple esterification chemistry to yield Boltorn-ene, which was subsequently photocrosslinked in a combinatorial array with

varying wt% of 10 kDa 4-armed PEG tetrathiol (0, 5, 15 and 25 wt%) and varying eq SH/ene pentaerythritol tetrakis(3-mercaptopropionate) (PETMP) small molecule crosslinker (0.00, 0.25, 0.50, 0.75 and 1.00 eq SH/ene). Reaction completion was monitored *via* IR spectroscopy. The film surface and bulk properties were characterized by Atomic Force Microscopy, Contact Angle, and tensile/ thermomechanical experiments. Additionally, a comprehensive anti-fouling study was performed against *Ulva* algae on Boltorn-PEG films across a wide range of PEG wt% (0-35 wt%).

## Experimental

**Instrumentation.** Infrared spectra were obtained from a Perkin–Elmer Spectrum BX FTIR system as neat films on NaCl plates. $^{1}$H-NMR (300 MHz) and $^{13}$C-NMR (75 MHz) spectra were recorded on a Varian Mercury 300 MHz spectrometer using the solvent as an internal reference. Tetrahydrofuran-based Gel Permeation Chromatography (GPC(THF)) was conducted on a Waters Chromatography, Inc. (Milford, MA) model 1515, equipped with a Waters model 5414 differential refractometer and a three-column set of Polymer Laboratories, Inc. (Amherst, MA) gel mixed-bed styrene-divinylbenzene columns ($PL_{gel}$ 5$\mu$m Mixed C, 500 Å, and $10^4$ Å, 300 x 7.5 mm columns). The system was equilibrated at 35 ºC in THF, which served as the polymer solvent and eluent (flow rate set to 1.00 mL/min). Polymer solutions were prepared at a known concentration (*ca*. 3 mg/mL) and an injection volume of 200 µL was used. Data collection and analysis was performed with Breeze software. The differential refractometer was calibrated with standard polystyrene material (SRM 706 NIST), of known refractive index increment,

dn/dc, (0.184 mL/g). The dn/dc values of the analyzed polymers were then determined from the differential refractometer response.

UV crosslinking was performed by passing pre-gel coated slides through a Fusion UV 300S conveyor system equipped with a H bulb (300 Watts/inch) at a speed of 1 m/min for a single pass.

Glass transition temperatures ($T_g$) were measured by Differential Scanning Calorimetry (DSC) on a Mettler-Toledo DSC822$^e$ (Mettler-Toledo, Inc., Columbus, OH), with a heating rate of 10 ºC/min. Measurements were analyzed using Mettler-Toledo Star SW 7.01 software. The $T_g$ was taken as the midpoint of the inflection tangent, upon the third heating scan. Thermogravimetric analysis was performed under $N_2$ atmosphere using a Mettler-Toledo model TGA/SDTA851$^e$, with a heating rate of 5 ºC/min. Measurements were analyzed using Mettler-Toledo Star SW 7.01 software.

In order to provide additional information into the actual thiol concentration remaining in the Boltorn-PEG films post-crosslinking, an experiment was devised wherein a 1.5 mM solution of the pro-fluorescent molecule, *N*-(7-dimethylamino-4-methylcoumarin-3-yl) maleimide (DACM) in 10 mM pH 7.4 buffer with a minute amount of DMF, was pipetted onto the Boltorn-PEG films and allowed to sit for 2 h. The films were then washed extensively in deionized water, dried, and then imaged using fluorescence microscopy and compared against controls. Optical microscopy was performed on an Nikon Eclipse E200 microscope (Nikon Corp., Tokyo, Japan) under bright-field conditions, and images were collected with an Nikon D-500 digital camera at 4x objective, 1/15 exposure time and ISO 1600. To probe surface thiol concentration, a 1.5 mM solution of the pro-fluorescent molecule, *N*-(7-dimethylamino-4-

methylcoumarin-3-yl) maleimide (DACM) in 10 mM pH 7.0 buffer with a minute amount of DMF, was pipetted onto the Boltorn-PEG films and allowed to sit for 2 h. The films were then washed extensively in deionized water, dried, imaged using fluorescence microscopy and compared against controls. The fluorescence was generated using a Semrock Brightline Calcofluor White Filter cube (CFW-BP01-Clinical-NTE) with an adsorption of 350 nm and emission of 440 nm. The fluorescence properties of DACM are Abs/Em 383/463 nm. The control images were digitally subtracted from the fluorescent images using ImageJ software (NIST).

Tapping-mode AFM measurements were conducted in air with a Nanoscope III BioScope system (Digital Instruments, Santa Barbara, CA) operated under ambient conditions with standard silicon tips [type, OTEPSA-70; length (L), 160 μm; normal spring constant, 50 N/m; resonant frequency, 246–282 kHz].

Contact angles were measured as static contact angles using the sessile drop technique(64) with a Tantec CAM micro-contact-angle meter and the half-angle measuring method. Advancing and receding contact angles ($\theta_a$ and $\theta_r$) of 18 $M\Omega \cdot cm^{-1}$ nanopure water were measured on the films by placing a 2 μL drop on the surface, then increasing or decreasing the drop size by 1 μL, respectively. Dynamic contact angle was measured over three hours in a similar manner, however, in between data points the film was submerged in DI water and prior to measurement the surface was quickly dried with a Kimwipe. The reported values are an average of five such measurements on different regions of the same sample.

Elemental analysis was performed by Midwest Microlabs. A single run was performed on each sample for the elements C, H and S, and the results were contrasted against theoretical concentration values based on component weight percentages.

Tensile tests were performed on the combinatorial Boltorn-PEG series based upon a method adapted from ASTM D882-95a and conducted using a Rheometrics Solids Analyzer, RSA III (TA Instruments, New Castle, DE), at 22 °C at a constant rate of strain of 0.01 $s^{-1}$ (Hencky Model) with an initial grip separation of ~5 mm. For each sample: (1) at least five dry specimens (dimensions: 10 mm x 5 mm x 0.5–1.0 mm) were tested; (2) three pre-swollen specimens (incubation time: >7 d) were tested in an RSA III Immersion Fixture filled with artificial seawater. Only samples in the "C" and "2" series (**C1**, **C2**, **C3**, **C4**, **C5** and **A2**, **B2**, **C2**, **D2**) were tested wet. The tensile modulus ($E_{dry}$ or $E_{wet}$, MPa) was calculated as the slope of the initial linear (Hookean) portion of the stress-strain curve, and the ultimate tensile strength ($\sigma_{UTS}$, MPa) and strain to failure ($\varepsilon_f$, %) were also recorded.

**Materials.** 3-butenoic acid (97%), pentaerythritol tetrakis (3-mercaptopropionate) (PETMP, 97%), 1-hydroxycyclohexylphenyl ketone (99%), vinyltrimethoxysilane (vinyl-TMS, 98%), *N*-(7-dimethylamino-4-methylcoumarin-3-yl) maleimide (98%), 1,4-dioxane (99%), dichloromethane (DCM) (99%), magnesium sulfate (anhydrous, *ReagentPlus*®, ≥99.5%) and toluene (99.8% anhydrous) were obtained from Sigma-Aldrich, Inc. (St. Louis, MO) and were used as received. 4-armed PEG tetrathiol (10,000 Da) was obtained from Laysan Biochem. Boltorn H30™ was supplied by Perstorp. Chloroform-*d* (D, 99.8%) and *d*-MeOH (D, 99.8%) were obtained from Cambridge Isotope Labs. 4-(Dimethylamino)pyridinium 4-toluenesulfonate (DPTS) was prepared using standard

literature procedures.(65, 66) Vinyl-trimethoxysilane-modified glass slides were prepared by submerging fresh microscope slides in a 5 v/v% solution of vinyl-TMS in anhydrous toluene for one hour, followed by copious rinsing with toluene. Argon ultra-high purity grade gas (99.999%) was used as received from Praxair (St. Louis, MO). Coralife® Scientific Grade Marine Salt that was used for the preparation of artificial seawater was mixed according to directions from the manufacturer.

**Boltorn-ene (1).** 30.001 g of Boltorn H30 ($8.57 \times 10^{-3}$ mol, 1.0 eq) was added to a 500 mL round bottom flask equipped with a Teflon-coated stir bar. Toluene (100 mL) was added to the flask, which was fitted with a distillation apparatus, and contents were heated at reflux for an hour to ensure that the polymer was dissolved while residual water was removed *via* azeotropic distillation. DPTS (6.665 g, $2.26 \times 10^{-2}$ mol, 10 wt%) and 3-butenoic acid (38.758 g, $4.50 \times 10^{-1}$ mol, 1.6 eq COOH per Boltorn-OH) were added to the flask, which was then equipped with a condenser and allowed to heat at reflux at a high stir rate for 2 days. After the reaction was complete and slightly cooled, 300 mL of water was added to the mixture and the product was extracted with DCM (3 x 150 mL). The organic layer was dried over anhydrous $MgSO_4$ and then concentrated, yielding 44.1 g of a transparent, thick oil (90% yield). $^1$H NMR spectroscopy showed quantitative conversion. The oil was stored at 4 °C to prevent side-reaction of the alkene groups. $M_n^{NMR}$ = 5700 Da, $M_w^{GPC}$ = 4800 Da (polystyrene equivalent), $M_n^{GPC}$ = 2800 Da (polystyrene equivalent), $M_w/M_n$ = 1.69. $T_g$ = -37 °C. $T_{decomp}$: 427 °C, 94% mass loss. IR = 2944, 2882, 1736, 1650, 1564, 1470, 1222, 1126, 1010, 814, 684, 570 cm$^{-1}$. $^1$H-NMR (300 MHz, $CDCl_3$, ppm): δ 6.0-5.8 (br, —C*H*=$CH_2$, 5.2-5.1 (br, =C*H*$_2$, 4.4-4.1 (br, peripheral —C*H*$_2$-C(O)-), 3.8-3.5 (br, internal —C*H*$_2$-O-C(O)), 3.2-3.1 (br, —C*H*$_2$-

$CH=CH_2$, 1.3-1.1 (br, multiplet -C$H_3$). $^{13}$C-NMR (75 MHz, $CDCl_3$, ppm): δ 206.4, 173.4, 172.2, 170.8, 139.6, 130.6, 128.7, 126.2, 118.5, 107.2, 65.5, 48.8, 46.8, 39.9, 38.7, 25.7, 21.1, 17.7. Elemental analysis: C, 57.21%. H, 6.51%.

**Combinatorial Boltorn-PEG film production.** A combinatorial array of Boltorn-PEG networks were prepared at varying PEG wt% (0, 5, 15 and 25 w/w% of Boltorn-ene, corresponding to **A**, **B**, **C** and **D**, respectively) and PETMP concentrations (0, 0.25, 0.50, 0.75 and 1.0 eq SH/ene, corresponding to **1**, **2**, **3**, **4** and **5**, respectively). Therefore, as an example, film **C3** refers to a crosslinked film with 15 wt% PEG and 0.50 eq SH/ene PETMP concentration. The "SH" refers to thiols in the PETMP crosslinker and not from the PEG-tetrathiol, which are negligible in comparison. The photoinitiator 1-hydroxycyclohexylphenyl ketone was added as 5 w/w% of total solids to all samples.

*Preparation of Boltorn-PEG film **A1***. Boltorn-ene (0.869 g, 1.52 x $10^{-4}$ mol) was mixed with 1-hydroxycyclohexylphenyl ketone (0.0516 g, 2.53 x $10^{-4}$ mol) in a scintillation vial. The vial was charged with 16.0 mL of 1,4-dioxane, and the contents were vortexed until homogeneous. The contents were then syringed (1 mL/slide) onto vinyl-TMS-modified glass slides and the solvent was allowed to evaporate over a 20 min period, producing a thick pre-gel on the surface of the glass slide. The coated slides were then passed through a Fusion UV 300S conveyor system equipped with an H bulb (600 Watts) at a speed of 1 m/min for a single pass. $T_g$ = -17 °C. $T_{decomp}$: 424 °C, 98% mass loss. IR = 3492, 3082, 2944, 1736, 1644, 1472, 1244, 1130, 1010, 872, 762, 614 $cm^{-1}$. Elemental analysis: C, 54.44%. H, 6.65%. S, 0.00%. Contact angle: Advancing ($\theta_a$) = 60 ± 4°, Receding ($\theta_r$) = 49 ± 1°, hysteresis = 11°.

*Preparation of Boltorn-PEG film **A2***. The film was prepared in a similar manner as was film **A1**, with Boltorn-ene (1.749 g, 3.07 x $10^{-4}$ mol), PETMP (0.271 g, 5.55 x $10^{-4}$ mol) and 1-hydroxycyclohexylphenyl ketone (0.104 g, 5.08 x $10^{-4}$ mol) mixed in a scintillation vial, dissolved in 16.0 mL of 1,4-dioxane. $T_g$ = -14 °C. $T_{decomp}$: 419 °C, 97% mass loss. IR = 3492, 3082, 2944, 1736, 1644, 1472, 1244, 1130, 1010, 872, 762, 614 $cm^{-1}$. Elemental analysis: C, 55.75%. H, 6.48%. S, 3.80%. Contact angle: Advancing ($\theta_a$) = 74 ± 1°, Receding ($\theta_r$) = 60 ± 1°, hysteresis = 14°.

*Preparation of Boltorn-PEG film **A3***. The film was prepared in a similar manner as was film **A1**, with Boltorn-ene (0.870 g, 1.53 x $10^{-4}$ mol), PETMP (0.279 g, 5.71 x $10^{-4}$ mol) and 1-hydroxycyclohexylphenyl ketone (0.0589 g, 2.88 x $10^{-4}$ mol) mixed in a scintillation vial, dissolved in 16.0 mL of 1,4-dioxane. $T_g$ = 15 °C. $T_{decomp}$: 423 °C, 96% mass loss. IR = 3492, 3082, 2944, 2856, 1736, 1644, 1472, 1244, 1130, 1010, 872, 762, 614 $cm^{-1}$. Elemental analysis: C, 53.81%. H, 6.46%. S, 6.39%. Contact angle: Advancing ($\theta_a$) = 77 ± 2°, Receding ($\theta_r$) = 60 ± 2°, hysteresis = 17°.

*Preparation of Boltorn-PEG film **A4***. The film was prepared in a similar manner as was film **A1**, with Boltorn-ene (0.865 g, 1.52 x $10^{-4}$ mol), PETMP (0.425 g, 8.69 x $10^{-4}$ mol) and 1-hydroxycyclohexylphenyl ketone (0.0662 g, 3.24 x $10^{-4}$ mol) mixed in a scintillation vial, dissolved in 16.0 mL of 1,4-dioxane. $T_g$ = 18 °C. $T_{decomp}$: 413 °C, 96% mass loss. IR = 3492, 2944, 2856, 2754, 1736, 1472, 1244, 1130, 1010, 872, 762, 614 $cm^{-1}$. Elemental analysis: C, 52.70%. H, 6.45%. S, 8.42%. Contact angle: Advancing ($\theta_a$) = 79 ± 2°, Receding ($\theta_r$) = 64 ± 2°, hysteresis = 15°.

*Preparation of Boltorn-PEG film **A5***. The film was prepared in a similar manner as was film **A1**, with Boltorn-ene (0.869 g, 1.52 x $10^{-4}$ mol), PETMP (0.559 g, 1.14 x $10^{-3}$

mol) and 1-hydroxycyclohexylphenyl ketone (0.0713 g, 3.49 x $10^{-4}$ mol) mixed in a scintillation vial, dissolved in 16.0 mL of 1,4-dioxane. $T_g$ = 16 °C. $T_{decomp}$: 428 °C, 94% mass loss. IR = 3492, 2944, 2856, 2754, 2692, 1736, 1472, 1244, 1130, 1010, 872, 762, 614 $cm^{-1}$. Elemental analysis: C, 51.16%. H, 6.33%. S, 9.91%. Contact angle: Advancing ($\theta_a$) = 65 ± 2°, Receding ($\theta_r$) = 51 ± 1°, hysteresis = 14°.

*Preparation of Boltorn-PEG film **B1***. The film was prepared in a similar manner as was film **A1**, with Boltorn-ene (0.877 g, 1.54 x $10^{-4}$ mol), with 4-armed PEG tetrathiol (0.0434 g, 4.34 x $10^{-6}$ mol) and 1-hydroxycyclohexylphenyl ketone (0.0501 g, 2.45 x $10^{-4}$ mol) mixed in a scintillation vial, dissolved in 16.0 mL of 1,4-dioxane. $T_g$ = -21 °C. $T_{decomp}$: 412 °C, 98% mass loss. IR = 3488, 3084, 2930, 1740, 1644, 1472, 1234, 1138, 1011, 872, 762, 612 $cm^{-1}$. Elemental analysis: C, 57.63%. H, 6.82%. S, 0.19%. Contact angle: Advancing ($\theta_a$) = 69 ± 3°, Receding ($\theta_r$) = 50 ± 2°, hysteresis = 19°.

*Preparation of Boltorn-PEG film **B2***. The film was prepared in a similar manner as was film **A1**, with Boltorn-ene (1.736 g, 3.05 x $10^{-4}$ mol), with 4-armed PEG tetrathiol (0.0879 g, 8.79 x $10^{-6}$ mol), PETMP (0.277 g, 5.67 x $10^{-4}$ mol) and 1-hydroxycyclohexylphenyl ketone (0.108 g, 5.27 x $10^{-4}$ mol) mixed in a scintillation vial, dissolved in 16.0 mL of 1,4-dioxane. $T_g$ = -15 °C. $T_{decomp}$: 403 °C, 97% mass loss. IR = 3488, 3084, 2930, 1740, 1644, 1472, 1234, 1138, 1011, 872, 762, 612 $cm^{-1}$. Elemental analysis: C, 55.36%. H, 6.64%. S, 4.08%. Contact angle: Advancing ($\theta_a$) = 71 ± 1°, Receding ($\theta_r$) = 49 ± 6°, hysteresis = 21°.

*Preparation of Boltorn-PEG film **B3***. The film was prepared in a similar manner as was film **A1**, with Boltorn-ene (0.864 g, 1.52 x $10^{-4}$ mol), with 4-armed PEG tetrathiol (0.0445 g, 4.45 x $10^{-6}$ mol), PETMP (0.283 g, 5.86 x $10^{-4}$ mol) and 1-

hydroxycyclohexylphenyl ketone (0.0596 g, 2.92 x $10^{-4}$ mol) mixed in a scintillation vial, dissolved in 16.0 mL of 1,4-dioxane. $T_g$ = 10 °C. $T_{decomp}$: 384 °C, 96% mass loss. IR = 3488, 3084, 2930, 1740, 1644, 1472, 1234, 1138, 1011, 872, 762, 612 $cm^{-1}$. Elemental analysis: C, 53.72%. H, 6.60%. S, 6.94%. Contact angle: Advancing ($\theta_a$) = 73 ± 2°, Receding ($\theta_r$) = 52 ± 5°, hysteresis = 21°.

*Preparation of Boltorn-PEG film **B4***. The film was prepared in a similar manner as was film **A1**, with Boltorn-ene (0.869 g, 1.53 x $10^{-4}$ mol), with 4-armed PEG tetrathiol (0.0433 g, 4.33 x $10^{-6}$ mol), PETMP (0.415 g, 8.49 x $10^{-4}$ mol) and 1-hydroxycyclohexylphenyl ketone (0.0682 g, 3.34 x $10^{-4}$ mol) mixed in a scintillation vial, dissolved in 16.0 mL of 1,4-dioxane. $T_g$ = 21 °C. $T_{decomp}$: 384 °C, 97% mass loss. IR = 3488, 2930, 2852, 2754, 2696, 1740, 1472, 1234, 1138, 1011, 872, 762, 612 $cm^{-1}$. Elemental analysis: C, 52.84%. H, 6.51%. S, 8.64%. Contact angle: Advancing ($\theta_a$) = 80 ± 2°, Receding ($\theta_r$) = 63 ± 4°, hysteresis = 17°.

*Preparation of Boltorn-PEG film **B5***. The film was prepared in a similar manner as was film **A1**, with Boltorn-ene (0.870 g, 1.53 x $10^{-4}$ mol), with 4-armed PEG tetrathiol (0.0444 g, 4.44 x $10^{-6}$ mol), PETMP (0.564 g, 1.15 x $10^{-3}$ mol) and 1-hydroxycyclohexylphenyl ketone (0.0757 g, 3.71 x $10^{-4}$ mol) mixed in a scintillation vial, dissolved in 16.0 mL of 1,4-dioxane. $T_g$ = 23 °C. $T_{decomp}$: 381 °C, 95% mass loss. IR = 3488, 2930, 2852, 2754, 2696, 1740, 1472, 1234, 1138, 1011, 872, 762, 612 $cm^{-1}$. Elemental analysis: C, 51.79%. H, 6.31%. S, 10.05%. Contact angle: Advancing ($\theta_a$) = 70 ± 1°, Receding ($\theta_r$) = 52 ± 2°, hysteresis = 18°.

*Preparation of Boltorn-PEG film **C1***. The film was prepared in a similar manner as was film **A1**, with Boltorn-ene (3.486 g, 6.12 x $10^{-4}$ mol), with 4-armed PEG tetrathiol

(0.525 g, 5.25 x $10^{-5}$ mol) and 1-hydroxycyclohexylphenyl ketone (0.203 g, 9.95 x $10^{-3}$ mol) mixed in a scintillation vial, dissolved in 24.0 mL of 1,4-dioxane. $T_g$ = -29 °C. $T_{decomp}$: 397 °C, 98% mass loss. IR = 3478, 3082, 2938, 1738, 1642, 1466, 1246, 1136, 1008, 872, 764, 614 $cm^{-1}$. Elemental analysis: C, 56.98%. H, 6.86%. S, 0.36%. Contact angle: Advancing ($\theta_a$) = 58 ± 3°, Receding ($\theta_r$) = 41 ± 3°, hysteresis = 17°.

*Preparation of Boltorn-PEG film **C2***. The film was prepared in a similar manner as was film **A1**, with Boltorn-ene (1.747 g, 3.07 x $10^{-4}$ mol), with 4-armed PEG tetrathiol (0.260 g, 2.60 x $10^{-5}$ mol), PETMP (0.274 g, 5.60 x $10^{-4}$ mol) and 1-hydroxycyclohexylphenyl ketone (0.116 g, 5.66 x $10^{-4}$ mol) mixed in a scintillation vial, dissolved in 24.0 mL of 1,4-dioxane. $T_g$ = -16 °C. $T_{decomp}$: 388 °C, 98% mass loss. IR = 3478, 3082, 2938, 1738, 1642, 1466, 1246, 1136, 1008, 872, 764, 614 $cm^{-1}$. Elemental analysis: C, 55.26%. H, 6.77%. S, 3.47%. Contact angle: Advancing ($\theta_a$) = 76 ± 2°, Receding ($\theta_r$) = 59 ± 3°, hysteresis = 15°.

*Preparation of Boltorn-PEG film **C3***. The film was prepared in a similar manner as was film **A1**, with Boltorn-ene (3.494 g, 6.13 x $10^{-4}$ mol), with 4-armed PEG tetrathiol (0.526 g, 5.23 x $10^{-5}$ mol), PETMP (1.110 g, 2.27 x $10^{-3}$ mol) and 1-hydroxycyclohexylphenyl ketone (0.245 g, 1.20 x $10^{-3}$ mol) mixed in a scintillation vial, dissolved in 24.0 mL of 1,4-dioxane. $T_g$ = -4 °C. $T_{decomp}$: 378 °C, 97% mass loss. IR = 3478, 3082, 2938, 1738, 1642, 1466, 1246, 1136, 1008, 872, 764, 614 $cm^{-1}$. Elemental analysis: C, 53.68%. H, 6.39%. S, 6.04%. Contact angle: Advancing ($\theta_a$) = 86 ± 3°, Receding ($\theta_r$) = 69 ± 3°, hysteresis = 17°.

*Preparation of Boltorn-PEG film **C4***. The film was prepared in a similar manner as was film **A1**, with Boltorn-ene (3.486 g, 6.11 x $10^{-4}$ mol), with 4-armed PEG tetrathiol

(0.525 g, 5.25 x $10^{-5}$ mol), PETMP (1.669 g, 3.42 x $10^{-3}$ mol) and 1-hydroxycyclohexylphenyl ketone (0.281 g, 1.38 x $10^{-3}$ mol) mixed in a scintillation vial, dissolved in 24.0 mL of 1,4-dioxane. $T_g$ = -10 °C. $T_{decomp}$: 376 °C, 94% mass loss. IR = 3478, 2938, 2858, 1752, 2692, 1738, 1466, 1246, 1136, 1008, 872, 764, 614 $cm^{-1}$. Elemental analysis: C, 52.62%. H, 6.59%. S, 8.12%. Contact angle: Advancing ($\theta_a$) = 76 ± 2°, Receding ($\theta_r$) = 61 ± 2°, hysteresis = 15°.

*Preparation of Boltorn-PEG film **C5***. The film was prepared in a similar manner as was film **A1**, with Boltorn-ene (3.473 g, 6.09 x $10^{-4}$ mol), with 4-armed PEG tetrathiol (0.528 g, 5.28 x $10^{-5}$ mol), PETMP (2.223 g, 4.55 x $10^{-3}$ mol) and 1-hydroxycyclohexylphenyl ketone (0.308 g, 1.51 x $10^{-3}$ mol) mixed in a scintillation vial, dissolved in 24.0 mL of 1,4-dioxane. $T_g$ = -10 °C. $T_{decomp}$: 373 °C, 92% mass loss. IR = 3478, 2938, 2858, 1752, 2692, 1738, 1466, 1246, 1136, 1008, 872, 764, 614 $cm^{-1}$. Elemental analysis: C, 51.44%. H, 6.44%. S, 10.51%. Contact angle: Advancing ($\theta_a$) = 19 ± 3°, Receding ($\theta_r$) = 4 ± 2°, hysteresis = 15°.

*Preparation of Boltorn-PEG film **D1***. The film was prepared in a similar manner as was film **A1**, with Boltorn-ene (0.877 g, 1.54 x $10^{-4}$ mol), with 4-armed PEG tetrathiol (0.215 g, 2.15 x $10^{-5}$ mol) and 1-hydroxycyclohexylphenyl ketone (0.0526 g, 2.58 x $10^{-4}$ mol) mixed in a scintillation vial, dissolved in 16.0 mL of 1,4-dioxane. $T_g$ = -23 °C. $T_{decomp}$: 386 °C, 97% mass loss. IR = 3492, 3082, 2926, 1738, 1642, 1472, 1238, 1132, 1014, 872, 762, 614 $cm^{-1}$. Elemental analysis: C, 56.61%. H, 7.00%. S, 0.49%. Contact angle: Advancing ($\theta_a$) = 80 ± 3°, Receding ($\theta_r$) = 62 ± 1°, hysteresis = 18°.

*Preparation of Boltorn-PEG film **D2***. The film was prepared in a similar manner as was film **A1**, with Boltorn-ene (1.744 g, 2.52 x $10^{-4}$ mol), with 4-armed PEG tetrathiol

(0.436 g, 4.36 x $10^{-5}$ mol), PETMP (0.274 g, 5.62 x $10^{-4}$ mol) and 1-hydroxycyclohexylphenyl ketone (0.120 g, 5.89 x $10^{-4}$ mol) mixed in a scintillation vial, dissolved in 16.0 mL of 1,4-dioxane. $T_g$ = -22 °C. $T_{decomp}$: 373 °C, 97% mass loss. IR = 3492, 3082, 2926, 1738, 1642, 1472, 1238, 1132, 1014, 872, 762, 614 $cm^{-1}$. Elemental analysis: C, 54.54%. H, 6.81%. S, 3.50%. Contact angle: Advancing ($\theta_a$) = 72 ± 3°, Receding ($\theta_r$) = 52 ± 2°, hysteresis = 20°.

*Preparation of Boltorn-PEG film **D3***. The film was prepared in a similar manner as was film **A1**, with Boltorn-ene (0.862 g, 1.51 x $10^{-4}$ mol), with 4-armed PEG tetrathiol (0.218 g, 2.18 x $10^{-5}$ mol), PETMP (0.282 g, 5.77 x $10^{-4}$ mol) and 1-hydroxycyclohexylphenyl ketone (0.0636 g, 3.11 x $10^{-4}$ mol) mixed in a scintillation vial, dissolved in 16.0 mL of 1,4-dioxane. $T_g$ = -15 °C. $T_{decomp}$: 357 °C, 96% mass loss. IR = 3492, 3082, 2926, 1738, 1642, 1472, 1238, 1132, 1014, 872, 762, 614 $cm^{-1}$. Elemental analysis: C, 53.47%. H, 6.62%. S, 5.84%. Contact angle: Advancing ($\theta_a$) = 83 ± 2°, Receding ($\theta_r$) = 65 ± 3°, hysteresis = 18°.

*Preparation of Boltorn-PEG film **D4***. The film was prepared in a similar manner as was film **A1**, with Boltorn-ene (0.875 g, 1.53 x $10^{-4}$ mol), with 4-armed PEG tetrathiol (0.215 g, 2.15 x $10^{-5}$ mol), PETMP (0.417 g, 8.53 x $10^{-3}$ mol) and 1-hydroxycyclohexylphenyl ketone (0.0743 g, 3.64 x $10^{-4}$ mol) mixed in a scintillation vial, dissolved in 16.0 mL of 1,4-dioxane. $T_g$ = -9 °C. $T_{decomp}$: 367 °C, 97% mass loss. IR = 3492, 2926, 2860, 2752, 2696, 1738, 1472, 1238, 1132, 1014, 872, 762, 614 $cm^{-1}$. Elemental analysis: C, 52.66%. H, 6.45%. S, 7.77%. Contact angle: Advancing ($\theta_a$) = 74 ± 3°, Receding ($\theta_r$) = 59 ± 1°, hysteresis = 15°.

*Preparation of Boltorn-PEG film **D5**.* The film was prepared in a similar manner as was film **A1**, with Boltorn-ene (0.876 g, 1.54 x $10^{-4}$ mol), with 4-armed PEG tetrathiol (0.219 g, 2.19 x $10^{-5}$ mol), PETMP (0.557 g, 1.14 x $10^{-3}$ mol) and 1-hydroxycyclohexylphenyl ketone (0.0822 g, 4.02 x $10^{-3}$ mol) mixed in a scintillation vial, dissolved in 16.0 mL of 1,4-dioxane. $T_g$ = -8 °C. $T_{decomp}$: 362 °C, 96% mass loss. IR = 3492, 2926, 2860, 2752, 2696, 1738, 1472, 1238, 1132, 1014, 872, 762, 614 $cm^{-1}$. Elemental analysis: C, 51.50%. H, 6.39%. S, 13.44%. Contact angle: Advancing ($\theta_a$) = 10 ± 1°, Receding ($\theta_r$) = 3 ± 2°, hysteresis = 7°.

**Anti-fouling Boltorn-PEG film production.** A series of eight films were prepared for anti-fouling tests. The synthesis is similar to that of the previous Boltorn-PEG films, but the films were prepared at a constant 0.25 eq SH/ene PETMP concentration at varying PEG wt% (0, 5, 10, 15, 20, 25, 30 and 35 wt%), producing films **AF0**, **AF5**, **AF10**, **AF15**, **AF20**, **AF25**, **AF30** and **AF35**, respectively.

*Preparation of Boltorn-PEG film **AF0**.* The film was prepared in a similar manner as was film **A1**, with Boltorn-ene (1.208 g, 2.12 x $10^{-4}$ mol), PETMP (0.189 g, 3.87 x $10^{-4}$ mol) and 1-hydroxycyclohexylphenyl ketone (0.0652 g, 3.19 x $10^{-4}$ mol) mixed in a scintillation vial, dissolved in 12.0 mL of 1,4-dioxane. $T_g$ = -14 °C. $T_{decomp}$: 419 °C, 97% mass loss. IR = 3492, 3082, 2944, 1736, 1644, 1472, 1244, 1130, 1010, 872, 762, 614 $cm^{-1}$. Elemental analysis: C, 55.75%. H, 6.48%. S, 3.80%. Contact angle: Advancing ($\theta_a$) = 74 ± 4°, Receding ($\theta_r$) = 60 ± 1°, hysteresis = 14°.

*Preparation of Boltorn-PEG film **AF5**.* The film was prepared in a similar manner as was film **A1**, with Boltorn-ene (1.208 g, 2.12 x $10^{-4}$ mol), with 4-armed PEG tetrathiol (0.0610 g, 6.10 x $10^{-6}$ mol), PETMP (0.190 g, 3.89 x $10^{-4}$ mol) and 1-

hydroxycyclohexylphenyl ketone (0.0721 g, 3.53 x $10^{-4}$ mol) mixed in a scintillation vial, dissolved in 12.0 mL of 1,4-dioxane. $T_g$ = -15 °C. $T_{decomp}$: 403 °C, 97% mass loss. IR = 3488, 3084, 2930, 1740, 1644, 1472, 1234, 1138, 1011, 872, 762, 612 $cm^{-1}$. Elemental analysis: C, 55.36%. H, 6.64%. S, 4.08%. Contact angle: Advancing ($\theta_a$) = 71 ± 1°, Receding ($\theta_r$) = 49 ± 6°, hysteresis = 22°.

*Preparation of Boltorn-PEG film **AF10**.* The film was prepared in a similar manner as was film **A1**, with Boltorn-ene (1.207 g, 2.12 x $10^{-4}$ mol), with 4-armed PEG tetrathiol (0.121 g, 1.22 x $10^{-6}$ mol), PETMP (0.189 g, 3.86 x $10^{-4}$ mol) and 1-hydroxycyclohexylphenyl ketone (0.0727 g, 3.56 x $10^{-4}$ mol) mixed in a scintillation vial, dissolved in 12.0 mL of 1,4-dioxane. $T_g$ = -15 °C. $T_{decomp}$: 383 °C, 98% mass loss. IR = 3488, 3084, 2930, 1740, 1644, 1472, 1234, 1138, 1011, 872, 762, 612 $cm^{-1}$. Elemental analysis: C, 54.44%. H, 6.71%. S, 4.25%. Contact angle: Advancing ($\theta_a$) = 64 ± 2°, Receding ($\theta_r$) = 40 ± 2°, hysteresis = 24°.

*Preparation of Boltorn-PEG film **AF15**.* The film was prepared in a similar manner as was film **A1**, with Boltorn-ene (1.211 g, 2.13 x $10^{-4}$ mol), with 4-armed PEG tetrathiol (0.181 g, 1.81 x $10^{-5}$ mol), PETMP (0.198 g, 4.05 x $10^{-4}$ mol) and 1-hydroxycyclohexylphenyl ketone (0.0797 g, 3.90 x $10^{-4}$ mol) mixed in a scintillation vial, dissolved in 12.0 mL of 1,4-dioxane. $T_g$ = -16 °C. $T_{decomp}$: 388 °C, 98% mass loss. IR = 3478, 3082, 2938, 1738, 1642, 1466, 1246, 1136, 1008, 872, 764, 614 $cm^{-1}$. Elemental analysis: C, 55.26%. H, 6.77%. S, 3.47%. Contact angle: Advancing ($\theta_a$) = 76 ± 2°, Receding ($\theta_r$) = 59 ± 3°, hysteresis = 15°.

*Preparation of Boltorn-PEG film **AF20**.* The film was prepared in a similar manner as was film **A1**, with Boltorn-ene (1.199 g, 3.49 x $10^{-4}$ mol), with 4-armed PEG

tetrathiol (0.302 g, 3.02 x $10^{-5}$ mol), PETMP (0.197 g, 4.03 x $10^{-4}$ mol) and 1-hydroxycyclohexylphenyl ketone (0.0822 g, 4.02 x $10^{-4}$ mol) mixed in a scintillation vial, dissolved in 12.0 mL of 1,4-dioxane. $T_g$ = -17 °C. $T_{decomp}$: 400 °C, 99% mass loss. IR = 3492, 3082, 2926, 1738, 1642, 1472, 1238, 1132, 1014, 872, 762, 614 $cm^{-1}$. Elemental analysis: C, 54.51%. H, 6.79%. S, 3.51%. Contact angle: Advancing ($\theta_a$) = 72 ± 2°, Receding ($\theta_r$) = 46 ± 6°, hysteresis = 26°.

*Preparation of Boltorn-PEG film **AF25***. The film was prepared in a similar manner as was film **A1**, with Boltorn-ene (1.216 g, 2.13 x $10^{-4}$ mol), with 4-armed PEG tetrathiol (0.302 g, 3.02 x $10^{-5}$ mol), PETMP (0.210 g, 4.30 x $10^{-4}$ mol) and 1-hydroxycyclohexylphenyl ketone (0.0822 g, 4.02 x $10^{-3}$ mol) mixed in a scintillation vial, dissolved in 12.0 mL of 1,4-dioxane. $T_g$ = -22 °C. $T_{decomp}$: 373 °C, 97% mass loss. IR = 3492, 3082, 2926, 1738, 1642, 1472, 1238, 1132, 1014, 872, 762, 614 $cm^{-1}$. Elemental analysis: C, 54.54%. H, 6.81%. S, 3.50%. Contact angle: Advancing ($\theta_a$) = 72 ± 3°, Receding ($\theta_r$) = 52 ± 2°, hysteresis = 20°.

*Preparation of Boltorn-PEG film **AF30***. The film was prepared in a similar manner as was film **A1**, with Boltorn-ene (1.198 g, 2.10 x $10^{-4}$ mol), with 4-armed PEG tetrathiol (0.363 g, 3.63 x $10^{-5}$ mol), PETMP (0.187 g, 3.83 x $10^{-4}$ mol) and 1-hydroxycyclohexylphenyl ketone (0.0874 g, 4.28 x $10^{-4}$ mol) mixed in a scintillation vial, dissolved in 12.0 mL of 1,4-dioxane. $T_g$ = -21 °C. $T_{decomp}$: 379 °C, 97% mass loss. IR = 3492, 3082, 2926, 1738, 1642, 1472, 1238, 1132, 1014, 872, 762, 614 $cm^{-1}$. Elemental analysis: C, 53.44%. H, 6.78%. S, 3.35%. Contact angle: Advancing ($\theta_a$) = 59 ± 2°, Receding ($\theta_r$) = 39 ± 2°, hysteresis = 20°.

*Preparation of Boltorn-PEG film **AF35**.* The film was prepared in a similar manner as was film **A1**, with Boltorn-ene (1.203 g, 2.11 x $10^{-4}$ mol), with 4-armed PEG tetrathiol (0.423 g, 4.23 x $10^{-5}$ mol), PETMP (0.187 g, 3.83 x $10^{-4}$ mol) and 1-hydroxycyclohexylphenyl ketone (0.0902 g, 4.42 x $10^{-4}$ mol) mixed in a scintillation vial, dissolved in 12.0 mL of 1,4-dioxane. $T_g$ = -21 °C. $T_{decomp}$: 390 °C, 98% mass loss. IR = 3492, 3082, 2926, 1738, 1642, 1472, 1238, 1132, 1014, 872, 762, 614 $cm^{-1}$. Elemental analysis: C, 55.11%. H, 6.76%. S, 3.21%. Contact angle: Advancing ($\theta_a$) = 37 ± 1°, Receding ($\theta_r$) = 24 ± 2°, hysteresis = 13°.

**Biofouling assays**

*Leaching:* Coatings were supplied in nanopure deionised water from which they were transferred to seawater 24 hours before the start of the experiment. The slides remained wet and fully hydrated throughout the process.

*Settlement of spores:* Reproductive tissue from *Ulva linza* was collected from Llantwit Major, Wales (51840'N; 3848'W). Zoospores released from the seaweed were diluted with seawater to produce a zoospore suspension of 1.5 × $10^6$ zoospores $mL^{-1}$ using the method of Callow, *et al.*(67) A suspension of zoospores (10 mL containing 1.0 x$10^6$ spores $mL^{-1}$) was added to individual compartments of quadriperm dishes (Greiner) each containing a test surface. After 1 h in darkness at *ca.* 20 $^oC$, the slides were gently washed in seawater to remove unsettled (*i.e.* motile) zoospores. Slides were fixed using 2.5% glutaraldehyde in seawater. The density of zoospores attached to the surface was counted on each of 3 replicates. Counts were made for 30 fields of view (each 0.17 $mm^2$), 1 mm apart across the central region of each slide, using a Zeiss epifluorescence microscope in conjunction with image analysis software (Imaging Associates Ltd.).(68)

*Growth of sporelings:* Zoospores were settled on test samples and washed as described above. The spores germinated and developed into sporelings (young plants) over 10 days. Cultures were maintained in quadriperm dishes containing 10 mL of supplemented seawater medium that was changed every 2 days(69) and housed in an illuminated incubator (75 μmol $m^{-2}$ $s^{-1}$ incident irradiation).

Sporeling biomass was determined *in situ* by measuring the fluorescence of the chlorophyll contained within the cells in a Tecan fluorescence plate reader (excitation = 430 nm, emission = 670 nm).(70) The biomass was quantified in terms of relative fluorescence units (RFU). The RFU value for each slide was the mean of 70 point fluorescence readings. The data are expressed as the mean RFU of 6 replicate slides; bars show SEM (standard error of the mean).

*Attachment strength of sporelings:* Strength of attachment of sporelings was assessed using an automated water jet which traversed the central region of each slide.(71) Individual slides of each treatment were exposed to a single impact pressure. The range of pressures used were selected to span from low to high biomass removal. The biomass remaining in the sprayed area was assessed using a fluorescence plate reader (as above). Percentage removal of biomass was calculated from readings taken before and after exposure to the water jet. The critical impact pressure to remove 50% of the biomass was determined from plots of percentage removal *vs* water impact pressure.(70) A polydimethylsiloxane elastomer (PDMSe; Silastic® T2, Dow Corning, provided by Dr AB Brennan, University of Florida) was included in the assays as a standard fouling-release coating.(70)

## Results and discussion

The highly alkenylated Boltorn-ene macromolecule was prepared in a manner similar to those previously published, wherein the dendritic polyester Boltorn H30 was esterified with 3-butenoic acid using a catalytic amount of DPTS (Scheme 1). Water was

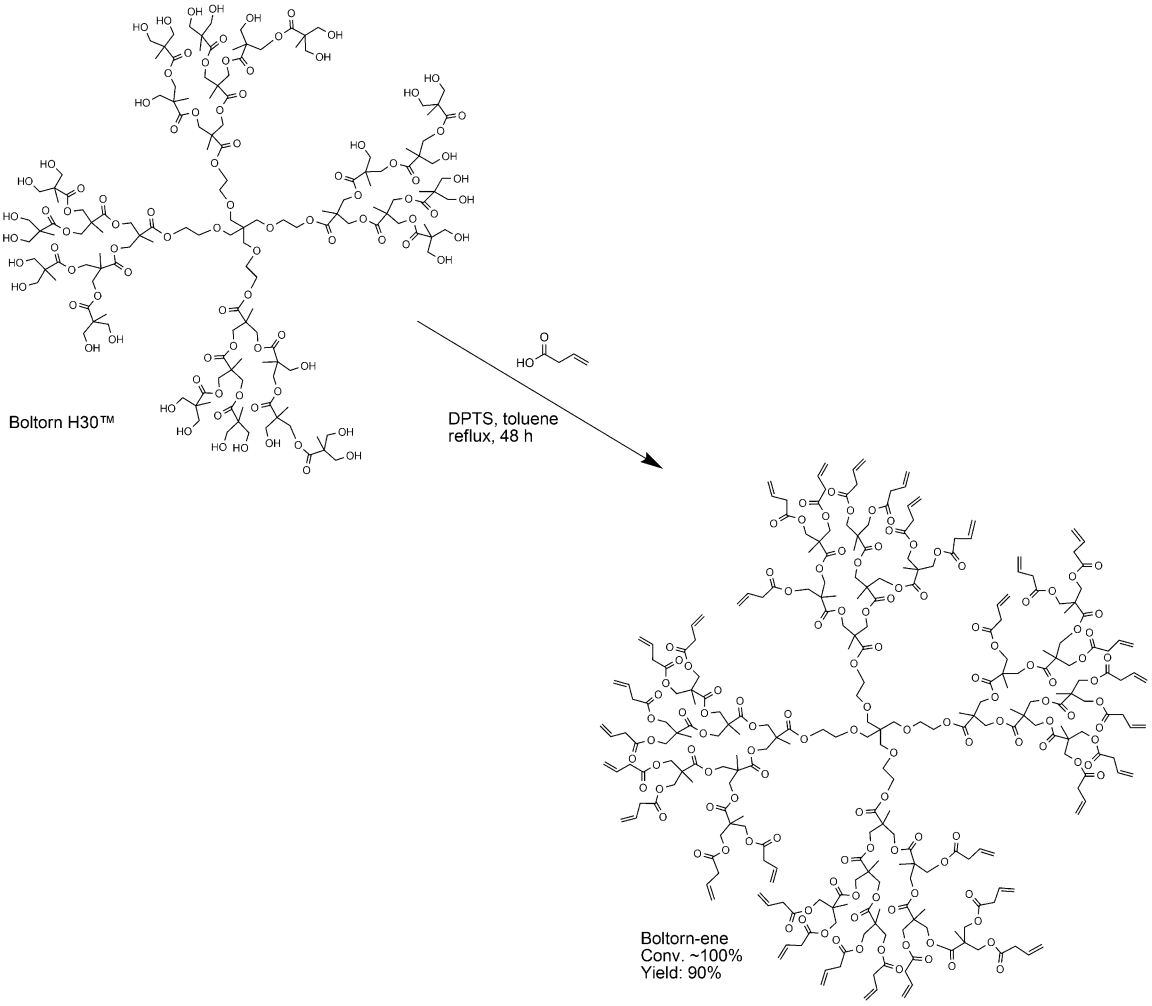


**Scheme 2-1.** Esterification of Boltorn H30 to produce Boltorn-ene.

carefully removed from the carefully removed from the Boltorn H30 prior to reaction *via* distillation, and the mixture was allowed to reflux in anhydrous toluene for two days,

producing Boltorn-ene, **1**, as a thick clear oil in high yield and quantitative conversion. $^{1}$H-NMR spectroscopy shows a product that appears to be in high purity (Figure 2-1).

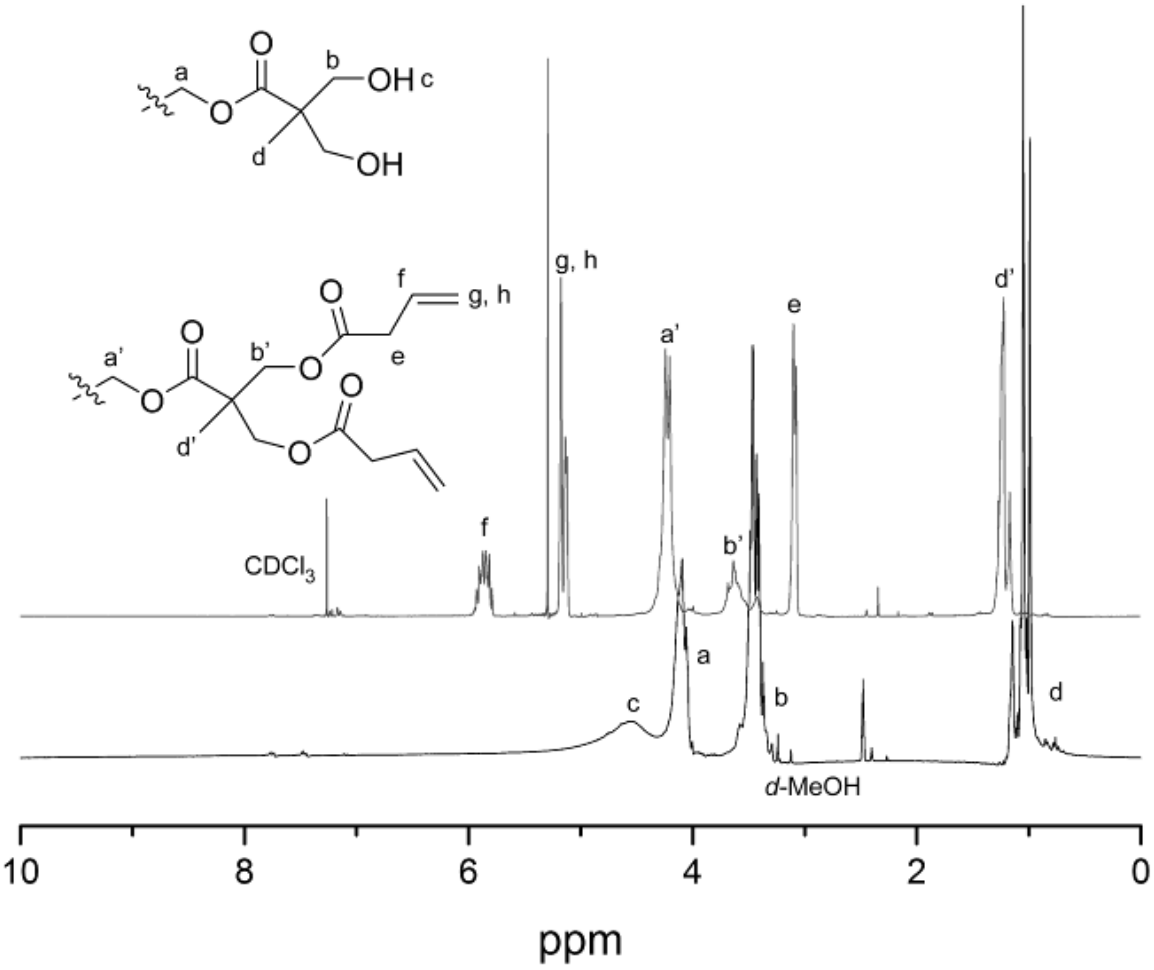


**Figure 2-1.** $^{1}$H-NMR spectroscopy images of Boltorn H30 (*d*-MeOH) and esterified Boltorn-ene ($CDCl_3$).

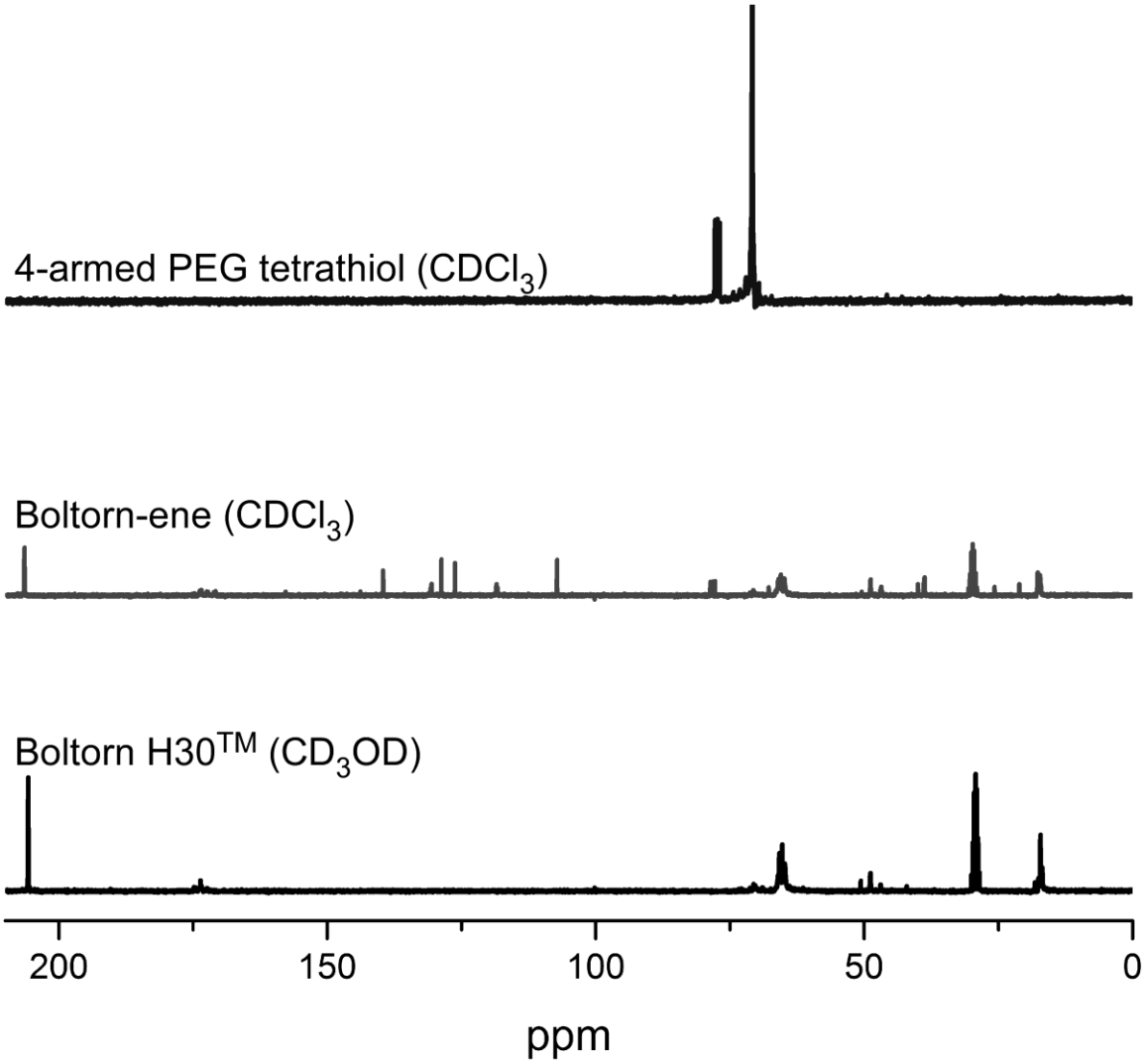


**Figure 2-2.** $^{13}C$ NMR spectroscopy of Boltorn H30, Boltorn-ene, and 4-armed PEG tetrathiol.

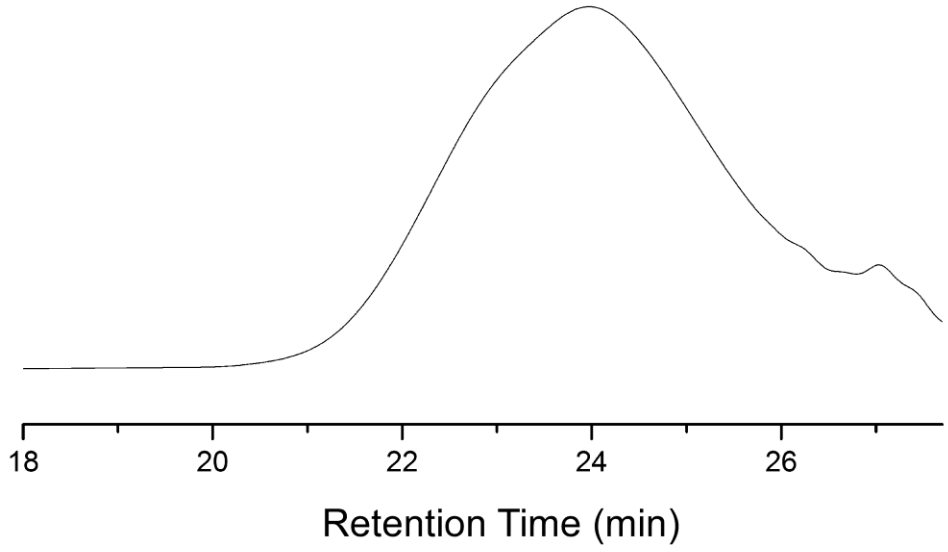


**Figure 2-3.** GPC chromatogram of Boltorn-ene (THF).

Additional information, such as $^{13}$C-NMR spectrum and GPC can be viewed in Figures 2-2 and 2-3, respectively. The oil was readily prepared and stored in plastic syringes inside a 4 °C refrigerator in order to minimize side reactions between the alkenes and atmospheric oxygen. Due to the low $T_g$ of the polymer, the syringes acted as an ideal dispensing tool for weighing Boltorn-ene in formulations.

A combinatorial approach was used to ascertain to what extent the PEG and the PETMP contributed to the thermomechanical, tensile, and surface energy properties of crosslinked Boltorn-PEG films. A 5 x 4 grid was prepared at constant Boltorn-ene

weight, with five thiol concentrations (0, 0.25, 0.50, 0.75 and 1.0 eq SH of the PETMP crosslinker per eq alkene of Boltorn-ene molecule, corresponding to **1**, **2**, **3**, **4** and **5**, respectively, against four PEG weight percentages (0, 5, 15, and 25 wt % of the Boltorn-ene weight, corresponding to **A**, **B**, **C** and **D,** respectively). For example, **C3** would refer to a Boltorn-PEG coating containing 15 wt% PEG and 0.50 eq SH/ene PETMP (Scheme

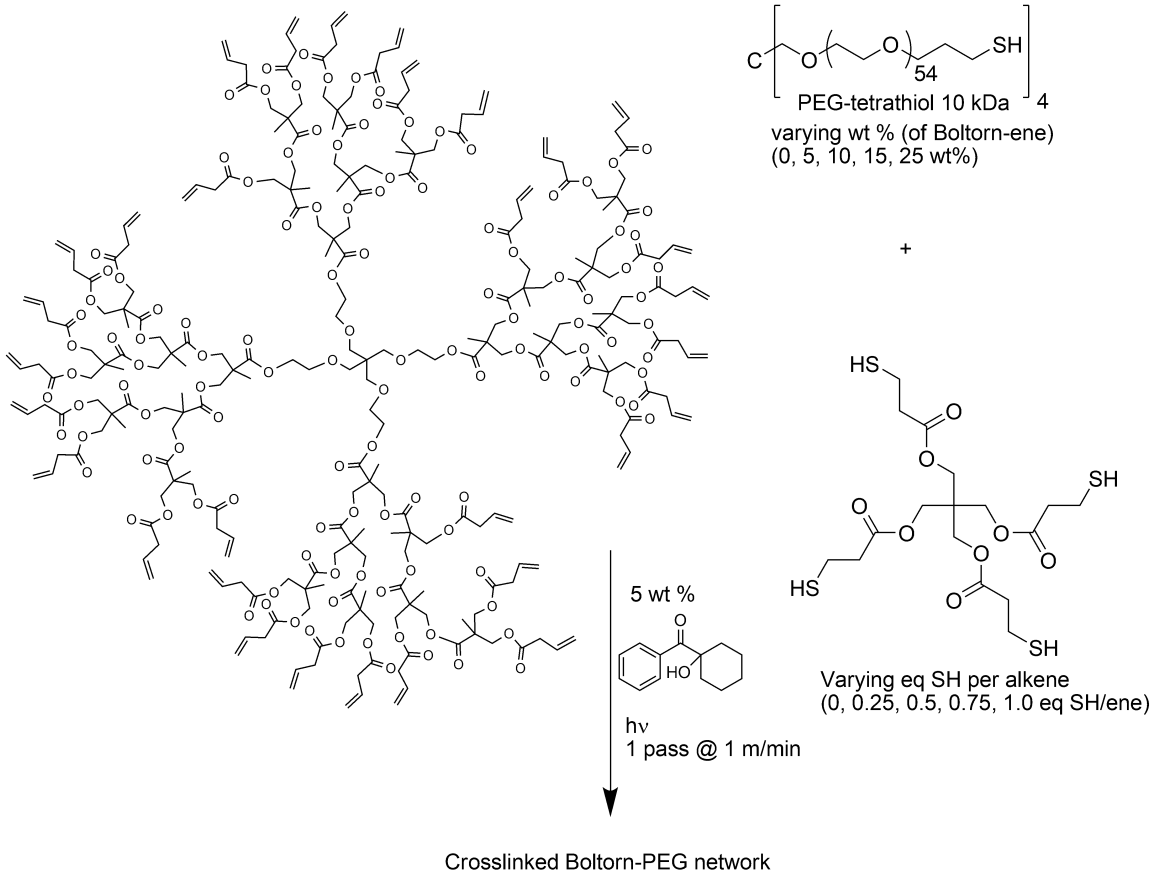


**Scheme 2-2.** Preparation of Boltorn-PEG films at varying PEG and PETMP concentrations.

2-2). The photoinitiator, 1-hydroxycyclohexylphenyl ketone, was added at 5 wt% (w/w% of total solids), and the mixtures dissolved in 1,4-dioxane to ensure complete homogeneity during mixing and pre-gel dispersion. The pre-gel solutions appear to be

shelf-stable at room temperature for several hours with no signs of premature crosslinking or gelation. The pre-gel solutions were syringed onto freshly prepared vinyl-trimethoxysilyl-modified glass slides to provide covalent crosslinks between the glass and the Boltorn-PEG film, whereby free thiols incorporated in the network react with the surface vinyl silane groups. After the solutions were cast on the modified glass slides, a 20 min time period allowed for excess solvent to evaporate leaving a thickened optically transparent pre-gel mixture. The coated slides were then passed through a Fusion UV 300S conveyor system equipped with a H bulb (600 Watts) at a speed of 1 m/min for a single pass, producing transparent, covalently bound coated glass of varying thicknesses between 100 and 500 μm. The coated slides were then checked closely for defects, such as incomplete slide coverage, cracking or uneven thickness, prior to further analysis.

The films were analyzed using infrared spectroscopy to determine relative amounts of thiol and alkene remained in the final crosslinked product. This was accomplished by crosslinking a drop of pre-gel solution on a NaCl IR plate, followed by collection of the IR spectrum. An example of the relevant IR regions can be seen in

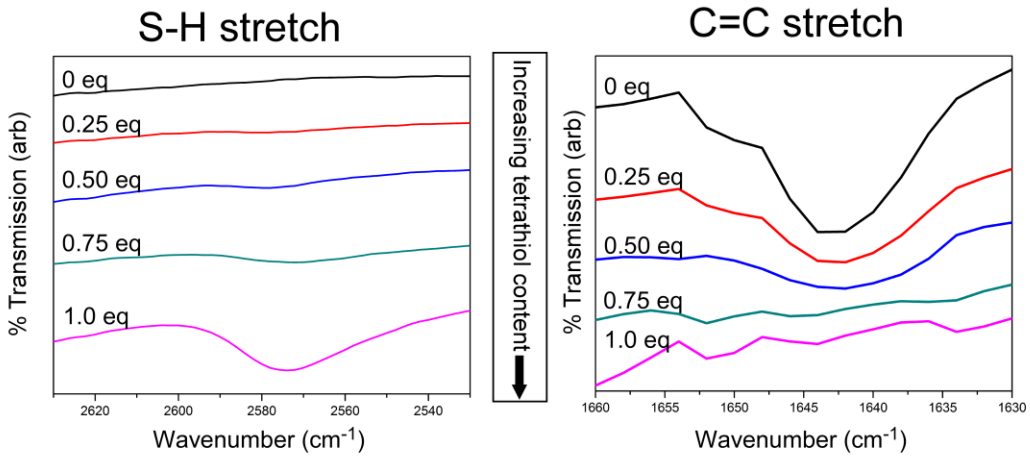


**Figure 2-4.** Example IR spectroscopy of Boltorn-PEG0 films ("A series") at varying PETMP concentration. The specific bands highlighted are the S-H stretch at *ca.* 2500 $cm^{-1}$ and the C=C stretch at *ca.* 1645 $cm^{-1}$.

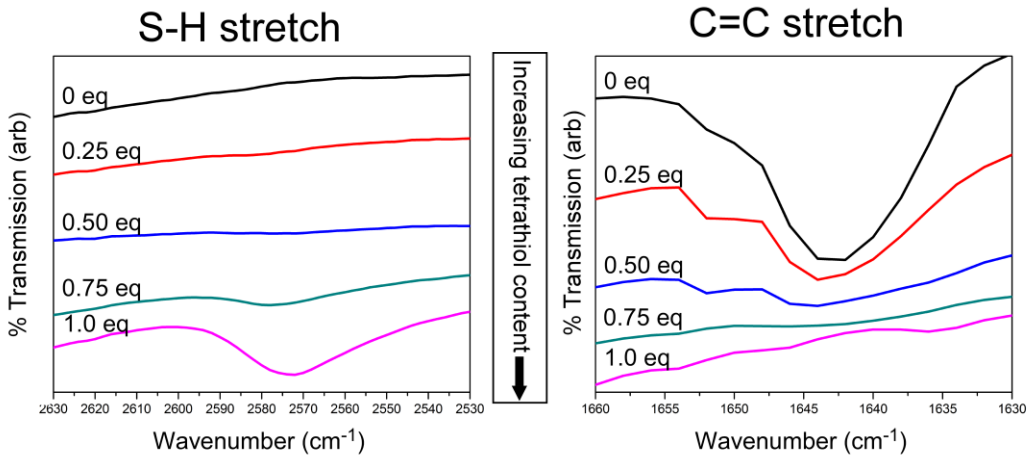


**Figure 2-5.** Example of IR spectroscopy results for Boltorn-PEG5 films ("**B** series") at varying PETMP concentrations.

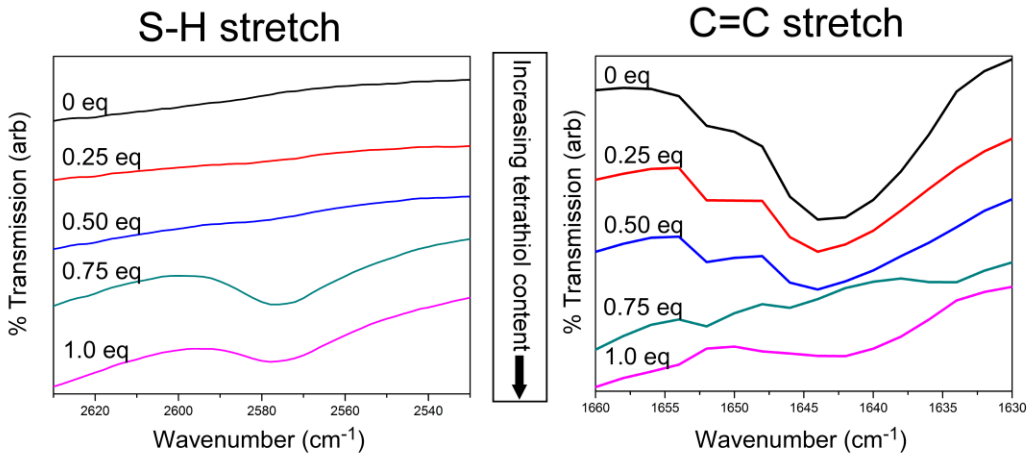


**Figure 2-6.** Example IR spectroscopy of Boltorn-PEG15 films ("C series") at varying PETMP concentration. The specific bands highlighted are the S-H stretch at *ca.* 2500 $cm^{-1}$ and the C=C stretch at *ca.* 1645 $cm^{-1}$.

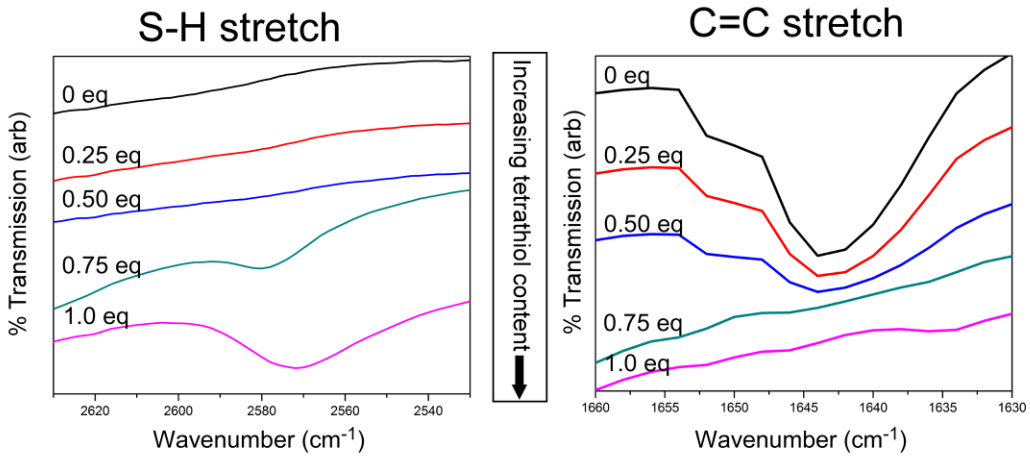


**Figure 2-7.** Example IR spectroscopy of Boltorn-PEG25 films ("D series") at varying PETMP concentration. The specific bands highlighted are the S-H stretch at *ca.* 2500 $cm^{-1}$ and the C=C stretch at *ca.* 1645 $cm^{-1}$.

Figure 2-5, which shows the "**B** series" as a typical example of the Boltorn-PEG films. The specific bands highlighted are the S-H stretch at *ca.* 2570 $cm^{-1}$ and the C=C stretch at *ca.* 1645 $cm^{-1}$, values which were normalized against the C=O stretch for the constant-concentration Boltorn component. It should be noted that the C-S stretch and S-S stretch are not easily observed and therefore cannot serve as an adequate measure for the formation of films. As PETMP concentration was increased the band in the IR spectra corresponding to the S-H bond intensified providing evidence of excess or unconsumed thiol groups in the network while the stretch associated with the C=C bond decreased rapidly as the groups were consumed. There appeared to be an equivalency at approximately 0.75 eq SH/ene PETMP concentration and an overabundance of thiol at 1.0 eq SH/ene. This deviation, which would predict an equivalency at 1.0 eq SH/ene, can likely be attributed to restricted mobility in the crosslinked films, where free thiol cannot readily access the small amount of free remaining alkene in the highly crosslinked network. Varying PEG wt% does not appear to affect the extent of crosslinking. This is due to PEG being relatively dilute with respect to the total thiol concentration across all of the mixtures (4 SH/10,000 Da molecule) compared to PETMP (4 SH/488 Da

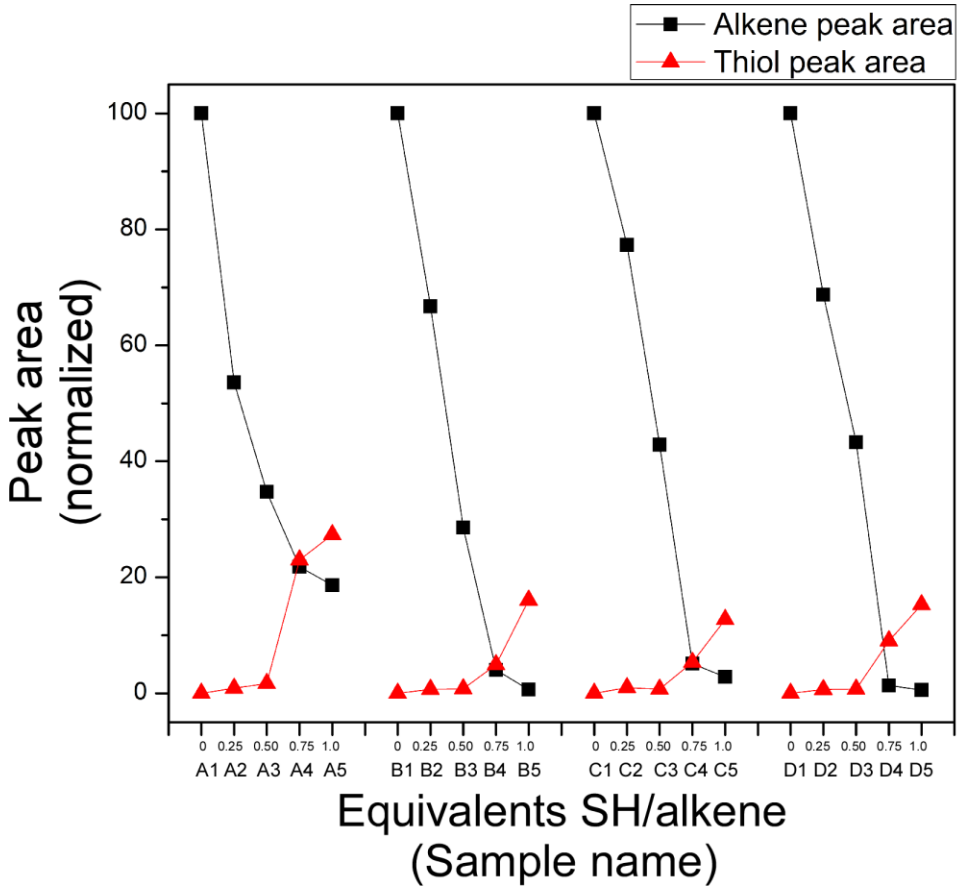


**Figure 2-8.** Normalized peak area of S-H and C=C stretches across the combinatorial series.

molecule), which can be quantified and evaluated by comparing peak areas (Figure 2-8). It was observed that alkene consumption is relatively similar for all film compositions until 0.75 eq SH/ene PETMP. At this ratio, films with no PEG ("**A** series") appear to reach reaction completion with approximately 10% of the free alkenes remaining in the bulk. An excess of thiol remains at 1.0 eq SH/ene PETMP, which could either be in the form of partially reacted or non-reacted PETMP trapped in the bulk; whichever the form, an odor of PETMP can be noted from the films at this concentration.

The mobility and degradability of the films were assessed using thermal analysis to determine how the components of the film can affect mechanical properties. The $T_g$'s of the polymer films increase by approximately 20 °C as the PETMP concentration is increased from 0.0 to 1.0 eq SH/ene, regardless of PEG wt%, due to higher degrees of crosslinking achieved (Table 2-1, Figures 2-9 and 2-10). However, there is an inverse

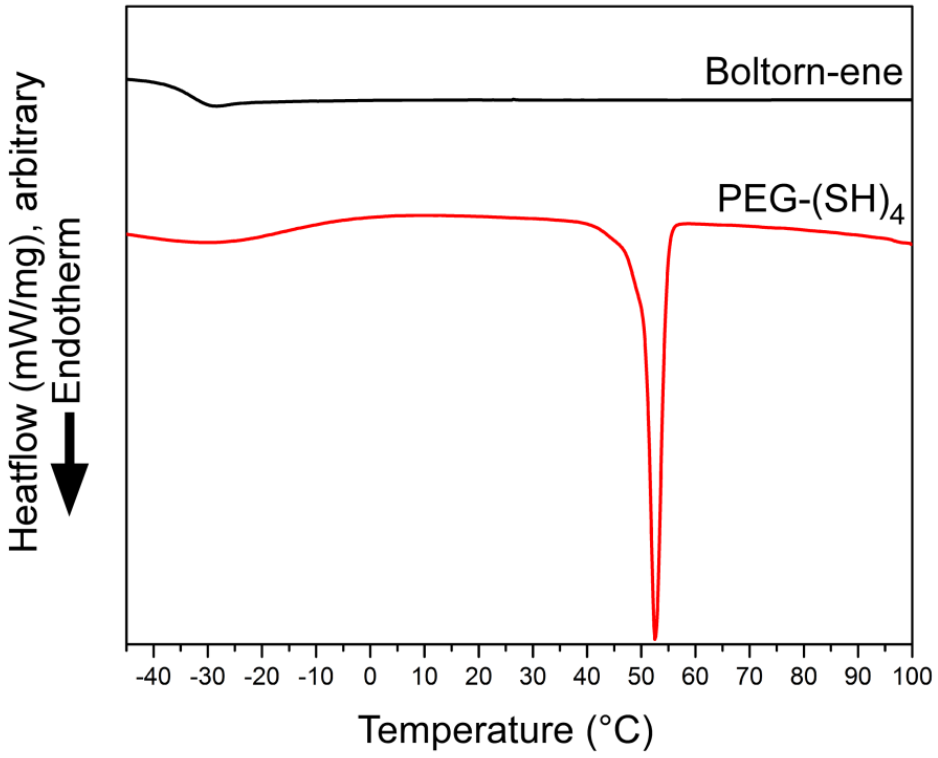


**Figure 2-9.** DSC of the Boltorn-PEG components.

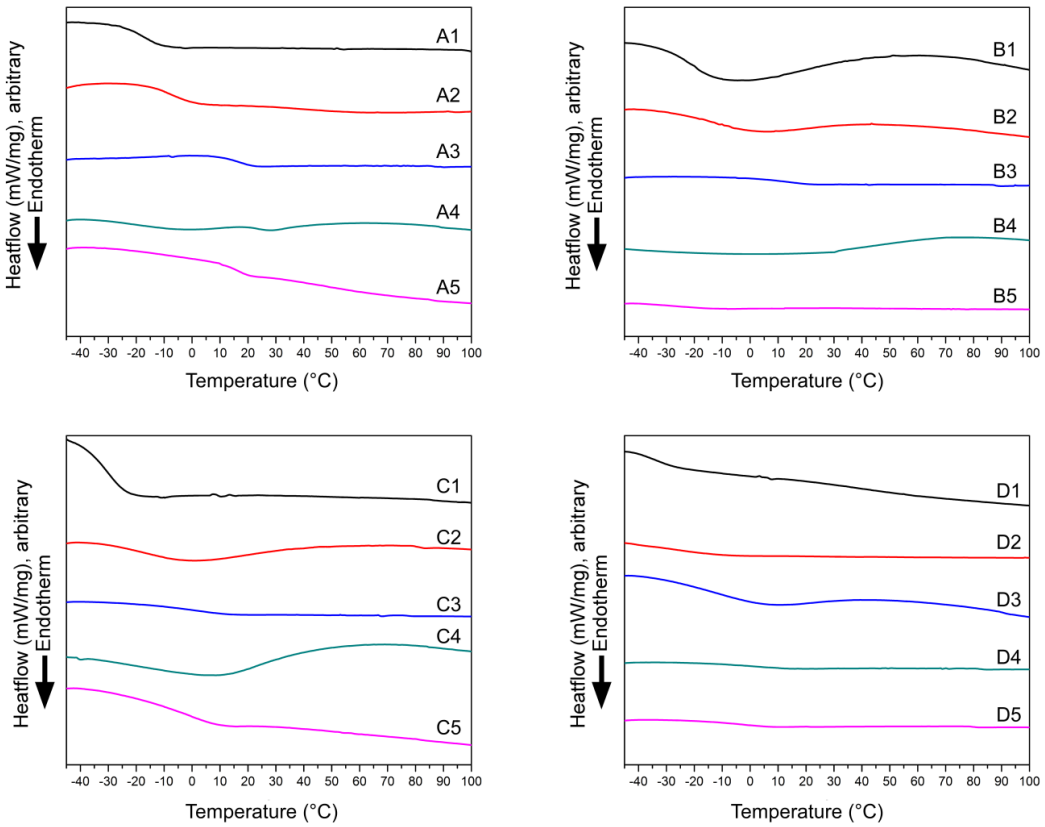


**Figure 2-10.** DSC plots for Boltorn-PEG films.

relationship with PEG wt%, where the film's $T_g$ decreases by as much as 30 °C (depending on PETMP concentration) as PEG content is increased, . The PEG $T_m$ peak (Figure 2-9), was not observed in any of the Boltorn-PEG film DSC plots, potentially due to the restricted mobility of crosslinked or partially crosslinked PEG prohibiting crystallization. TGA analysis of the films (Table 2-1 and Figure 2-11) shows decreases in peak degradation with increasing PEG wt% and/or PETMP concentration, a logical finding considering both components have slightly lower peak degradation temperatures than that of the parent Boltorn-ene polymer (Figure 2-12).

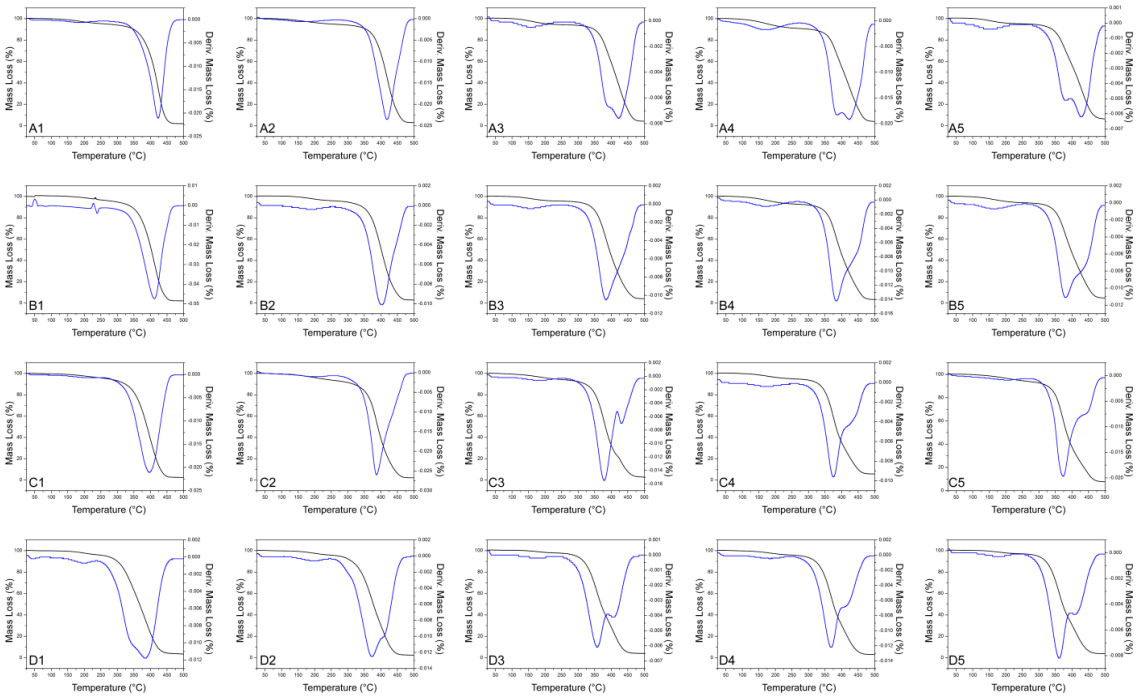


**Figure 2-11.** TGA mass loss and derivative mass loss for Boltorn-PEG films at varying PEG wt% and PETMP concentration.

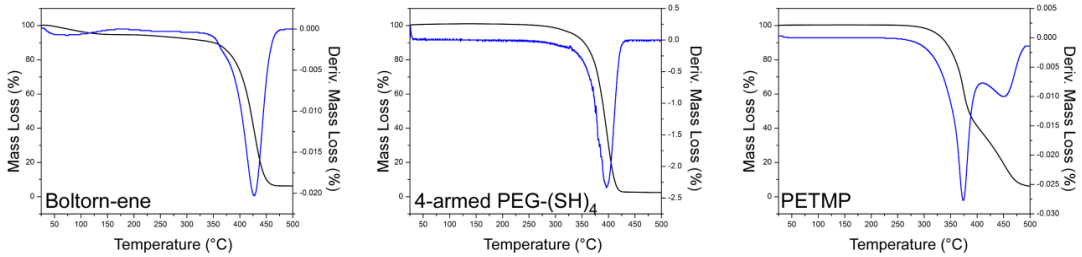


**Figure 2-12.** TGA mass loss and derivative mass loss for Boltorn-PEG components.

The surface features of the films were examined using contact angle analysis and AFM. There are a few trends that can be detected from the static initial contact angles (Table 2-1) and dynamic contact angles which were measured over a 3 h time period. Interestingly, regardless of PEG wt%, both advancing and receding contact angle appear to increase until 0.50-0.75 eq SH/ene, followed by a decline at 1.0 eq SH/ene. This increase can be

**Table 2-1.** Summary of the thermomechanical properties, elemental analysis and contact angle for the Boltorn-PEG films and components. Data for the antifouling (AF) series can be found in the following table, Table 2-2.

| Sample | PEG (wt%) | Thiol content (eq SH/ene) | Thermomechanical Data | | Elemental Analysis | | | Contact angle | | |
|---|---|---|---|---|---|---|---|---|---|---|
| | | | $T_g$, (°C) | $T_{decomp}$ (°C) | Carbon (%) | Hydrogen (%) | Sulfur (%) | Advancing ($\theta_a$, °) | Receding ($\theta_r$ °) | Hysteresis ($\theta_a$ - $\theta_r$) |
| Boltorn-ene | - | - | -37 | 427 | 57.21 | 6.51 | - | - | - | - |
| PEG-$SH_4$ | - | - | n/a ($T_m$ = 54) | 396 | 52.19 | 8.78 | 2.15 | - | - | - |
| PETMP | - | - | n/a | 373 | 41.88 | 5.77 | 26.34 | - | - | - |
| A1 | 0 | 0 | -17 | 424 | 54.44 | 6.65 | 0.00 | 60 ± 4 | 49 ± 1 | 11 |
| A2 | 0 | 0.25 | -14 | 419 | 55.75 | 6.48 | 3.80 | 74 ± 4 | 60 ± 1 | 14 |
| A3 | 0 | 0.50 | 15 | 423 | 53.81 | 6.46 | 6.39 | 77 ± 2 | 60 ± 2 | 17 |
| A4 | 0 | 0.75 | 18 | 413 | 52.70 | 6.45 | 8.42 | 79 ± 2 | 64 ± 2 | 15 |
| A5 | 0 | 1.00 | 16 | 428 | 51.16 | 6.33 | 9.91 | 65 ± 2 | 51 ± 1 | 14 |
| B1 | 5 | 0 | -21 | 412 | 57.63 | 6.82 | 0.19 | 69 ± 3 | 50 ± 2 | 19 |
| B2 | 5 | 0.25 | -15 | 403 | 55.36 | 6.64 | 4.08 | 71 ± 1 | 49 ± 6 | 21 |
| B3 | 5 | 0.50 | 10 | 384 | 53.72 | 6.60 | 6.94 | 73 ± 2 | 52 ± 5 | 21 |
| B4 | 5 | 0.75 | 21 | 384 | 52.84 | 6.51 | 8.64 | 80 ± 2 | 63 ± 4 | 17 |
| B5 | 5 | 1.00 | 23 | 381 | 51.79 | 6.31 | 10.05 | 70 ± 1 | 52 ± 2 | 18 |
| C1 | 15 | 0 | -29 | 397 | 56.98 | 6.86 | 0.36 | 58 ± 3 | 41 ± 3 | 17 |
| C2 | 15 | 0.25 | -16 | 388 | 55.26 | 6.77 | 3.47 | 76 ± 2 | 59 ± 3 | 15 |
| C3 | 15 | 0.50 | -4 | 378 | 53.68 | 6.39 | 6.04 | 86 ± 3 | 69 ± 3 | 17 |
| C4 | 15 | 0.75 | -10 | 376 | 52.62 | 6.59 | 8.12 | 76 ± 2 | 61 ± 2 | 15 |
| C5 | 15 | 1.00 | -10 | 373 | 51.84 | 6.44 | 10.51 | 19 ± 3 | 4 ± 2 | 15 |
| D1 | 25 | 0 | -23 | 386 | 56.61 | 7.00 | 0.49 | 80 ± 3 | 62 ± 1 | 18 |
| D2 | 25 | 0.25 | -22 | 373 | 54.54 | 6.81 | 3.50 | 72 ± 3 | 52 ± 2 | 20 |
| D3 | 25 | 0.50 | -15 | 357 | 53.47 | 6.62 | 5.84 | 83 ± 2 | 65 ± 3 | 18 |
| D4 | 25 | 0.75 | -9 | 367 | 52.66 | 6.45 | 7.77 | 74 ± 3 | 59 ± 1 | 15 |
| D5 | 25 | 1.00 | -8 | 362 | 51.00 | 6.39 | 13.44 | 10 ± 1 | 3 ± 2 | 7 |

**Table 2-2.** Summation of thermomechanical properties, elemental analysis and contact angle for the Boltorn-PEG films and components.

| Sample | PEG (wt%) | Thiol content (eq SH/ene) | Thermomechanical Data | | Elemental Analysis | | | Contact angle | | |
|---|---|---|---|---|---|---|---|---|---|---|
| | | | $T_g$, (°C) | $T_{decomp}$ (°C) | Carbon (%) | Hydrogen (%) | Sulfur (%) | Advancing ($\theta_a$, °) | Receding ($\theta_r$ °) | Hysteresis ($\theta_a$ - $\theta_r$) |
| Boltorn-ene | - | - | -37 | 427 | 57.21 | 6.51 | - | - | - | - |
| PEG-$SH_4$ | - | - | n/a ($T_m$ = 54) | 396 | 52.19 | 8.78 | 2.15 | - | - | - |
| PETMP | - | - | n/a | 373 | 41.88 | 5.77 | 26.34 | - | - | - |
| AF0 | 0 | 0.25 | -14 | 419 | 55.75 | 6.48 | 3.80 | 74 ± 4 | 60 ± 1 | 14 |
| AF5 | 5 | 0.25 | -15 | 403 | 55.36 | 6.64 | 4.08 | 71 ± 1 | 49 ± 6 | 22 |
| AF10 | 10 | 0.25 | -15 | 383 | 54.44 | 6.71 | 4.25 | 64 ± 2 | 40 ± 2 | 24 |
| AF15 | 15 | 0.25 | -16 | 388 | 55.26 | 6.77 | 3.47 | 76 ± 2 | 59 ± 3 | 15 |
| AF20 | 20 | 0.25 | -17 | 400 | 54.51 | 6.79 | 3.51 | 72 ± 2 | 46 ± 6 | 26 |
| AF25 | 25 | 0.25 | -22 | 373 | 54.54 | 6.81 | 3.50 | 72 ± 3 | 52 ± 2 | 20 |
| AF30 | 30 | 0.25 | -21 | 379 | 53.44 | 6.78 | 3.35 | 59 ± 2 | 39 ± 2 | 20 |
| AF35 | 35 | 0.25 | -21 | 390 | 55.11 | 6.76 | 3.21 | 37 ± 1 | 24 ± 2 | 13 |

attributed to increased crosslinking density, in addition to increased hydrophobicity from the crosslinker. The decline at 1.0 eq SH/ene. This increase can be attributed to increased crosslinking density, in addition to increased hydrophobicity from the crosslinker. The decline at 1.0 eq SH/ene is likely due to the presence of an excess of non-crosslinked/partially-crosslinked PETMP in the film, expressing excess hydrophilic thiol groups throughout the polymer bulk and surface which would lower contact angle. Contact angle hysteresis does not seem to change across PEG wt% or PETMP concentration, and is typically between 15° and 20°. Visualization of the surface with AFM allows for additional investigation into surface roughness. As can be seen in Figure 2-13, the surface is nanoscopically rough in both dry and wet state, although the roughness decreases slightly as a function of wetness (see Figure 2-14 and 2-15 for all

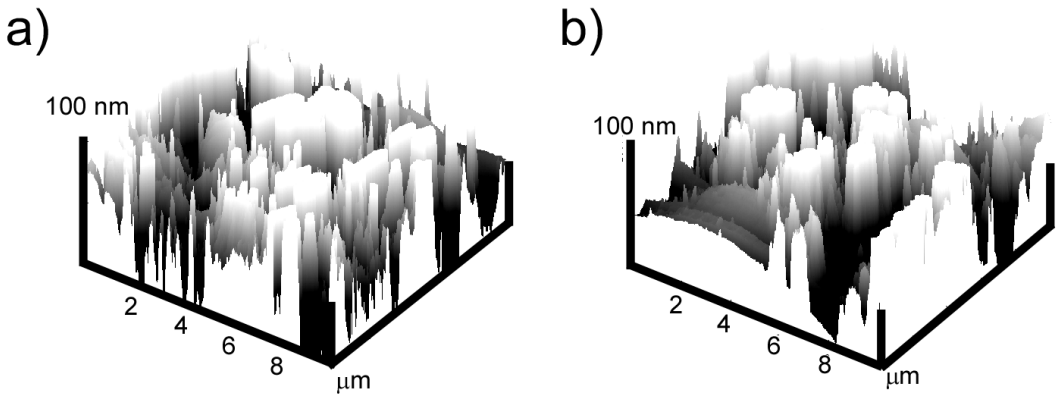


**Figure 2-13.** AFM images of Boltorn-PEG film D2 in both (a) dry and (b) wet state.

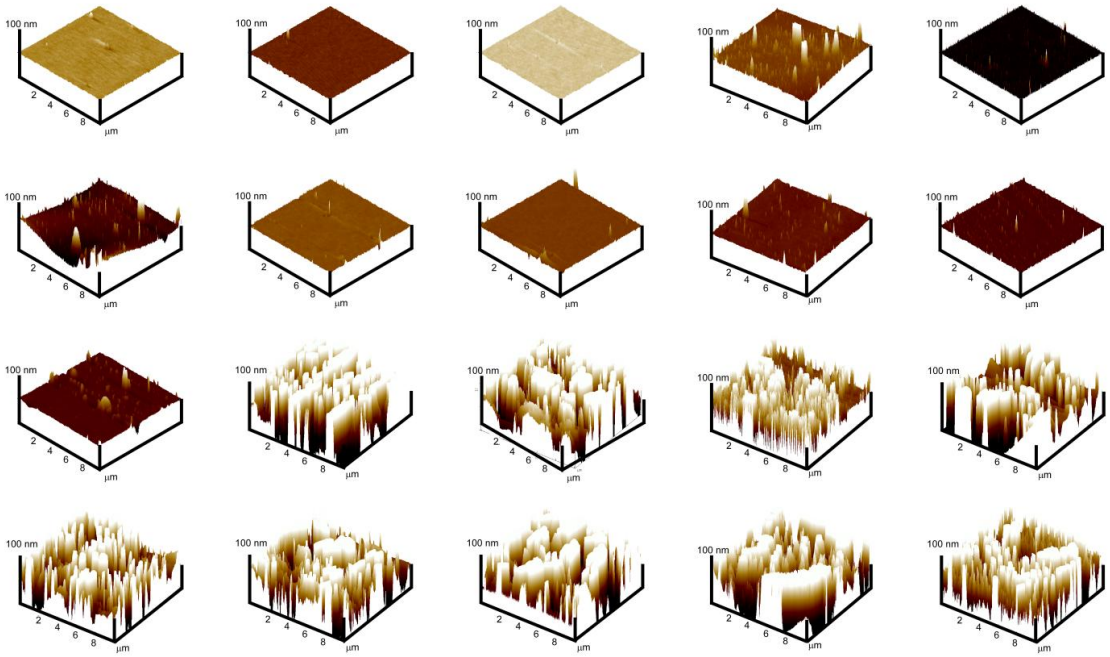


**Figure 2-14.** Dry AFM images of the combinatorial series of films as a function of PEG and PETMP. All images are scaled at 100 nm height and are 10 x 10 µm.

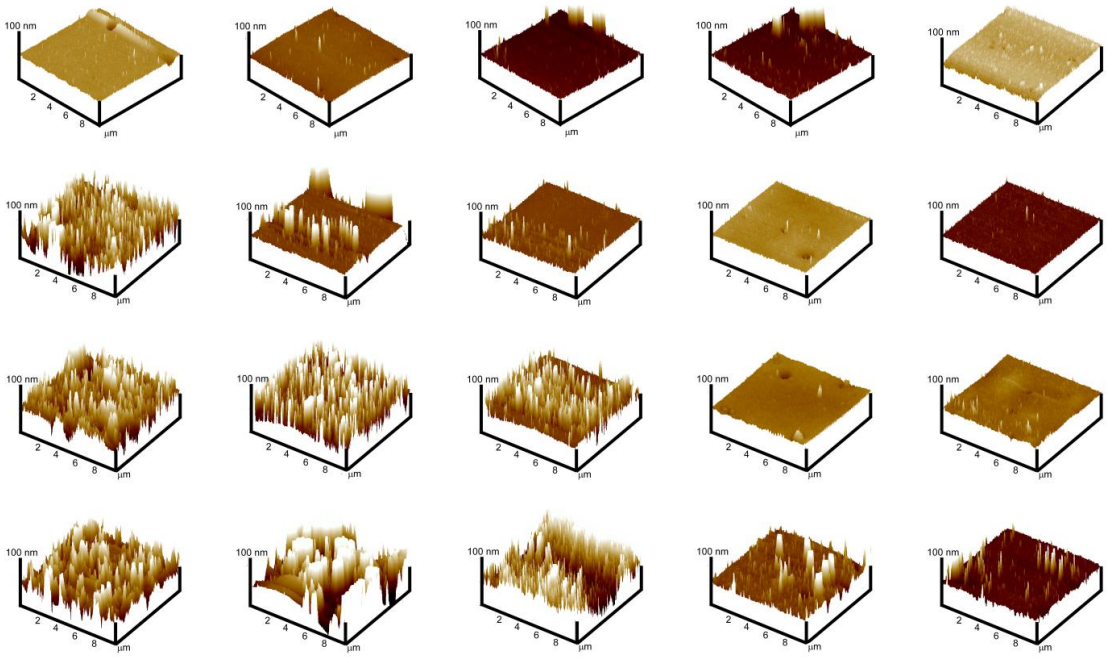


**Figure 2-15.** AFM images of the combinatorial series of films wetted for >24 h, as a function of PEG and PETMP. All images are scaled at 100 nm height and are 10 x 10 µm.

AFMs). In order to further examine this premise, a dynamic contact angle experiment was designed to measure the contact angle of the Boltorn-PEG films over 3 h to see how the surface reorganizes (Figure 2-16). Depending on PEG wt% and PETMP concentration, the contact angle typically decreases over time, which can be observed in AFM as a decrease in surface roughness.

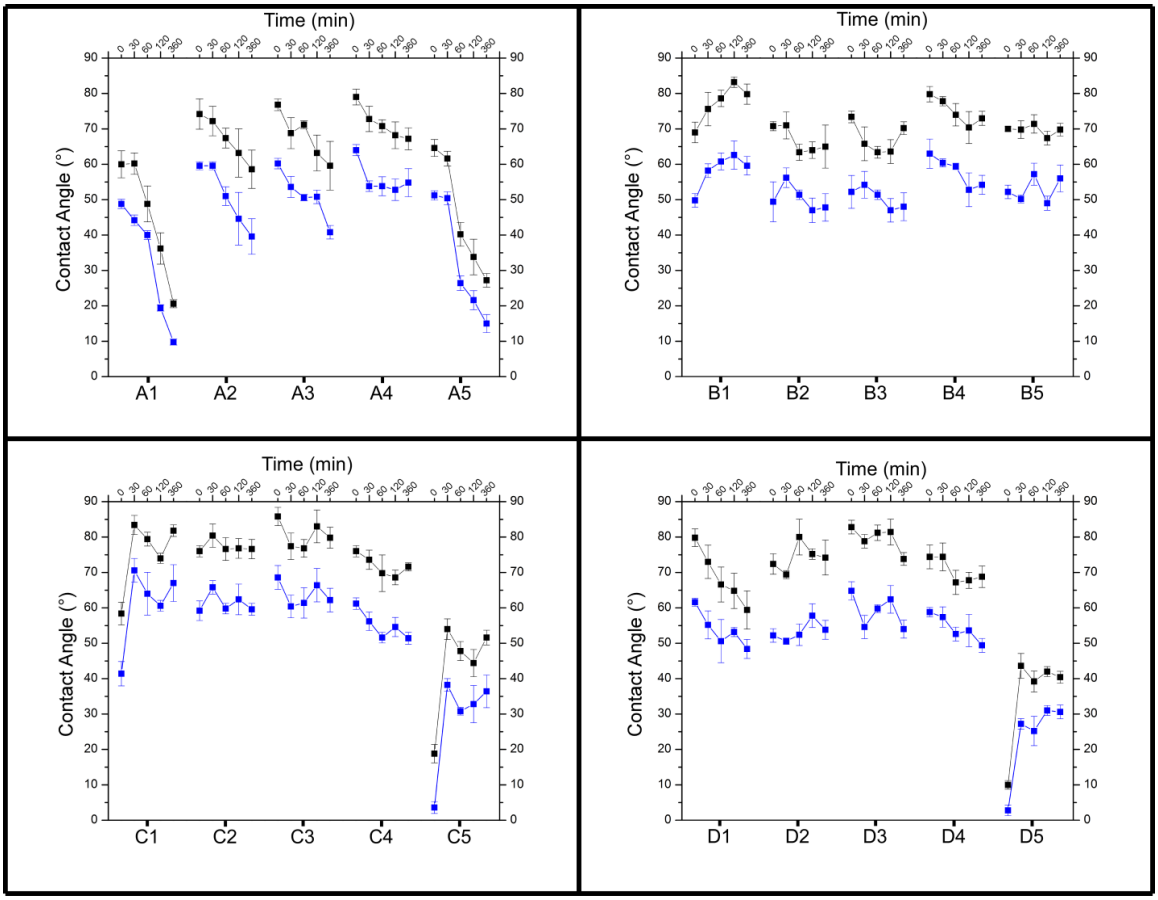


**Figure 2-16.** Dynamic water contact angle (advancing and receiving) of the Boltorn-PEG films at 0, 30, 60, 120 and 360 min.

Mechanical properties of anti-fouling films were measured using tensile testing. The samples were run using a constant (Hencky) strain of $0.01s^{-1}$. As can be seen in the contour plot of Young's modulus, $E_{dry}$, as a function of PEG wt% and PETMP

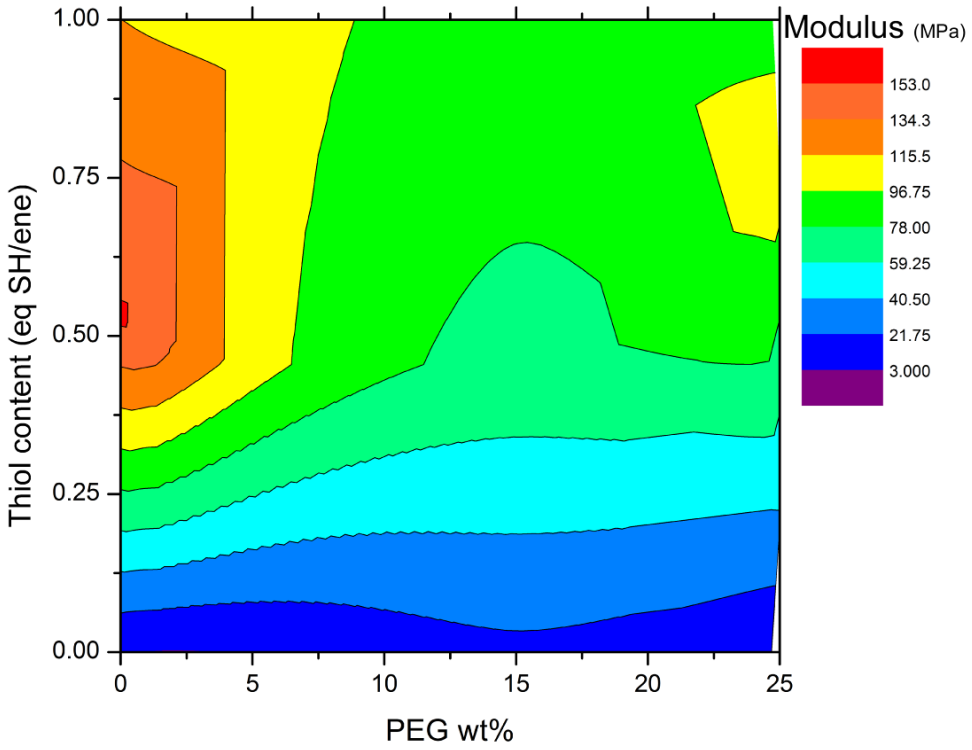


**Figure 2-17.** Contour plot of Young's modulus data for the combinatorial series as a function of PEG wt% (X axis) and PETMP concentration (Y axis).

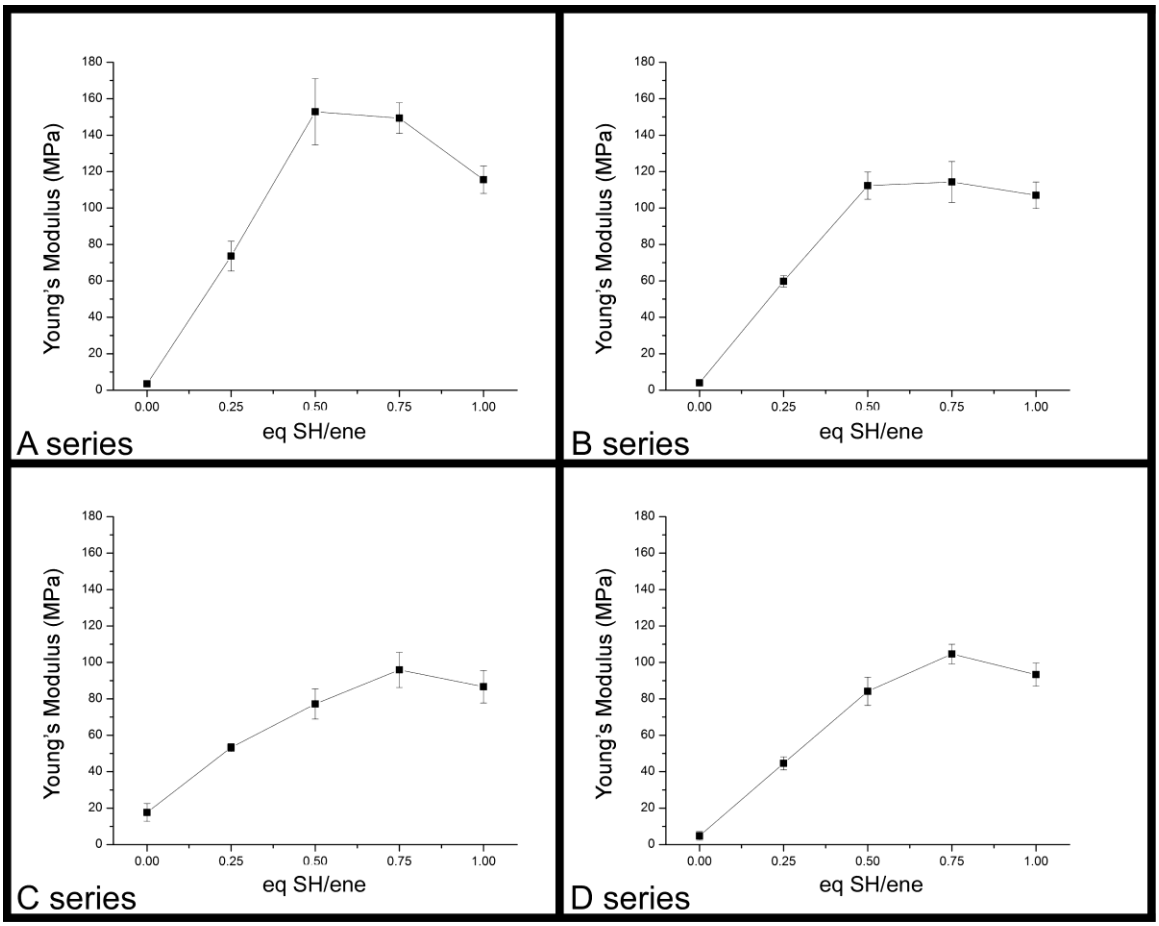


**Figure 2-18.** 2D representation of Young's modulus of the combinatorial series as a function of varying PETMP concentration.

concentration (Figure 2-17 and 2-18), there is a strong dependence of modulus on thiol content, with maxima found at approximately 0.50-0.75 eq SH/ene crosslinker concentration for all PEG wt%. The drop off from 0.75 eq SH/ene to 1.00 eq SH/ene likely is a result of excess crosslinker, as verified by IR

**Table 2-3.** Summary of the mechanical properties for the Boltorn-PEG films in both dry and wet conditions.

| | | | Before swelling in water | | | After swelling in water | | |
|---|---|---|---|---|---|---|---|---|
| Sample | PEG (wt%) | Thiol content (eq SH/ene) | Ultimate tensile strength ($\sigma_{UTS}$, MPa) | Strain to failure ($\varepsilon_f$, %) | $E_{dry}$ (MPa) | Ultimate tensile strength ($\sigma_{UTS}$, MPa) | Strain to failure ($\varepsilon_f$, %) | $E_{wet}$ (MPa) |
| A1 | 0 | 0 | 140.8 ± 35.6 | 48 ± 8 | 3.46 ± 1.28 | - | - | - |
| A2 | 0 | 0.25 | 790.7 ± 205.4 | 19 ± 6 | 72.61 ± 8.20 | 1095.3 ± 293.2 | 26 ± 3 | 69.8 ± 10.13 |
| A3 | 0 | 0.50 | 2811.3 ± 679.3 | 34 ± 6 | 152.83 ± 18.12 | - | - | - |
| A4 | 0 | 0.75 | 2095.9 ± 352.4 | 38 ± 11 | 149.21 ± 7.28 | - | - | - |
| A5 | 0 | 1.00 | 1922.0 ± 477.4 | 27 ± 7 | 118.86 ± 9.86 | - | - | - |
| B1 | 5 | 0 | 134.7 ± 51.2 | 32 ± 20 | 4.02 ± 0.93 | - | - | - |
| B2 | 5 | 0.25 | 532.4 ± 155.0 | 13 ± 4 | 59.80 ± 3.12 | 952.9 ± 137.2 | 21 ± 2 | 63.55 ± 5.52 |
| B3 | 5 | 0.50 | 2313.1 ± 374.2 | 45 ± 11 | 112.23 ± 7.46 | - | - | - |
| B4 | 5 | 0.75 | 2098.6 ± 437.1 | 32 ± 10 | 120.82 ± 17.48 | - | - | - |
| B5 | 5 | 1.00 | 1281.1 ± 356.8 | 20 ± 10 | 106.04 ± 6.69 | - | - | - |
| C1 | 15 | 0 | 558.1 ± 212.7 | 78 ± 39 | 17.68 ± 4.82 | 71.0 ± 16.8 | 38 ± 13 | 2.81 ± 0.57 |
| C2 | 15 | 0.25 | 540.5 ± 173.3 | 14 ± 5 | 53.30 ± 2.15 | 853.2 ± 307.9 | 29 ± 13 | 38.44 ± 1.87 |
| C3 | 15 | 0.50 | 688.5 ± 106.5 | 11 ± 1 | 77.20 ± 8.30 | 788.7 ± 495.7 | 13 ± 11 | 63.40 ± 20.42 |
| C4 | 15 | 0.75 | 1192.1 ± 455.0 | 19 ± 8 | 95.89 ± 9.65 | 521.4 ± 168.0 | 11 ± 2 | 83.82 ± 20.42 |
| C5 | 15 | 1.00 | 651.7 ± 250.6 | 11 ± 2 | 86.66 ± 8.93 | 1261.1 ± 153.9 | 27 ± 3 | 84.90 ± 13.72 |
| D1 | 25 | 0 | 208.4 ± 49.1 | 66 ± 24 | 4.22 ± 1.96 | - | - | - |
| D2 | 25 | 0.25 | 351.9 ± 40.1 | 11 ± 1 | 44.57 ± 3.56 | 461.3 ± 197.8 | 14 ± 5 | 47.34 ± 4.80 |
| D3 | 25 | 0.50 | 1330.2 ± 296.9 | 27 ± 8 | 84.14 ± 7.80 | - | - | - |
| D4 | 25 | 0.75 | 1634.0 ± 123.7 | 23 ± 2 | 104.62 ± 5.39 | - | - | - |
| D5 | 25 | 1.00 | 1591.6 ± 144.0 | 30 ± 5 | 93.32 ± 6.35 | - | - | - |

spectroscopy, partially plasticizing the crosslinked film. There appears to be a minor effect with respect to the PEG, in that an increase in PEG wt% provides a small decrease in modulus. Similar trends with PEG wt% and PETMP can be observed for the ultimate tensile strength ($\sigma_{UTS}$). Interestingly, the failure strains for the Boltorn-PEG films were remarkably low, from approximately 10-30%, with the exception of the films with no PETMP (**A1**, **B1**, **C1** and **D1**), where the elongation was much higher, 30-80%, due to the low $T_g$ and subsequent flexibility of the films. A summary of measured modulus values, ultimate tensile strengths and % elongations have been compiled (Table 2-3). , There does not appear to be as large a disparity between the Young's modulus of wet and dry Boltorn-PEG films as was seen with the HBFP-PEG series, (REFS) however, there is a statistically significant difference in ultimate tensile strength (Figure 2-19). At a constant 0.25 eq SH/ene crosslinker concentration (films **A2**, **B2**, **C2** and **D2**),

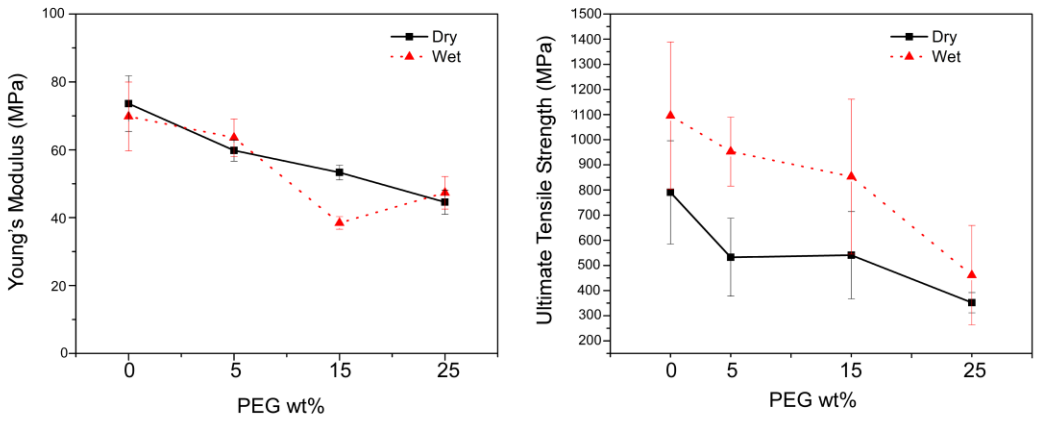


**Figure 2-19.** Young's modulus (left) and ultimate tensile strength (right) for the "2 series" (**A2**, **B2**, **C2** and **D2**) as measured dry and wetted by artificial seawater.

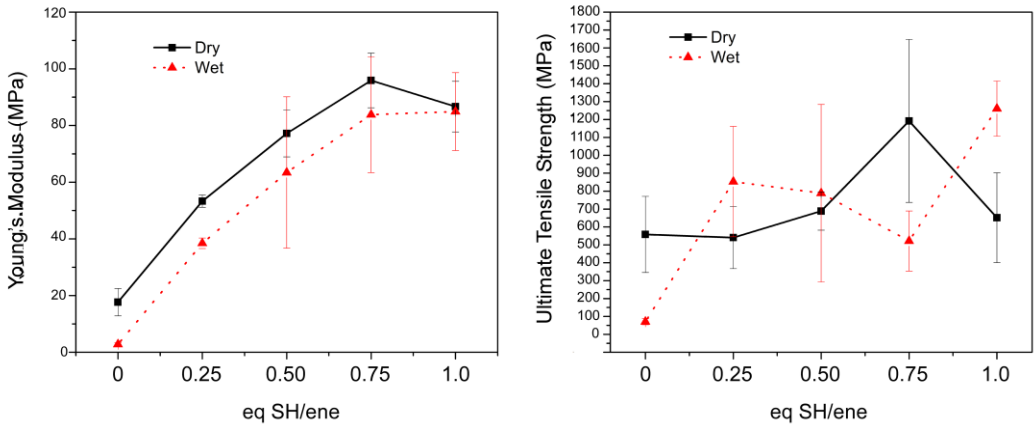


**Figure 2-20.** Young's modulus (left) and ultimate tensile strength (right) for the "C series" (**C1**, **C2**, **C3**, **C4** and **C5**) as measured dry and wetted by artificial seawater.

the modulus values for wet and dry films are similar with the exception of **C2**, which shows a decrease in modulus between the dry to wet state, whereas overall, the ultimate tensile strength actually increases when wet. Additional tensile tests were performed for the rest of the "C series" (**C1**, **C3**, **C4** and **C5**) (Figure 2-20), where similar trends can be observed for modulus, but not for ultimate tensile strength, which shows no apparent trends.

The anti-fouling ability of Boltorn-PEG films at a constant PETMP concentration of 0.25 eq SH/ene with varying PEG wt% (0, 5, 10, 15, 20, 25, 30 and 35 wt%) against a soft fouling marine alga was assessed through a series of two experiments, viz. spore settlement (attachment) and the strength of attachment of sporelings (young plants), which was assessed by exposure to a range of impact pressures generated by a water jet. Spore settlement densities were low on all the amphiphilic coatings compared to that on a PDMSe standard (Figure 2-21). Although spore density was low, it increased slowly with

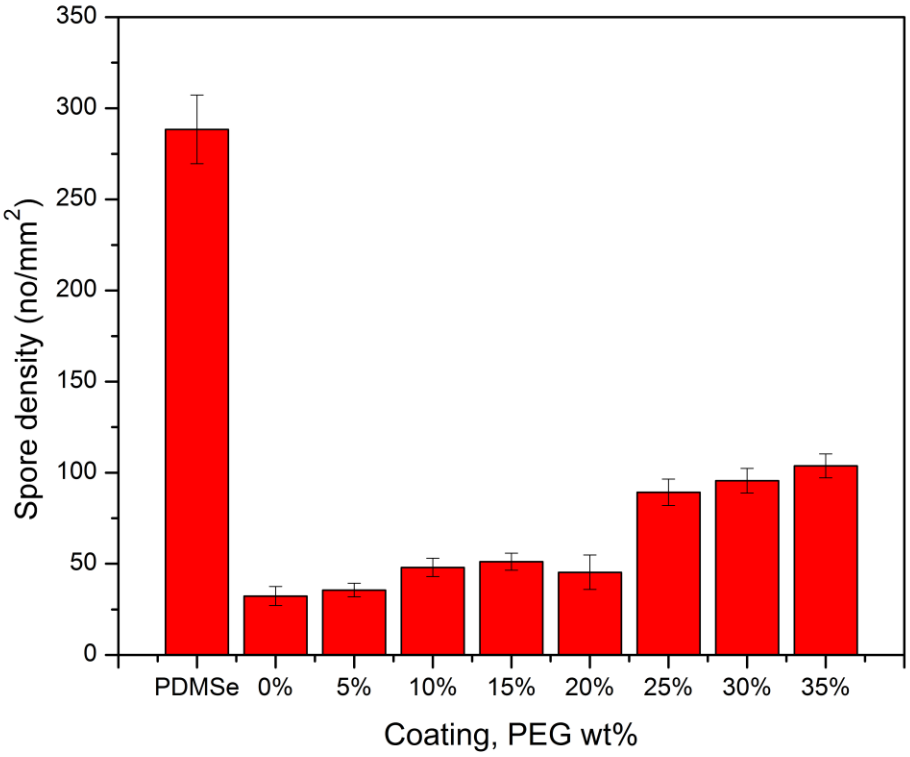


**Figure 2-21.** The settlement density of spores of *Ulva* on amphiphilic coatings after 1 h settlement. (Glass standards settled with spores at the same time had heavier settlement densities ~ 767 spores mm$^{-2}$). Each point is the mean from 90 counts on 3 replicate slides. Bars show 95% confidence limits.

the PEG content of the coating. One-way analysis of variance on spore density for the amphiphilic samples alone showed there were significant differences between the samples ($F_{7, 712} = 80$ $P<0.05$). A Tukey test showed that the settlement densities on the majority of coatings were significantly different to each other (at least at either end of the series), confirming the trend of increasing settlement density with increasing PEG content. Due to the increase in surface roughness with increasing PEG wt%, (*vide supra,*

AFM discussion), it is possible that the settlement increases as a function of PEG directly due to the loss of a smooth, highly hydrophilic surface. Self assembled monolayers formed from PEG inhibit the settlement of spores(72) and studies on PEG-containing systems have generally shown the opposite trend, *i.e.* settlement densities decrease with increasing PEG content.(73) For the PEG-SAMs, the inhibition of settlement has been attributed to the increased hydrophilicity and subsequent hydration of the coating and for amphiphilic coatings, surface restructuring following immersion produced changes to surface nanostructure,(74) possibly making it more difficult for spores to 'detect' and adhere to the surface. Sporeling biomass was evaluated on all the coatings after 10 days of growth. Sporelings grew normally on all the samples with no signs of toxicity, although as expected form the low density of settled spores, the amount of biomass was lower on the amphiphilic samples than on the PDMSe standard. It is possible that the reduced spore settlement density could be due to residual surface thiols that effectively "cap" cysteine residues in the algal adhesive, preventing the formation of disulfide linkages, either in the adhesive protein itself or cementing glycoproteins.(75) The DACM-thiol fluorescence experiment showed that there is a minor amount of surface thiols (~5-10 fluorescent %) present in the AF film series (Figure 2-22), which could be responsible for the non-fouling character of the Boltorn-PEG films.

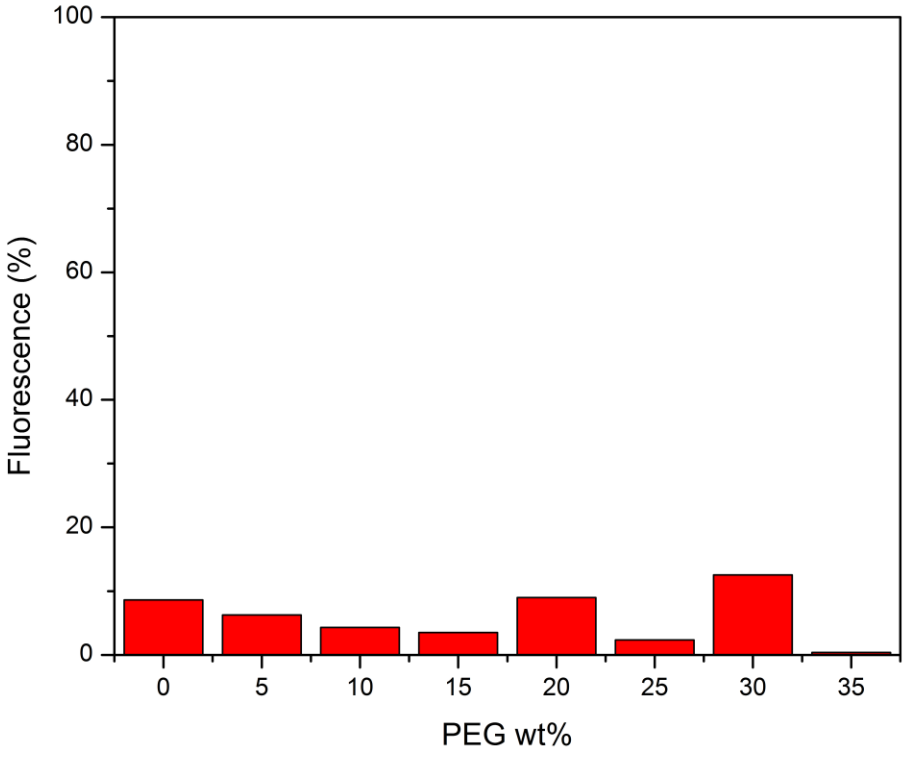


**Figure 2-22.** Surface DACM-thiol fluorescence of the anti-fouling coating series.

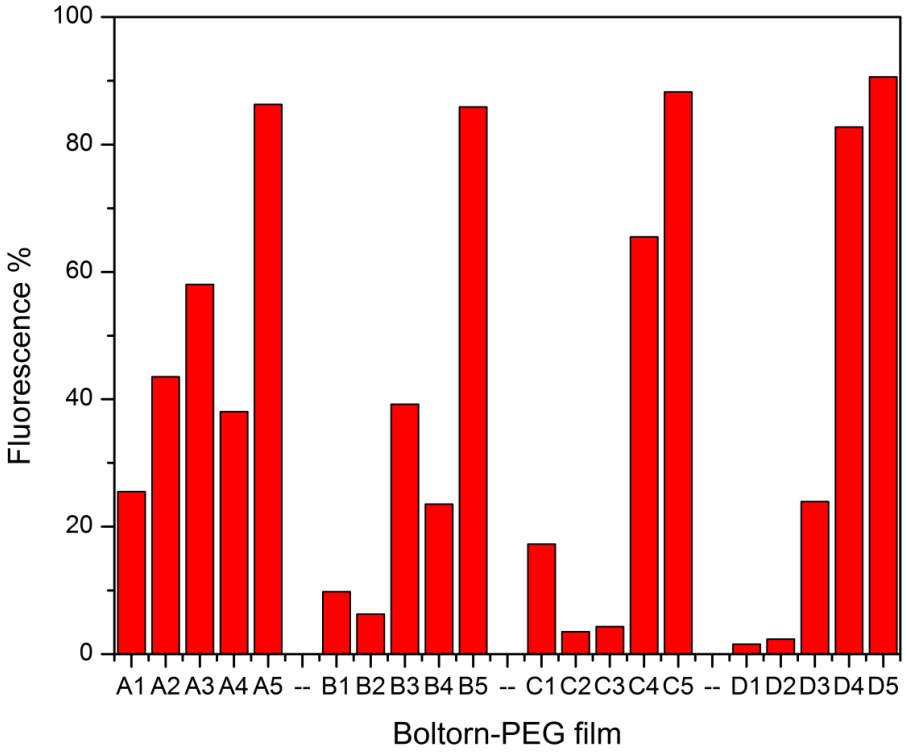


**Figure 2-23.** Fluorescence of DACM-thiol conjugated films on the combinatorial series.

It broadly followed that of spore settlement density and rose slightly with increasing PEG content of the coating. Due to delamination issues, sporeling strength of attachment was measured only for the 0%, 5%, 10% and 15% coatings. Sporelings were

**Figure 2-24.** Typical growth of *Ulva* sporelings on amphiphilic coatings after 10 days. From left; PDMSe, 0, 5, 10, 15, 20, 25, 30 and 35 PEG wt% coatings.

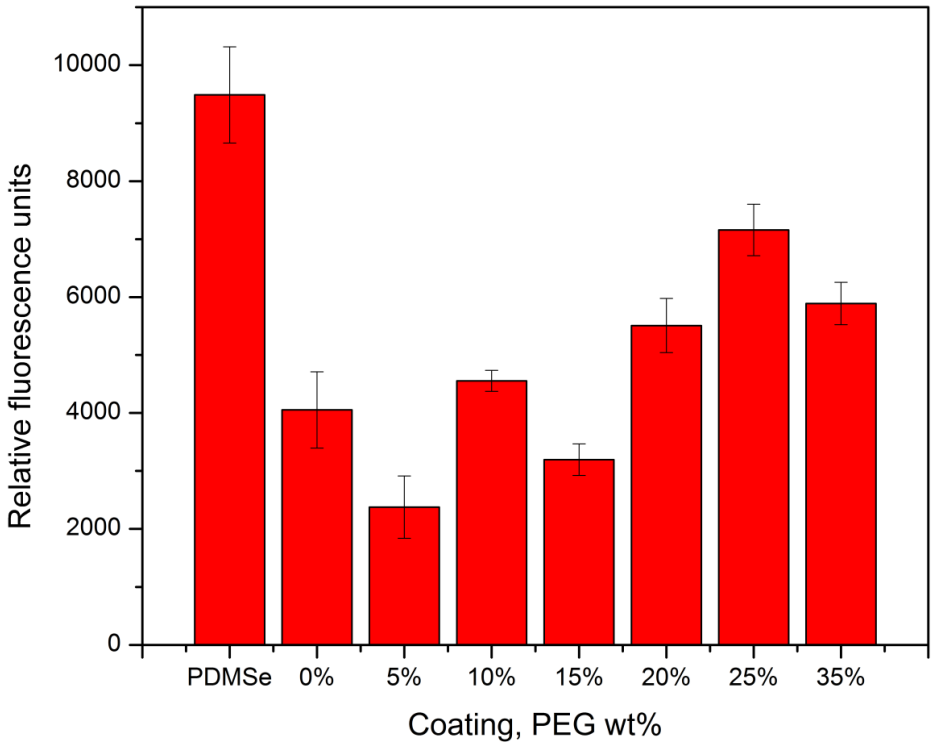


**Figure 2-25.** The growth of sporelings of *Ulva* on amphiphilic coatings after 10 days. Each point is the mean biomass from 6 replicate slides measured using a fluorescence

plate reader (RFU; relative fluorescence unit). Error bars show standard error of the mean.

attached more strongly on all the coatings than on the PDMSe standard, however, ease of removal increased with increasing PEG content, where the highest removal was observed from the 15% coating regardless of pressure. The critical water pressures to remove 50% of the biofilms are shown in Table 2-4 and Figure 2-26. The lines in Figure 2-26 have a distinctive shape that is not typical for sporeling detachment and was not seen in the previous experiments with the films (*i.e.* they contain a large flat region corresponding to mid-range water

**Table 2-4.** Critical surface pressures for 50% removal of sporeling biofilms derived from curves in Figure 2-25 and percent removal of sporeling biofilms at the single water pressure of 64 kPa. Samples listed in order of ease of removal.

| Label | Critical water pressure to remove 50% of biomass (kPa) | | % removal at pressure of 64 kPa |
|---|---|---|---|
| PDMSe | 50 | | 75% |
| 15 | Approx 93 | | 57% |
| 10 | Approx. 112 | | 45% |
| 5 | 184 | | 18% |
| 0 | 184 | | 8% |

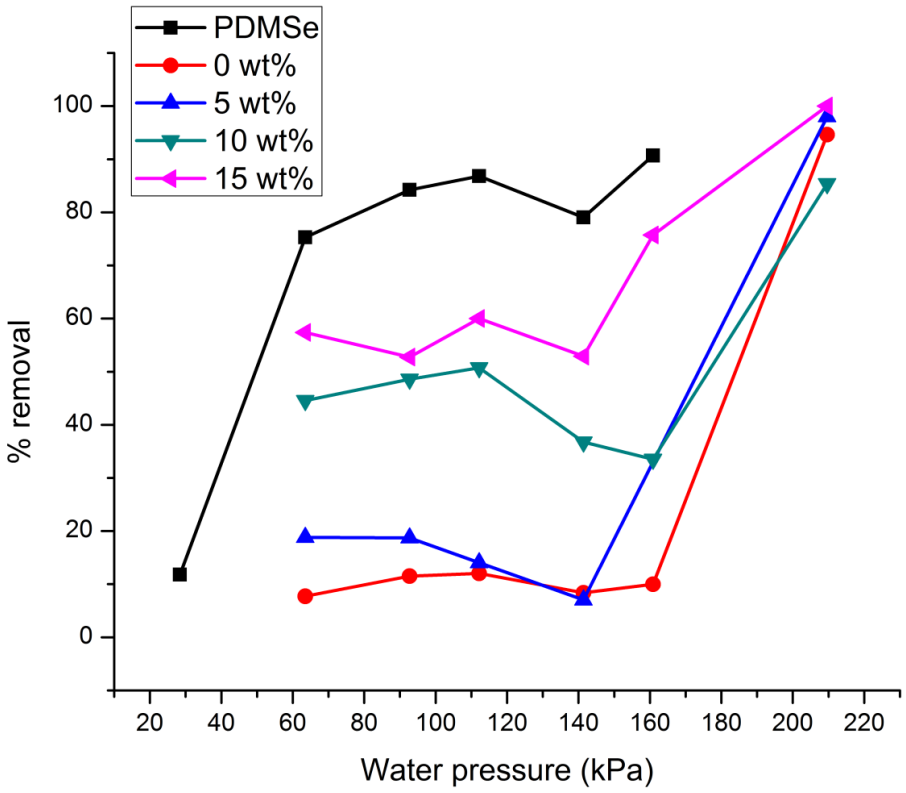


**Figure 2-26.** Percent removal of 10 day old sporelings of *Ulva* from amphiphilic coatings plotted as a function of surface water pressure (kPa). Coatings were exposed to a range of different surface pressures from the water jet. PDMSe is T2 Silastic.

pressures). The phenomenon might be connected with the extended growth period given to the sporelings in this experiment (10 rather than 7 days), but we do not know why this would cause a change in the shape of the release curve. The coatings with PEG content greater than 15% delaminated and were not tested.

## Conclusions

Optimization of the design and synthesis of thiol-ene crosslinked Boltorn-PEG films was performed at varying PETMP concentration and PEG wt%. Spectroscopic monitoring allowed for monitoring of the crosslinking reaction, where it was found that near-complete crosslinking occurs above 0.75 eq SH/ene PETMP concentration, regardless of PEG wt%. Thermomechanical analysis was performed on the film set, where it was observed that there is a general increase in film $T_g$ as a function of PEG wt%. Tensile tests of films in both the dry and wet state revealed a dramatic increase in Young's modulus as a function of PETMP, reaching a peak at 0.75 eq SH/ene. Young's modulus reduced slightly when saturated in artificial seawater, however, ultimate tensile strength increased at constant PETMP concentration. The nanotopography of the films was analyzed using AFM, where increasing nanoroughness occurred with increasing PEG wt%. A comprehensive anti-fouling study was performed against the green alga, *Ulva,* on Boltorn-PEG films at constant 0.25 eq SH/ene PETMP concentration across a wide range of PEG wt% (0-35 wt%), where it was observed that spore settlement density was lower when compared to a PDMSe coating. There was a slight compromise in using a 0.25 eq SH/ene PETMP concentration, in that the films have lower $T_g$ and modulus than films at higher PETMP concentration, however a balance was needed in order to prepare completely non-toxic films. Additional studies looking into the improving adhesion to glass substrates to allow for complete fouling release studies are underway.

A similar system will be introduced in Chapter 3, using a radically different architecture. A transformation from Boltorn-ene, a hydrophobic polymer with extensive amounts of alkenes on the periphery, to a block copolymer morphology with alkenes along the backbone with PEG/PEO directly coupled to the polymer. The synthesis and

characterization of this new polymer, PEO-b-PIp, is presented in total, as well as investigations into producing thiol-ene crosslinked coatings. This system takes advantage of the unique assembly abilities of block copolymers, as well as the low polydispersity.

**Acknowledgement**

The authors would like to thank Perstorp for the sample of Boltorn H30. This material is based on work supported by the Office of Naval Research under grant number N00014-08-1-0398 and the National Science Foundation DMR-0451490. Assistant Professor fellowship from the Knut and Alice Wallenberg Foundation (to A.M.N), as well as financial support from Åke Wibergs foundation, Karolinska Insitutet, The Swedish Medical Nanoscience Center and from the Swedish Research Council 2009-3259, are also gratefully acknowledged.

**References**

(1) Yebra, D. M.; Kiil, S.; Dam-Johansen, K. (2004) Antifouling technology - past, present and future steps towards efficient and environmentally friendly antifouling coatings. *Progress in Organic Coatings 50*(2), 75-104.

(2) Chambers, L. D.; Stokes, K. R.; Walsh, F. C.; Wood, R. J. K. (2006) Modern approaches to marine antifouling coatings. *Surface & Coatings Technology 201*(6), 3642-3652.

(3) Bartels, J. W.; Cheng, C.; Powell, K. T.; Xu, J. Q.; Wooley, K. L. (2007) Hyperbranched fluoropolymers and their hybridization into complex amphiphilic

crosslinked copolymer networks. *Macromolecular Chemistry and Physics 208*(15), 1676-1687.

(4) Gudipati, C. S.; Finlay, J. A.; Callow, J. A.; Callow, M. E.; Wooley, K. L. (2005) The antifouling and fouling-release perfomance of hyperbranched fluoropolymer (HBFP)-poly(ethylene glycol) (PEG) composite coatings evaluated by adsorption of biomacromolecules and the green fouling alga Ulva. *Langmuir 21*(7), 3044-3053.

(5) Yarbrough, J. C.; Rolland, J. P.; DeSimone, J. M.; Callow, M. E.; Finlay, J. A.; Callow, J. A. (2006) Contact angle analysis, surface dynamics, and biofouling characteristics of cross-linkable, random perfluoropolyether-based graft terpolymers. *Macromolecules 39*(7), 2521-2528.

(6) Youngblood, J. P.; Andruzzi, L.; Ober, C. K.; Hexemer, A.; Kramer, E. J.; Callow, J. A.; Finlay, J. A.; Callow, M. E. (2003) Coatings based on side-chain ether-linked poly(ethylene glycol) and fluorocarbon polymers for the control of marine biofouling. *Biofouling 19*, 91-98.

(7) Aldred, N.; Clare, A. S. (2008) The adhesive strategies of cyprids and development of barnacle-resistant marine coatings. *Biofouling 24*(5), 351-363.

(8) Beigbeder, A.; Degee, P.; Conlan, S. L.; Mutton, R. J.; Clare, A. S.; Pettitt, M. E.; Callow, M. E.; Callow, J. A.; Dubois, P. (2008) Preparation and characterisation of silicone-based coatings filled with carbon nanotubes and natural sepiolite and their application as marine fouling-release coatings. *Biofouling 24*, 291-302.

(9) Majumdar, P.; Lee, E.; Patel, N.; Ward, K.; Stafslien, S. J.; Daniels, J.; Boudjouk, P.; Callow, M. E.; Callow, J. A.; Thompson, S. E. M. (2008) Combinatorial materials research applied to the development of new surface coatings IX: An

investigation of novel anti-fouling/fouling-release coatings containing quaternary ammonium salt groups. *Biofouling 24*, 185-200.

(10) Marabotti, I.; Morelli, A.; Orsini, L. M.; Martinelli, E.; Galli, G.; Chiellini, E.; Lien, E. M.; Pettitt, M. E.; Callow, J. A.; Conlan, S. L.; Mutton, R. J.; Clare, A. S.; Kocijan, A.; Donik, C.; Jenko, M. (2009) Fluorinated/siloxane copolymer blends for fouling release: Chemical characteristion and biological evaluation with algae and barnacles. *Biofouling 25*, 481-493.

(11) McMaster, D. M.; Bennett, S. M.; Tang, Y.; Finlay, J. A.; Kowalke, G. L.; Nedved, B.; Bright, S. M.; Callow, M. E.; Callow, J. A.; Wendt, D. E.; Hadfield, M. G.; Detty, M. R. (2009) Antifouling character of 'active' hybrid xerogel coatings with sequestered catalysts for the activation of hydrogen peroxide. *Biofouling 25*, 21-33.

(12) Li, G. Z.; Xue, H.; Gao, C. L.; Zhang, F. B.; Jiang, S. Y. (2010) Nonfouling Polyampholytes from an Ion-Pair Comonomer with Biomimetic Adhesive Groups. *Macromolecules 43*(1), 14-16.

(13) Yang, W.; Zhang, L.; Wang, S. L.; White, A. D.; Jiang, S. Y. (2009) Functionalizable and ultra stable nanoparticles coated with zwitterionic poly(carboxybetaine) in undiluted blood serum. *Biomaterials 30*(29), 5617-5621.

(14) Zhang, Z.; Finlay, J. A.; Wang, L. F.; Gao, Y.; Callow, J. A.; Callow, M. E.; Jiang, S. Y. (2009) Polysulfobetaine-Grafted Surfaces as Environmentally Benign Ultralow Fouling Marine Coatings. *Langmuir 25*(23), 13516-13521.

(15) Unsworth, L. D.; Sheardown, H.; Brash, J. L. (2005) Protein resistance of surfaces prepared by sorption of end-thiolated poly(ethylene glycol) to gold: Effect of surface chain density. *Langmuir 21*(3), 1036-1041.

(16) Rydholm, A. E.; Bowman, C. N.; Anseth, K. S. (2005) Degradable thiol-acrylate photopolymers: polymerization and degradation behavior of an in situ forming biomaterial. *Biomaterials 26*(22), 4495-4506.

(17) Feng, S. J.; Wang, Q.; Gao, Y.; Huang, Y. G.; Qing, F. L. (2009) Synthesis and Characterization of a Novel Amphiphilic Copolymer Capable as Anti-Biofouling Coating Material. *Journal of Applied Polymer Science 114*(4), 2071-2078.

(18) Brady, R. F.; Singer, I. L. (2000) Mechanical factors favouring release from fouling release coatings. *Biofouling 15*, 73-81.

(19) Genzer, J.; Efimenko, K. (2006) Recent developments in superhydrophobic surfaces and their relevance to marine fouling: a review. *Biofouling 22*(5), 339-360.

(20) Hoipkemeier-Wilson, L.; Schumacher, J.; Carman, M.; Gibson, A.; Feinberg, A.; Callow, M.; Finlay, J.; Callow, J.; Brennan, A. (2004) Antifouling potential of lubricious, micro-engineered, PDMS elastomers against zoospores of the green fouling alga Ulva (Enteromorpha). *Biofouling 20*(1), 53-63.

(21) Scardino, A. J.; Zhang, H.; Cookson, D. J.; Lamb, R. N.; de Nys, R. (2009) The role of nano-roughness in antifouling. *Biofouling 25*(8), 757-767.

(22) Morgan, C. R.; Ketley, A. D. (1978) The effect of phosphines on thiol/ene curing systems. *Journal of Polymer Science: Polymer Letters Edition 16*(2), 75-79.

(23) Morgan, C. R.; Magnotta, F.; Ketley, A. D. (1977) Thiol/ene photocurable polymers. *Journal of Polymer Science: Polymer Chemistry Edition 15*(3), 627-645.

(24) Kade, M. J.; Burke, D. J.; Hawker, C. J. (2010) The power of thiol-ene chemistry. *Journal of Polymer Science Part A: Polymer Chemistry 48*(4), 743-750.

(25) Ma, J.; Cheng, C.; Wooley, K. L. (2009) The Power of RAFT for Creating Polymers Having Imbedded Side-Chain Functionalities: Norbornenyl-Functionalized Polymers and their Transformations via ROMP and Thiol-ene Reactions. *Australian Journal of Chemistry 62*(11), 1507-1519.

(26) Jones, M. W.; Mantovani, G.; Ryan, S. M.; Wang, X. X.; Brayden, D. J.; Haddleton, D. M. (2009) Phosphine-mediated one-pot thiol-ene "click" approach to polymer-protein conjugates. *Chem. Commun.* (35), 5272-5274.

(27) Killops, K. L.; Campos, L. M.; Hawker, C. J. (2008) Robust, Efficient, and Orthogonal Synthesis of Dendrimers via Thiol-ene “Click” Chemistry. *J. Am. Chem. Soc. 130*(15), 5062-5064.

(28) Chan, J. W.; Yu, B.; Hoyle, C. E.; Lowe, A. B. (2008) Convergent synthesis of 3-arm star polymers from RAFT-prepared poly(N,N-diethylacrylamide) via a thiol-ene click reaction. *Chem. Commun.* (40), 4959-4961.

(29) O'Brien, A. K.; Cramer, N. B.; Bowman, C. N. (2006) Oxygen inhibition in thiol-acrylate photopolymerizations. *Journal of Polymer Science Part A-Polymer Chemistry 44*(6), 2007-2014.

(30) Cramer, N. B.; Scott, J. P.; Bowman, C. N. (2002) Photopolymerizations of thiol-ene polymers without photoinitiators. *Macromolecules 35*(14), 5361-5365.

(31) Hoyle, C. E.; Lee, T. Y.; Roper, T. (2004) Thiol-enes: Chemistry of the past with promise for the future. *Journal of Polymer Science Part A-Polymer Chemistry 42*(21), 5301-5338.

(32) Ihre, H.; Johansson, M.; Malström, E.; Hult, A. (1996) *Dendrimers and hyperbranched aliphatic polyesters based on 2,2-bis(hydroxymethyl)propionic acid (Bis-MPA)*. JAI Press Inc.: Vol. 3.

(33) Mespouille, L.; Hedrick, J. L.; Dubois, P. (2009) Expanding the role of chemistry to produce new amphiphilic polymer (co)networks. *Soft Matter 5*(24), 4878-4892.

(34) Campos, L. M.; Meinel, I.; Guino, R. G.; Schierhorn, M.; Gupta, N.; Stucky, G. D.; Hawker, C. J. (2008) Highly Versatile and Robust Materials for Soft Imprint Lithography Based on Thiol-ene Click Chemistry. *Advanced Materials 20*, 3728-3733.

(35) Hagberg, E. C.; Malkoch, M.; Ling, Y. B.; Hawker, C. J.; Carter, K. R. (2007) Effects of modulus and surface chemistry of thiol-ene photopolymers in nanoimprinting. *Nano Lett. 7*(2), 233-237.

(36) Roper, T. M.; Kwee, T.; Lee, T. Y.; Guymon, C. A.; Hoyle, C. E. (2004) Photopolymerization of pigmented thiol-ene systems. *Polymer 45*(9), 2921-2929.

(37) Guenthner, A. J.; Hess, D. M.; Cash, J. J. (2008) Morphology development in photopolymerization-induced phase separated mixtures of UV-curable thiol-ene adhesive and low molecular weight solvents. *Polymer 49*(25), 5533-5540.

(38) Lu, H.; Carioscia, J. A.; Stansbury, J. W.; Bowman, C. N. (2005) Investigations of step-growth thiol-ene polymerizations for novel dental restoratives. *Dent. Mater. 21*(12), 1129-1136.

(39) Hu, Z. K.; Finlay, J. A.; Chen, L.; Betts, D. E.; Hillmyer, M. A.; Callow, M. E.; Callow, J. A.; DeSimone, J. M. (2009) Photochemically Cross-Linked Perfluoropolyether-Based Elastomers: Synthesis, Physical Characterization, and Biofouling Evaluation. *Macromolecules 42*(18), 6999-7007.

(40) Anseth, K. S.; Metters, A. T.; Bryant, S. J.; Martens, P. J.; Elisseeff, J. H.; Bowman, C. N. (2002) In situ forming degradable networks and their application in tissue engineering and drug delivery. *J. Control. Release 78*(1-3), 199-209.

(41) Lundberg, P.; Bruin, A.; Klijnstra, J. W.; Nyström, A. M.; Johansson, M.; Malkoch, M.; Hult, A. (2009) Poly(ethylene glycol) based thiol-ene coatings for marine antifouling - curing chemistry, aqueous stability and bioassay evaluation. *Submitted for publication in ACS Applied materials and interfaces*

(42) Fu, Q.; Cheng, L.; Zhang, Y.; Shi, W. (2008) Preparation and reversible photo-crosslinking/photo-cleavage behavior of 4-methylcoumarin functionalized hyperbranched polyester. *Polymer 49*, 4981-4988.

(43) Fu, Q.; Liu, J.; Shi, W. (2008) Preparation and photopolymerization behavior of multifunctional thiol-ene systems based on hyperbranched aliphatic polyesters. *Progress in Organic Coatings 63*, 100-109.

(44) Fogelström, L.; Antoni, P.; Malmström, E.; Hult, A. (2006) UV-curable hyperbranched nanocomposite coatings. *Progress in Organic Coatings 55*, 284-290.

(45) Ikladious, N. E.; Mansour, S. H.; Rozik, N. N.; Dirnberger, K.; Eisenbach, C. D. (2008) New aliphatic hyperbranched polyester polyols based on 1,3,5-tris(2-hydroxyethyl) cyanuric acid as a core. *Journal of Polymer Science Part A-Polymer Chemistry 46*(16), 5568-5579.

(46) Ihre, H.; De Jesus, O. L. P.; Frechet, J. M. J. (2001) Fast and convenient divergent synthesis of aliphatic ester dendrimers by anhydride coupling. *Journal of the American Chemical Society 123*(25), 5908-5917.

(47) Giles, M. D.; Liu, S. M.; Emanuel, R. L.; Gibb, B. C.; Grayson, S. M. (2008) Dendronized Supramolecular Nanocapsules: pH Independent, Water-Soluble, Deep-Cavity Cavitands Assemble via the Hydrophobic Effect. *Journal of the American Chemical Society 130*(44), 14430-+.

(48) Grayson, S. M.; Frechet, J. M. J. (2001) Divergent synthesis of dendronized poly(p-hydroxystyrene). *Macromolecules 34*(19), 6542-6544.

(49) Lee, C. C.; Grayson, S. M.; Frechet, J. M. J. (2004) Synthesis of narrow-polydispersity degradable dendronized aliphatic polyesters. *Journal of Polymer Science Part A-Polymer Chemistry 42*(14), 3563-3578.

(50) Nystrom, A. M.; Furo, I.; Malmstrom, E.; Hult, A. (2005) Bulk properties of dendronized polymers with tailored end-groups emanating from the same backbone. *Journal of Polymer Science Part A-Polymer Chemistry 43*(19), 4496-4504.

(51) Chen, S.; Zhang, X.-Z.; Cheng, S.-X.; Zhuo, R.-X.; Gu, Z.-W. (2008) Functionalized Amphiphilic Hyperbranched Polymers for Targeted Drug Delivery. *Biomacromolecules 9*(10), 2578-2585.

(52) Prabaharan, M.; Grailer, J. J.; Pilla, S.; Steeber, D. A.; Gong, S. Q. (2009) Folate-conjugated amphiphilic hyperbranched block copolymers based on Boltorn (R) H40, poly(L-lactide) and poly(ethylene glycol) for tumor-targeted drug delivery. *Biomaterials 30*(16), 3009-3019.

(53) Christina, K.; Zili, S.; Theodossis, T.; Leto-Aikaterini, T.; Dimitris, T.; Constantinos, M. P. (2008) A Novel Micellar PEGylated Hyperbranched Polyester as a Prospective Drug Delivery System for Paclitaxel. *Macromolecular Bioscience 8*(9), 871-881.

(54) Kontoyianni, C.; Sideratou, Z.; Theodossiou, T.; Tziveleka, L. A.; Tsiourvas, D.; Paleos, C. M. (2008) A novel micellar PEGylated hyperbranched polyester as a prospective drug delivery system for paclitaxel. *Macromolecular Bioscience 8*(9), 871-881.

(55) Prabaharan, M.; Grailer, J. J.; Pilla, S.; Steeber, D. A.; Gong, S. (2009) Amphiphilic multi-arm-block copolymer conjugated with doxorubicin via pH-sensitive hydrazone bond for tumor-targeted drug delivery. *Biomaterials 30*(29), 5757-5766.

(56) Nilsson, C.; Malmstrom, E.; Johansson, M.; Trey, S. M. (2009) Dendrimers in Thiol-ene Crosslinked Networks and the Effect of Subsequent Generations on Thermoset Properties. *Journal of Polymer Science Part A-Polymer Chemistry 47*(2), 589-601.

(57) Nilsson, C.; Simpson, N.; Malkoch, M.; Johansson, M.; Malmstrom, E. (2008) Synthesis and thiol-ene photopolymerization of allyl-ether functionalized dendrimers. *Journal of Polymer Science Part A-Polymer Chemistry 46*(4), 1339-1348.

(58) Schmidt, L. E.; Schmah, D.; Leterrier, Y.; Manson, J. A. E. (2007) Time-intensity transformation and internal stress in UV-curable hyperbranched acrylates. *Rheol. Acta 46*(5), 693-701.

(59) Sangermano, M.; Bongiovanni, R.; Malucelli, G.; Priola, A.; Harden, A.; Rehnberg, N. (2002) Synthesis of new fluorinated allyl ethers for the surface modification of thiol-ene ultraviolet-curable formulations. *Journal of Polymer Science Part A-Polymer Chemistry 40*(15), 2583-2590.

(60) Gudipati, C. S.; Greenlief, C. M.; Johnson, J. A.; Prayongpan, P.; Wooley, K. L. (2004) Hyperbranched fluoropolymer and linear poly(ethylene glycol) based Amphiphilic crosslinked networks as efficient antifouling coatings: An insight into the surface compositions, topographies, and morphologies. *Journal of Polymer Science Part A-Polymer Chemistry 42*(24), 6193-6208.

(61) Xu, J.; Bartels, J. W.; Bohnsack, D. A.; Tseng, T.-C.; Mackay, M. E.; Wooley, K. L. (2008) Hierarchical Inorganic-Organic Nanocomposites Possessing Amphiphilic and Morphological Complexities: Influence of Nanofiller Dispersion on Mechanical Performance. *Advanced Functional Materials 18*(18), 2733-2744.

(62) Xu, J. Q.; Bohnsack, D. A.; Mackay, M. E.; Wooley, K. L. (2007) Unusual mechanical performance of amphiphilic crosslinked polymer networks. *Journal of the American Chemical Society 129*(3), 506-507.

(63) Brown, G. O.; Bergquist, C.; Ferm, P.; Wooley, K. L. (2005) Unusual, Promoted Release of Guests from Amphiphilic Crosslinked Polymer Networks. *J. Am. Chem. Soc. 127*, 11238-11239.

(64) Neumann, A. W.; Good, R. J. (1979) *Journal of Surface and Colloid Science 11*, 31-91.

(65) Haynes, R. K.; Katsifis, A.; Vonwiller, S. C. (1984) Preparation of Tert-Butyl 2-(Phenylthiomethyl)Propenoate, Tert-Butyl 3-(Phenylthio)-2-(Phenylthiomethyl)Propenoate and Related-Compounds. *Australian Journal of Chemistry 37*(7), 1571-1578.

(66) Moore, J. S.; Stupp, S. I. (1990) Room-Temperature Polyesterification. *Macromolecules 23*(1), 65-70.

(67) Callow, M. E.; Callow, J. A.; Pickett-Heaps, J. D.; Wetherbee, R. (1997) Primary adhesion of Enteromorpha (Chlorophyta, Ulvales) propagules: Quantitative settlement studies and video microscopy. *J. Phycol. 33*, 938-947.

(68) Callow, M. E.; Jennings, A. R.; Brennan, A. B.; Seegert, C. E.; Gibson, A.; Wilson, L.; Feinberg, A.; Baney, R.; Callow, J. A. (2002) Microtopographic cues

for settlement of zoospores of the green fouling alga Enteromorpha. *Biofouling 18*, 237-245.

(69) Starr, R. C.; Zeikus, J. A. (1987) UTEX - the culture collection at the University of Texas at Austin. *J. Phycol. 23*, 1-47.

(70) Finlay, J. A.; Fletcher, B. R.; Callow, M. E.; Callow, J. A. (2008) Effect of background colour on growth and adhesion strength of *Ulva* sporelings. *Biofouling 24*, 219-225.

(71) Finlay, J. A.; Callow, M. E.; Schultz, M. P.; Swain, G. W.; Callow, J. A. (2002) Adhesion strength of settled spores of the green alga Enteromorpha. *Biofouling 18*, 251 - 256.

(72) Schilp, S.; Rosenhahn, A.; Pettitt, M. E.; Bowen, J.; Callow, M. E.; Callow, J. A.; Grunze, M. (2009) The influence of chain length and termination of (ethylene glycol)-containing self-assembled monolayers on settlement and adhesion of algal cells. *Langmuir 25*, 10077-100082.

(73) Park, D.; Weinman, C. J.; Finlay, J. A.; Fletcher, B. R.; Paik, M. Y.; Sundaram, H. S.; Dimitriou, M.; Sohn, K. E.; Callow, M. E.; Callow, J. A.; Handlin, D. L.; Willis, C. L.; Fischer, D. A.; Kramer, E. J.; Ober, C. K. Amphiphilic Surface Active Triblock Copolymers with Mixed Hydrophobic and Hydrophilic Side Chains for Tuned Marine Fouling-Release Properties

*submitted*.

(74) Martinelli, E.; Agostini, S.; Galli, G.; Chiellini, E.; Glisenti, A.; Pettitt, M. E.; Callow, M. E.; Callow, J. A.; Graf, K.; Bartels, F. W. (2008) Nanostructured films of amphiphilic fluorinated block copolymers for fouling release application. *Langmuir 24*, 13138-13147.

(75) Humphrey, A. J.; Finlay, J. A.; Pettitt, M. E.; Stanley, M. S.; Callow, J. A. (2005) Effect of Ellman's reagent and dithiothreitol on the curing of the spore adhesive glycoprotein of the green alga Ulva. *J. Adhes. 81*(7-8), 791-793.

# Chapter 3

## Evaluation of Isoprene Chain Extension from PEO Macromolecular Chain Transfer Agents for the Preparation of Dual, Invertible Block Copolymer Nanoassemblies and Anti-fouling Coatings

[Portions of this work have been submitted for publications as Jeremy W. Bartels, Solène I. Cauët, Peter L. Billings, Lily Yun Lin, Jiahua Zhu, Darrin J. Pochan, Karen L. Wooley *Macromolecules*, **2010**]

**Abstract.**

Two RAFT-capable PEO macro-CTAs, 2 and 5 kDa, were prepared and used for the polymerization of isoprene which yielded well-defined block copolymers of varied lengths and compositions. GPC analysis of the PEO macro-CTAs and block copolymers showed remaining unreacted PEO macro-CTA. Mathematical deconvolution of the GPC chromatograms allowed for the estimation of the blocking efficiency, about 50% for the 5 kDa PEO macro-CTA and 64% for the 2 kDa CTA. Self assembly of the block copolymers in both water and decane was investigated and the resulting regular and inverse assemblies, respectively, were analyzed with DLS, AFM, and TEM to ascertain their dimensions and properties. Assembly of PEO-*b*-PIp block copolymers in aqueous

solution resulted in well-defined micelles of varying sizes while the assembly in hydrophobic, organic solvent resulted in the formation of different morphologies including large aggregates and well-defined cylindrical and spherical structures. Additional investigation into the bulk assembly and thiol-ene crosslinking of PEO-*b*-PIp films was performed. The coatings were evaluated for anti-biofouling activity against fluorescently-tagged biomolecules.

## Introduction

Interesting chemical, physical and morphological complexity can be inherited from the self assembly of amphiphilic block copolymers.(1-7) The generation of micelles in a solvent selective for a portion of the overall block copolymer structure,(8-10) and transformation into their stable, crosslinked variants,(11-13) have been achieved using a wide variety of well-defined multiblock copolymers. Block copolymers within discrete self-assembled particles adopt a range of morphologies and dimensions, giving these micelle-based nanoobjects promise as devices to be applied to the emerging fields of nanomedicine(14-16) and nanomaterials.(17-20)

The properties of polymer assemblies are dependent on the nature of the block copolymer components and their molecular-level organization within the nanoscale framework.(4, 5, 21) Among the many types of amphiphilic block copolymers that have been investigated,(7, 20, 22) those containing poly(ethylene oxide) (PEO) as a hydrophilic chain segment, such as PEO-*b*-PCL(16, 23, 24) and PEO-*b*-PS,(25, 26) incorporate a non-ionic, anti-fouling shell layer, which has been shown to be important for biological applications.(27) For instance, PEO-*b*-PCL filomicelle assemblies were capable of *in vivo* blood circulation for several days.(28) In addition to these interesting cylindrical filomicelles, many other morphologies can be accessed from PEO-containing block copolymers.(3, 29-32) However, because the PEO segment lacks reactive side chain groups, multi-functionality is often incorporated *via* the other polymer block segment(s).

The utility of polymer nanostructures, ultimately, relies on access to polymer building blocks that possess well-defined structures and that include functionality. The advent of controlled radical polymerization (CRP)(33-36) has allowed for significantly greater access to functional block copolymer materials(37, 38) by a broader scientific population, providing for investigations into increased numbers and types of block copolymer assemblies in the bulk- and solution-states. PEO-*b*-poly(diene) polymers are particularly attractive, because they combine the interesting properties of PEO with reactive, hydrophobic chain segments, which then gives an overall amphiphilic and functional block copolymer structure. Although poly(ethylene oxide)-*block*-polybutadiene(6, 39-42) or poly(ethylene oxide)-*block*-polyisoprene, PEO-*b*-PIp,(9, 43-45) have long been used for materials applications,(46) their preparation by anionic polymerization methods(47) has hampered their wide-scale availability.

The polymerization of isoprene under controlled radical polymerization conditions has been developed recently, and is emerging as a general method for the preparation of PIp-containing block copolymers (including PEO-*b*-PIp), which is allowing access to functional nanomaterials. Controlled radical polymerization of isoprene was initially reported using nitroxide mediated polymerization (NMP).(9, 44, 48, 49) Diblock copolymers of PEO-*b*-PIp have been successfully prepared by Grubbs *via* NMP methods using a PEO macro-initiator.(9, 44) The solution-state properties of nanoassemblies derived from di- and triblock copolymers that include PEO and PIp segments have been investigated, including the formation of micelles and stable vesicles with small molecule additives,(8, 21, 50) or the formation of unusual assemblies with unique properties when thermoresponsive intermediate blocks were incorporated.(9) Additionally, studies have been performed on PEO-*b*-PIp at various aqueous concentrations, expanding knowledge

of the physical properties of the block copolymers as they changed from micelle to gel-like phases.(51)

We were interested in investigating the solution-state assemblies of PEO-*b*-PIp in either water or organic solvents, to afford invertible, functional nanoscale objects, which could carry the reactive PIp units either in the core or the shell. To gain access to these block copolymers, reversible addition-fragmentation chain transfer (RAFT) polymerization was employed, as we have experience with this system.(52-55) Moreover, we were interested in studying in detail the efficiency of RAFT polymerization of isoprene from macromolecular chain transfer agents (macro-CTAs). PEO macro-CTAs were, therefore, generated from simple amidation chemistry of an amino-terminated PEO and an acid-functionalized RAFT agent known to polymerize isoprene readily, and used to afford block copolymers of PEO and PIp that possess interesting physical and solution-state properties.

Previous studies using both dithioester-(56-61) and trithiocarbonate-based (26, 29, 62, 63) PEO macro-CTAs have been reported for the synthesis of well-defined block copolymers with second blocks varying from hydrophilic(57, 58, 60, 61, 63) to hydrophobic.(29, 56, 59, 62, 64) Problems related to low chain extension efficiency can remain when chain-extending from a hydrophilic polymeric CTA with a hydrophobic monomer, potentially due to the incompatibility between the polymer and the added monomer.(57) The remaining PEO macro-CTA can be removed, typically, using precipitation and/or dialysis techniques, however, this depends upon the chemical nature of the block copolymers obtained and cannot always be achieved. Knowing the exact composition of the final block copolymer and the amount of unreacted macroCTA contaminant is important when preparing nanoassemblies.(1) Incomplete chain extension

is readily visible as a low molecular weight component through the use of gel permeation chromatography (GPC), so that mathematical treatment of the chromatograms provides a tool to fully characterize blocking efficiency and final product composition.

Herein, is reported the use of two RAFT-capable, trithiocarbonate-based, PEO macro-CTAs ($M_n$ = 2 and 5 kDa), for the polymerization of isoprene to yield well defined block copolymers of varied lengths and compositions. Analysis of the GPC chromatograms, including mathematical deconvolution, allowed for estimation of chain extension efficiencies from the PEO macro-CTAs and final product composition. The resultant polymers were investigated for their abilities to assemble in both water and decane, and the resulting regular and inverse micellar nanostructures were analyzed with dynamic light scattering (DLS), atomic force microscopy (AFM), and transmission electron microscopy (TEM).

## Experimental

**Instrumentation.** Infrared spectra were obtained on a Perkin–Elmer Spectrum BX FTIR system as neat films on NaCl plates. $^{1}$H NMR (300 and 500 MHz) and $^{13}$C NMR (75 and 125 MHz) spectra were recorded on either a Varian Mercury 300 MHz or Inova 500 MHz spectrometer using the solvent as internal reference. Glass transition ($T_g$), melting ($T_m$), and crystallization ($T_c$) temperatures were measured by differential scanning calorimetry on a Mettler Toledo DSC822$^e$ (Mettler Toledo Inc., Columbus, OH), with a heating rate of 10 ºC/min. Measurements were analyzed using Mettler Toledo Star SW 7.01 software. The $T_g$ was taken as the midpoint of the inflection tangent, upon the third heating scan. Thermogravimetric analysis was performed under $N_2$ atmosphere using a Mettler Toledo model TGA/SDTA851$^e$, with a heating rate of 10

ºC/min. Measurements were analyzed using Mettler Toledo Star SW 7.01 software. Gel permeation chromatography was conducted on a system equipped with a Waters Chromatography, Inc. (Milford, MA) model 1515 isocratic pump, a model 2414 differential refractometer, and a Precision Detectors, Inc. (Bellingham, MA) model PD-2026 dual-angle (15 ° and 90 °) light scattering detector and a three-column set of Polymer Laboratories, Inc. (Amherst, MA) Styragel columns ($PL_{gel}$ 5$\mu$m Mixed C, 500 Å, and $10^4$ Å, 300 x 7.5 mm columns). The system was equilibrated at 35 °C in tetrahydrofuran (THF), which served as the polymer solvent and eluent (flow rate set to 1.00 mL/min). Polymer solutions were prepared at a known concentration (*ca*. 3 mg/mL) and an injection volume of 200 $\mu$L was used. Data collection was performed with Precision Detectors, Inc. Precision Acquire software. Data analysis was performed with Precision Detectors, Inc. Discovery 32 software. The differential refractometer was calibrated with standard polystyrene material (SRM 706 NIST), of known refractive index increment dn/dc (0.184 mL/g). The dn/dc values of the analyzed polymers were determined using refractive index detector data. Tapping-mode AFM measurements were conducted in air with a Nanoscope III BioScope system (Digital Instruments, Santa Barbara, CA) operated under ambient conditions with standard silicon tips [type, OTEPSA-70; length (L), 160 lm; normal spring constant, 50 N/m; resonant frequency, 246–282 kHz]. Hydrodynamic diameters ($D_h$) and distributions for the micelles in aqueous or decane solutions were determined by DLS. The DLS instrumentation consisted of a Brookhaven Instruments Limited (Worcestershire, U.K.) system, including a model BI-200SM goniometer, a model BI-9000AT digital correlator, a model EMI-9865 photomultiplier, and a model 95-2 Ar ion laser (Lexel, Corp.; Farmindale, NY) operated at 514.5 nm. Measurements were made at 25 ± 1 °C. Prior to analysis,

solutions were filtered through a 0.45 μm Nylon filter (aqueous samples) or not filtered at all (decane). Samples were then centrifuged in a model 5414 microfuge (Brinkman Instruments, Inc.; Westbury, NY) for 4 min to remove dust particles. Scattered light was collected at a fixed angle of 90°. The digital correlator was operated with 522 ratio spaced channels and initial delay of 0.5 μs, a final delay of 800 ms, and a duration of 10 min. A photomulitplier aperture of 400 μm was used, and the incident laser intensity was adjusted to obtain a photon counting of 300 kcps. Only measurements in which the measured and calculated baselines of the intensity autocorrelation function agreed to within 0.1% were used to calculate particle size. Particle size distributions were performed with the ISDA software package (Brookhaven Instruments Company), which employed single-exponential fitting, cumulants analysis, and non-negatively constrained least-squares particle size distribution analysis routines.

Fluorescently-tagged biomolecule (Alexa-Fluor488-tagged Bovine Serum Albumin (BSA), Lipopolysaccharides from *E. coli* (LPSE) and *S. minnesota* (LPSS), and Lectin from *C. Fragile* (CFL)) adsorption testing of the PEO-*b*-PIp coatings (1.5 eq SH/alkene crosslinked) were tested in the following manner: Approximately 100 μL of biomolecule solution was transferred onto a coated glass slide and allowed to sit for 10 min, followed by extensive rinsing in pH 7.4 (5.0 mM) PBS buffer for 30 s. The coatings were then allowed to dry before being imaged by fluorescence microscopy. The images were analyzed using Image J software and the histograms were transformed into percent fluorescence values. Because there was approximately 1 tag/biomolecule, quantitative correlation between fluorescence and the number of biomolecules adsorbed onto surfaces could be quantified and compared.

**Materials** Isoprene (Ip) (99 %) was obtained from Sigma-Aldrich, Inc. (St. Louis, MO) and was purified by passage over a column of neutral alumina prior to use. Amine-terminated poly(ethylene oxide), 5 kDa and 2 kDa, (Intezyne Labs) were used as received. 1-[Dimethylamino)propyl]-3-ethylcarbodiimide methiodide (EDCI) (Aldrich), and hydroxybenzotriazole monohydrate (HOBt) (Novabiochem) were used as received. 1,4-Dioxane (99%), *N*,*N*-dimethylformamide (DMF, 99.8% anhydrous), tetrahydrofuran (THF, 99.9%), dichloromethane (≥99%), diethyl ether, (≥99 %, anhydrous), methanol (≥99.9%), 1-hydroxycyclohexylphenyl ketone (99%) and di-*tert*-butyl peroxide (98%), were used as received from Sigma Aldrich. Chloroform-*d* (Cambridge Isotope Labs) was used as received. 1,10 decanedithiol (98%) was obtained from TCI and used as received. Argon ultra-high purity grade gas (99.999%) was used as received from Praxair (St. Louis, MO). The RAFT agent, *S*-1-dodecyl-*S*'-(α, α'-dimethyl- α"-acetic acid)trithiocarbonate, **1**, was prepared as previously reported.(65) Due to the high volatility of isoprene and the high temperatures employed in the polymerization thereof, only thick-walled glass flasks, free of visible defects, were used for these experiments, each conducted with at least 50 % of the volume of the flask remaining free.(53, 54) As further precaution, all polymerizations were performed in a fume hood with additional shielding. Percent conversions of the isoprene polymerizations were determined using the method of Grubbs and co-workers,(44) where the molecular weight of the isolated polymer was determined with high field $^{1}$H NMR spectroscopy (500 MHz) and then set equal to the theoretical molecular weight. While this method does introduce some error (assuming $M_n^{Theory} = M_n^{Actual}$), it is not excessive when compared with the error associated with attempting to determine conversion of isoprene directly.(53)

**Synthesis of 5 kDa PEO macro chain-transfer agent, 2.** To a 250 mL round bottom flask equipped with a Teflon-coated stir-bar, was added chain transfer agent **1** (0.5476 g, 1.579 mmol, 1.5 eq), EDCI (0.4447 g, 1.497 mmol, 1.5 eq), and HOBt (0.2037 g, 1.507 mmol, 1.5 eq). After addition of DMF (50 mL), the flask was sealed with a rubber septum and its contents were allowed to stir for 1 h at ambient temperature. In a separate 250 mL round bottom flask, mono-amino-terminated 5 kDa PEO (5.0023 g, 1.000 mmol, 1.0 eq, $M_n^{GPC}$ = 7,700 Da (polystyrene equivalent)) was dissolved in dichloromethane (30 mL), to which DMF (50 mL) was added. After the contents of the initial round bottom flask had stirred for 1 h, the 5 kDa PEO solution was added and the reaction mixture was allowed to stir for 4 h at ambient temperature. The product was purified *via* silica gel-based flash chromatography (eluting with $CH_2Cl_2$, gradient to 10% MeOH:$CH_2Cl_2$). The product was dried *in vacuo* overnight, yielding 1.5496 g as a light yellow powder (30% yield). $M_n^{NMR}$ = 7,800 Da, $M_w^{GPC}$ = 7,900 Da, $M_n^{GPC}$ = 7,600 Da (polystyrene equivalent), $M_w/M_n$ = 1.04. $T_m$ = 61.0 °C, $T_c$ = 31.5 °C. $T_{decomp}$ = 395.3 °C. IR ($cm^{-1}$): 3000-2760, 1672, 1467, 1360, 1343, 1280, 1242, 1148, 1112, 1061, 963, 842, 529. $^1$H NMR (500 MHz, chloroform-*d*, ppm): δ 3.7 – 3.5 (br, -C*H*$_2$-C*H*$_2$-O-), 3.5 (s, -O-C*H*$_3$), 3.4 (br, m, -SC(S)S-C*H*$_2$-$(CH_2)_{10}$-$CH_3$), 1.9 (s, O-C(O)-C(C*H*$_3$)$_2$-S-), 1.3-1.2 (br, -SC(S)S-$CH_2$-(C*H*$_2$)$_{10}$-$CH_3$), 0.9 (br t, -SC(S)S-$CH_2$-$(CH_2)_{10}$-C*H*$_3$). $^{13}$C NMR (75 MHz, chloroform-*d*, ppm): δ 173.1, 70.8, 65.3, 58.3, 56.2, 37.1, 32.1, 29.8, 25.6, 22.9, 14.4.

**Synthesis of 2 kDa PEO macro chain-transfer agent, 3.** The 2 kDa PEO macro chain-transfer agent, **3**, was prepared following the same procedure as for 5 kDa PEO macro chain-transfer agent, **2**, using chain transfer agent **1** (1.3699 g, 3.757 mmol, 1.5

eq), EDCI (1.1166 g, 3.759 mmol, 1.5 eq), HOBt (0.5075 g, 3.756 mmol, 1.5 eq), mono-amino-terminated 2 kDa PEO (5.0019 g, 2.500 mmol, 1.0 eq, $M_n^{GPC}$ = 2,500 Da (polystyrene equivalent)), DMF (100 mL) and dichloromethane (30 mL). The reaction yielded 2.7791 g of **3** as a yellowish-white powder (47% yield). $^1$H NMR spectroscopy confirmed complete functionalization. $M_n^{NMR}$ = 2,400 Da, $M_w^{GPC}$ = 3,270 Da, $M_n^{GPC}$ = 3,200 Da (polystyrene equivalent), $M_w/M_n$ = 1.03. $T_m$ = 50.4 °C, $T_c$ = 9.9 °C. $T_{decomp}$: = 377.5 °C. IR (cm$^{-1}$): 2990-2770, 1671, 1467, 1360, 1344, 1280, 1242, 1148, 1114, 1061, 946, 843, 530. $^1$H NMR (500 MHz, chloroform-*d*, ppm): δ 3.6 – 3.3 (br, -C*H*$_2$-C*H*$_2$-O-), 3.4 (s, -O-C*H*$_3$), 3.2 (br, m, -SC(S)S-C*H*$_2$-(CH$_2$)$_{10}$-CH$_3$), 1.6 (s, O-C(O)-C(C*H*$_3$)$_2$-S-), 1.3-1.2 (br, -SC(S)S-CH$_2$-(C*H*$_2$)$_{10}$-CH$_3$), 0.8 (br t, -SC(S)S-CH$_2$-(CH$_2$)$_{10}$-C*H*$_3$). $^{13}$C NMR (75 MHz, chloroform-*d*, ppm): δ 172.6, 70.8, 59.3, 57.3, 40.1, 37.2, 32.1, 29.9, 26.1, 22.9, 14.4.

**General procedure for synthesis of PEO$_{112}$-*b*-PIp$_{187}$ (4).** To a 50 mL bomb-type Schlenk flask equipped with a Teflon coated magnetic stir bar was added Ip (2.5396 g, 37.28 mmol, 373.0 eq), macro chain transfer agent **2**, (0.5002 g, 0.100 mmol, 1.0 eq), and di-*tert*-butylperoxide (0.0070 g, 4.780 x 10$^{-5}$ mol, 0.4 eq), along with 1,4-dioxane (15 mL). The mixture was degassed *via* 3 freeze-pump-thaw cycles. Upon the final thaw the Schlenk flask was backfilled with Ar and placed in a temperature-regulated mineral oil bath set at 125 °C and left to react for 24 h. After cooling the residual solvent and monomer were removed *in vacuo*. Leftover contents of the flask were dissolved in a minimal amount of dichloromethane and precipitated 3 times into 500 mL methanol producing a transparent yellow oil. The excess solvent was decanted off and the product was dried *in vacuo*, yielding 1.035 g (87% yield based on 27% conversion) of sticky yellow powder. $M_n^{NMR}$ = 18,000 Da, $M_w^{GPC}$ = 23,200 Da, $M_n^{GPC}$ = 18,000 Da

(polystyrene equivalent), $M_w/M_n$ = 1.28. $(T_g)_{PIp}$ = -60.0 °C, $(T_m)_{PEO}$ = 56.0 °C, $(T_c)_{PEO}$ = 31.4 °C. $T_{decomp}$: = 401.8 °C. IR ($cm^{-1}$): 3020-2760, 1726, 1665, 1644, 1466, 1449, 1343, 1280, 1242, 1148, 1114, 1061, 964, 842, 530. $^1$H NMR (500 MHz, chloroform-*d*, ppm): δ 5.8-5.7 (br, 1,2 C*H*=$CH_2$), 5.2-5.1 (br, 1,4 -$CH_2$-C($CH_3$)-C*H*-$CH_2$-), 5.0-4.8 (br, 1,2 CH=C$H_2$), 4.8-4.6 (br, 4,3 C($CH_3$)-C$H_2$), 3.7 – 3.5 (br, -C$H_2$-C$H_2$-O-), 3.4 (s, -O-C$H_3$), 3.2 (br, m, -SC(S)S-C$H_2$-($CH_2$)$_{10}$-$CH_3$), 2.2-1.8 (br, C$H_2$ isoprene backbone), 1.7-1.5 (br, isoprene backbone C$H_3$), 1.6 (s, O-C(O)-C(C$H_3$)$_2$-S-), 1.4-1.2 (br, -SC(S)S-$CH_2$-(C$H_2$)$_{10}$-$CH_3$), 0.9 (br t, -SC(S)S-$CH_2$-($CH_2$)$_{10}$-C$H_3$). $^{13}$C NMR (75 MHz, chloroform-*d*, ppm): δ 147.8, 135.1, 125.2, 124.5, 111.5, 72.2, 70.8, 69.3, 63.7, 62.2, 59.3, 52.2, 44.8, 40.0, 38.7, 32.2, 31.0, 28.5, 26.9, 23.7, 19.0, 16.3, 14.4.

**General procedure for synthesis of $PEO_{112}$-*b*-$PIp_{47}$ (5).** $PEO_{112}$-*b*-$PIp_{47}$, **5**, was prepared following the same procedure as for polymer **4** using the following amounts Ip (1.1927 g, 17.50 mmol, 186.5 eq), macro transfer agent **2** (0.5016 g, 9.381 x $10^{-5}$ mol, 1.0 eq), and di-*tert*-butylperoxide (0.0041 g, 2.803 x $10^{-5}$ mol, .29 eq), along with 1,4-dioxane (*ca.* 5 mL). Purification was attempted repeatedly using precipitation in a variety of hydrophobic and hydrophilic solvents with no success, however a mixture of 400 mL deionized water and 350 mL methanol worked well, yielding a yellow oil. Solvent was removed *via* rotary evaporation and the remaining polymer was dried *in vacuo*. The final product consisted of 0.4500 g of sticky pale yellow powder (56% yield based on 25% conversion). $M_n^{NMR}$ = 8,500 Da, $M_w^{GPC}$ = 11,500 Da, $M_n^{GPC}$ = 8,600 Da (polystyrene equivalent), $M_w/M_n$ = 1.34. $(T_g)_{PIp}$ = -61.0 °C, $(T_m)_{PEO}$ = 55.3 °C, $(T_c)_{PEO}$ = 23.0 °C. $T_{decomp}$: = 399.2 °C. IR ($cm^{-1}$): 2990-2770, 1649, 1466, 1360, 1343, 1280, 1148, 1114, 1061, 946, 842, 668, 530. $^1$H NMR (500 MHz, dichloromethane-$d_2$, ppm): δ 5.9-5.8 (br,

1,2 C*H*=$CH_2$), 5.3-5.1 (br, 1,4 -$CH_2$-C($CH_3$)-C*H*-$CH_2$-), 5.1-4.9 (br, 1,2 CH=C*H*$_2$), 4.9-4.7 (br, 4,3 C($CH_3$)-C*H*$_2$), 3.9 – 3.7 (br, -C*H*$_2$-C*H*$_2$-O-), 3.5 (s, -O-C*H*$_3$), 3.2 (br, m, -SC(S)S-C*H*$_2$-($CH_2$)$_{10}$-$CH_3$), 2.3-2.0 (br, C*H*$_2$ isoprene backbone), 1.8-1.6 (br, isoprene backbone C*H*$_3$), 1.6 (s, O-C(O)-C(C*H*$_3$)$_2$-S-), 1.4-1.2 (br, -SC(S)S-$CH_2$-(C*H*$_2$)$_{10}$-$CH_3$), 1.0 (br t, -SC(S)S-$CH_2$-($CH_2$)$_{10}$-C*H*$_3$). $^{13}$C NMR (75 MHz, dichloromethane-*d*$_2$, ppm): δ 148.0, 135.1, 111.6, 70.8, 59.3, 52.1, 44.9, 40.0, 38.8, 37.2, 32.3, 31.1, 29.9, 28.6, 27.0, 26.0, 23.7, 22.9, 22.3, 16.3, 14.4.

**General procedure for synthesis of PEO$_{44}$-*b*-PIp$_{60}$ (6).** PEO$_{44}$-*b*-PIp$_{60}$, **6**, was prepared following the same procedure as for polymer **4** using the following amounts Ip (0.5089 g, 7.471 mmol, 150 eq), macro transfer agent **3** (0.1158 g, 4.936 x $10^{-5}$ mol, 1.0 eq), and di-*tert*-butylperoxide (0.0027 g, 1.846 x $10^{-5}$ mol, 0.30 eq), along with 1,4-dioxane (*ca.* 5 mL). The crude product was dissolved in THF and precipitated into ice cold diethyl ether, which yielded a cloudy precipitate. The final product consisted of 0.1990 g of sticky yellow powder (97% yield based on 18% conversion). $M_n^{NMR}$ = 6,400 Da, $M_w^{GPC}$ = 8,300 Da, $M_n^{GPC}$ = 6,500 Da (polystyrene equivalent), $M_w/M_n$ = 1.29. $(T_g)_{PIp}$ = -62.7 °C, $(T_m)_{PEO}$ = 47.3 °C, $(T_c)_{PEO}$ = 12.7 °C. $T_{decomp}$: = 397.0 °C. IR (cm$^{-1}$): 3040-2720, 1732, 1660, 1644, 1520, 1466, 1360, 1344, 1280, 1242, 1147, 1114, 1061, 964, 843, 734, 646, 532. $^1$H NMR (500 MHz, chloroform-*d*, ppm): δ 5.8-5.7 (br, 1,2 C*H*=$CH_2$), 5.2-5.0 (br, 1,4 -$CH_2$-C($CH_3$)-C*H*-$CH_2$-), 5.0-4.8 (br, 1,2 CH=C*H*$_2$), 4.8-4.6 (br, 4,3 C($CH_3$)-C*H*$_2$), 3.7 – 3.5 (br, -C*H*$_2$-C*H*$_2$-O-), 3.4 (s, -O-C*H*$_3$), 3.2 (br, m, -SC(S)S-C*H*$_2$-($CH_2$)$_{10}$-$CH_3$), 2.2-1.8 (br, C*H*$_2$ isoprene backbone), 1.7-1.5 (br, isoprene backbone C*H*$_3$), 1.6 (s, O-C(O)-C(C*H*$_3$)$_2$-S-), 1.4-1.2 (br, -SC(S)S-$CH_2$-(C*H*$_2$)$_{10}$-$CH_3$), 0.9 (br t, -SC(S)S-$CH_2$-($CH_2$)$_{10}$-C*H*$_3$). $^{13}$C NMR (75 MHz, chloroform-*d*, ppm): δ 148.0,

135.3, 125.3, 124.5, 111.6, 70.8, 59.3, 52.0, 51.0, 44.9, 42.3, 40.0, 38.8, 37.1, 34.5, 32.2, 30.6, 28.6, 27.0, 26.0, 23.7, 23.0, 16.3, 14.4.

**General procedure for synthesis of $PEO_{44}$-*b*-$PIp_{43}$ (7).** $PEO_{44}$-*b*-$PIp_{43}$, **7**, was prepared following the same procedure as for polymer **4** using the following amounts Ip (0.5224 g, 7.660 mmol, 77.0 eq), macro transfer agent **3** (0.2251 g, 9.595 x $10^{-5}$ mol, 1.0 eq), and di-*tert*-butylperoxide (0.0050 g, 3.419 x $10^{-5}$ mol, .30 eq), along with 1,4-dioxane (*ca.* 5 mL). The crude product was dissolved in THF and precipitated into ice cold diethyl ether which yielded a cloudy precipitate. The final product consisted of 0.3302 g of sticky yellow powder (88% yield based on 27% conversion). $M_n^{NMR}$ = 5,500 Da, $M_w^{GPC}$ = 6,900 Da, $M_n^{GPC}$ = 5,300 Da (polystyrene equivalent), $M_w/M_n$ = 1.30. $(T_g)_{PIp}$ = -64.5 °C, $(T_m)_{PEO}$ = 49.0 °C, $(T_c)_{PEO}$ = 42.5 °C. $T_{decomp}$: = 399.5 °C. IR ($cm^{-1}$): 2990-2770, 1733, 1644, 1523, 1466, 1360, 1344, 1280, 1242, 1147, 1112, 1061, 946, 842, 530. $^1$H NMR (500 MHz, chloroform-*d*, ppm): δ 5.8-5.7 (br, 1,2 C*H*=$CH_2$), 5.2-5.1 (br, 1,4 -$CH_2$-C($CH_3$)-C*H*-$CH_2$-), 5.0-4.8 (br, 1,2 CH=C$H_2$), 4.8-4.6 (br, 4,3 C($CH_3$)-C$H_2$), 3.7 – 3.5 (br, -C$H_2$-C$H_2$-O-), 3.4 (s, -O-C$H_3$), 3.2 (br, m, -SC(S)S-C$H_2$-$(CH_2)_{10}$-$CH_3$), 2.2-1.8 (br, C$H_2$ isoprene backbone), 1.7-1.5 (br, isoprene backbone C$H_3$), 1.6 (s, O-C(O)-C(C$H_3$)$_2$-S-), 1.4-1.2 (br, -SC(S)S-$CH_2$-(C$H_2$)$_{10}$-$CH_3$), 0.9 (br t, -SC(S)S-$CH_2$-$(CH_2)_{10}$-C$H_3$). $^{13}$C NMR (75 MHz, chloroform-*d*, ppm): δ 178.1, 148.0, 135.3, 129.1, 125.3, 124.5, 111.6, 72.2, 70.8, 67.0, 63.9, 59.3, 52.1, 50.9, 44.9, 42.3, 40.0, 38.8, 37.2, 32.2, 31.1, 29.9, 28.5, 27.0, 26.0, 23.7, 23.0, 18.3, 17.5, 16.3, 14.4.

**Preparation of polymer micelles (8)** In a 100-mL, round-bottom flask equipped with a magnetic stirring bar, diblock copolymer **4** (14.8 mg, 8.22 x $10^{-6}$ mol) was dissolved in DMF (15.0 mL), yielding a transparent pale yellow solution. Water (15 mL)

was added dropwise *via* a syringe pump, complete with vigorous stirring, over a period of 3 h, resulting in a clear solution. The mixture was transferred to dialysis tubing (MWCO 3,500 Da) and was dialyzed against DI water for 3 days to result in 37 mL of micelle solution. For TEM imaging, phosphotungstic acid was used as a negative stain and osmium tetroxide (OsO4) as a positive stain. Final concentration: 0.58 mg/mL. Hydrodynamic diameter (DLS): $(D_h)_i$ = 154 ± 49 nm, $(D_h)_v$ = 93 ± 37 nm, $(D_h)_n$ = 54 ± 38 nm. $D_{av}$(TEM) = 55 ± 18 nm. $H$ (AFM) = 8 ± 3 nm.

**Preparation of polymer micelles (9)** The same procedure as performed to produce micelle solution **8** was followed using diblock copolymer **5** (16.3 mg, 1.91 x $10^{-5}$ mol), affording micelle solution **9.** Final concentration: 1.95 mg/mL. Hydrodynamic diameter (DLS): $(D_h)_i$ = 114 ± 9 nm, $(D_h)_v$ = 26 ± 4 nm, $(D_h)_n$ = 18 ± 4 nm. $D_{av}$ (TEM) = 31 ± 4 nm. $H$ (AFM) = 4 ± 1 nm.

**Preparation of polymer micelles (10)** The same procedure as performed to produce micelle solution **8** was followed using diblock copolymer **6** (5.0 mg, 7.8 x $10^{-7}$ mol), affording micelle solution **10**. Final concentration: 3.17 mg/mL. Hydrodynamic diameter (DLS): $(D_h)_i$ = 83 ± 12 nm, $(D_h)_v$ = 31 ± 8 nm, $(D_h)_n$ = 21 ± 6 nm. $D_{av}$(TEM) = 30 ± 5 nm. $H$ (AFM) = 4 ± 1 nm.

**Preparation of polymer micelles (11)** The same procedure as performed to produce micelle solution **8** was followed using diblock copolymer **7** (20.0 mg, 3.6 x $10^{-5}$ mol), affording micelle solution **11**. Final concentration: 1.4 mg/mL. Hydrodynamic diameter (DLS): $(D_h)_i$ = 32 ± 9 nm, $(D_h)_v$ = 18 ± 4 nm, $(D_h)_n$ = 15 ± 4 nm. $D_{av}$(TEM) = 18 ± 3 nm. $H$ (AFM) = 2 ± 1 nm.

**Preparation of inverse polymer micelles (12)** In a 100 mL round-bottom flask equipped with a magnetic stirring bar, diblock copolymer **4** (13.8 mg, 6.4 x $10^{-6}$ mol) was

dissolved in THF (15.0 mL), yielding a transparent pale yellow solution. Decane (25 mL) was added dropwise *via* a syringe pump, complete with vigorous stirring, over a period of 2 h, resulting in an opaque solution. Final concentration: 0.35 mg/mL. Hydrodynamic diameter (DLS): $(D_h)_i$ = 569 ± 142 nm, $(D_h)_v$ = 515 ± 160 nm, $(D_h)_n$ = 252 ± 167 nm. (cylindrical micelles) $D_{av}$(TEM) = 34 ± 6 nm, (spherical micelles) $D_{av}$(TEM) = 25 ± 3 nm. *H* (AFM) = 11 ± 2 nm.

**Preparation of inverse polymer micelles (13)** The same procedure was performed to produce micelle solution **12** was followed using diblock copolymer **5** (13.7 mg, 1.61 x $10^{-5}$ mol), affording micelle solution **13**. Final concentration: 0.34 mg/mL. Hydrodynamic diameter (DLS): $(D_h)_i$ = 556 ± 102 nm, $(D_h)_v$ = 641 ± 134 nm, $(D_h)_n$ = 434 ± 76 nm. $D_{av}$(TEM) = 117 ± 42 nm. *H* (AFM) = 6 ± 1 nm.

**Preparation of inverse polymer micelles (14)** The same procedure was performed to produce micelle solution **12** was followed using diblock copolymer **6** (5.9 mg, 9.2 x $10^{-7}$ mol), affording micelle solution **14**. Final concentration: 0.20 mg/mL. Hydrodynamic diameter (DLS): $(D_h)_i$ = 414 ± 122 nm, $(D_h)_v$ = 487 ± 187 nm, $(D_h)_n$ = 308 ± 84 nm. $D_{av}$(TEM) = 179 ± 54 nm. *H* (AFM) = 7 ± 2 nm.

**Preparation of inverse polymer micelles (15)** The same procedure was performed to produce micelle solution **12** was followed using diblock copolymer **7 (**12.7 mg, 2.3 x $10^{-5}$ mol), affording micelle solution **15**. Final concentration: 0.32 mg/mL. Hydrodynamic diameter: $D_{av}$(TEM) = 356 ± 71 nm. *H* (AFM) = 4 ± 2 nm. DLS did not yield suitable correlation for data analysis.

**General procedure for synthesis of $PEO_{112}$-*b*-$PIp_{114}$ for anti-fouling tests (16).** To a 50 mL bomb-type Schlenk flask equipped with a Teflon coated magnetic stir bar was added Ip (4.5201 g, 6.636 x $10^{-2}$ mol, 175 eq), macro chain transfer agent **2**, (2.0329

g, 3.789 x $10^{-4}$ mol, 1.0 eq), and di-*tert*-butylperoxide (0.0170 g, 1.16 x $10^{-4}$ mol, 0.3 eq), along with 1,4-dioxane (15.5 mL). The mixture was degassed *via* 3 freeze-pump-thaw cycles. Upon the final thaw the Schlenk flask was backfilled with Ar and placed in a temperature-regulated mineral oil bath set at 125 °C and left to react for 24 h. After cooling the residual solvent and monomer were removed *in vacuo*. Leftover contents of the flask were dissolved in a minimal amount of dichloromethane and precipitated 3 times into 1L 1:1 methanol:water producing a transparent yellow oil. The excess solvent was decanted off and the product was dried *in vacuo*, yielding 2.931 g (94% yield based on 24% conversion) of sticky yellow powder. $M_n^{NMR}$ = 14 kDa, $M_w^{GPC}$ = 40 kDa, $M_n^{GPC}$ = 28 kDa, $M_w/M_n$ = 1.40. IR ($cm^{-1}$): 3020-2760, 1726, 1665, 1644, 1466, 1449, 1343, 1280, 1242, 1148, 1114, 1061, 964, 842, 530. $^1$H NMR (500 MHz, chloroform-*d*, ppm): δ 5.8-5.7 (br, 1,2 C*H*=$CH_2$), 5.2-5.1 (br, 1,4 -$CH_2$-C($CH_3$)-C*H*-$CH_2$-), 5.0-4.8 (br, 1,2 CH=C$H_2$), 4.8-4.6 (br, 4,3 C($CH_3$)-C$H_2$), 3.7 – 3.5 (br, -C$H_2$-C$H_2$-O-), 3.4 (s, -O-C$H_3$), 3.2 (br, m, -SC(S)S-C$H_2$-$(CH_2)_{10}$-$CH_3$), 2.2-1.8 (br, C$H_2$ isoprene backbone), 1.7-1.5 (br, isoprene backbone C$H_3$), 1.6 (s, O-C(O)-C(C$H_3$)$_2$-S-), 1.4-1.2 (br, -SC(S)S-$CH_2$-(C$H_2$)$_{10}$-$CH_3$), 0.9 (br t, -SC(S)S-$CH_2$-$(CH_2)_{10}$-C$H_3$). $^{13}$C NMR (75 MHz, chloroform-*d*, ppm): δ 147.8, 135.1, 125.2, 124.5, 111.5, 72.2, 70.8, 69.3, 63.7, 62.2, 59.3, 52.2, 44.8, 40.0, 38.7, 32.2, 31.0, 28.5, 26.9, 23.7, 19.0, 16.3, 14.4.

**Procedure for the synthesis of UV-promoted thiol-ene crosslinked PEO-*b*-PIp coatings (17).** A large batch of $PEO_{112}$-*b*-$PIp_{114}$ thiolene crosslinked films was prepared by first weighing the polymer (0.7544 g, 9.2 x $10^{-5}$ mol, 8200 Da), decanedithiol (0.6349 g, 3.1 x $10^{-3}$ mol, 1.5 eq SH/alkene), 1-hydroxycyclohexylphenyl ketone (0.0680 g, 5 wt %) and 15 mL of 1,4 dioxane into a scintillation vial and stirring at 60 ºC for 20 min to ensure homogeneity of all the components. Argon was bubbled through the solution for 5

minutes, then solution was cast (ca. 1 mL) onto vinyltrimethoxysilane-modified glass slides and allowed to evaporate for 10 minutes. Slides were then passed through a Fusion UV 300S conveyor unit (H bulb) at 1 m/min for three passes to ensure complete crosslinking. Post-crosslinking, the films were incubated in artificial seawater for 72 hours, followed by copious rinsing with distilled water, followed by air drying.

## Results and Discussion

### Synthesis and characterization of PEO-*b*-PIp block copolymers

Mono-functional RAFT PEO macro-CTAs **2** and **3** were prepared through amidation reaction between acid-functionalized RAFT agent DDMAT, **1**, and monoamino-functionalized PEO polymers of 5 and 2 kDa molecular weight, respectively (Scheme 4-1).

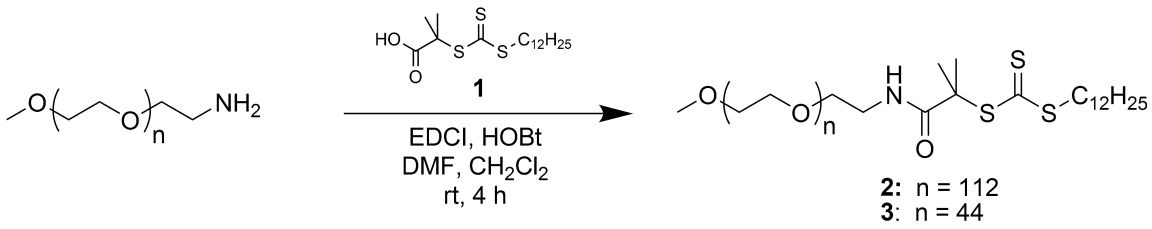


**Scheme 4-1**. Preparation of PEO macro-CTAs **2** and **3**.

The macro-CTAs were obtained in modest yield, moderate losses likely occurred during the chromatography required to purify the final product. Both the α-methoxy and the ω-dodecyl chain ends were visible in the $^1$H NMR spectra and the integration of their respective peaks agreed with a 1:1 theoretical ratio. The PEO macro-CTAs, therefore, showed complete trithiocarbonate functionality by $^1$H NMR spectroscopy, which allowed for polymerization of isoprene for the formation of amphiphilic block copolymers.

Differing degrees of isoprene chain extension from the two macro-CTAs gave a series of block copolymers having variation in the hydrophilic-hydrophobic balance and overall polymer chain lengths, by control of the relative individual block lengths. Two lengths of poly(isoprene) were chain extended from each PEO precursor, **2** and **3**, (Scheme 4-2), using standard RAFT conditions. The initial reaction mixtures of **2** or **3** in 1,4-dioxane, to which is added isoprene and then *t*-butyl peroxide, existed as opaque heterogeneous

poorly dissolved solutions. After only *ca.* 1 h of heating at 125 °C, as the polymerization progressed, the solutions became transparent, and had reached ca. 25-30% conversion of isoprene after 24 h. The polymers were obtained in high yields by precipitation into methanol or cold diethyl ether, with the exception of polymer **5**, which required the addition of water to methanol. For polymer 5, the high weight fraction of PEO rendered methanol inadequate as a non-solvent for the block and water had to be added to allow for the precipitation to occur. Polymers 4-7 had interesting solubility properties across a wide range of solvent polarity showing a potential ability to spontaneously form assemblies in different solvents. This finding triggered our consideration of the invertible nature that the assemblies might possess.

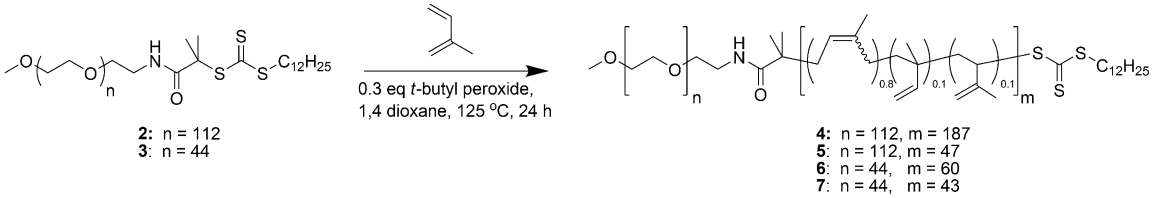


**2:** n = 112
**3**: n = 44

**4:** n = 112, m = 187
**5**: n = 112, m = 47
**6**: n = 44, m = 60
**7**: n = 44, m = 43

**Scheme 4-2**. Preparation of $PEO_n$-*b*-$PIp_m$ polymers

Both $^{1}H$ and $^{13}C$ NMR spectroscopy were used to determine the compositions of the polymers (Figures 4-1 and 4-2) and to confirm the removal of non-reacted isoprene monomer. The final degree of polymerization of isoprene was determined using $^{1}H$ NMR by integration of the vinyl peaks of the polyisoprene block against the methoxy peak of the PEO chain end.

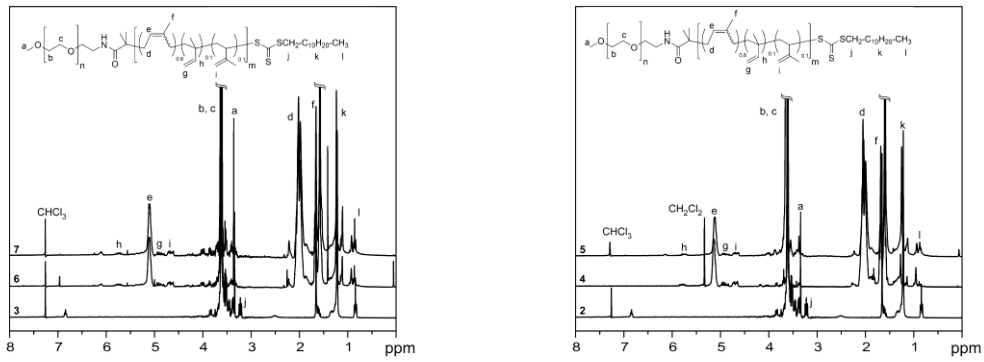


**Figure 4-1**. $^{1}H$ NMR spectra (500 MHz, $CDCl_3$ and $CD_2Cl_2$) for 5 kDa PEO-block series, macro-CTA **2**, and PEO-*b*-PIp block copolymers **4** and **5** (left) and 2 kDa PEO-block series, macro-CTA **3**, and PEO-*b*-PIp block copolymers **6** and **7** (right).

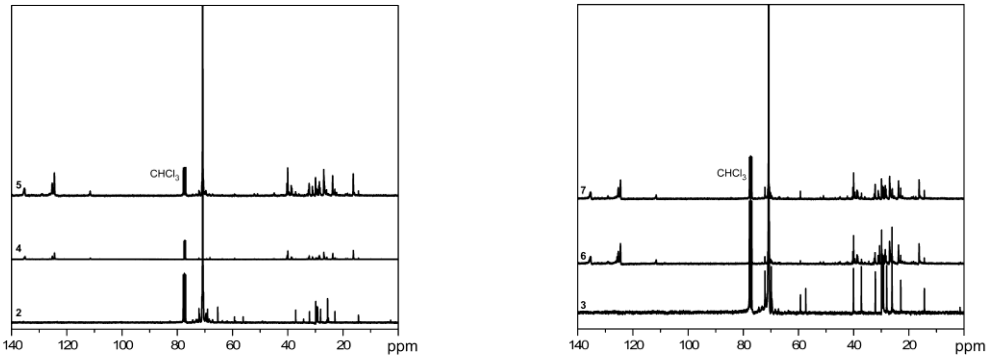


**Figure 4-2.** $^{13}C$ NMR spectra of 5k series polymers (left) and 2k series polymers (right). Detailed assignments can be found in the experimental section.

**Table 4-1**. Molecular weight, polydispersity, and thermal analysis data for PEO macro-CTAs and PEO-*b*-PIp block copolymers.

| Polymer | $M_n^{NMR}$ (Da) | $M_n^{GPC}$ (Da)[a] | PDI[a] | $T_g$ (°C)[b] | $T_m$ (°C)[c] | $T_{decomp}$ (°C) |
|---|---|---|---|---|---|---|
| **2** | 7,800 | 7,600 | 1.04 | n/a | 61.0 | 395.3 |
| **3** | 2,400 | 3,200 | 1.03 | n/a | 50.4 | 377.5 |
| **4** | 18,000 | 18,000 | 1.28 | -60.0 | 56.0 | 401.8 |
| **5** | 8,500 | 8,600 | 1.34 | -61.0 | 55.3 | 399.2 |
| **6** | 6,400 | 6,500 | 1.29 | -62.7 | 47.3 | 397.0 |
| **7** | 5,500 | 5,300 | 1.30 | -64.7 | 49.0 | 399.5 |

[a]Pre-dialysis value. [b]Polyisoprene region. [c]Poly(ethylene oxide) region.

In addition, thermogravimetric analysis (TGA, Figure 4-3) and differential scanning calorimetry (DSC, Figure 4-4) were performed to assess thermal properties for the block copolymers. Results are presented

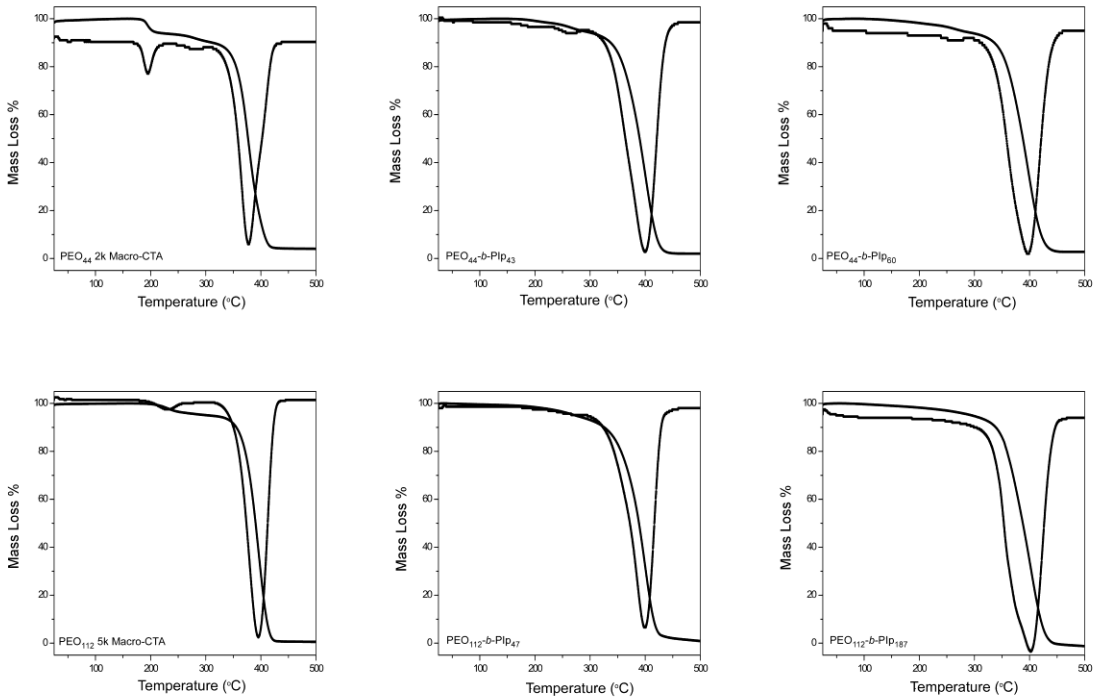


**Figure 4-3**. Thermogravimetric analysis (TGA) mass loss and derivative mass loss plots of 2k series (top) and 5k series (bottom).

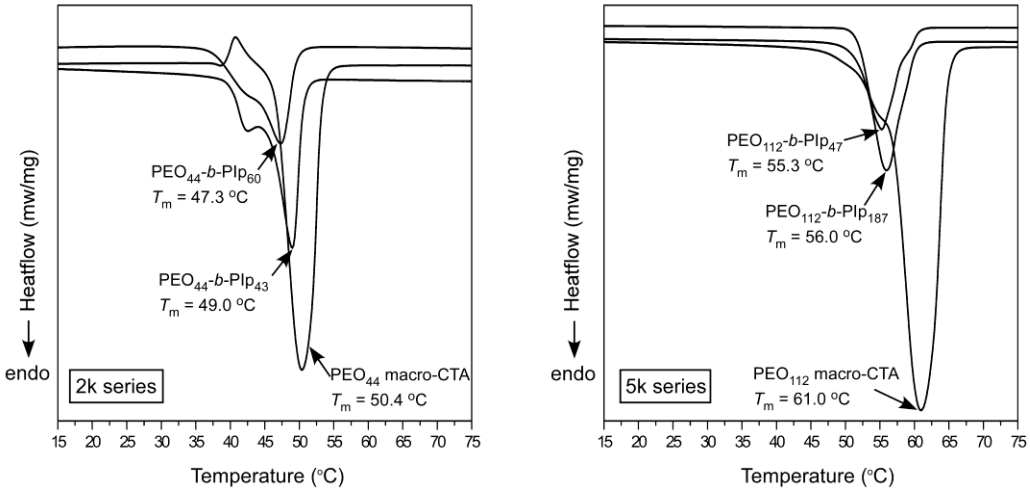


**Figure 4-4.** Differential Scanning Calorimetry (DSC) plots of 2k series (left) and 5k series (right) zoomed in on the PEG $T_m$ region (full plot not shown).

with molecular weight and polydispersity data in Table 4-1. Longer block lengths of both PEO and PIp resulted in higher glass transition temperatures. As would be expected, incorporation of isoprene resulted in lower melting transition temperatures of the PEO block.

**GPC Analysis**

In order to better understand the relationship between polymer size/composition and structure obtained during solution assembly, accurate determination of block sizes must be obtained. GPC analysis of the PEO macro-CTAs and block copolymers (Figure 4-5) showed that unreacted PEO macro-CTA remained present in all block copolymer samples. The elution volume of the low molecular weight shoulder present in the chromatogram of the block copolymers corresponded to that of the PEO macro-CTA. Multi-peak mathematical deconvolution of the peaks (Figure 4-6) enabled the calculation

of $M_n$ for both the block copolymer and remaining PEO macro-CTA with respect to the polystyrene calibration curve (Table 4-2). The molecular weight calculated for the shoulder corresponded to that obtained for the PEO macro-CTA itself.

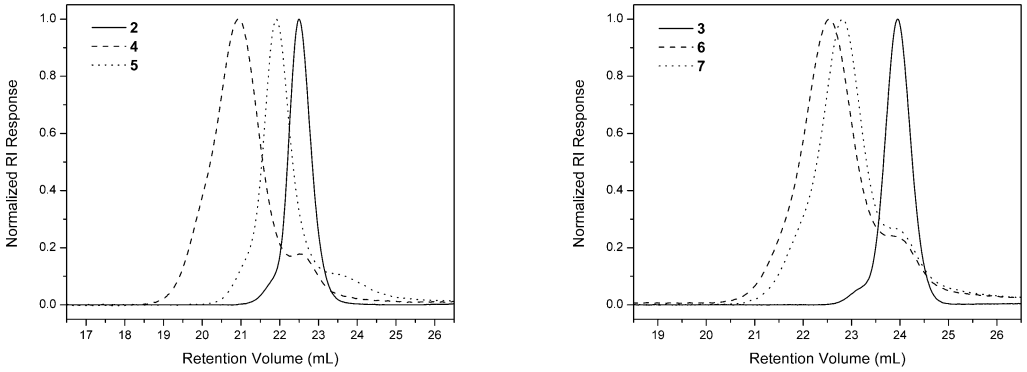


**Figure 4-5**. THF-GPC chromatograms of 5 kDa PEO-block series, macro-CTA **2**, and PEO-*b*-PIp block copolymers **4** and **5** (left) and 2 kDa PEO-block series, macro-CTA **3**, and PEO-*b*-PIp block copolymers **6** and **7** (right).

A variety of factors can cause incomplete chain extension or blocking including low functionality of the chain-transfer agent or low chain-extension efficiency. It is not believed that low functionality of the macro-CTAs can be a cause of incomplete blocking in this case. Incomplete amidation reaction during preparation of the PEO macro-CTAs would leave PEO-$NH_2$ in the reaction mixture unable to participate in further polymerization. $^1$H NMR analysis of the PEO macro-CTAs after column chromatography showed good correlation between methoxy chain-end and dodecyl chain-end of the trithiocarbonate and demonstrated high functionalization of the macro-CTAs. However, it is believed that incompatibility between the hydrophilic macro-CTA and hydrophobic isoprene monomer could be a major contributor to low or slow chain-transfer in this case. Due to the presence of unreacted PEO macro-CTA, the DP of

isoprene as calculated by $^{1}$H NMR is inexact. In order to calculate the actual DP of isoprene the unreacted PEO macro-CTA should be removed. Dialysis was performed on each of the copolymers against water for five days to attempt to remove unreacted starting material, with mixed results. Therefore, an estimation of the amount of unreacted PEO macro-CTA present and blocking efficiency was carried out through mathematical deconvolution of GPC chromatograms.

**Table 4-2**: $M_n$ values for low and high molecular weight peaks, *dn/dc* of block copolymers and blocking efficiency calculated from multi-peak mathematical deconvolution of GPC chromatograms and other GPC data.

| Polymer | $M_{n,\ shoulder}^{GPC}$ (Da) | $M_{n,\ block}^{GPC}$ (Da) | *dn/dc* | Blocking Efficiency |
|---|---|---|---|---|
| **4** | 7,700 | 22,900 | 0.1057 | 0.46 |
| **5** | 4,200 | 11,800 | 0.1029 | 0.52 |
| **6** | 3,100 | 8,300 | 0.1076 | 0.63 |
| **7** | 3,000 | 7,000 | 0.0911 | 0.65 |

Following the method used by Gao *et al*.(66), gel permeation chromatography was used to estimate the chain extension efficiency of the PEO macro-CTAs for each polymerization. Mathematical deconvolution of the GPC chromatograms provided a multi-peak fitting for all polymer peaks with a low molecular weight peak corresponding to the unreacted macro-CTA and one or several peaks corresponding to the actual block copolymer. Using the polystyrene calibration of the DRI detector it was possible to calculate $M_n$ for each component individually, $M_{CTA}$ the molecular weight of the

remaining PEO macro-CTA and $M_{block}$ the molecular weight of the block copolymer. (*dn/dc*) values for PEO macro-CTAs and for pure polyisoprene were determined as 0.0740 and 0.1246 respectively using response *vs.* concentration plots from the differential refractometer.

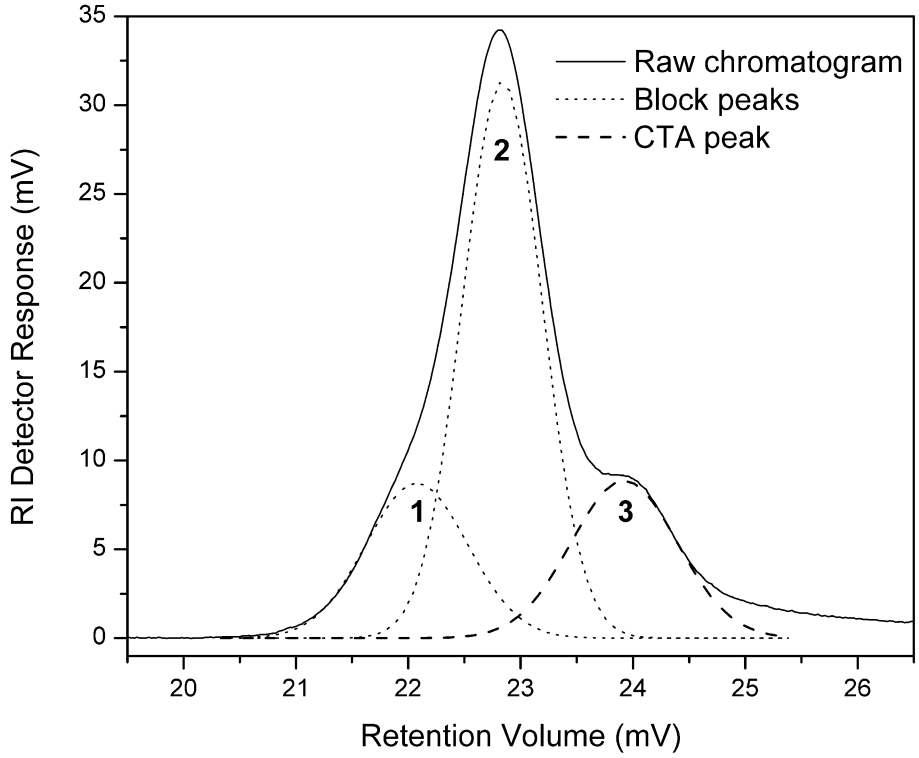


**Figure 4-6**. Example of multi-peak mathematical deconvolution of GPC chromatogram of polymer **7**. $A_{block}$ corresponds to the area of peaks 1 + 2 and $A_{CTA}$ corresponds to the area of peak 3.

(*dn/dc*) values for the "pure" block copolymers were calculated following equation 1 using the calculated $M_n$ of the peaks (Table 4-2) and the (*dn/dc*) values for PEO macro-CTAs and pure polyisoprene determined earlier.

$$\left(\frac{dn}{dc}\right)_{block} = w_{CTA} \times \left(\frac{dn}{dc}\right)_{CTA} + w_{IP} \times \left(\frac{dn}{dc}\right)_{IP} \qquad (1)\ (67)$$

with $w_{CTA}$ and $w_{IP}$ weight fractions of PEO-CTA and polyisoprene in block copolymer sample, calculated using $M_n$ of the CTA peak and block copolymer peak (Table 4-2).

The instantaneous response from the DRI detector at a given retention volume *i*, $R_i$, is given by equation 2. The area of a peak on the GPC chromatogram, $A_P$, can be expressed as a sum of the response from the DRI detector over the elution volume of the peak, equation 3.

$$R_i = k \times \left(\frac{dn}{dc}\right)_i \times c_i \qquad (2)$$

with $k$ DRI detector constant, $\left(\frac{dn}{dc}\right)_i$ specific refractive index of the fraction (mL/g) and $c_i$ instantaneous mass concentration in retention volume *i* (g/mL).

$$A_P = \sum_{i=0}^{N} R_i.\Delta V = \sum_{i=0}^{N} k \times \left(\frac{dn}{dc}\right)_i \times c_i.\Delta V = k\sum_{i=0}^{N}\left(\frac{dn}{dc}\right)_i \times m_i \qquad (3)$$

with $m_i = c_i \times \Delta V$ instantaneous mass of polymer in retention volume *i* and $\Delta V$ volume fraction measured.

Equation 3 can be simplified to express $A_P$ as a function of *dn/dc* of the polymer, $M_n$ of the polymer and number of moles of polymer in the sample. The area of the peak corresponding to the unreacted macro-CTA, $A_{CTA}$, and the total area of the peak corresponding to the block copolymer, $A_{block}$, have been expressed in this way in equation 4 and 5, respectively.

$$A_{CTA} = k\left(\frac{dn}{dc}\right)_{CTA} \times M_{CTA} \times n_{CTA} \qquad (4)$$

with $n_{CTA}$ number of moles of remaining macro-CTA.

$$A_{block} = k\left(\frac{dn}{dc}\right)_{block} \times M_{block} \times n_{block} \quad (5)$$

with $n_{block}$ number of moles of block copolymer in the sample.

$$x_b = \frac{\frac{A_{block}}{A_{CTA}} \times \left(\frac{dn}{dc}\right)_{CTA} \times M_{CTA}}{\left(\frac{dn}{dc}\right)_{block} \times M_{block} + \frac{A_{block}}{A_{CTA}} \times \left(\frac{dn}{dc}\right)_{CTA} \times M_{CTA}} \quad (6)$$

Finally, the mole fraction of block copolymer or blocking efficiency, $x_b$, can be developed from equation 4 and 5 to get equation 6 in which all terms have either been previously calculated or measured from the GPC chromatogram. Using equation 6, it was possible to calculate the blocking efficiency for all polymers (Table 4-2). The blocking efficiency was estimated to be around 50% for the 5 kDa and 64% for the 2 kDa PEO macro-CTA polymer series. The length of the PEO macro-CTA seems to have an influence on the blocking efficiency for the chain extension of isoprene, however, the effect of the PEO macro-CTA chain length on the extension of other hydrophobic monomers has not yet been reported.

**Micellization of PEO-*b*-PIp in both aqueous and organic solvent**

Block copolymers **4-7**, respectively, were assembled into micelles using solvent-induced micellization procedures, giving water-stable micelles **8-11** and decane-stable inverse assemblies **12-15** (Scheme 4-3). The resulting structures were analyzed *via* DLS, AFM and TEM to evaluate the type of morphologies obtained and their domain sizes (Tables 4-3 and 4-4).

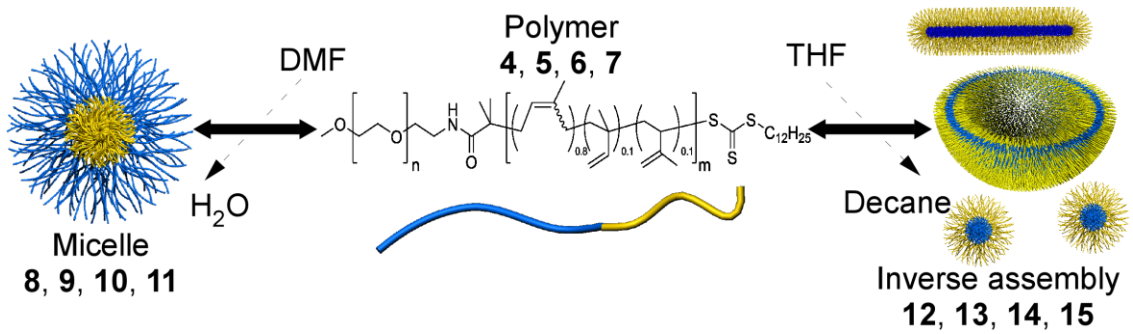


**Scheme 4-3.** Schematic illustrations of the aqueous assembly of **4-7** to give micelles **8-11**, respectively, and decane assembly of **4-7** to give inverse micellar assemblies **12-15**, respectively.

**Table 4-3**. Micellization data (aqueous solution).

| Micelle | $D_h$ (Int.), nm | $D_h$ (Vol.), nm | $D_h$ (Num.), nm | D (TEM)[a], nm | $D_{core}$ (TEM)[b, c], nm | Height (AFM), nm |
|---|---|---|---|---|---|---|
| **8** | 154 ± 49 | 93 ± 37 | 54 ± 38 | 55 ± 18 | 30 ± 6 | 8 ± 3 |
| **9** | 114 ± 9 | 26 ± 4 | 18 ± 4 | 31 ± 4 | 13 ± 3 | 4 ± 1 |
| **10** | 83 ± 12 | 31 ± 8 | 21 ± 6 | 30 ± 5 | 24 ± 5 | 4 ± 1 |
| **11** | 32 ± 9 | 18 ± 4 | 15 ± 4 | 18 ± 3 | 8 ± 2 | 2 ± 1 |

[a] Phosphotungstic acid stain; [b] $OsO_4$ stain; [c] See Figure 4-9 for images

**Table 4-4**. Inverse micellization data (decane solution).

| Micelle | $D_h$ (Int.), nm | $D_h$ (Vol.), nm | $D_h$ (Num.), nm | D (TEM)[a], nm | Height (AFM), nm |
|---|---|---|---|---|---|
| **12** | 569 ± 142 | 515 ± 160 | 252 ± 167 | 34 ± 6 [c]<br>25 ± 3 [d] | 11 ± 2 |
| **13** | 556 ± 102 | 641 ± 134 | 434 ± 76 | -[e] | 6 ± 1 |
| **14** | 414 ± 122 | 487 ± 187 | 308 ± 84 | -[e] | 7 ± 2 |
| **15** | -[b] | -[b] | -[b] | -[e] | 4 ± 2 |

[a] $OsO_4$ stain; [b] Insufficient correlation; [c] cylindrical inverse micelle; [d] spherical inverse micelle; [e] the dimensions of the assemblies could not be accurately determined, as they are not confirmed as spherical or vesicular in nature.

Aqueous-based micellization was achieved through the dissolution of block copolymers **4**-**7** into DMF followed by the slow addition of an excess of water. The micellar solutions, **8**-**11**, were then dialyzed against nanopure water for several days to remove traces of organic solvent. All of the block copolymers readily formed mono-modal aqueous spherical micelles, whose particle diameters followed trends relative to the parent copolymer, *e.g*. longer block length PEO relative to PIp gave smaller particles, and shorter overall polymer chain length afforded smaller particle assemblies. These trends, summarized in Table 4-3, can be easily observed through DLS data, Figure 4-7, and on both negatively- and positively-stained TEM images (Figures 4-8 and 4-9, respectively).

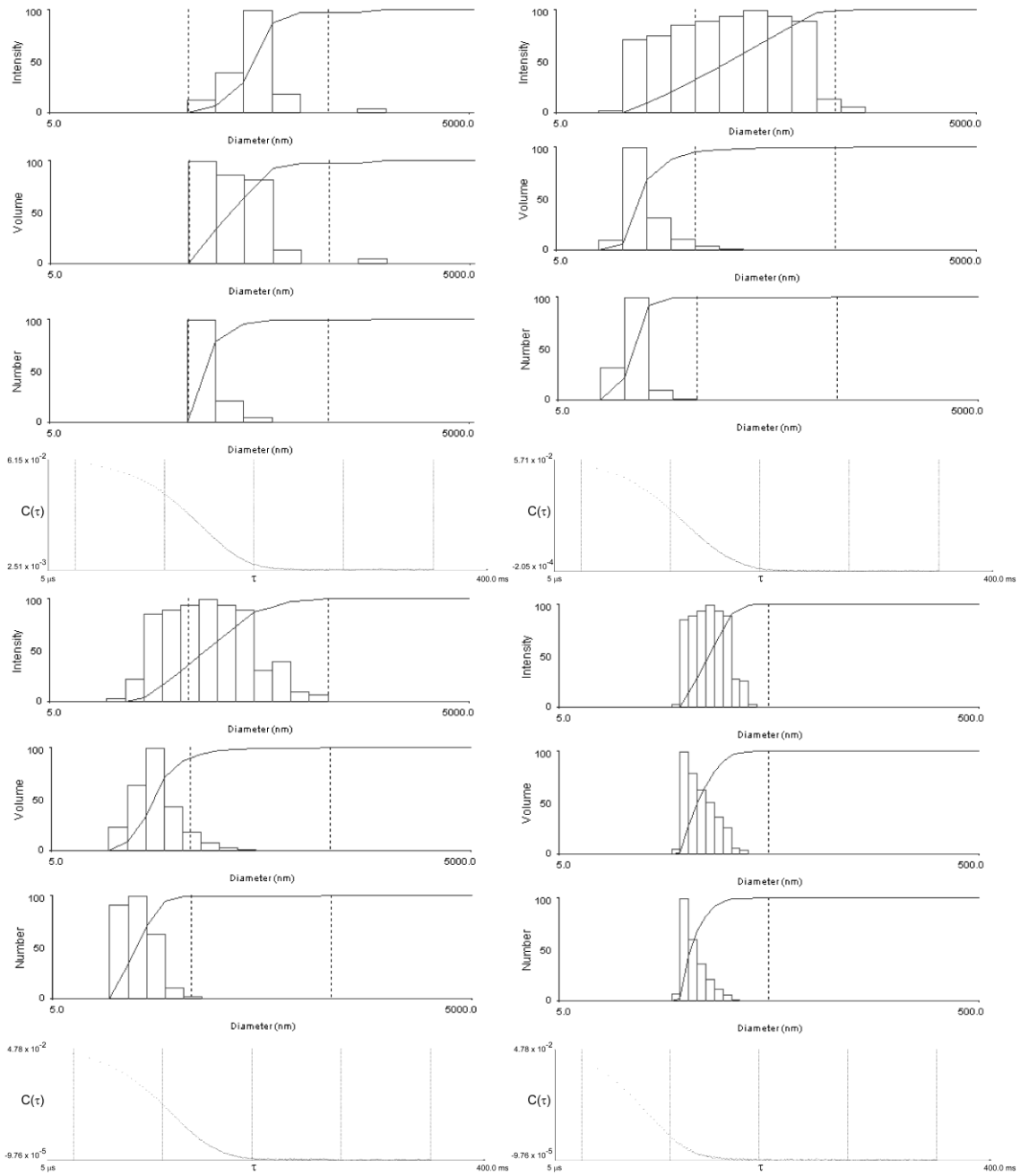


**Figure 4-7.** Typical DLS plots and corresponding correlation curve obtained for micelle solution **8** produced from polymer **4** (upper left), micelle solution **9** produced from polymer **5** (upper right), micelle solution **10** produced from polymer **6** (lower left), and micelle solution **11** produced from polymer **7** (lower right).

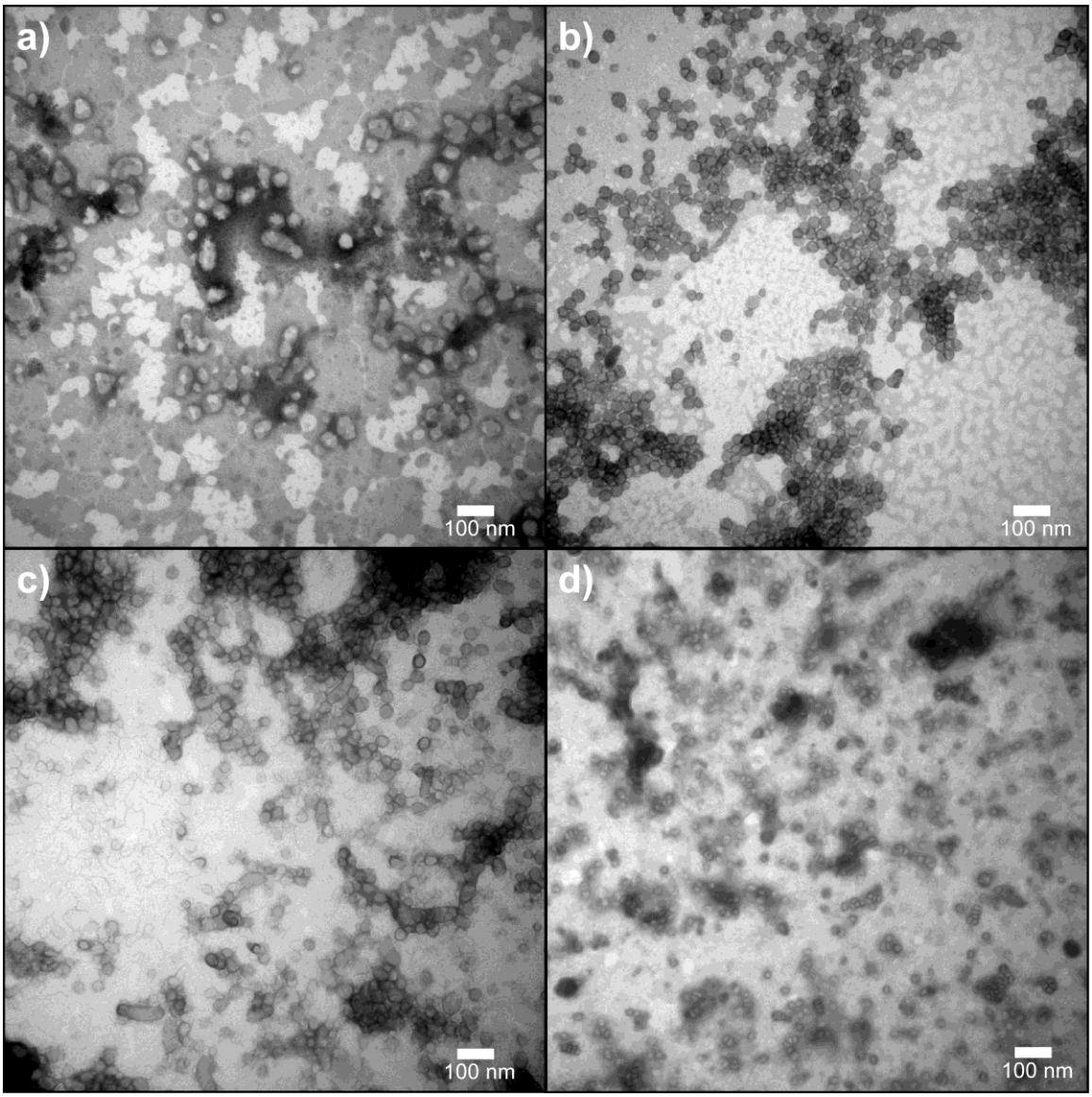


**Figure 4-8**. TEM images of PEO-*b*-PIp diblock copolymer aqueous micelles **8**, **9**, **10** and **11** using phosphotungstic acid as negative stain.

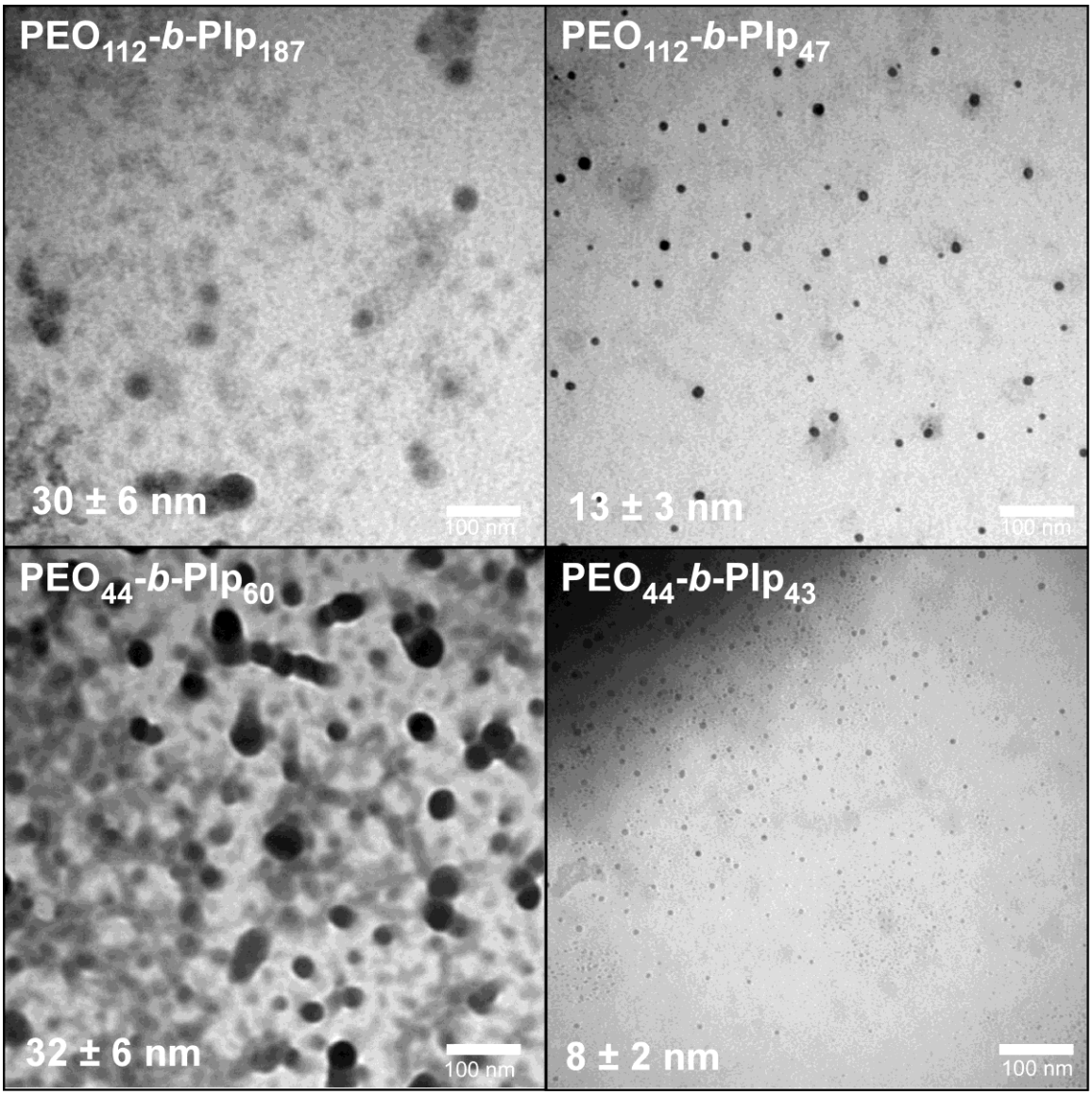


**Figure 4-9.** TEM images of aqueous micelles of PEO-*b*-PIp block copolymers with $OsO_4$ staining. Core diameter (PIp) is listed in the lower left corner of each image.

As measured by TEM, block copolymer **4** formed large particles of 55 ± 18 nm diameter with slight irregularities, whereas **5** formed more regularly-shaped particles of 31 ± 4 nm diameter, with the smaller deviation reflecting the particle quality. The particles were also analyzed by AFM to obtain an estimate of particle height on a mica substrate (Figure 4-10). Although the TEM and DLS diameter values were in good

agreement, the AFM-measured heights were substantially low, which is likely due to an affinity of the PEO shell for the hydrophilic mica surface, perhaps combined with PEO crystallization events that occur upon drying, resulting in a spreading and reorganization of micelle structure as has been noted before for this block copolymer system by Glynos *et al*.(45) The combination of these data demonstrates that the PEO-*b*-PIp block copolymers can readily form well-defined micelles of varying sizes in aqueous solution.

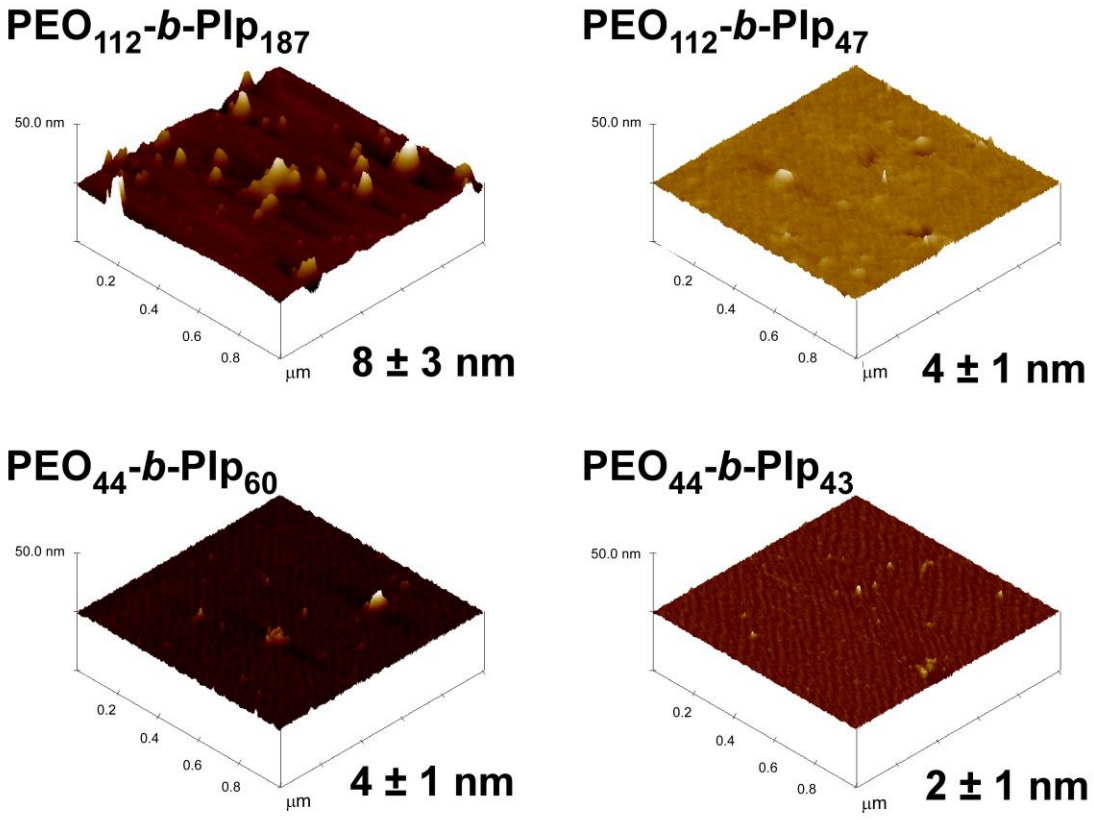


**Figure 4-10**. AFM images PEO-*b*-PIp diblock copolymer aqueous micelles **8**, **9**, **10** and **11**, together with average height values.

To determine how the polymers assemble in hydrophobic solvent, micellization conditions were altered to induce formation of inverse micelles in decane. Decane provides a hydrophobic non-reactive solvent environment with a high boiling point.

Inverse assemblies, **12**-**15**, of block copolymers **4**-**7**, respectively, were obtained through dissolution the copolymers into THF followed by the slow addition of an excess of decane. It should be noted that post-assembly dialysis was not performed, as had been done for the aqueous micelles, due to solvent cost. All solutions had minute amounts of precipitate that appeared post-assembly.

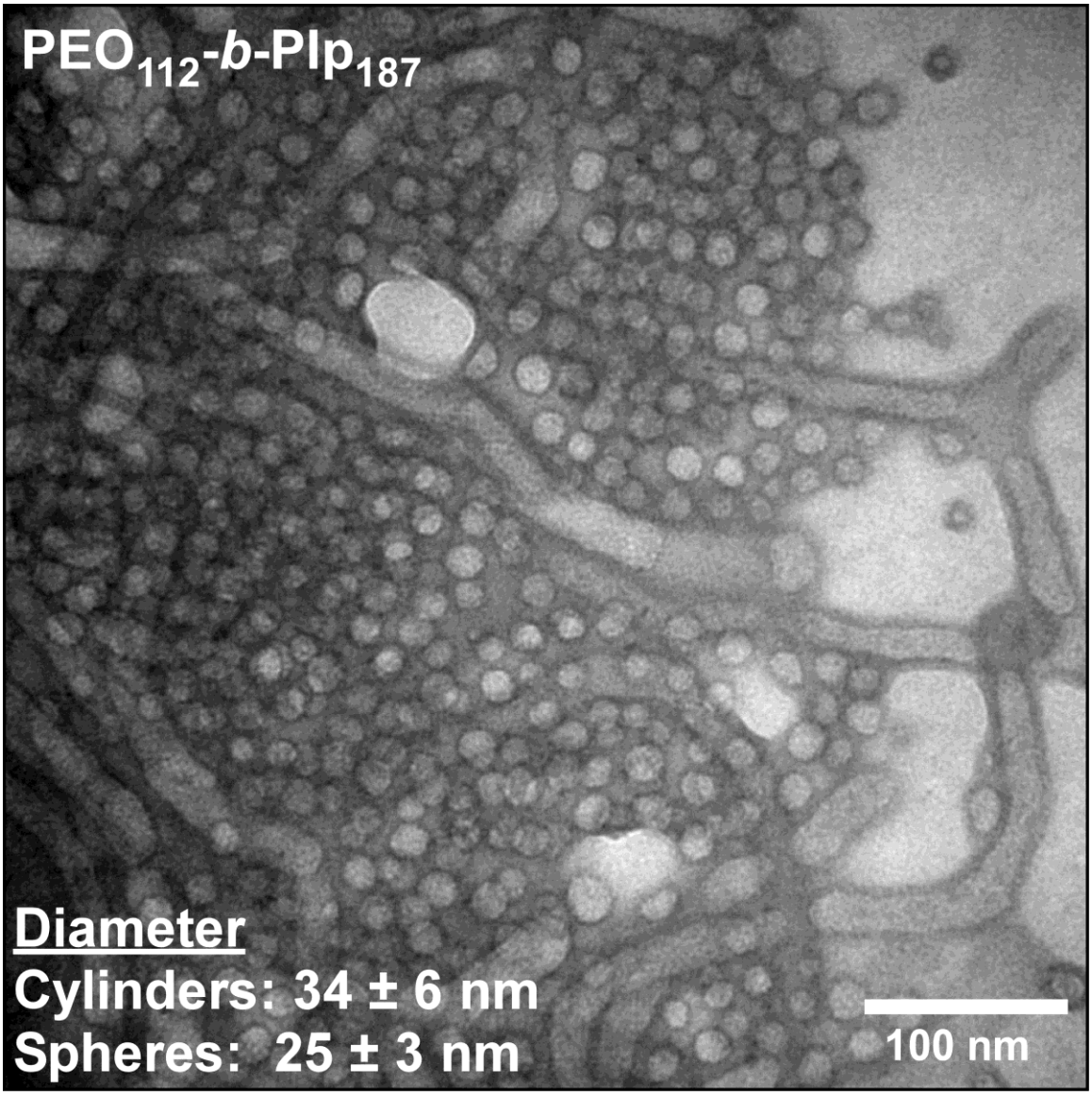


**Figure 4-11**. TEM images of PEO-*b*-PIp diblock copolymer inverse assemblies **12** using $OsO_4$ as positive stain.

Each block copolymer readily formed assemblies of interesting sizes and morphologies, yet each was heterogeneous. DLS analysis of the assemblies **12-14** showed larger structures, in comparison to the aqueous assemblies (see Figure 4-12 for representative DLS figures or Table 4-4 for listing). In the case of assembly **12**, sub-100 nm structures were also present. DLS examination of inverse micelle **15** yielded insufficient correlation, and further attempts to inspect the solution post-centrifugation and filtration

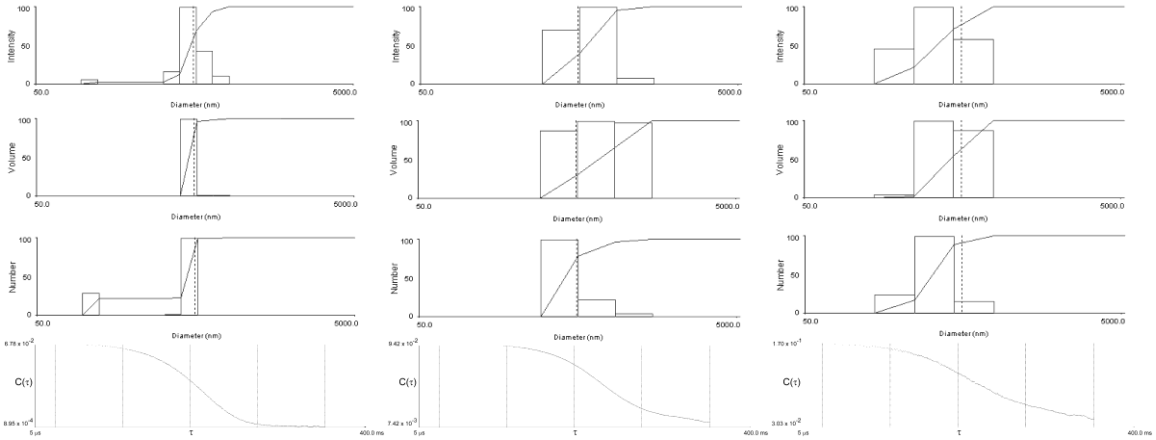

**Figure 4-12.** Typical DLS plots and corresponding correlation curve obtained for inverse assembly solution **11** produced from polymer **4** (left), assembly **12** produced from polymer **5** (center), assembly **13** produced from polymer **6** (right). Polymer **7** did not produce well-correlated inverse assemblies by DLS.

yielded no results. TEM analysis of assembly **12**, stained using $OsO_4$-stain, which selectively stains PIp, showed bundled mixtures of long cylinders and sub-100 nm spheres (Table 4-4) which was also confirmed by DLS and AFM (Figures 4-11 and 4-13). AFM and DLS analysis of assemblies **13-15** showed larger aggregates (Figure 4-13 and Table 4-4), consistent with vesicles, but the exact nature of these supramolecular structures could not be confirmed by TEM. Due to the difficulties in performing cryo-

TEM with high boiling and crystallizable solvents, such as decane, attempts to obtain cryo-TEM images were unsuccessful. The assembly of PEO-*b*-PIp block copolymers in hydrophobic, organic solvent resulted in the formation of either a mixture of cylindrical and spherical morphologies or large aggregates of sizes consistent with vesicular structures, depending on the block lengths.

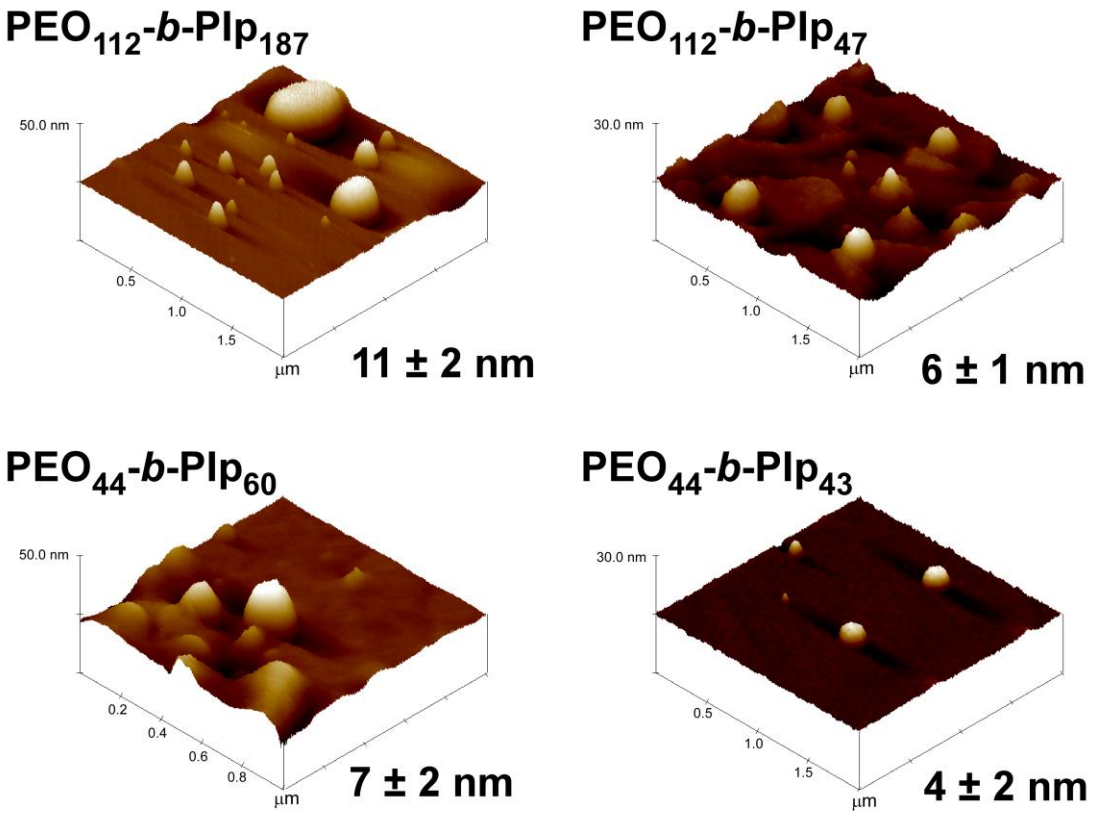


**Figure 4-13**. AFM images of PEO-*b*-PIp diblock copolymer inverse assemblies **12**, **13**, **14** and **15**.

**PEO-*b*-PIp Anti-fouling coatings**

A large batch of PEO-*b*-PIp (**16**) was synthesized and characterized in a similar manner to the previous polymers (see Figure 4-14 for NMR). The polymer was then crosslinked

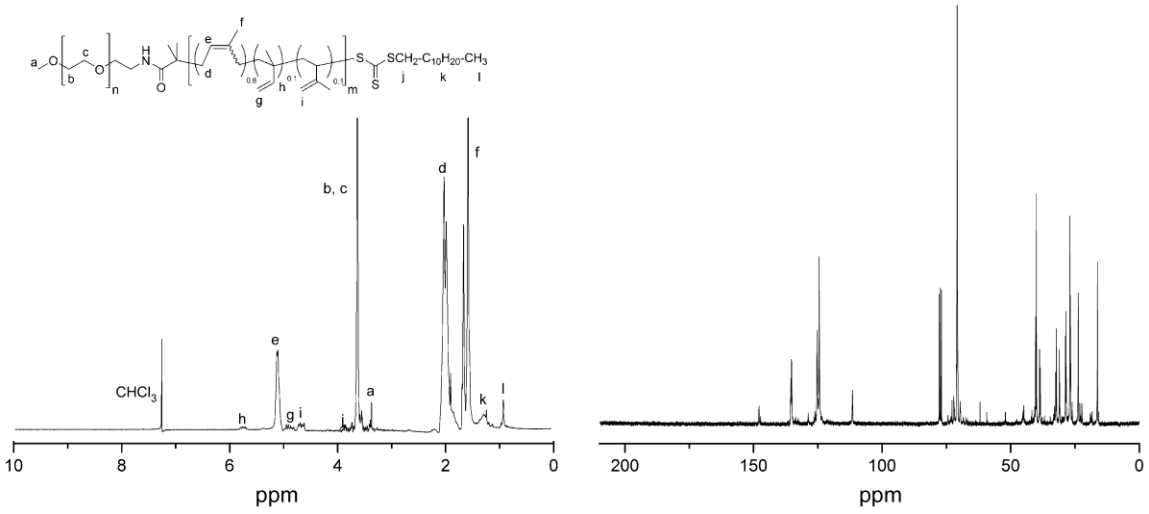


**Figure 4-14.** $PEO_{112}$-*b*-$PIp_{114}$ $^{1}H$ NMR spectrum (left) and $^{13}C$ NMR spectrum (right).

across several dithiol concentrations (Figure 4-15) using UV-promoted thiol-ene methods (Scheme 4-4), and in a large batch (**17**) of a single dithiol concentration. The films were

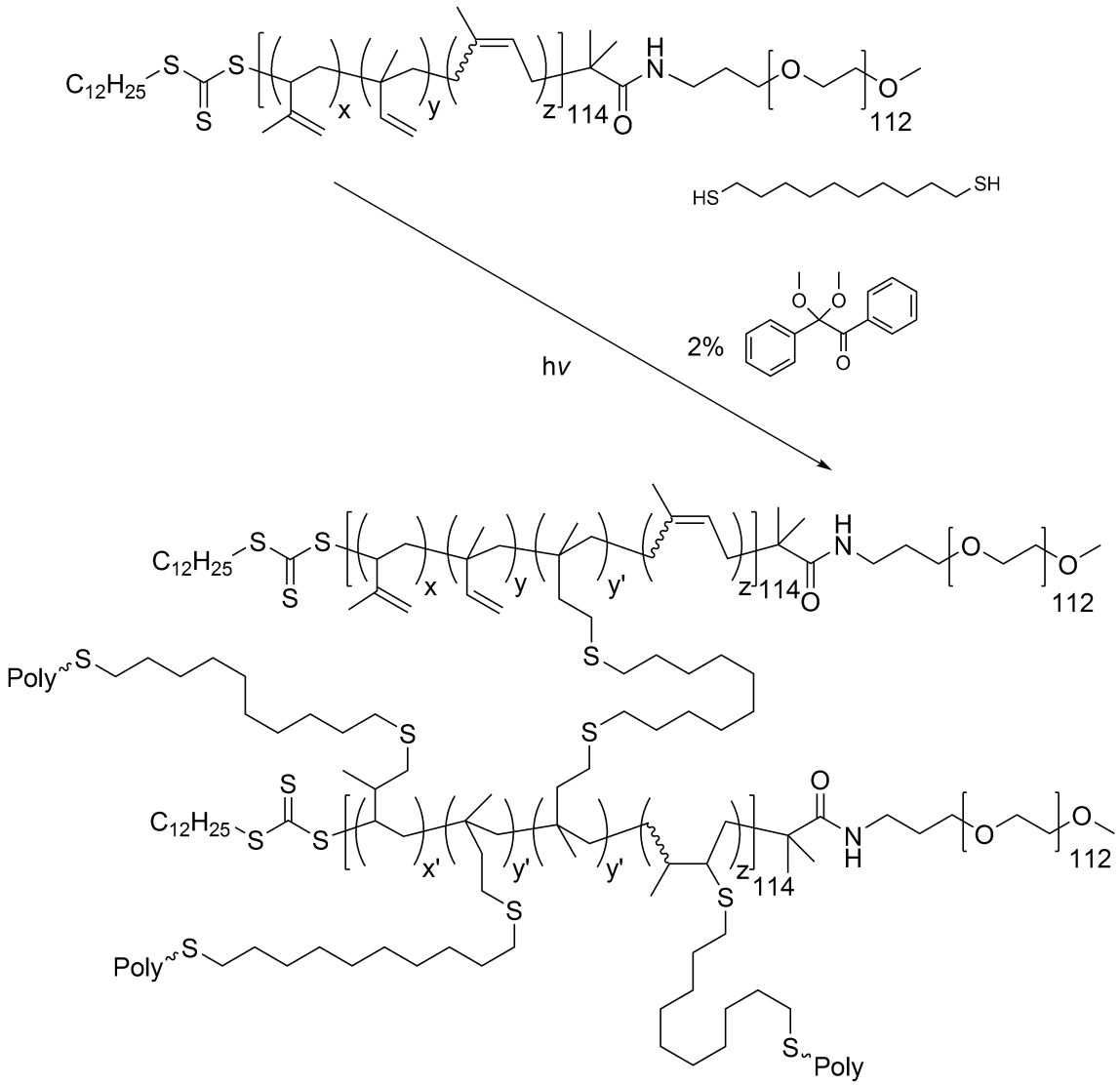


**Scheme 4-4.** PEO-*b*-PIp UV-promoted thiol-ene crosslinking with 1,10 decanedithiol.

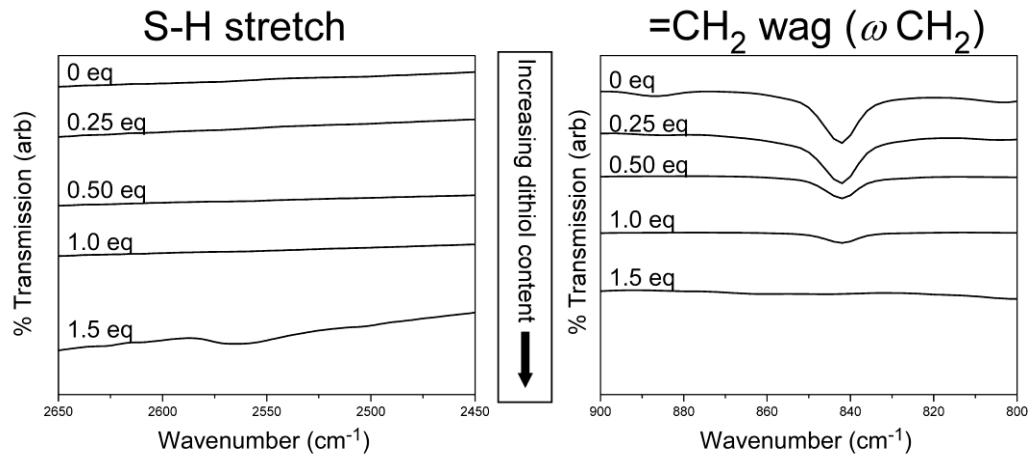


**Figure 4-15.** IR spectra of UV-promoted thiol-ene crosslinked PEO-*b*-PIp films at varying dithiol content. The specific bands highlighted are the S-H stretch at *ca.* 2500 $cm^{-1}$ and the $=CH_2$ wag at *ca.* 840 $cm^{-1}$

optically transparent across all dithiol concentrations, however upon wetting the films would take on an opaque character. The surfaces were interesting on a nanoscale, as probed by AFM (Figure 4-16) in both the dry and wet state. The PEO-*b*-PIp coatings (1.5

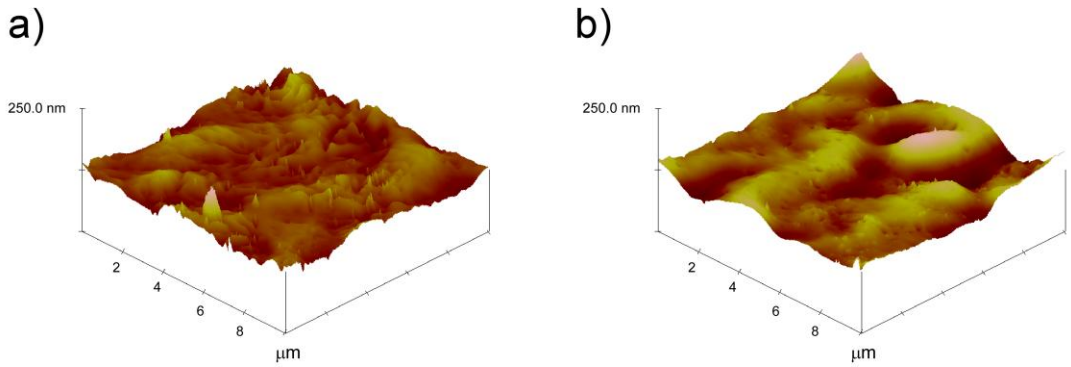


**Figure 4-16.** AFM images of PEO-*b*-PIp crosslinked films at 1.5 eq SH/alkene concentration of dithiol, both in dry state (a) and post-1 hr minute artificial seawater incubation (b).

eq SH/alkene crosslinked) were tested against four fluorescently tagged (Alexa-Fluor 488) biomolecules (0.8-1.3 tags/ biomolecule): Bovine Serum Albumin (BSA), Lipopolysaccharides from *E. coli* (LPSE) and *S. minnesota* (LPSS), and Lectin from *C. Fragile* (CFL). The images were analyzed using Image J software and the histograms were transformed into percent fluorescence values (see Figure 4-17). Because there was

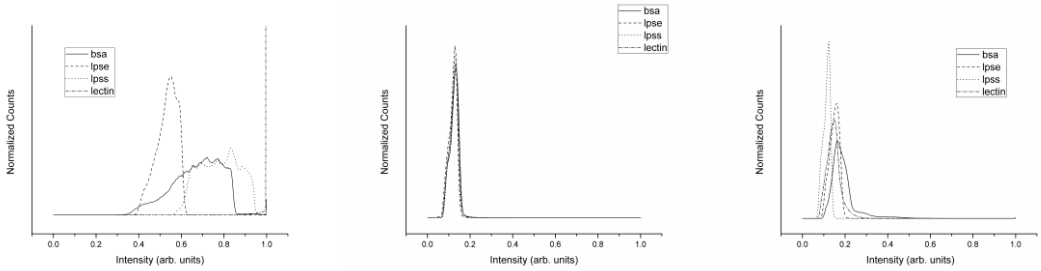


**Figure 4-17.** Fluorescence histograms of the (left) glass control sample, (center) Intersleek control and (right) PEO-*b*-PIp thiol-ene crosslinked surface.

approximately 1 tag/biomolecule, quantitative correlation between fluorescence and the number of biomolecules adsorbed onto surfaces could be quantified and compared. Results demonstrated that the test coatings performed comparably to a commercial example (Intersleek 900) and much better than glass controls (see Figure 4-18), a finding which could show potential for marine anti-fouling ability.

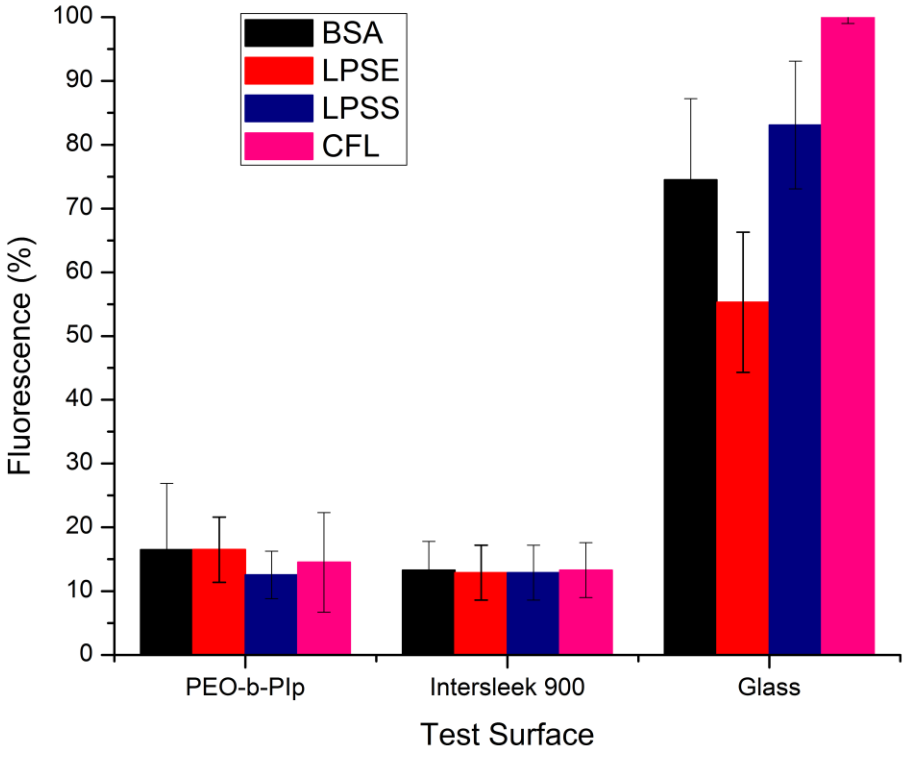


**Figure 4-18.** Fluorescence of various tagged-biomolecules on PEO-*b*-PIp thiol-ene crosslinked surface versus Intersleek 900 and glass controls.

## Conclusions

Highly interesting, multi-functional, amphiphilic PEO-*b*-PIp block copolymers were prepared *via* RAFT polymerization, for which challenges were encountered, yet well-defined structures were obtained. In this study, two RAFT-capable PEO macro-CTAs, having $M_n$ values of 2 and 5 kDa, were prepared and used for the polymerization of isoprene, affording block copolymers of varied lengths and compositions. GPC analysis of the PEO macro-CTAs and block copolymers showed remaining unreacted PEO macro-CTA. Following analysis of the GPC chromatograms using mathematical deconvolution,

the blocking efficiency was estimated to be around 50% for the 5 kDa PEO macro-CTA and 64% for the 2 kDa CTA. The resultant polymers were also investigated for their abilities to self assemble in both water and decane, and the resulting regular and inverse assemblies, respectively, were analyzed with DLS, AFM, and TEM to ascertain their dimensions and properties. Assembly of PEO-*b*-PIp block copolymers in aqueous solution resulted in uniform micelles of varying sizes while the assembly in hydrophobic, organic solvent resulted in the formation of heterogeneous morphologies, including large aggregates, cylindrical and spherical structures. Thiol-ene crosslinked films of PEO-*b*-PIp showed promise against fouling biomacromolecules in the form of fluorescently-tagged proteins, lipopolysaccarhides and lectin.

In an attempt to duplicate the success of this polymer system, an alternative hydrophilic polymer, poly(*N*-vinylpyrrolidinone) (PNVP), was substituted in the place of PEO as can be seen in Chapter 4. This new polymer, PNVP-*b*-PIp, has advantages over PEO-*b*-PIp in that the lactam of PNVP is highly chemically and oxidatively resistant (compared to PEO, which is oxidatively susceptible). The polymer was crosslinked using a different methodology, involving vulcanization using sulfur monochloride, leading to interesting films that were investigated using advanced surface characterization techniques such as XPS and IRIR imaging.

**Acknowledgements.**

This material is based on work supported by the Office of Naval Research under grant number N00014-08-1-0398, the National Science Foundation grant numbers DMR-0451490 and DMR-0906815, and the National Heart Lung and Blood Institute of the

National Institutes of Health as a Program of Excellence in Nanotechnology grant number HL080729.

**References.**

(1) Blanazs, A.; Armes, S. P.; Ryan, A. J. (2009) Self-Assembled Block Copolymer Aggregates: From Micelles to Vesicles and their Biological Applications. *Macromol. Rapid Commun. 30*(4-5), 267-277.

(2) Hamley, I. W. (2003) Nanostructure fabrication using block copolymers. *Nanotechnology 14*(10), R39-R54.

(3) Letchford, K.; Burt, H. (2007) A review of the formation and classification of amphiphilic block copolymer nanoparticulate structures: micelles, nanospheres, nanocapsules and polymersomes. *European Journal of Pharmaceutics and Biopharmaceutics 65*(3), 259-269.

(4) Pochan, D. J.; Chen, Z. Y.; Cui, H. G.; Hales, K.; Qi, K.; Wooley, K. L. (2004) Toroidal triblock copolymer assemblies. *Science 306*(5693), 94-97.

(5) Li, Z. B.; Kesselman, E.; Talmon, Y.; Hillmyer, M. A.; Lodge, T. P. (2004) Multicompartment micelles from ABC miktoarm stars in water. *Science 306*(5693), 98-101.

(6) Jain, S.; Bates, F. S. (2003) On the origins of morphological complexity in block copolymer surfactants. *Science 300*, 460-464.

(7) Discher, D. E.; Eisenberg, A. (2002) Polymer vesicles. *Science 297*(5583), 967-973.

(8) Zhao, F.; Xie, D. H.; Zhang, G. Z.; Pispas, S. (2008) Thermoresponsive complex amphiphilic block copolymer micelles investigated by laser light scattering. *J. Phys. Chem. B 112*(20), 6358-6362.

(9) Sundararaman, A.; Stephan, T.; Grubbs, R. B. (2008) Reversible restructuring of aqueous block copolymer assemblies through stimulus-induced changes in amphiphilicity. *J. Am. Chem. Soc. 130*(37), 12264-12265.

(10) Allen, C.; Maysinger, D.; Eisenberg, A. (1999) Nano-engineering block copolymer aggregates for drug delivery. *Colloids Surf., B 16*(1-4), 3-27.

(11) O'Reilly, R. K.; Joralemon, M. J.; Hawker, C. J.; Wooley, K. L. (2006) Facile syntheses of surface-functionalized micelles and shell cross-linked nanoparticles. *J. Polym. Sci., Part A: Polym. Chem. 44*(17), 5203-5217.

(12) Bütün, V.; Billingham, N. C.; Armes, S. P. (1998) Synthesis of shell cross-linked micelles with tunable hydrophilic/hydrophobic cores. *J. Am. Chem. Soc. 120*(46), 12135-12136.

(13) Iijima, M.; Nagasaki, Y.; Okada, T.; Kato, M.; Kataoka, K. (1999) Core-polymerized reactive micelles from heterotelechelic amphiphilic block copolymers. *Macromolecules 32*(4), 1140-1146.

(14) Simone, E. A.; Dziubla, T. D.; Muzykantov, V. R. (2008) Polymeric carriers: role of geometry in drug delivery. *Expert Opin. Drug Deliv. 5*(12), 1283-1300.

(15) Branco, M. C.; Schneider, J. P. (2009) Self-assembling materials for therapeutic delivery. *Acta Biomaterialia 5*(3), 817-831.

(16) Kim, B. S.; Park, S. W.; Hammond, P. T. (2008) Hydrogen-bonding layer-by-layer assembled biodegradable polymeric micelles as drug delivery vehicles from surfaces. *ACS Nano 2*(2), 386-392.

(17) Krishnan, R. S.; Mackay, M. E.; Duxbury, P. M.; Pastor, A.; Hawker, C. J.; Van Horn, B.; Asokan, S.; Wong, M. S. (2007) Self-assembled multilayers of nanocomponents. *Nano Lett. 7*(2), 484-489.

(18) Lazzari, M.; Lopez-Quintela, M. A. (2003) Block copolymers as a tool for nanomaterial fabrication. *Adv. Mater. 15*(19), 1583-1594.

(19) Mitragotri, S.; Lahann, J. (2009) Physical approaches to biomaterial design. *Nature Materials 8*(1), 15-23.

(20) Förster, S.; Antonietti, M. (1998) Amphiphilic block copolymers in structure-controlled nanomaterial hybrids. *Adv. Mater. 10*(3), 195-217.

(21) Soo, P. L.; Eisenberg, A. (2004) Preparation of block copolymer vesicles in solution. *J. Polym. Sci., Part B: Polym. Phys. 42*(6Journal of Polymer Science Part A: Polymer Chemistry), 923-938.

(22) Zhang, L. F.; Eisenberg, A. (1996) Multiple morphologies and characteristics of "crew-cut" micelle-like aggregates of polystyrene-b-poly(acrylic acid) diblock copolymers in aqueous solutions. *J. Am. Chem. Soc. 118*(13), 3168-3181.

(23) Gan, Z. H.; Jim, T. F.; Li, M.; Yuer, Z.; Wang, S. G.; Wu, C. (1999) Enzymatic biodegradation of poly(ethylene oxide-b-epsilon-caprolactone) diblock copolymer and its potential biomedical applications. *Macromolecules 32*(3), 590-594.

(24) Shuai, X. T.; Merdan, T.; Schaper, A. K.; Xi, F.; Kissel, T. (2004) Core-cross-linked polymeric micelles as paclitaxel carriers. *Bioconjugate Chem. 15*(3), 441-448.

(25) dos Santos, A. M.; Le Bris, T.; Graillat, C.; D'Agosto, F.; Lansalot, M. (2009) Use of a Poly(ethylene oxide) MacroRAFT Agent as Both a Stabilizer and a

Control Agent in Styrene Polymerization in Aqueous Dispersed System. *Macromolecules 42*(4), 946-956.

(26) Jia, Z. F.; Xu, X. W.; Fu, Q.; Huang, J. L. (2006) Synthesis and self-assembly morphologies of amphiphilic multiblock copolymers [poly(ethylene oxide)b-polystyrene](n) via trithiocarbonate-embedded PEO macro-RAFT agent. *J. Polym. Sci., Part A: Polym. Chem. 44*(20), 6071-6082.

(27) Sun, G.; Hagooly, A.; Xu, J.; Nystrom, A. M.; Li, Z. C.; Rossin, R.; Moore, D. A.; Wooley, K. L.; Welch, M. J. (2008) Facile, efficient approach to accomplish tunable chemistries and variable biodistributions for shell cross-linked nanoparticles. *Biomacromolecules 9*(7), 1997-2006.

(28) Geng, Y.; Dalhaimer, P.; Cai, S. S.; Tsai, R.; Tewari, M.; Minko, T.; Discher, D. E. (2007) Shape effects of filaments versus spherical particles in flow and drug delivery. *Nature Nanotechnology 2*(4), 249-255.

(29) Sun, G.; Fang, H. F.; Cheng, C.; Lu, P.; Zhang, K.; Walker, A. V.; Taylor, J. S. A.; Wooley, K. L. (2009) Benzaldehyde-Functionalized Polymer Vesicles. *ACS Nano 3*(3), 673-681.

(30) Rosler, A.; Vandermeulen, G. W. M.; Klok, H. A. (2001) Advanced drug delivery devices via self-assembly of amphiphilic block copolymers. *Advanced Drug Delivery Reviews 53*(1), 95-108.

(31) Kohut, A.; Voronov, A.; Samaryk, V.; Peukert, W. (2007) Amphiphilic invertible polyesters as reducing and stabilizing agents in the formation of metal nanoparticles. *Macromol. Rapid Commun. 28*(13), 1410-1414.

(32) McCormick, C. L.; Sumerlin, B. S.; Lokitz, B. S.; Stempka, J. E. (2008) RAFT-synthesized diblock and triblock copolymers: thermally-induced supramolecular assembly in aqueous media. *Soft Matter 4*(9), 1760-1773.

(33) Matyjaszewski, K.; Xia, J. H. (2001) Atom transfer radical polymerization. *Chem. Rev. 101*(9), 2921-2990.

(34) Moad, G.; Rizzardo, E.; Thang, S. H. (2005) Living radical polymerization by the RAFT process. *Aust. J. Chem. 58*(6), 379-410.

(35) Kamigaito, M.; Ando, T.; Sawamoto, M. (2001) Metal-catalyzed living radical polymerization. *Chem. Rev. 101*(12), 3689-3745.

(36) Hawker, C. J.; Bosman, A. W.; Harth, E. (2001) New polymer synthesis by nitroxide mediated living radical polymerizations. *Chem. Rev. 101*(12), 3661-3688.

(37) Evans, A. C.; Skey, J.; Wright, M.; Qu, W. J.; Ondeck, C.; Longbottom, D. A.; O'Reilly, R. K. (2009) Functional and Tuneable Amino Acid Polymers Prepared by RAFT Polymerization. *J. Polym. Sci., Part A: Polym. Chem. 47*(24), 6814-6826.

(38) Schumers, J. M.; Fustin, C. A.; Can, A.; Hoogenboom, R.; Schubert, U. S.; Gohy, J. F. (2009) Are o-Nitrobenzyl (Meth)acrylate Monomers Polymerizable by Controlled-Radical Polymerization? *J. Polym. Sci., Part A: Polym. Chem. 47*(23), 6504-6513.

(39) Zhu, J. T.; Hayward, R. C. (2008) Spontaneous generation of amphiphilic block copolymer micelles with multiple morphologies through interfacial instabilities. *J. Am. Chem. Soc. 130*(23), 7496-7502.

(40) Won, Y. Y.; Davis, H. T.; Bates, F. S. (1999) Giant wormlike rubber micelles. *Science 283*(5404), 960-963.

(41) Mihut, A. M.; Chiche, A.; Drechsler, M.; Schmalz, H.; Di Cola, E.; Krausch, G.; Ballauff, M. (2009) Crystallization-induced switching of the morphology of poly(ethylene oxide)-block-polybutadiene micelles. *Soft Matter 5*(1), 208-213.

(42) Mueller, W.; Koynov, K.; Fischer, K.; Hartmann, S.; Pierrat, S.; Basche, T.; Maskos, M. (2009) Hydrophobic Shell Loading of PB-b-PEO Vesicles. *Macromolecules 42*(1), 357-361.

(43) Allgaier, J.; Poppe, A.; Willner, L.; Richter, D. (1997) Synthesis and characterization of poly[1,4-isoprene-b-(ethylene oxide)] and poly[ethylene-co-propylene-b-(ethylene oxide)] block copolymers. *Macromolecules 30*(6), 1582-1586.

(44) Wegrzyn, J. K.; Stephan, T.; Lau, R.; Grubbs, R. B. (2005) Preparation of poly(ethylene oxide)-block-poly(isoprene) by nitroxide-mediated free radical polymerization from PEO macroinitiators. *J. Polym. Sci., Part A: Polym. Chem. 43*(14), 2977-2984.

(45) Glynos, E.; Pispas, S.; Koutsos, V. (2008) Amphiphilic diblock copolymers on mica: Formation of flat polymer nanoislands and evolution to protruding surface micelles. *Macromolecules 41*(12), 4313-4320.

(46) Gournis, D.; Floudas, G. (2004) "Hairy" Plates: Poly(ethylene oxide)-b-polyisoprene Copolymers in the Presence of Laponite Clay. *Chem. Mater. 16*(9), 1686-1692.

(47) Förster, S.; Kramer, E. (1999) Synthesis of PB−PEO and PI−PEO Block Copolymers with Alkyllithium Initiators and the Phosphazene Base t-BuP4. *Macromolecules 32*(8), 2783-2785.

(48) Benoit, D.; Harth, E.; Fox, P.; Waymouth, R. M.; Hawker, C. J. (2000) Accurate structural control and block formation in the living polymerization of 1,3-dienes by nitroxide-mediated procedures. *Macromolecules 33*(2), 363-370.

(49) Ruehl, J.; Nilsen, A.; Born, S.; Thoniyot, P.; Xu, L. P.; Chen, S. W.; Braslau, R. (2007) Nitroxide-mediated polymerization to form symmetrical ABA triblock copolymers from a bidirectional alkoxyamine initiator. *Polymer 48*(9), 2564-2571.

(50) Pispas, S.; Sarantopoulou, E. (2007) Self-Assembly in Mixed Aqueous Solutions of Amphiphilic Block Copolymers and Vesicle-Forming Surfactant. *Langmuir 23*(14), 7484-7490.

(51) Messe, L.; Corvazier, L.; Young, R. N.; Ryan, A. J. (2002) Phase Behavior of a Poly(ethylene oxide)-block- Poly(isoprene) Copolymer in Aqueous Solutions: From Liquid to Solid State. *Langmuir 18*(7), 2564-2570.

(52) Germack, D. S.; Harrisson, S.; Brown, G. O.; Wooley, K. L. (2006) Influence of the structure of nanoscopic building blocks on the assembly of micropatterned surfaces. *J. Polym. Sci., Part A: Polym. Chem. 44*(17), 5218-5228.

(53) Germack, D. S.; Wooley, K. L. (2007) Isoprene polymerization via reversible addition fragmentation chain transfer polymerization. *J. Polym. Sci., Part A: Polym. Chem. 45*(17), 4100-4108.

(54) Jitchum, V.; Perrier, S. (2007) Living radical polymerization of isoprene via the RAFT process. *Macromolecules 40*(5), 1408-1412.

(55) Germack, D. S.; Wooley, K. L. (2007) RAFT-based synthesis and characterization of ABC versus ACB triblock copolymers containing tert-butyl acrylate, isoprene, and styrene blocks(a). *Macromol. Chem. Phys. 208*(23), 2481-2491.

(56) Achilleos, M.; Legge, T. M.; Perrier, S.; Patrickios, C. S. (2008) Poly(ethylene glycol)-Based Amphiphilic Model Conetworks: Synthesis by RAFT Polymerization and Characterization. *J. Polym. Sci., Part A: Polym. Chem. 46*(22), 7556-7565.

(57) Li, Y. T.; Lokitz, B. S.; McCormick, C. L. (2006) RAFT synthesis of a thermally responsive ABC triblock copolymer incorporating N-acryloxysuccinimide for facile in situ formation of shell cross-linked micelles in aqueous media. *Macromolecules 39*(1), 81-89.

(58) Peng, Z. P.; Wang, D.; Liu, X. X.; Tong, Z. (2007) RAFT synthesis of a water-soluble triblock copolymer of poly(styrenesulfonate)-b-poly(ethylene glycol)-b-poly(styrenesulfonate) using a macromolecular chain transfer agent in aqueous solution. *J. Polym. Sci., Part A: Polym. Chem. 45*(16), 3698-3706.

(59) Walther, A.; Millard, P. E.; Goldmann, A. S.; Lovestead, T. M.; Schacher, F.; Barner-Kowollik, C.; Muller, A. H. E. (2008) Bis-Hydrophilic Block Terpolymers via RAFT Polymerization: Toward Dynamic Micelles with Tunable Corona Properties. *Macromolecules 41*(22), 8608-8619.

(60) Yan, J. J.; Ji, W. X.; Chen, E. Q.; Li, Z. C.; Liang, D. H. (2008) Association and aggregation behavior of poly(ethylene oxide)-b-poly (N-isopropylacrylamide) in aqueous solution. *Macromolecules 41*(13), 4908-4913.

(61) Yusa, S.; Yokoyama, Y.; Morishima, Y. (2009) Synthesis of Oppositely Charged Block Copolymers of Poly(ethylene glycol) via Reversible Addition-Fragmentation Chain Transfer Radical Polymerization and Characterization of Their Polyion Complex Micelles in Water. *Macromolecules 42*(1), 376-383.

(62) Skrabania, K.; Laschewsky, A.; von Berlepsch, H.; Boettcher, C. (2009) Synthesis and Micellar Self-Assembly of Ternary Hydrophilic-Lipophilic-Fluorophilic Block Copolymers with a Linear PEO Chain. *Langmuir 25*(13), 7594-7601.

(63) Xu, X. W.; Smith, A. E.; Kirkland, S. E.; McCormick, C. L. (2008) Aqueous RAFT Synthesis of pH-Responsive Triblock Copolymer mPEO-PAPMA-PDPAEMA and Formation of Shell Cross-Linked Micelles. *Macromolecules 41*(22), 8429-8435.

(64) Jia, Z. F.; Liu, C.; Huang, J. L. (2006) Synthesis of (ABCB)(n) type ternary amphiphilic multiblock copolymer via poly(ethylene oxide) macro-chain transfer agent. *Polymer 47*(22), 7615-7620.

(65) Lai, J. T. (2000) S,S'-bis-(a,a'-disubstituted-a"-acetic acid)-trithiocarbonates and derivatives as initiator-chain transfer agent-terminators for controlled radical polymerizations and their manufacture. *U.S. Patent 6 596 899*.

(66) Gao, H. F.; Tsarevsky, N. V.; Matyjaszewski, K. (2005) Synthesis of degradable miktoarm star copolymers via atom transfer radical polymerization. *Macromolecules 38*(14), 5995-6004.

(67) (2004) *Handbook of size exclusion chromatography and related techniques*. Second ed.; Marcel Decker, Inc. : New York.

# Chapter 4

## Amphiphilic Crosslinked Networks Produced From the Vulcanization of Nanodomains Within Thin Films of Poly(*N*-vinylpyrrolidinone)-*b*-Poly(isoprene)

[Portions of this work have been published previously as Jeremy W. Bartels, Peter L. Billings, Biswajit Ghosh, Marek W. Urban, C. Michael Greenlief, and Karen L. Wooley *Langmuir*, **2009**, 25(16), 9535–9544]

### ABSTRACT

Diblock copolymers of poly(*N*-vinylpyrrolidinone) (PNVP) and poly(isoprene) (PIp) were employed as building blocks for the construction of complex crosslinked networks that present surfaces having amphiphilic character, imparted by covalent trapping of compositionally heterogeneous phase-separated morphologies. The kinetics for the homopolymerization of N-vinylpyrrolidinone by RAFT techniques was studied, and the initially obtained PNVP-based macro-RAFT agents were then extended to PNVP-b-PIp block copolymers. Therefore, the PNVP chain length was held constant at a number-averaged degree of polymerization of 120, while the PIp chain length was varied to afford a series of three $PNVP_{120}$-*b*-$PIp_x$ block copolymers (where x = 710, 53 and 25). These materials were then crosslinked individually using sulfur monochloride, to produce complex amphiphilic networks. The nanoscopically-resolved topographies of these films

were analyzed using atomic force microscopy, and their compositional heterogeneities were probed by X-ray photoelectron spectroscopy and internal reflectance infrared imaging techniques. Additionally, the surfaces were analyzed to determine the extent of surface reorganization under aqueous conditions.

## Introduction

Recent work in non-toxic fouling release or anti-fouling coatings has demonstrated that a wide array of properties can influence anti-biofouling ability. Properties such as surface roughness,(1-3) topography,(4) free energy,(5, 6) polymer composition,(7-9) and the mechanical properties of the bulk substrate(10) all play large roles in inhibiting or promoting adhesion of biomacromolecules and, thereby, whole organisms, onto substrates.(11) An interesting switching behavior between hydrophobicity and hydrophilicity can be generated for responsive nanocomposite surfaces,(12) whereas we have focused on coincident combinations of hydrophobic and hydrophilic components in complex networks. Surfaces made from amphiphilic crosslinked networks of poly(ethylene glycol) (PEG) and hyperbranched fluoropolymers(13-17) or linear block fluorocopolymers containing PEG-based segments,(7, 8, 18-20) have demonstrated excellent anti-fouling ability. Polymers composed of polydimethylsiloxane (PDMS),(9, 10, 21) hybrid xerogels,(22) and zwitterionic block copolymers(23-25) undergo self-cleaning in water. Interestingly, lithographically micropatterned PDMS surfaces further inhibit fouling organisms from attaching to surfaces,(2, 26) indicating that surface features are as important as composition in developing anti-biofouling coatings. Therefore, the key message has been that high degrees of complexity are needed to combat the various mechanisms that fouling organisms rely upon for adhesion to substrates.

Previous work in our lab has shown that hyperbranched fluoropolymers crosslinked with polyethylene glycol (HBFP-PEG) form phase-segregated domains on the nano- and microscales.(13-17, 27) The formation of an amphiphilically-, morphologically- and

topographically-complex surface environment as a result of the phase segregation is believed to be responsible for inhibiting biomacromolecule adsorption and adhesion of *Ulva* algae spores.(21, 28, 29) Despite HBFP-PEG's excellent ability to resist adhesion, the fluorinated polymer domain is relatively expensive and difficult to produce, and has unknown toxicity or bioaccumulation data, similar to most fluoropolymers currently being researched in this area. PEG, while relatively cheap and available, is known to undergo oxidative degradation,(30) which would be problematic in the highly oxygenated marine environment over prolonged periods of time. Our most recent interest has been in the duplication of the successes of the amphiphilic HBFP-PEG system, both in anti-biofouling ability and interesting mechanical(31),(32) and other related properties,(33) while exploring the importance of the particular hydrophobic and hydrophilic polymer compositions, expanding the types of materials that can achieve similar degrees of surface complexities, and doing so by using common, commercially-available components.

This strategy involved the synthesis of a non-fluorinated, non-PEGylated analog of the HBFP-PEG system that was expected to exhibit similar surface topography and compositional heterogeneity. In addition to replacing the compositions of the polymer components, our new design replaces the combination of hyperbranched and linear architectures with two linear structures and, moreover, preconnects those two units into a block copolymer precursor, providing an amphiphilic block polymer coating that is inexpensive and mechanically tough with potential anti-biofouling character. It was hypothesized that the non-ionic polar polymer, poly(*N*-vinylpyrrolidinone) (PNVP), would work as a durable replacement for the hydrophilic PEG of the original system,(34-

36) and that the hydrophobic polymer polyisoprene (PIp) could be used as a low surface energy, potentially multi-crosslinkable analog of HBFP.(37) In the HBFP-PEG system, two homopolymers were blended together and crosslinked during their phase segregation, driven by differences in composition and macromolecular topology. The highly branched architecture of the HBFP, which provided large numbers of chemically reactive chain ends, allowed for rapid, kinetic trapping of the phase segregation events before equilibrium was reached. The new design differs not only in the chemical compositions (PIp for HBFP and PNVP for PEG), but also in the macromolecular architecture. Rather than working with two homopolymers, we chose to employ a block copolymer, which restricts the degree of phase segregation by covalently pre-attaching the two incompatible hydrophobic and hydrophilic polymer chains.

A major synthetic challenge, then, was faced, in the need to prepare the block copolymer structure comprised of PNVP and PIp chain segments. The reactivities of NVP and Ip differ substantially, and monomer reactivity and choice of polymerization methodology both play roles in the ability to achieve well-controlled polymerizations and afford well-defined block copolymers. NVP has been reported to be polymerized in a controlled radical method by reversible addition-fragmentation chain transfer (RAFT) polymerization using as a chain transfer agent, a xanthate,(34, 35) a dithiocarbamate,(38) or, in one instance involving copolymerization with acrylates, a trithiocarbonate.(39) Controlled radical polymerization of isoprene was initially reported using nitroxide mediated polymerization,(40-42) and also recently has been reported to be performed with RAFT, specifically with trithiocarbonate chain transfer agents.(43-45) Since control of both blocks with any one RAFT agent is not yet possible, the decision was made to use

a trithiocarbonate, as this functionality is known to afford good control for the polymerization of isoprene and to offer a reasonable level of control for the polymerization of NVP. This single RAFT agent was selected as a compromise.

The final amphiphilic block copolymers were then investigated as micro- and nanoscopically-resolved amphiphilic crosslinked networks. Coincident with the phase-segregation process, crosslinking was performed by vulcanization methods using sulfur monochloride, previously reported for PIp block copolymers(37) and other block copolymer-containing polydienes.(46) The existence of micro- and nano-domains enriched in each of the components of PNVP or PIp and their ability to undergo dynamic reorganization upon swelling with water were confirmed using X-ray photoelectron spectroscopy (XPS), internal reflectance infrared imaging (IRIRI) spectroscopy, and atomic force microscopy (AFM).

## Experimental

**Instrumentation.** Infrared spectra were obtained on a Perkin–Elmer Spectrum BX FTIR system as neat films on NaCl plates. $^{1}$H NMR (300 and 500 MHz) and $^{13}$C-NMR (75 and 125 MHz) spectra were recorded on either a Varian Mercury 300 MHz or Inova 500 MHz spectrometer using the solvent as internal reference. Tetrahydrofuran-based gel permeation chromatography (GPC(THF)) was conducted on a Waters Chromatography, Inc. (Milford, MA) model 1515, equipped with a Waters model 5414 differential refractometer, a Precision Detectors, Inc. (Bellingham, MA) model PD-2026 dual-angle (15 º and 90 º) light scattering detector and a three-column set of Polymer Laboratories, Inc. (Amherst, MA) gel mixed-bed styrene-divinylbenzene columns ($PL_{gel}$ 5$\mu$m Mixed C,

500 Å, and $10^4$ Å, 300 x 7.5 mm columns). The system was equilibrated at 35 ºC in THF, which served as the polymer solvent and eluent (flow rate set to 1.00 mL/min). Polymer solutions were prepared at a known concentration (*ca*. 3 mg/mL) and an injection volume of 200 $\mu$L was used. Data collection was performed with Precision Detectors, Inc. Precision Acquire software. Data analysis was performed with Precision Detectors, Inc. Discovery 32 software. Inter-detector delay volume and the light scattering detector calibration constant were determined from a nearly monodisperse, linear polystyrene standard (Pressure Chemical Co., $M_p$ = 90,000 g/mol, $M_w/M_n$ < 1.04). The differential refractometer was calibrated with standard polystyrene material (SRM 706 NIST), of known refractive index increment dn/dc (0.184 mL/g). The dn/dc values of the analyzed polymers were then determined from the differential refractometer response. *N*,*N*-Dimethylformamide-based gel permeation chromatography (GPC(DMF)) was conducted on a Waters Chromatography, Inc. (Milford, MA) system equipped with an isocratic pump model 1515, a differential refractometer model 2414, and a two-column set of Styragel HR 4 and HR 4E 5 μm DMF 7.8 × 300 mm columns. The system was equilibrated at 70 °C in pre-filtered DMF containing 0.05 M LiBr, which served as polymer solvent and eluent (flow rate set to 1.00 mL/min). Polymer solutions were prepared at a concentration of *ca*. 3 mg/mL and an injection volume of 200 μL was used. Data collection and analysis was performed with Empower Pro software (Waters, Inc.). The system was calibrated with poly(ethylene glycol) standards (Polymer Laboratories, Amherst, MA) ranging from 615 to 442,800 Da.

Glass transition temperatures ($T_g$) were measured by differential scanning calorimetry on a Mettler-Toledo DSC822$^e$ (Mettler-Toledo, Inc., Columbus, OH), with a heating rate

of 10 ºC/min. Measurements were analyzed using Mettler-Toledo Star SW 7.01 software. The $T_g$ was taken as the midpoint of the inflection tangent, upon the third heating scan. Thermogravimetric analysis was performed under $N_2$ atmosphere using a Mettler-Toledo model TGA/SDTA851[e], with a heating rate of 5 ºC/min. Measurements were analyzed using Mettler-Toledo Star SW 7.01 software.

Tapping-mode AFM measurements were conducted in air with a Nanoscope III BioScope system (Digital Instruments, Santa Barbara, CA) operated under ambient conditions with standard silicon tips [type, OTEPSA-70; length (L), 160 μm; normal spring constant, 50 N/m; resonant frequency, 246–282 kHz]. Contact angles were measured as static contact angles with the sessile drop technique(47) with a Tantec CAM micro-contact-angle meter and the half-angle measuring method. Advancing and receding contact angles ($\theta_a$ and $\theta_r$) of 18 MΩ·cm$^{-1}$ nanopure water were measured on the films by placing a 2 uL drop on the surface, then increasing or decreasing the drop size by 1 uL, respectfully. The reported values are an average of five such measurements on different regions of the same sample. Hydrodynamic diameters ($D_h$) and size distributions for the micelles in aqueous solutions were determined by dynamic light scattering (DLS). Dynamic light scattering measurements were conducted with a Brookhaven Instruments, Co. (Holtsville, NY) DLS system equipped with a model BI-200SM goniometer, BI-9000AT digital correlator, and a model EMI-9865 photomultiplier, and a model Innova 300 (Coherent Inc., Santa Clara, CA), or a model 95-2 (Lexel, Corp.; Farmindale, NY) Ar ion laser operated at 514.5 nm. Measurements were made at 20 ± 1°C. Prior to analysis, solutions were filtered through a 0.22 $\mu$m Millex-GV PVDF membrane filter (Millipore Corp., Medford, MA) and then centrifuged in a model 5414 microfuge

(Brinkman Instruments, Inc., Westbury, NY) for 10 min to remove dust particles. Scattered light was collected at a fixed angle of 90°. The digital correlator was operated with 522 ratio spaced channels, an initial delay of 5 μs, a final delay of 100 ms, for a duration of 10 min. A photomultiplier aperture of 400 $\mu$m was used, and the incident laser intensity was adjusted to obtain a photon counting of between 200 and 300 kcps. Only measurements in which the measured and calculated baselines of the intensity autocorrelation function agreed to within 0.1% were used to calculate particle size. The calculations of the particle size distributions and distribution averages were performed with the ISDA software package (Brookhaven Instruments Company), which employed single-exponential fitting, cumulants analysis, non-negatively constrained least-squares (NNLS), and CONTIN particle size distribution analysis routines. All determinations were made in triplicate.

The XPS measurements for the PNVP, PIp, and crosslinked PNVP-*b*-PIp network coatings were collected to examine the compositions of the polymer surfaces before and after incubation in water. A VSW twin X-ray source was used in this study. X-ray photoelectron spectra were taken with Al $K_\alpha$ radiation (1486.7 eV), with the anode operating at 400 W, with a take-off angle of 42 degrees. A cylindrical mirror analyzer (model 15-255GAR, Physical Electronics, Inc.) was operated at a fixed pass energy of 25 eV. For each sample, O(1s), N(1s), C(1s), Cl(1s), and S(2p) core level spectra were collected, and nonlinear curve fitting software was used for data analysis. The spectra were fit to the sums of Lorentzian and Gaussian line shapes. Through peak fitting, the components associated with different surface bonded species in the spectra were identified. For studying the effect of the water treatment on the surface composition, the

samples were incubated in DI water, and this was followed by drying at room temperature *in vacuo* overnight. The shifts in the binding energies in the C(1s) region in each of the samples due to surface charging were corrected by all the C(1s) component peaks being referenced to the saturated C binding energy of 285.0 eV. All the samples were found to contain Si contaminants (2 – 8%) at the surface, and rinsing with THF before the experiments did not reduce the contamination level.

Internal reflection infrared (IRIR) images were obtained using a Bio-Rad FTS 7000 Stingray system equipped with internal reflection IR imaging (IRIRI) providing 1 $\mu m^2$ spatial resolution.(48) This system consists of a Bio-Rad FTS 7000 spectrometer, a Varian 600 UMA microscope, an Image IR focal plane array (FPA) image detector, and IRIRI. The IRIR images were collected using the following spectral acquisition parameters: under sampling ratio 2, rapid-scan speed 5 Hz, number of images per step 64, and spectral resolution 4 $cm^{-1}$. In a typical experiment, spectral data set acquisition time was 1 min and image processing was performed using ENVI software (The Environment for Visualizing Images, Research Systems, Inc.) version 3.5.(48)

**Materials.** Isoprene (Ip) (99 %), and *N*-vinylpyrrolidinone (NVP) (99 %) were obtained from Sigma-Aldrich, Inc. (St. Louis, MO) and were purified by passage over a column of neutral alumina prior to use. 1,4-dioxane (99%, Sigma-Aldrich), diethyl ether, (≥99 %, ACS Grade, anhydrous, Sigma-Aldrich), methanol (Chromasolv, ≥99.9%, Sigma-Aldrich), 1,4 dimethoxybenzene (99%, Sigma-Aldrich), *tert*-butyl peroxide (98%, Sigma-Aldrich), sulfur monochloride ($S_2Cl_2$, 98%, Sigma-Aldrich), and chloroform-*d* (Cambridge Isotope Labs) were used as received. Azobiscyanovaleric acid (ACVA, Sigma-Aldrich) was recrystallized from methanol and stored in a freezer prior to use.

Argon ultra-high purity grade gas (99.999%) was used as received from Praxair (St. Louis, MO). The RAFT agent, *S*-1-dodecyl-*S*'-(α,α'-dimethyl-α"-acetic acid)trithiocarbonate, **1**, was prepared as previously reported.(49, 50) Coralife® Scientific Grade Marine Salt that was used for the preparation of artificial seawater was mixed according to directions from the manufacturer. Due to the high volatility of isoprene and the high temperatures employed in the polymerization thereof, only thick-walled glass flasks, free of visible defects, were used for these experiments, each conducted with at least 50 % of the volume of the flask remaining free. As further precaution, all polymerizations were performed in a fume hood with additional shielding. Percent conversions of the isoprene polymerizations were determined using the method of Grubbs and co-workers,(42) where the molecular weight of the isolated polymer was determined with high field $^{1}$H-NMR spectroscopy (500 MHz) and then set equal to the theoretical molecular weight. While this method does introduce some error (assuming $M_n^{Theory} = M_n^{Actual}$), it is not excessive when compared with the error associated with attempting to determine conversion of isoprene directly.(37)

**Poly(N-vinyl pyrrolidinone) (2).** To a 50 mL Schlenk flask equipped with a Teflon-coated stir bar, was added chain transfer agent **1** (0.3282 g, 9.001 x $10^{-4}$ mol, 1 eq), NVP (20.0106 g, 0.1800 mol, 200 eq), ACVA (0.0253 g, 9.03 x $10^{-5}$ mol, 0.1 eq), and 1, 4-dimethoxybenzene (0.0385 g, 2.79 x $10^{-4}$, 0.3 eq). After adding 20.0 mL of 1, 4-dioxane, the flask was fitted with a rubber septum and the mixture was degassed *via* three freeze pump thaw cycles. After the final thaw, the flask was backfilled with argon and a 100 μL aliquot was removed for conversion analysis. Once the flask equilibrated to room temperature, it was immersed in an 80 °C oil bath under constant stirring for 24 h. At 24

h, a final aliquot was removed, for monomer conversion analysis, and the reaction was quickly quenched by submersion into liquid nitrogen. After thawing, the flask was temporarily evacuated to remove excess monomer and solvent. The resultant crude mass was re-dissolved in minimal dichloromethane and precipitated three times into diethyl ether, producing a fluffy white powder, which was dried *in vacuo* in a dessicator, yielding 8.1176 g (54 % yield based on a conversion of 75 %) of polymer. The polymer was maintained in a vacuum desiccator in order to prevent water accumulation. $M_n^{NMR}$ = 13700 Da, $M_w^{GPC(DMF)}$ = 28300 Da (poly(ethylene oxide) equivalent), $M_n^{GPC(DMF)}$ = 17600 Da (poly(ethylene oxide) equivalent), $M_w/M_n$ = 1.61. $T_g$ = 82.5 °C. TGA in $N_2$: 338-468 °C, 79% mass loss. IR = 3457, 2951, 1669, 1492, 1459, 1422, 1287, 924, 727, 643, 422 $cm^{-1}$. $^1$H NMR (500 MHz, chloroform-*d*, ppm): δ 4.1-3.4 (br, —C*H*-N-C(O)), 3.4–3.0 (br, —C*H*$_2$-N-C(O)), 2.5–2.1 (br, —N-C(O)-C*H*$_2$), 2.1-1.9 (br, —C*H*$_2$-CH$_2$-N-C(O)), 1.9-1.5 (br, —C*H*$_2$-CH-N-C(O)), 3.34 (br, multiplet —C(S)-S-C*H*$_2$-C$_{10}$H$_{20}$-CH$_3$), 1.5-1.2 (br, —C(S)-S-CH$_2$-C$_{10}$*H*$_{20}$-CH$_3$), 0.8-0.9 (br triplet, —C(S)-S-CH$_2$-C$_{10}$H$_{20}$-C*H*$_3$). $^{13}$C NMR (75 MHz, $CDCl_3$, ppm): δ 174.3, 43.7, 40.8, 33.7, 30.3, 21.4, 17.1, 12.9.

**General procedure for analysis of poly(*N*-vinylpyrrolidinone) polymerization kinetics**. To a 25 mL round bottom Schlenk flask equipped with a magnetic stir bar was charged chain transfer agent, **1**, (0.3034 g, 8.32 x $10^{-4}$ mol, 1.00 eq), *N*-vinylpyrrolidinone (7.6391 g, 6.87 x $10^{-2}$ mol, 83 eq), and ACVA (0.0224 g, 7.99 x $10^{-5}$ mol, 0.3 eq) and 1, 4-dimethoxybenzene (0.0349 g, 2.52 x $10^{-4}$ mol, 0.3 eq), along with 6.0 mL of 1, 4-dioxane. The mixture was then degassed by three freeze-pump-thaw cycles, after the third thaw cycle the flask was backfilled with argon and a small aliquot (*ca.* 100 μL) was removed for conversion analysis. The polymerization was initiated by

immersion in a temperature-regulated oil bath set to 80 °C. Aliquots (*ca.* 100 μL) were removed *via* gas-tight syringe at the following time points: 30, 60, 120, 180, 240, 300, and 360 minutes. Each aliquot was dissolved in 1 mL of chloroform-*d* and then placed into an NMR tube and immersed in an ice-water bath to quench further reaction. After 360 min the polymerization was quenched by immersion in liquid nitrogen and purified as previously mentioned (*vide supra*). The aliquots were then analyzed by $^{1}$H NMR spectroscopy to determine percent conversion.

**Preparation of Poly(*N*-vinylpyrrolidinone-*b*-polyisoprene) ($PNVP_{120}$-*b*-$PIp_{710}$) (3).** To a 25 mL reinforced-wall Schlenk flask equipped with a Teflon coated stir bar, was added macrotransfer agent **2** (1.0129 g, 7.60 x $10^{-5}$ mol, 1 eq), isoprene (8.3594 g, 0.1227 mol, 1600 eq), *tert*-butyl peroxide (0.0117 g, 8.00 x $10^{-5}$ mol, 0.95 eq), and 1, 4 dimethoxybenzene (0.0102 g, 7.38 x $10^{-5}$, 0.95 eq). After adding 10.0 mL of 1, 4-dioxane, a 100 μL aliquot was withdrawn and the flask was screwed tight with a Teflon stopcock, and the cloudy mixture was subjected to three freeze pump thaw cycles. After the final thaw, the flask was backfilled with argon and immersed in a 125 °C oil bath under constant stirring for 24 h. After *ca*. 1 hour reaction time, the flask contents became clear and homogeneous. At the 24 h mark, the reaction mixture was quickly quenched by submersion into liquid nitrogen, and upon thaw, a final aliquot was removed for monomer conversion analysis. After thawing, the flask was evacuated to remove excess monomer and solvent, then the resultant sticky mass was re-dissolved in minimal dichloromethane and precipitated three times into methanol, yielding a sticky white mass, which was collected and dried in a desiccator under vacuum, yielding 4.827 g of opaque tacky polymer (59 % yield based on a conversion of 44 %). $M_n^{NMR}$ = 62000 Da,

$M_w^{GPC(THF)}$ = 186000 Da (polystyrene equivalent), $M_n^{GPC(THF)}$ = 76100 Da (polystyrene equivalent), $M_w/M_n$ = 2.44. $(T_g)_{PIp}$ = -59.7 °C, $(T_g)_{PNVP}$ = 88.8 °C. TGA in $N_2$: 246-393 °C, 55% mass loss (PIp block); 393-473 °C, 38% mass loss (PNVP block). IR = 3419, 2961, 2922, 2853, 1671, 1440, 1376, 1288, 1002, 888, 841, 570, 420 $cm^{-1}$. $^1H$ NMR (500 MHz, chloroform-*d*, ppm): δ 5.8-5.6 (br, 1,2 —C*H*=$CH_2$), 5.3-5.1 (br, 4,1 —$CH_2$-C($CH_3$)-C*H*-$CH_2$-), 5.1-4.8 (br, 1,2 —CH=C$H_2$), 4.8-4.6 (br, 4,3 —C($CH_3$)-C$H_2$), 4.1-3.4 (br, —C*H*-N-C(O)), 3.4–3.0 (br, —C$H_2$-N-C(O)), 2.5–2.1 (br, —N-C(O)-C$H_2$), 2.1-1.7 (br, —C$H_2$-$CH_2$-N-C(O) and —C$H_2$ isoprene backbone), 1.7-1.5 (br, —C$H_2$-CH-N-C(O) and isoprene backbone —C$H_3$), 3.34 (br, multiplet —C(S)-S-C$H_2$-$C_{10}H_{20}$-$CH_3$), $^{13}C$-NMR (75 MHz, $CDCl_3$, ppm): δ 174.2, 146.1, 133.7, 123.4, 122.6, 109.7, 50.2, 43.3, 38.4, 36.8, 30.5, 26.8, 25.0, 21.9, 21.5, 17.0, 14.4. A film was cast of this polymer by drop deposition from $CH_2Cl_2$ onto a glass microscope slide followed by drying under ambient conditions for analysis by contact angle ($(\theta_{water})_{advancing}$ = 95 ± 1° and $(\theta_{water})_{receding}$ = 70 ± 6°) and AFM (rms roughness = 2 nm).

**Preparation of Poly(*N*-vinylpyrrolidinone-*b*-polyisoprene) ($PNVP_{120}$-*b*-$PIp_{53}$) (4).** Polymerization was carried out as outlined in experimental section for polymer **3**, where 5.0065 g macrotransfer agent **2** (3.85 x $10^{-4}$ mol, 1 eq), 25.6405 g isoprene (3.76 x $10^{-1}$ mol, 980 eq), and 0.0107 g *tert*-butyl peroxide (7.3 x $10^{-5}$ mol, 0.2 eq) were reacted together, yielding 8.809 g of a rough-textured slightly tacky polymer (**4**) (67 % yield based on a conversion of 6 %). $M_n^{NMR}$ = 17300 Da, $M_w^{GPC(THF)}$ = 226000 Da (polystyrene equivalent), $M_n^{GPC(THF)}$ = 77800 Da (polystyrene equivalent), $M_w/M_n$ = 2.903. $(T_g)_{PIp}$ = -58.8 °C, $(T_g)_{PNVP}$ = 84.9 °C. TGA in $N_2$: 312-392 °C, 21% mass loss (PIp block); 392-475 °C, 69% mass loss (PNVP block). IR = 3420, 2960, 2924, 2853,

1659, 1494, 1462, 1441, 1375, 1318, 1291, 911, 843, 736, 649, 470, 420 $cm^{-1}$. $^{1}H$ NMR (500 MHz, chloroform-*d*, ppm): δ 5.8-5.6 (br, 1,2 —C*H*=$CH_2$), 5.3-5.1 (br, 4,1 —$CH_2$-C($CH_3$)-C*H*-$CH_2$-), 5.1-4.8 (br, 1,2 —CH=C$H_2$), 4.8-4.6 (br, 4,3 —C($CH_3$)-C$H_2$), 4.1-3.4 (br, —C*H*-N-C(O)), 3.4–3.0 (br, —C$H_2$-N-C(O)), 2.5–2.1 (br, —N-C(O)-C$H_2$), 2.1-1.7 (br, —C$H_2$-$CH_2$-N-C(O) and —C$H_2$ isoprene backbone), 1.7-1.5 (br, —C$H_2$-CH-N-C(O) and isoprene backbone —C$H_3$), 3.34 (br, multiplet —C(S)-S-C$H_2$-$C_{10}H_{20}$-$CH_3$). $^{13}C$-NMR (75 MHz, $CDCl_3$, ppm): δ 170.4, 146.3, 133.8, 127.1, 123.6, 122.9, 109.9, 50.4, 43.2, 42.0, 38.3, 37.1, 33.3, 29.9, 26.9, 25.3, 22.1, 16.8, 14.6. A film was cast of this polymer by drop deposition from $CH_2Cl_2$ onto a glass microscope slide followed by drying under ambient conditions for analysis by contact angle ($(\theta_{water})_{advancing}$ = 81 ± 2° and $(\theta_{water})_{receding}$ = 61 ± 5°) and AFM (rms roughness = 5 nm).

**Preparation of Poly(*N*-vinylpyrrolidinone-*b*-polyisoprene) ($PNVP_{120}$-*b*-$PIp_{25}$) (5).** Polymerization was carried out in a manner similar to **3**, where 0.5016 g macrotransfer agent **2** ($3.78 \times 10^{-5}$ mol, 1 eq), 1.1538 g isoprene ($1.69 \times 10^{-2}$ mol, 450 eq), and 0.0027 g *tert*-butyl peroxide ($1.9 \times 10^{-5}$ mol, 0.5 eq) were reacted together, yielding 0.909 g of a tacky yellow powder polymer (80 % yield based on a conversion of 6 %). $M_n^{NMR}$ = 15400 Da, $M_w^{GPC(THF)}$ = 27900 Da (polystyrene equivalent), $M_n^{GPC(THF)}$ = 9000 Da (polystyrene equivalent), $M_w/M_n$ = 3.08. $(T_g)_{PIp}$ = -69.1 °C, $(T_g)_{PNVP}$ = 87.1 °C. TGA in $N_2$: 281-416 °C, 48% mass loss (PIp block); 416-476 °C, 41% mass loss (PNVP block). IR = 3417, 2961, 2925, 2133, 1651, 1495, 1463, 1445, 1376, 1293, 1173, 887, 649, 422 $cm^{-1}$. $^{1}H$ NMR (500 MHz, chloroform-*d*, ppm): δ 5.8-5.6 (br, 1,2 —C*H*=$CH_2$), 5.3-5.1 (br, 4,1 —$CH_2$-C($CH_3$)-C*H*-$CH_2$-), 5.1-4.8 (br, 1,2 —CH=C$H_2$), 4.8-4.6 (br, 4,3 —C($CH_3$)-C$H_2$), 4.1-3.4 (br, —C*H*-N-C(O)), 3.4–3.0 (br, —C$H_2$-N-C(O)), 2.5–2.1 (br, —

N-C(O)-C*H*$_2$), 2.1-1.7 (br, —C*H*$_2$-CH$_2$-N-C(O) and —C*H*$_2$ isoprene backbone), 1.7-1.5 (br, —C*H*$_2$-CH-N-C(O) and isoprene backbone —C*H*$_3$), 3.34 (br, multiplet —C(S)-S-C*H*$_2$-$C_{10}H_{20}$-$CH_3$), $^{13}$C-NMR (75 MHz, $CDCl_3$, ppm): δ175.5, 147.8, 135.3, 124.5, 111.5, 45.1, 42.0, 38.7, 32.2, 31.7, 28.5, 27.0, 23.7, 18.6, 16.3. A film was cast of this polymer by drop deposition from $CH_2Cl_2$ onto a glass microscope slide followed by drying under ambient conditions for analysis by contact angle ($(\theta_{water})_{advancing}$ = 107 ± 5° and $(\theta_{water})_{receding}$ = 73 ± 3°) and AFM (rms roughness = 36 nm).

**Procedure for producing crosslinked $PNVP_{120}$-*b*-$PIp_{710}$ *via* vulcanization with sulfur monochloride (6).**

In a 100 mL round bottom flask, $PNVP_{120}$-*b*-$PIp_{710}$ was dissolved in 50 mL dichloromethane under constant stirring at room temperature. A 1:1 mixture (v/v%) of sulfur monochloride and dichloromethane was slowly added dropwise to this flask, with 25 eq $S_2Cl_2$ per alkene to ensure complete crosslinking. The reaction mixture was left to stir overnight at room temperature. No significant aggregates or precipitates formed, but the solution turned a dark amber color after *ca.* 16 h reaction time. The solution was carefully drop-deposited onto pre-cleaned microscope slides. The evaporation of dichloromethane accelerated and completed crosslinking, leaving thin films with minimal bubbles or related defects, giving surface **6**. The slides were placed in a vacuum desiccator for 24 h in order to remove excess solvent and sulfur monochloride. In order to remove any unreacted sulfur monochloride and related small molecule sulfur byproducts, the slides were soaked in a benzene solution for 30 min, washed with dichloromethane, and placed in a vacuum desiccator for an additional 6 h. The films adhered strongly to glass, and did not delaminate, swell, or dissolve when exposed to a

wide variety of solvents. The film surfaces were analyzed with tapping-mode atomic force microscopy in order to ascertain topography and roughness. In addition to examining dry films, water-swollen films were analyzed by swelling the film slides in artificial seawater for one hour, removal of excess water by wicking with a Kimwipe, and AFM analysis was immediately performed thereafter on the surface. $(\theta_{water})_{advancing}$ = 96 ± 4° and $(\theta_{water})_{receding}$ = 75 ± 1°; $(\text{rms roughness})_{dry}$ = 86 nm and $(\text{rms roughness})_{wet}$ = 81 nm.

**Procedure for producing crosslinked $PNVP_{120}$-*b*-$PIp_{53}$ *via* vulcanization with sulfur monochloride (7).**

This sample was prepared in a similar manner as **6**, but with 29 eq $S_2Cl_2$ per alkene, giving surface **7**. The final film was stretchy and had a slight yellow color. $(\theta_{water})_{advancing}$ = 47 ± 10° and $(\theta_{water})_{receding}$ = 26 ± 5°; $(\text{rms roughness})_{dry}$ = 47 nm and $(\text{rms roughness})_{wet}$ = 43 nm.

**Procedure for producing crosslinked $PNVP_{120}$-*b*-$PIp_{25}$ *via* vulcanization with sulfur monochloride (8).**

This sample was prepared in a similar manner as **6**, but with 100 eq $S_2Cl_2$ per alkene, giving surface **8**. The final film was brittle and yellow. $(\theta_{water})_{advancing}$ = 57 ± 3° and $(\theta_{water})_{receding}$ = 41 ± 2°; $(\text{rms roughness})_{dry}$ = 76 nm and $(\text{rms roughness})_{wet}$ = 17 nm.

**Procedure for producing micelle 9, from $PNVP_{120}$-*b*-$PIp_{25}$.**

Polymer **5** (3.0 mg) was prepared as a 0.6 mg/mL THF solution inside a scintillation vial equipped with a rubber septum to prevent evaporation. To this solution, 10 mL of nanopure water was added slowly, over the course of 3 h under high stir. The resulting micelle solution was dialyzed (SpectraPor cellulose dialysis tubing having a MWCO = 6-

8 kDa) for two days against nanopure (18 MΩ·cm) water to remove THF, and based on final volume, the solution had a final concentration of approximately 0.3 mg/mL. DLS: $D_h$ (Intensity): 680 ± 120 nm, $D_h$ (Volume): 550 ± 80 nm, $D_h$ (Number): 290 ± 140 nm.

**Procedure for producing micelle 10, from $PNVP_{120}$-*b*-$PIp_{25}$.**

Additionally, polymer **5** (32.0 mg) was prepared as a 6.4 mg/mL THF solution inside a scintillation vial equipped with a rubber septum to prevent evaporation. To this solution, 5.0 mL of nanopure water was added slowly, over the course of 3 h under high stir. The resulting micelle solution was dialyzed (SpectraPor cellulose dialysis tubing having a MWCO = 6-8 kDa) for two days against nanopure (18 MΩ·cm) water to remove THF, and based on final volume, the solution had a final concentration of approximately 1.7 mg/mL. DLS: $D_h$ (Intensity): 430 ± 50 nm, $D_h$ (Volume): 490 ± 90 nm, $D_h$ (Number): 290 ± 130 nm.

**Results and Discussion**

Preparation of the amphiphilic block copolymers, $PNVP_{120}$-*b*-$PIp_n$, required conditions that would provide for controlled polymerization of the two monomers NVP and Ip, having significant differences in chemical reactivity and physical properties. Previous work in our lab on the RAFT-based polymerization and chain extension of isoprene involved the use of the trithiocarbonate, *S*-1-dodecyl-*S*'-(α,α'-dimethyl-α"-acetic acid) trithiocarbonate, DDMAT, **1**, initially reported by Lai in 2000.(49, 50) The trithiocarbonate unit does not decompose at the high temperature required for RAFT polymerization of isoprene,(43-45, 50) and it is compatible with a wide range of vinyl

monomers, from hydrophilic species like *N*-isopropylacrylamide,(51) to hydrophobic monomers such as isoprene.(44)

The synthetic approach began with the polymerization of NVP to generate $PNVP_{120}$, which then later served as a macroRAFT agent for the extension of Ip. RAFT polymerization of NVP was explored using **1** as the RAFT agent and azobiscyanovaleric acid, ACVA, as the initiator, under conditions that were similar to those employed by Gnanou(38) (80 ºC reaction temperature and 1,4-dioxane as solvent, Scheme 3-1). A small molecule, 1, 4-dimethoxybenzene, was added in small amounts as an internal standard for NMR spectroscopy to determine monomer conversion and evaluate the kinetics of the polymerization.

The kinetics of polymerization were established using $^1$H NMR spectroscopy analysis, showing linear $\ln[M_o]/[M]$ *vs*. time up to *ca*. 240 min, followed by a slight reduction in the rate of monomer consumption (Figure 3-1), as is observed typically during RAFT polymerization. A linear increase in $M_n$ *vs*. conversion was also observed, as further support of the controlled nature of this polymerization (Figure 3-2). The relatively slow kinetics are in contrast to the uncontrolled polymerization of NVP, using similar reaction conditions and stoichiometry but in the absence of CTA **1**, which results in a thick, viscous insoluble gel in less than one hour.

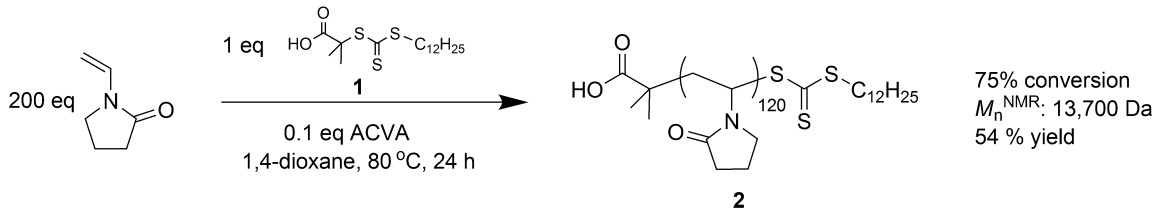


**2**

**Scheme 3-1**. RAFT polymerization of N-vinylpyrrolidinone, producing polymer **2**.

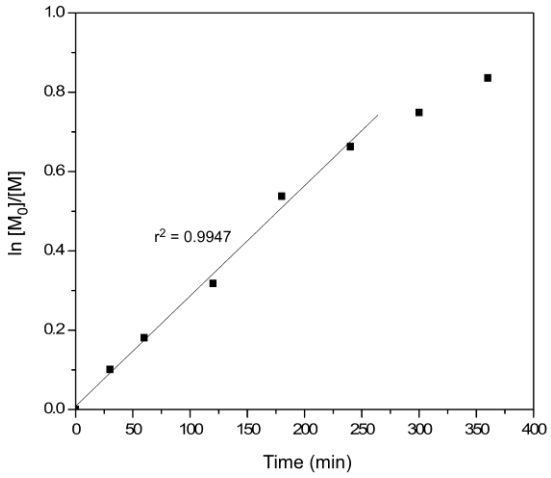


**Figure 3-1**. Pseudo first order kinetic plot of ln([$M_0$]/[M]) *vs*. time for the homopolymerization of NVP *via* RAFT.

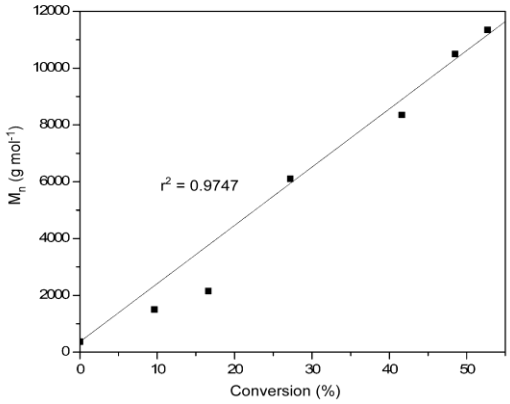


**Figure 3-2**. Molecular weight *vs*. conversion for homopolymerization of NVP *via* RAFT.

Although the polymer chain growth proceeded uniformly, GPC analysis showed that the polydispersity index (PDI) values were not ideal, *ca.* 1.6 (Figure 3-4). However, it should be noted that polydispersity was not a top priority for the preparation of polymer chains that would eventually become crosslinked networks, as the PDI of the hyperbranched fluoropolymer networks, which serve as the inspiration for this work, were based upon polymer precursors with PDI's >2.5. Recent reports from Klumperman have shown that numerous side reactions and chain terminations are possible for the polymerization of NVP, which may offer insight regarding the non-ideal GPC traces of the PNVP .(52) Of interest was the construction of PNVP having sufficient chain length and retention of the trithiocarbonate chain ends to allow for further chain extension reactions to provide for the growth of a series of PIp chain lengths and investigate a range of amphiphilic block copolymer hydrophobic:hydrophilic ratios. Therefore, using a stoichiometry of 200:1, monomer:CTA, the monomer conversion was continued to 75% to give PNVP, **2**, with a number average molecular weight ($M_n$) of 13700 Da, which corresponded to a degree of polymerization of 120, as determined by $^1$H end-group analysis (Scheme 3-1 and Figure 3-3 for NMR and Figure 3-3 for GPC).

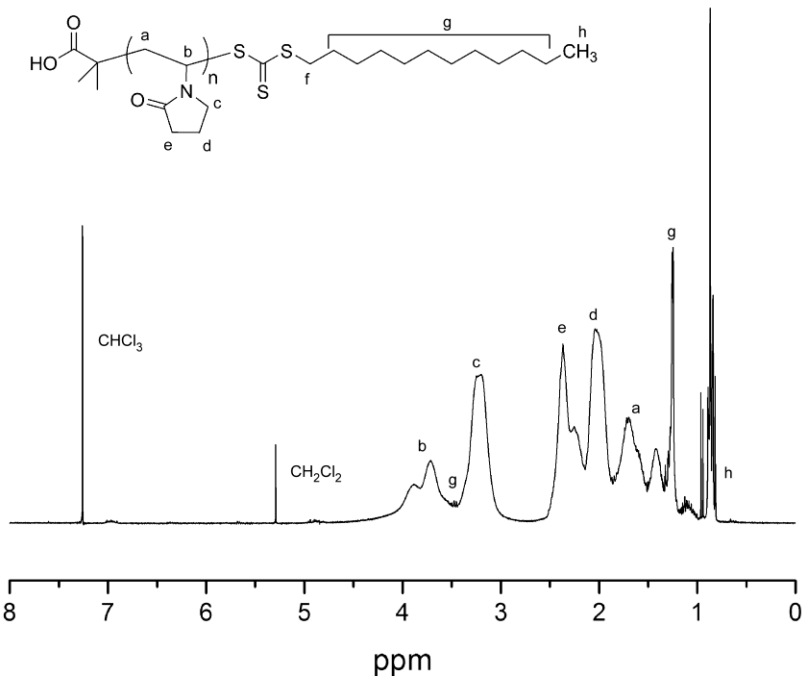


**Figure 3-3**. $^{1}$H NMR (500 MHz, $CDCl_3$) spectrum of P(NVP), **2**.

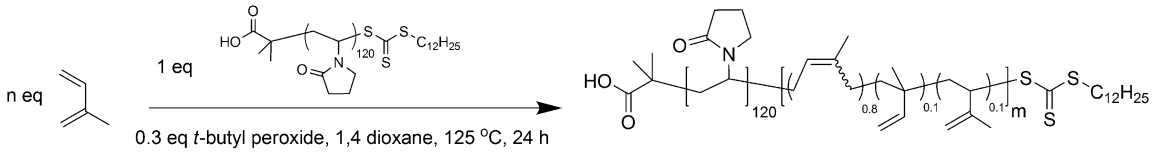


**Scheme 3-2**. Chain extension reaction to produce $PNVP_{120}$-*b*-$PIp_m$, where m = 710, 53, and 25 in the case of **3**, **4**, and **5**, respectively.

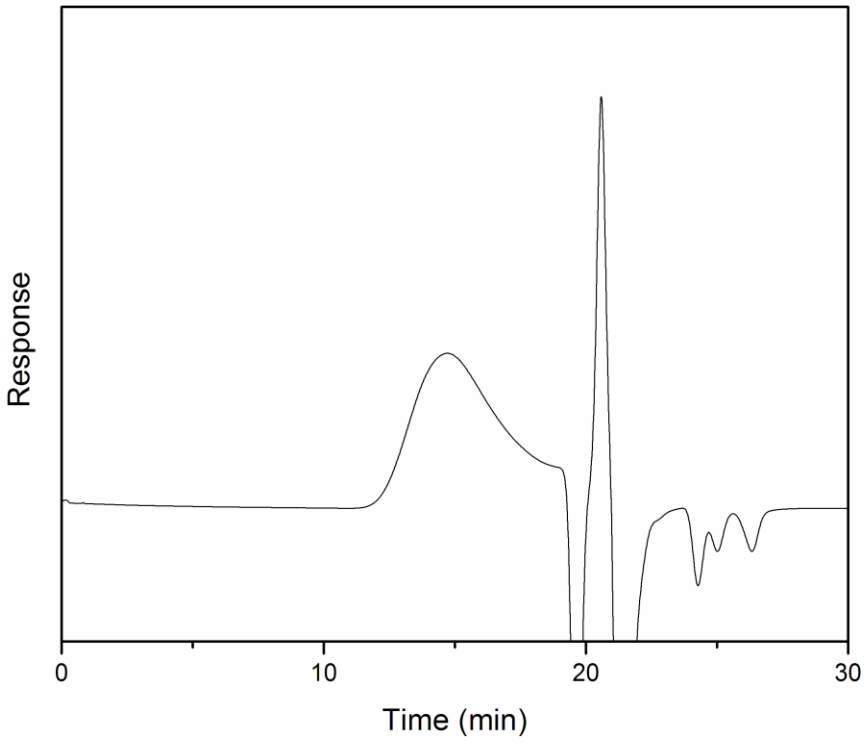


**Figure 3-4**. DMF GPC chromatogram of **2**. The sharp peak at ~21 minutes corresponds to a positive flow rate marker (0.5 % methanol).

Chain extension reactions were performed on the macroRAFT agent, **2**, with isoprene, employing conditions similar to those of Perrier(45) and Wooley(44) (Scheme 3-2), polymerizing at a reaction temperature of 125 and using *t*-butyl peroxide as the initiator. The feed ratio of Ip to the macroRAFT agent, **2**, was varied to allow for syntheses of three block copolymers, **3**, **4**, and **5**, and was set at a high value in each reaction to compensate for the low conversion typically achieved by RAFT polymerization of Ip. The number average molecular weight values, $M_n$, were determined *via* $^1$H NMR

spectroscopy post-purification, and GPC analysis confirmed the existence of a a block copolymer architecture (see Figures 3-5 and 3-6), however it should be noted that

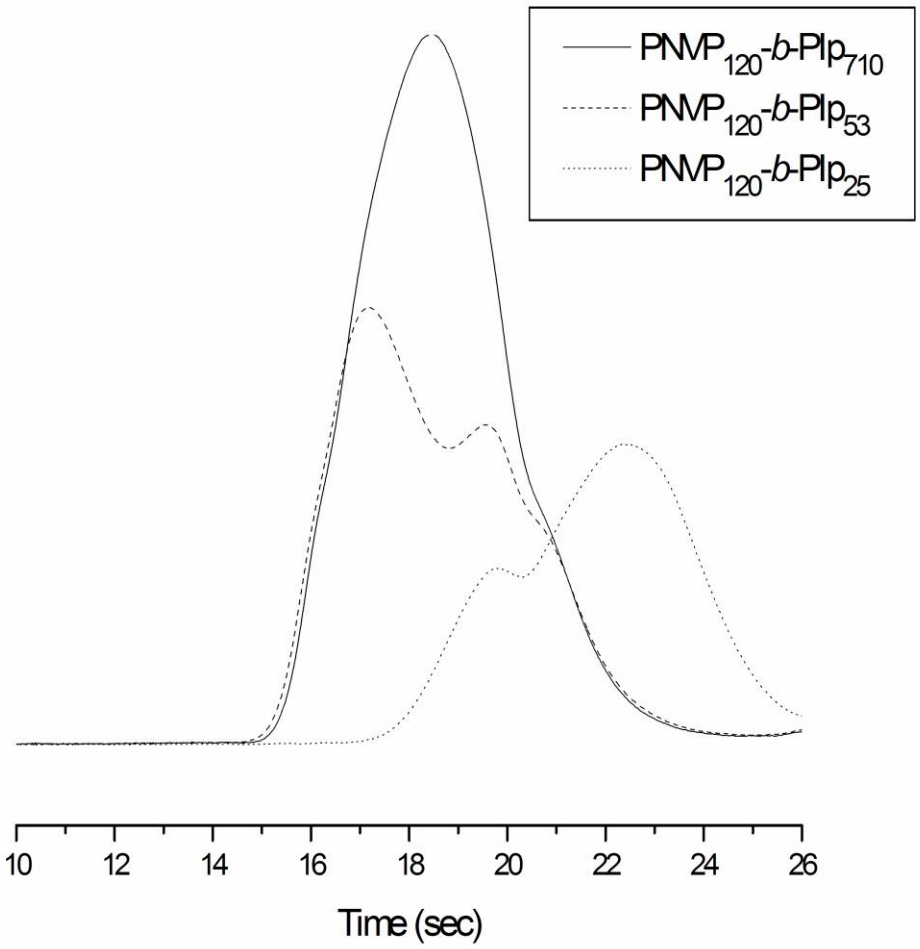


**Figure 3-5**. GPC chromatograms of **3-5** (*via* THF GPC).

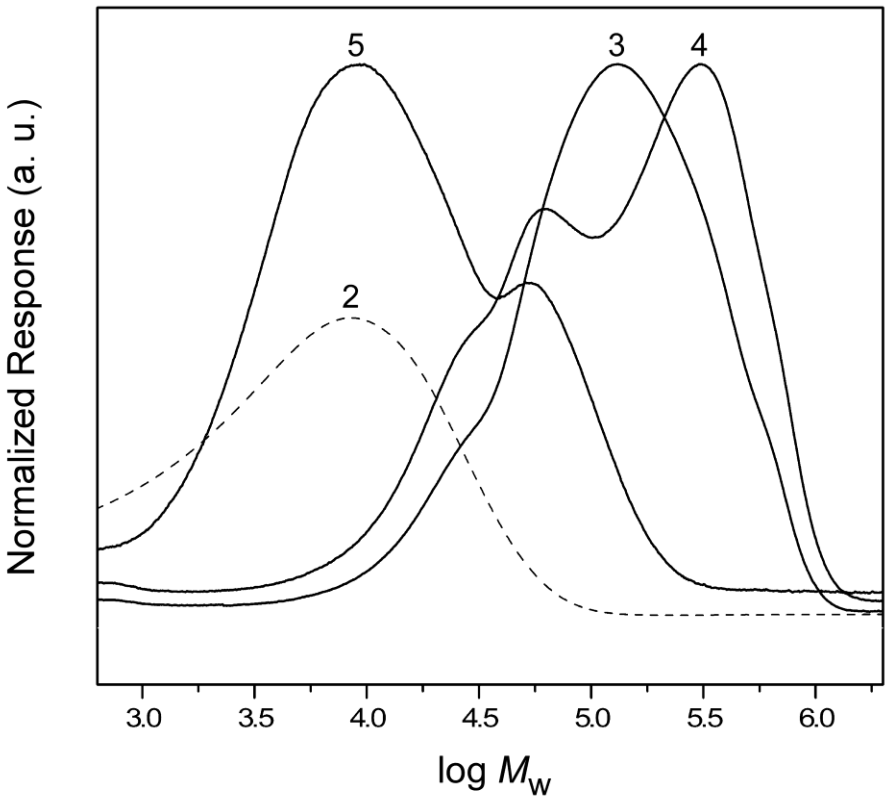


**Figure 3-6.** GPC stack plot of **2-5** plotted on a logarithmic scale.

homopolymer remains in the block copolymer after precipitation, giving evidence as to the partial blocking efficiency and subsequent incomplete removal of the PNVP macroCTA. $^1$H NMR spectroscopy also confirmed the presence of both PNVP and PIp blocks in **3** (Figure 3-7), with resonances diagnostic of PIp appearing along with resonances consistant with the parent polymer, **2.** The different regioisomers of the polyisoprene repeat units were readily observed in the region between 5.9 – 4.6 ppm of the $^1$H NMR spectrum, corresponding to the 1,2-, 4,1-, 1,2-, and 4,3- isomers (from high to low ppm). As was the case in all block copolymers studied, the 4,1- repeat unit makes up approximately 80% of the backbone. Comparison of the chain-end methyl protons of

the original RAFT agent, at 0.9 ppm, *versus* PNVP polymer peaks at 3.4 – 3.0 ppm was used to calculate the degree of polymerization and the molecular weight for PNVP, while comparison between existing backbone methine PNVP protons and new vinylic protons that arise from PIp was used to calculate molecular weight for all block copolymers. GPC and $^{13}C$ NMR spectroscopy were also used to confirm the structures (Figure 3-5, 3-6, 3-8).

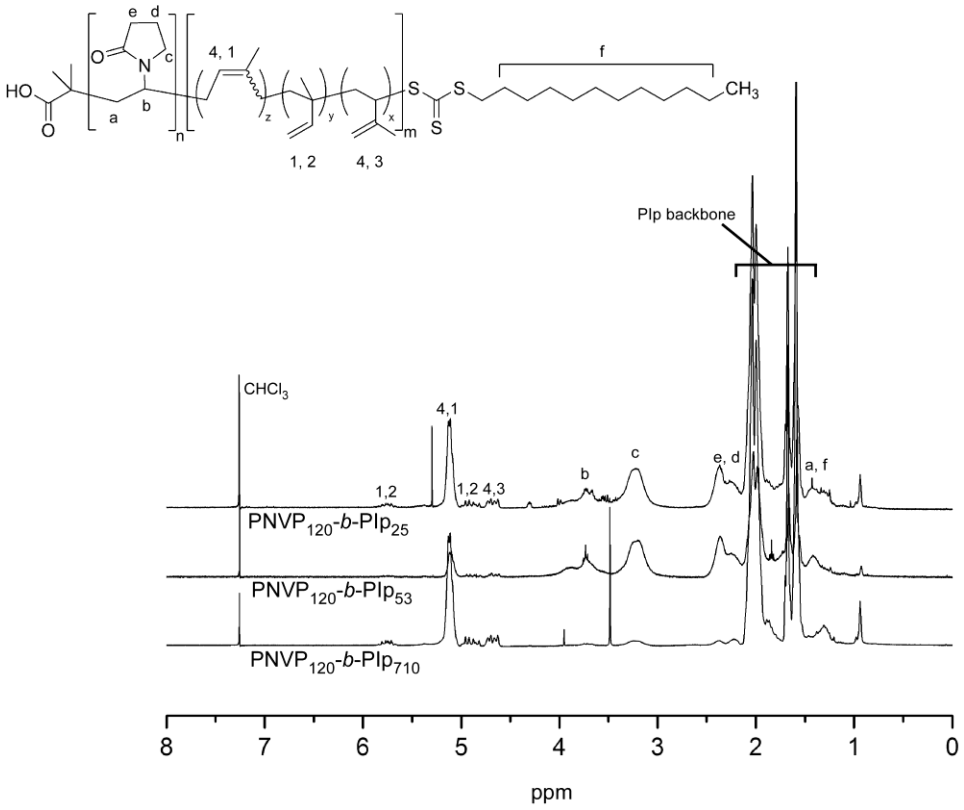


**Figure 3-7**. $^{1}H$ NMR spectra of $PNVP_n$-*b*-$PIp_m$, **3**, **4**, and **5**, where n = 120 and m = 710, 53 and 25, respectively.

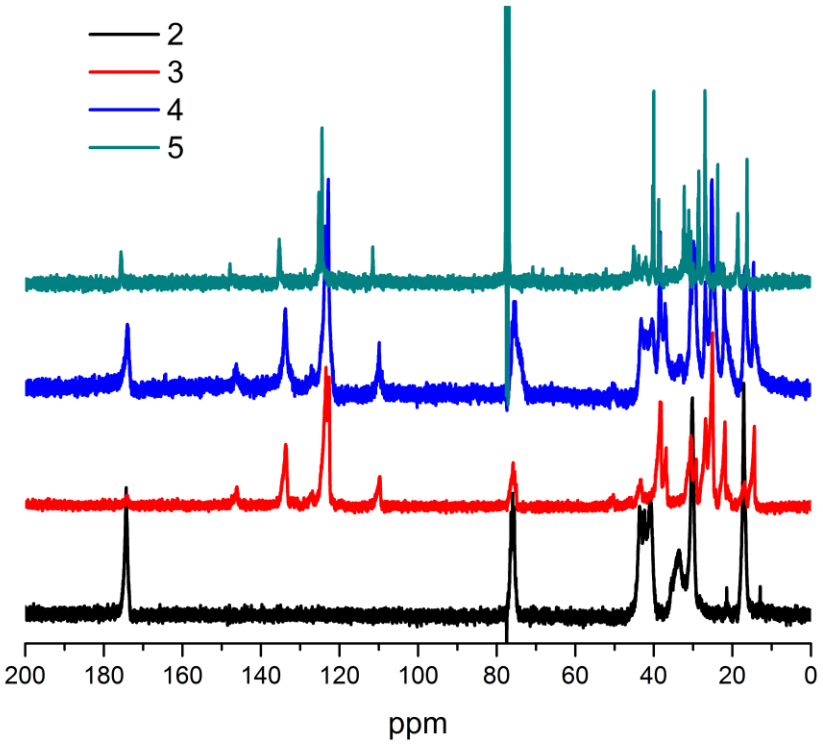


**Figure 3-8**. $^{13}$C NMR spectrum of **2, 3, 4** and **5.**

Thermal analysis of **2** and the block copolymers **3-5** by differential scanning calorimetry indicated a $T_g$ of 85 ºC for the PNVP component and $T_g$'s typical for PIp at *ca*. -60 ºC. The $T_g$ value for each block shifted slightly depending on the percent PIp incorporation, as shown in Figure 3-9; the relative intensities of the PIp *vs*. PNVP $T_g$ transitions were directly proportional to the relative block ratios. Thermogravimetric analysis can be seen in Figure 3-10.

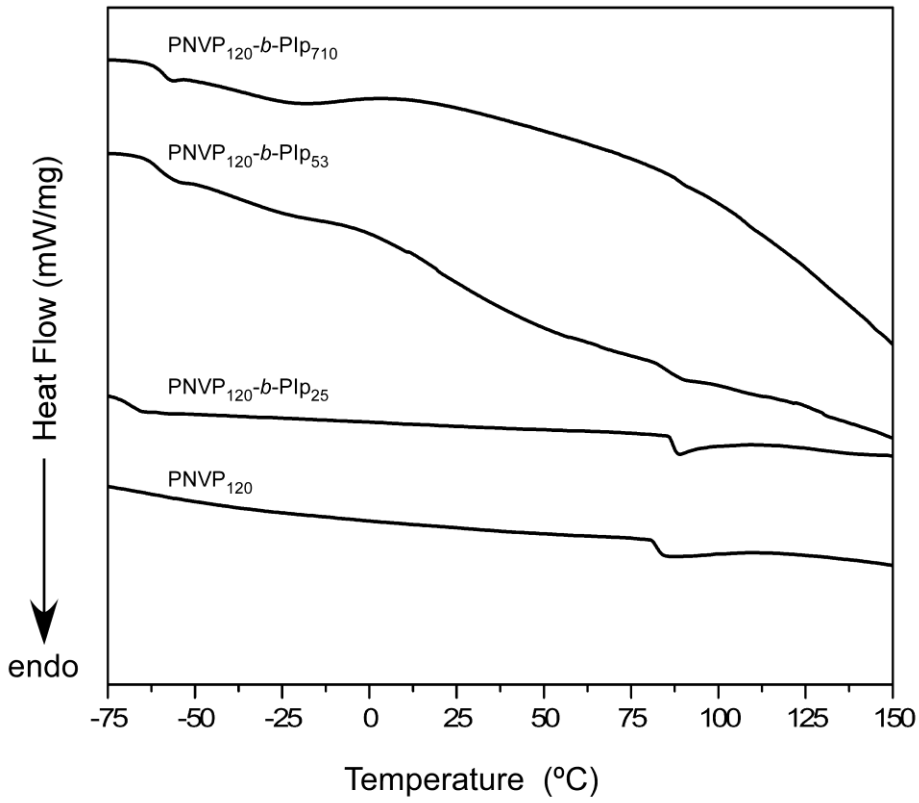


**Figure 3-9**. DSC traces of PNVP, **2**, and $PNVP_{120}$-*b*-$PIp_m$, **3-5**, block copolymers.

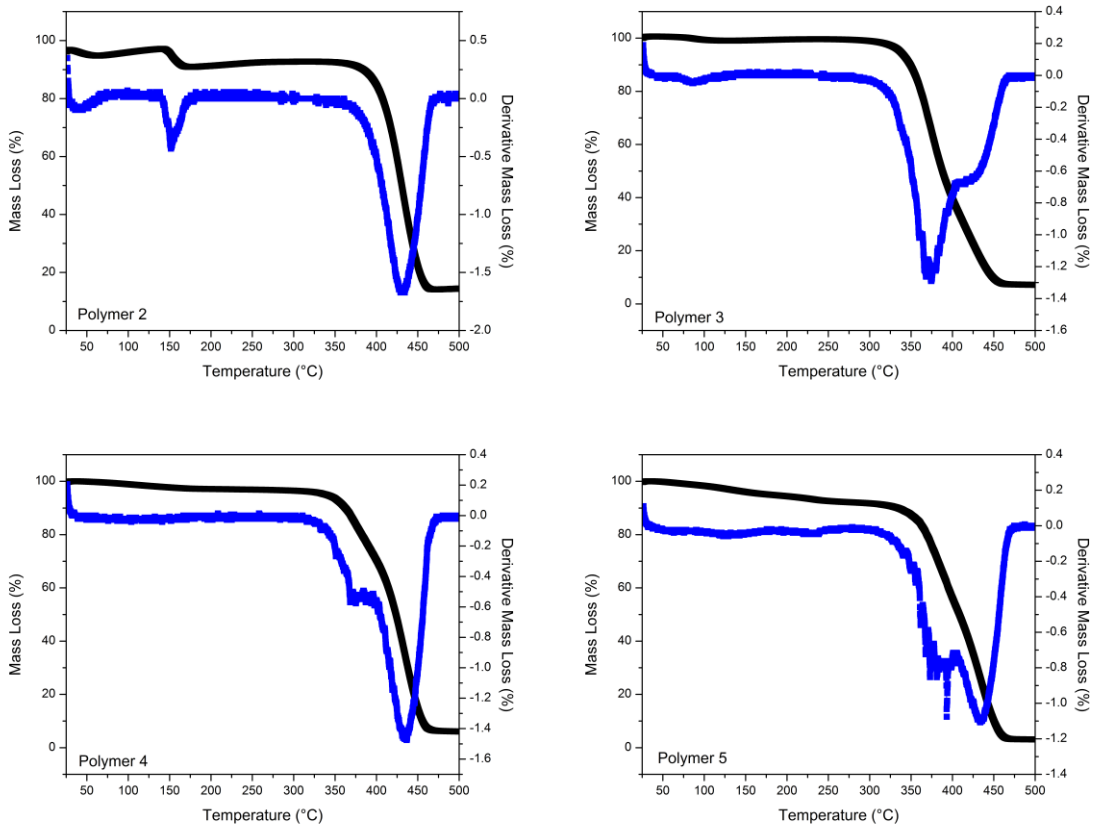


**Figure 3-10**. TGA mass loss (left) and derivative mass loss (right) plots of polymers **2**, **3**, **4** and **5**.

Complex surfaces of PNVP and PIp were prepared through crosslinking of the block copolymers with $S_2Cl_2$. Scheme 3-3 outlines the crosslinking methodology, wherein excess sulfur monochloride was added to dilute polymer solutions in dichloromethane and the mixture was allowed to undergo reaction overnight. Films of the resulting viscous reaction mixture were then cast onto glass microscope slides and were cured at ambient temperature, upon evaporation of the dichloromethane solvent. Once crosslinked, the films produced from polymers **3**, **4**, and **5**, are designated as **6**, **7**, and **8**,

respectively. Excessive washes of the films with benzene and dichloromethane produced only trace amounts of non-crosslinked leachate. The resultant film

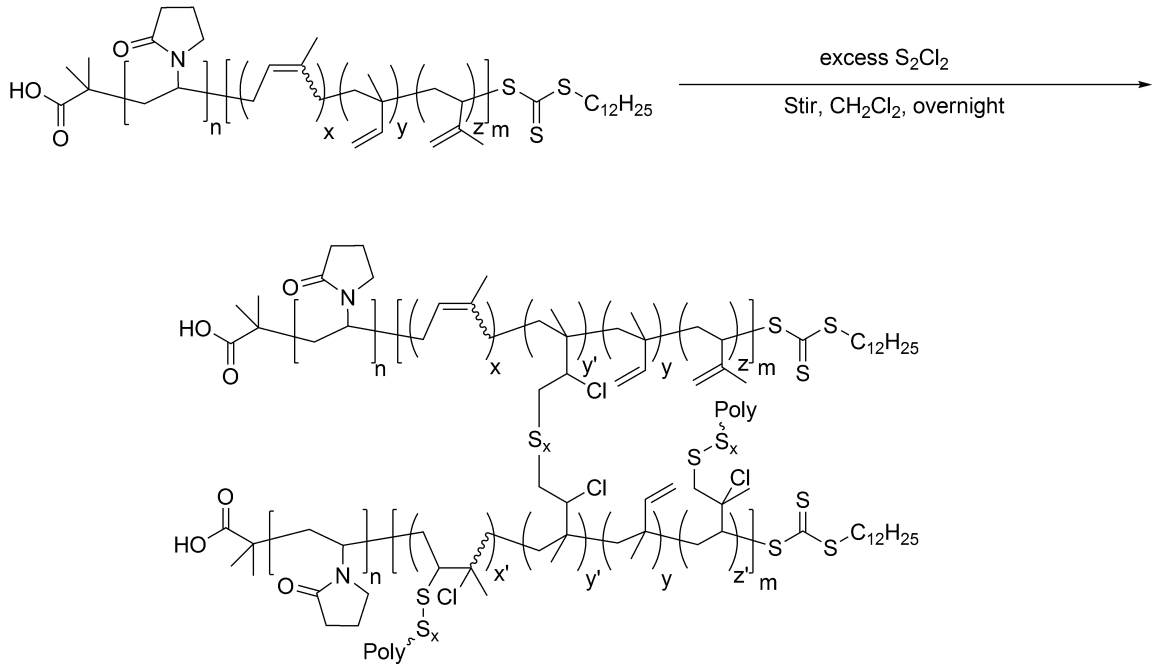


**Scheme 3-3**. $S_2Cl_2$ crosslinking of $PNVP_n$-*b*-$PIp_m$, showing the resultant sulfur-based linkages between polymer chains, where n = 120 and m = 710, 53 and 25 to afford crosslinked polymer films **6**, **7** and **8**, respectively.

properties depended on the mol percent PIp incorporation. Films with higher mol percent PIp, **6**, were brittle, whereas lower mol percent PIp produced stretchy and rubber-like films, **7** and **8**. Film **8**, which had the lowest PIp content was qualitatively less elastic than was **7** and was not as brittle as **6**.

AFM surface measurements indicated that the polymers had complex surface features, both before and after crosslinking (Figure 3-11). In the case of **6**, the higher PIp incorporation produced disordered surfaces, with RMS roughness 230 times more rough after crosslinking than was measured for the non-crosslinked film. It is expected that the

surface of **3** is dominated by the low $T_g$ PIp, which provides for smoothing to occur, whereas **6** contains complex topographic features that were trapped kinetically during the crosslinking process. A lower PIp incorporation ratio produced micro- and nano-topographies, which highlight the phase segregation inherent to the films, and the rigidity of the PNVP dominant phase. In the case of polymers **4** and **5**, the surface RMS roughness also increased upon the process of casting pre-gel solutions with coincident drying and covalent crosslinking. It should be noted that the addition of sulfur monochloride to the reactive surface can result potentially result in bulking or shrinkage effects, which would also have an effect on surface complexity and RMS roughness.

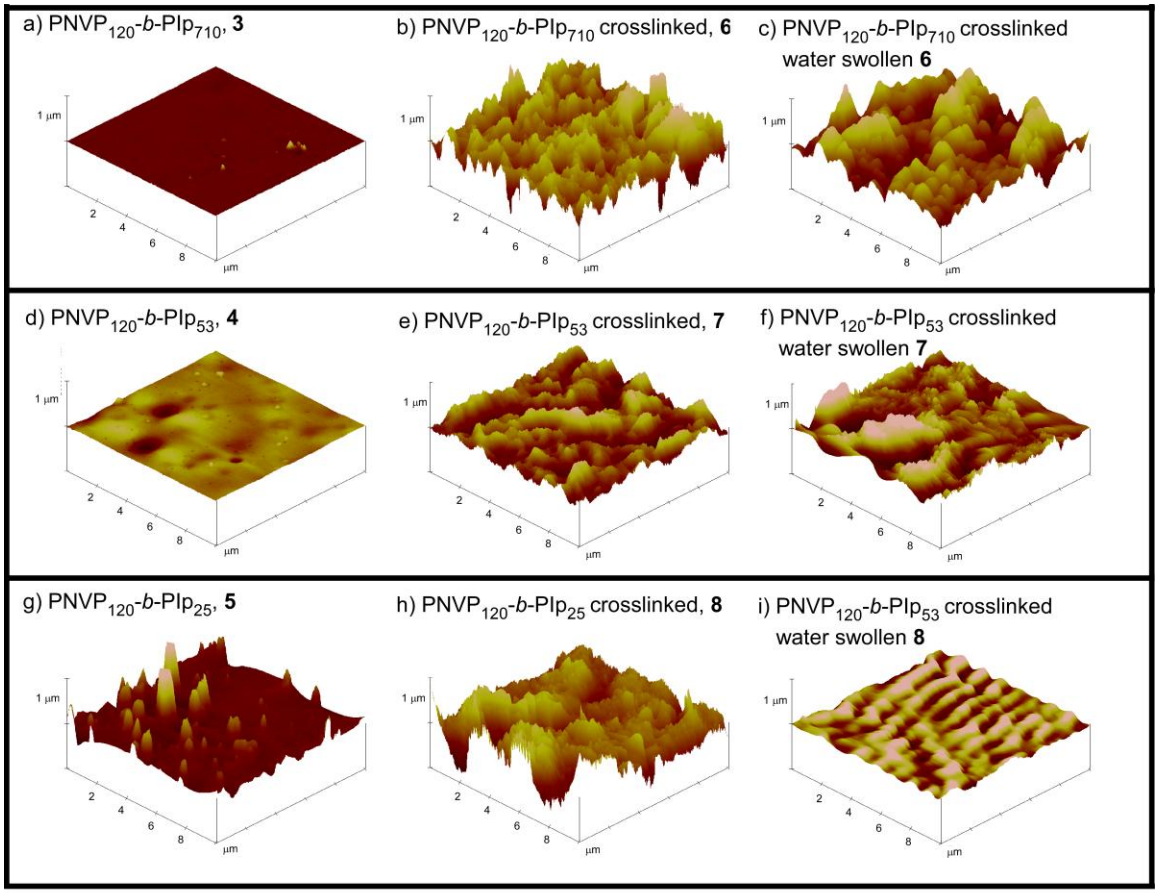


**Figure 3-11**. AFM images of $PNVP_{120}$-*b*-$PIp_m$ films, both non-crosslinked (a, d, g), $S_2Cl_2$-crosslinked (b, e, h), and crosslinked films swollen in artificial seawater (c, f, i).

Interestingly, when the crosslinked films were exposed to artificial seawater for 15 min, patted dry and imaged immediately in air under ambient conditions, there was an appearance of rounded, water-swollen peaks that dominate the nano-to-microscale landscape of all of the films. These observations are similar to previous results obtained with the HBFP-PEG system.(16) The roughness observed in the water-swollen films is essentially equivalent to dry films, providing evidence that the complex surface features remain intact in a marine environment.

Contact angle experiments were performed on each crosslinked and non-crosslinked film composition, with the data supporting the heterogeneity and complexity of these complex surfaces, as shown in Table 3-1. Interesting trends can be observed in the contact angle data. Primarily, the percent PIp incorporation did not seem to have a strong effect on the surface features before crosslinking, but there is evidence that is did affect surface characteristics at the post-crosslinked stage. Each of the three surfaces was hydrophobic prior to crosslinking, likely because of the migration of the low surface energy PIp to the surface during the casting of the non-crosslinked block copolymers. The block copolymer that contained the longest PIp chain segment, **3**, and having an overall majority of the composition being PIp, retained its hydrophobic character upon crosslinking also, to afford **6**. In contrast, the majority PNVP of **4** and **5** led to hydrophilic characteristics for the surfaces of their crosslinked networks, suggesting a chemically-fixed arrangement that arises from RMS surface roughness that presents PNVP on the surfaces of **7** and **8**.

**Table 3-1**. Contact Angles for both non-crosslinked and $S_2Cl_2$-crosslinked films.

| **Sample**[a] | **Advancing Contact Angle ($\theta_a$, °)**[b] | **Receding Contact Angle ($\theta_r$, °)**[b] | **Contact Angle Hysteresis ($\theta_a - \theta_r$, °)** | **Surface RMS roughness (nm)** |
|---|---|---|---|---|
| **3** | 95 ± 1 | 70 ± 6 | 25 | 2[c] |
| **4** | 81 ± 2 | 61 ± 5 | 20 | 5[c] |
| **5** | 107 ± 5 | 73 ± 3 | 34 | 36[c] |
| **6** | 96 ± 4 | 75 ± 1 | 21 | 86[c], 81[d] |
| **7** | 47 ± 10 | 26 ± 5 | 21 | 47[c], 43[d] |
| **8** | 57 ± 3 | 41 ± 2 | 16 | 76[c], 17[d] |

[a]Polymer **2** did not display a water contact angle, as it is readily soluble in water. [b]Contact angle values are averages obtained from pentuplicate measurements. [c]RMS roughness of dry film. [d]RMS roughness after swelling with artificial seawater.

To investigate the compositional heterogeneities of the surfaces, the atomic concentrations of the surface elements in each of the $PNVP_{120}$-*b*-$PIp_m$ coatings, **3**-**8**, were determined by X-ray photoelectron spectroscopy (XPS). The findings are summarized in Table 3-2. The change in atomic composition as the coatings changed from non-crosslinked to $S_2Cl_2$-crosslinked follows a trend common to all three compositions, wherein oxygen and nitrogen composition increased and carbon content decreased, indicative of a surface with increased pyrrolidinone-expression (the only source of N and O) and a reduction in the presentation of carbon-rich isoprene content when compared to

non-crosslinked surfaces. The presence of increased PNVP surface content upon crosslinking is in agreement with the contact angle data. The survey scans for all polymer film scans can be viewed in Figure 3-12.

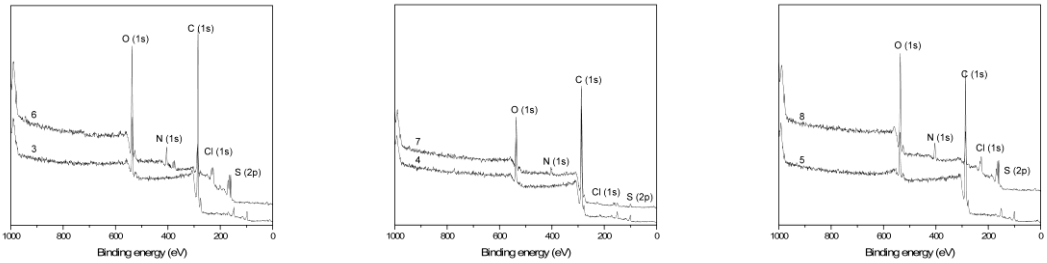


**Figure 3-12**. XPS plots of PNVP-*b*-PIp polymer films **3** and **6** (left), films **4** and **7** (center), and films **5** and **8** (right).

**Table 3-2**. Surface atomic concentrations of the non-crosslinked and $S_2Cl_2$ crosslinked $PNVP_{120}$-*b*-$PIp_m$ films, as determined by XPS (See Figure 3-12 for XPS survey scans). Small silica signals from Si(2P) were seen in a few samples, and were not taken into account for atomic concentration calculations.

| | Non-crosslinked, **3-5** | | | | | $S_2Cl_2$-crosslinked, dry, **6-8** | | | | |
|---|---|---|---|---|---|---|---|---|---|---|
| **Polymer** | O(1s) | N(1s) | C(1s) | Cl(1s) | S(2p) | O(1s) | N(1s) | C(1s) | Cl(1s) | S(2p) |
| $PNVP_{120}$-*b*-$PIp_{710}$ | 0.109 | 0.003 | 0.888 | N.A. | N.A. | 0.310 | 0.128 | 0.344 | 0.022 | 0.194 |
| $PNVP_{120}$-*b*-$PIp_{53}$ | 0.11 | 0.006 | 0.885 | N.A. | N.A. | 0.143 | 0.033 | 0.798 | 0.005 | 0.015 |
| $PNVP_{120}$-*b*-$PIp_{25}$ | 0.114 | 0.004 | 0.882 | N.A. | N.A. | 0.348 | 0.127 | 0.320 | 0.003 | 0.202 |

The amphiphilic compositional heterogeneity of the surfaces of these materials was assessed by internal reflectance infrared (IRIR) spectroscopy for the samples having intermediate PNVP and PIp content, **4** and **7**. Traditional IR spectroscopy was employed to obtain the bulk compositional information, and as a means to identify characteristic absorbance bands before and after crosslinking. For IRIR imaging, the films were cast on poly(tetrafluoroethylene) (PTFE) surfaces, and then imaged. PTFE was used as a substrate to avoid complications that had occurred in initial experiments from glass slide vibrational bands, which showed –CH=CH-Si bands in and around the region for lactams (*ca*. 1590 $cm^{-1}$) and led to poor images and IR spectra. Once cast on PTFE, two-dimensional IRIR images were collected by tuning into the 1664 and 1447 $cm^{-1}$ bands, which are attributed to –C=O stretching of the PNVP lactam and $–CH_2–$ deformation bands of PIp, respectively. All bands were normalized against the 1447 $cm^{-1}$ band. As seen in Figure 3-13, there is a certain degree of chemical heterogeneity manifested by color (red = high content; blue = low content) changes due to uneven distribution of PNVP and PIp components, consistent with the topographic features observed in the AFM images. Since IRIR imaging allows for the collection of IR images from 1 x 1 $\mu m^2$ areas and also obtains a chemical signature of those areas, IR spectra from areas labeled A and B were collected. Images A and B of Figure 3-13 illustrate a distribution of the PNVP and PIp for the non-crosslinked surface (Figure 3-13, sections (a) and (c)), as well as for the crosslinked surface (Figure 3-13, sections (b) and (d)), respectively. From this information, it was concluded that both films possess microscale heterogeneities, in addition to the nanoscopically diverse structures observed in AFM images. Additionally, while both images appear morphologically multi-faceted, yet similar to one another in

complexity, there are substantial differences between non-crosslinked and crosslinked films as confirmed by their respective IR signatures.

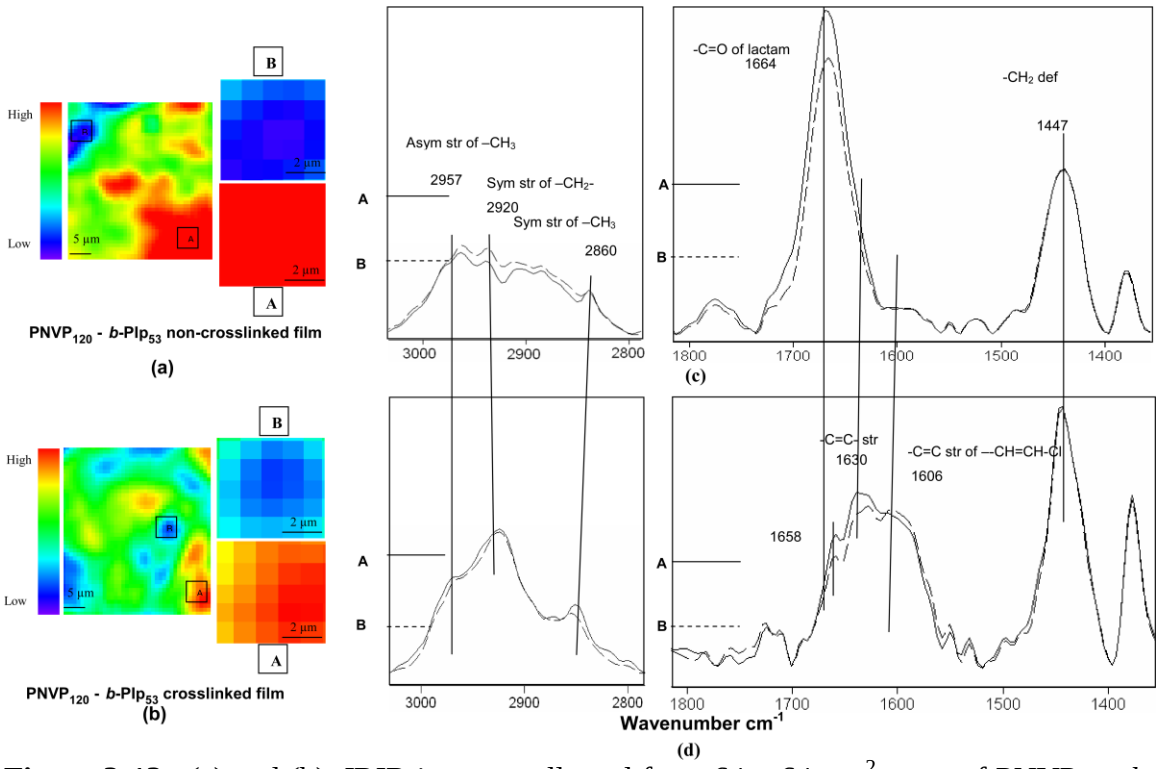


**Figure 3-13.** (a) and (b), IRIR images collected from 64 x 64 µm$^2$ areas of $PNVP_{120}$ -*b*-$PIp_{53}$ non-crosslinked and crosslinked films prepared on PTFE substrates, respectively, tuned to 1447 cm$^{-1}$. (c) and (d), IR spectra collected from areas A and B (5 x 5 µm$^2$) of IRIR (a) and (b), respectively.

Comparison of spectroscopic changes between non-crosslinked and crosslinked films demonstrates the increased band intensities of the 2957, 2860, and 2920 cm$^{-1}$ bands due to asymmetric and symmetric $–CH_3$ , and symmetric $–CH_2$- stretching vibrations, respectively. A summary of all tentative assignments can be seen in Table 3-3. Perhaps the most notable difference between the two surfaces can be seen in the decrease of the 1664 cm$^{-1}$ band(53) of the –C=O stretching vibrations when going from a non-

crosslinked to a crosslinked surface, which suggests a burrowing of the PNVP segments into the film and away from the air-surface interface. This result is in contrast to the water contact angle and XPS data, which indicated an increase in hydrophilic character and PNVP atomic signals, respectively, upon crosslinking. Although the sampling depth of XPS and IRIRI are somewhat different (a few nm in XPS and approximately 70 nm in IRIRI), the trends observed in both experiments are the same. Upon crosslinking the concentration of C diminishes, and IRIRI experiments indicate the loss C=O groups. Further experiments are needed to better understand this complex and heterogeneous system.

**Table 3-3**. IR bands observed for $PNVP_{120}$ -*b*-$PIp_{53}$ non-crosslinked, A, and $PNVP_{120}$ -*b*-$PIp_{53}$ $S_2Cl_2$-crosslinked, B, films and their tentative band assignments

| **Band** | **A ($cm^{-1}$)** | **B ($cm^{-1}$)** |
|---|---|---|
| $\nu_a$ of $CH_3$ | 2957 | 2957 |
| $\nu_s$ of $CH_2$ | 2920 | 2920 |
| $\nu_s$ of $CH_3$ | 2860 | 2860 |
| -C=O str of lactam | 1664 | 1658 |
| -CH=C - str | - | 1630 |
| -CH=CH str of –CH=CH-Cl | - | 1606 |
| $\delta$ -$CH_2$ | 1447 | 1447 |

$\nu_a$ = Asymmetric stretching
$\nu_s$ = Symmetric stretching
$\delta$ = Deformation

Differences in properties for the block copolymers were observed also in the solution state. The polymer with lower isoprene content, **5**, was found to disperse and undergo spontaneous self assembly into micelles when added directly from the solid state to water. This behavior was unique, as **3** and **4** were completely insoluble in water or related polar solvents, such as methanol or DMF. A closer look at a controlled addition of water to a THF solution containing **5** produced micelles **9** and **10**, containing two

different solution concentrations, 0.3 mg/mL and 1.7 mg/mL, respectively. The solutions were analyzed using dynamic light scattering (DLS), which showed bimodal hydrodynamic diameter ($D_h$) distributions, including the expected nanoscopic micelles having $D_h$ values around 70 – 100 nm and also the appearance of larger assemblies with $D_h$ values in the hundreds of nanometers.

**Conclusions**

With our interest in the preparation of non-toxic anti-fouling coatings that rely on combinations of surface morphology, topography and composition dispersed on the nano- and microscopic size scales, we have now extended the types of materials involved to include commodity polymers. To have appropriate building blocks, the generation of interesting and novel amphiphilic polymers, $PNVP_{120}$-*b*-$PIp_m$, was required to achieve the subsequent production of nanoscopically-resolved films having morphologically- and topographically-complex surface features. Controlled radical polymerization techniques were applied to the polymerization of common monomers to afford unique amphiphilic block copolymers, which served as the components for an attempted cheap production of these complex films. A variety of surface analysis methods were used to probe the heterogeneity, including methods such as XPS and AFM and IRIR imaging. The complex surface features could provide evidence as to which structure-property relationships are important in designing anti-fouling coatings, *i.e.* to what degree chemical composition plays *versus* that of morphological and topographical nano- or microscopic surface features in preventing adsorption and adhesion of proteins, marine organisms, *etc*. The interesting differences in surface characteristics of these unique

amphiphilic block copolymers carried to the solution state, for which only the polymer with the shortest PIp chain segment, $PNVP_{120}$-*b*-$PIp_{25}$, was capable of undergoing self assembly in an aqueous environment, giving rise to micelles.

**Acknowledgement**

This material is based on work supported by the Office of Naval Research under grant number N00014-08-1-0398 and the National Science Foundation DMR-0451490.

**References**:

(1) Chambers, L. D.; Stokes, K. R.; Walsh, F. C.; Wood, R. J. K. (2006) Modern approaches to marine antifouling coatings. *Surface & Coatings Technology 201*(6), 3642-3652.

(2) Schumacher, J. F.; Carman, M. L.; Estes, T. G.; Feinberg, A. W.; Wilson, L. H.; Callow, M. E.; Callow, J. A.; Finlay, J. A.; Brennan, A. B. (2007) Engineered antifouling microtopographies - effect of feature size, geometry, and roughness on settlement of zoospores of the green alga Ulva. *Biofouling 23*(1), 55-62.

(3) Hovgaard, M. B.; Rechendorff, K.; Chevallier, J.; Foss, M.; Besenbacher, F. (2008) Fibronectin adsorption on tantalum: The influence of nanoroughness. *Journal of Physical Chemistry B 112*(28), 8241-8249.

(4) Genzer, J.; Efimenko, K. (2006) Recent developments in superhydrophobic surfaces and their relevance to marine fouling: a review. *Biofouling 22*(5), 339-360.

(5) Callow, J. A.; Callow, M. E.; Ista, L. K.; Lopez, G.; Chaudhury, M. K. (2005) The influence of surface energy on the wetting behaviour of the spore adhesive of the marine alga Ulva linza (synonym Enteromorpha linza). *Journal of the Royal Society Interface 2*(4), 319-325.

(6) Schmidt, D. L.; Brady, R. F.; Lam, K.; Schmidt, D. C.; Chaudhury, M. K. (2004) Contact angle hysteresis, adhesion, and marine biofouling. *Langmuir 20*(7), 2830-2836.

(7) Krishnan, S.; Ayothi, R.; Hexemer, A.; Finlay, J. A.; Sohn, K. E.; Perry, R.; Ober, C. K.; Kramer, E. J.; Callow, M. E.; Callow, J. A.; Fischer, D. A. (2006) Anti-biofouling properties of comblike block copolymers with amphiphilic side chains. *Langmuir 22*(11), 5075-5086.

(8) Krishnan, S.; Wang, N.; Ober, C. K.; Finlay, J. A.; Callow, M. E.; Callow, J. A.; Hexemer, A.; Sohn, K. E.; Kramer, E. J.; Fischer, D. A. (2006) Comparison of the fouling release properties of hydrophobic fluorinated and hydrophilic PEGylated block copolymer surfaces: Attachment strength of the diatom Navicula and the green alga Ulva. *Biomacromolecules 7*(5), 1449-1462.

(9) Hoipkemeier-Wilson, L.; Schumacher, J.; Carman, M.; Gibson, A.; Feinberg, A.; Callow, M.; Finlay, J.; Callow, J.; Brennan, A. (2004) Antifouling potential of lubricious, micro-engineered, PDMS elastomers against zoospores of the green fouling alga Ulva (Enteromorpha). *Biofouling 20*(1), 53-63.

(10) Wendt, D. E.; Kowalke, G. L.; Kim, J.; Singer, I. L. (2006) Factors that influence elastomeric coating performance: the effect of coating thickness on basal plate

morphology, growth and critical removal stress of the barnacle Balanus amphitrite. *Biofouling 22*(1), 1-9.

(11) Aldred, N.; Clare, A. S. (2008) The adhesive strategies of cyprids and development of barnacle-resistant marine coatings. *Biofouling 24*(5), 351-363.

(12) Liao, K.-S.; Fu, H.; Wan, A.; Batteas, J. D.; Bergbreiter, D. E. (2009) Designing surfaces with wettability that varies in response to solute identity and concentration. *Langmuir 25*, 26-28.

(13) Bartels, J. W.; Cheng, C.; Powell, K. T.; Xu, J. Q.; Wooley, K. L. (2007) Hyperbranched fluoropolymers and their hybridization into complex amphiphilic crosslinked copolymer networks. *Macromolecular Chemistry and Physics 208*(15), 1676-1687.

(14) Gan, D. J.; Mueller, A.; Wooley, K. L. (2003) Amphiphilic and hydronhobic surface patterns generated from hyperbranched fluoropolymer/linear polymer networks: Minimally adhesive coatings via the crosslinking of hyperbranched fluoropolymers. *Journal of Polymer Science Part A-Polymer Chemistry 41*(22), 3531-3540.

(15) Gudipati, C. S.; Finlay, J. A.; Callow, J. A.; Callow, M. E.; Wooley, K. L. (2005) The antifouling and fouling-release perfomance of hyperbranched fluoropolymer (HBFP)-poly(ethylene glycol) (PEG) composite coatings evaluated by adsorption of biomacromolecules and the green fouling alga Ulva. *Langmuir 21*(7), 3044-3053.

(16) Gudipati, C. S.; Greenlief, C. M.; Johnson, J. A.; Prayongpan, P.; Wooley, K. L. (2004) Hyperbranched fluoropolymer and linear poly(ethylene glycol) based

Amphiphilic crosslinked networks as efficient antifouling coatings: An insight into the surface compositions, topographies, and morphologies. *Journal of Polymer Science Part A-Polymer Chemistry 42*(24), 6193-6208.

(17) Powell, K. T.; Cheng, C.; Wooley, K. L.; Singh, A.; Urban, M. W. (2006) Complex amphiphilic networks derived from diamine-terminated poly(ethylene glycol) and benzylic chloride-functionalized hyperbranched fluoropolymers. *Journal of Polymer Science Part A-Polymer Chemistry 44*(16), 4782-4794.

(18) Nguyen, T. L. U.; Eagles, K.; Davis, T. P.; Barner-Kowollik, C.; Stenzel, M. H. (2006) Investigation of the influence of the architectures of poly(vinyl pyrrolidone) polymers made via the reversible addition-fragmentation chain transfer/macromolecular design via the interchange of xanthates mechanism on the stabilization of suspension polymerizations. *Journal of Polymer Science Part A-Polymer Chemistry 44*(15), 4372-4383.

(19) Yarbrough, J. C.; Rolland, J. P.; DeSimone, J. M.; Callow, M. E.; Finlay, J. A.; Callow, J. A. (2006) Contact angle analysis, surface dynamics, and biofouling characteristics of cross-linkable, random perfluoropolyether-based graft terpolymers. *Macromolecules 39*(7), 2521-2528.

(20) Youngblood, J. P.; Andruzzi, L.; Ober, C. K.; Hexemer, A.; Kramer, E. J.; Callow, J. A.; Finlay, J. A.; Callow, M. E. (2003) Coatings based on side-chain ether-linked poly(ethylene glycol) and fluorocarbon polymers for the control of marine biofouling. *Biofouling 19*, 91-98.

(21) Anderson, C.; Atlar, M.; Callow, M.; Candries, M.; Milne, A.; Towsin, R. L. (2003) The development of foul-release coatings for seagoing vessels. *Journal of Marine Design and Operations B4*, 11-23.

(22) Tang, Y.; Finlay, J. A.; Kowalke, G. L.; Meyer, A. E.; Bright, F. V.; Callow, M. E.; Callow, J. A.; Wendt, D. E.; Detty, M. R. (2005) Hybrid xerogel films as novel coatings for antifouling and fouling release. *Biofouling 21*(1), 59-71.

(23) Zhang, Z.; Chao, T.; Chen, S. F.; Jiang, S. Y. (2006) Superlow fouling sulfobetaine and carboxybetaine polymers on glass slides. *Langmuir 22*(24), 10072-10077.

(24) Zhang, Z.; Chen, S. F.; Chang, Y.; Jiang, S. Y. (2006) Surface grafted sulfobetaine polymers via atom transfer radical polymerization as superlow fouling coatings. *Journal of Physical Chemistry B 110*(22), 10799-10804.

(25) Cheng, G.; Zhang, Z.; Chen, S. F.; Bryers, J. D.; Jiang, S. Y. (2007) Inhibition of bacterial adhesion and biofilm formation on zwitterionic surfaces. *Biomaterials 28*(29), 4192-4199.

(26) Carman, M. L.; Estes, T. G.; Feinberg, A. W.; Schumacher, J. F.; Wilkerson, W.; Wilson, L. H.; Callow, M. E.; Callow, J. A.; Brennan, A. B. (2006) Engineered antifouling microtopographies - correlating wettability with cell attachment. *Biofouling 22*(1), 11-21.

(27) Powell, K. T.; Cheng, C.; Wooley, K. L. (2007) Complex amphiphilic hyperbranched fluoropolymers by atom transfer radical self-condensing vinyl (co)polymerization. *Macromolecules 40*(13), 4509-4515.

(28) von Byern, J.; Klepal, W. (2006) Adhesive mechanisms in cephalopods: a review. *Biofouling 22*(5), 329-338.

(29) Wiegemann, M. (2005) Adhesion in blue mussels (Mytilus edulis) and barnacles (genus Balanus): Mechanisms and technical applications. *Aquatic Sciences 67*(2), 166-176.

(30) Gallet, G.; Carroccio, S.; Rizzarelli, P.; Karlsson, S. (2002) Thermal degradation of poly(ethylene oxide-propylene oxide-ethylene oxide) triblock copolymer: comparative study by SEC/NMR, SEC/MALDI-TOF-MS and SPME/GC-MS. *Polymer 43*(4), 1081-1094.

(31) Xu, J.; Bohnsack, D. A.; Mackay, M. E.; Wooley, K. L. (2007) Unusual mechanical performance of amphiphilic crosslinked polymer networks. *Journal of the American Chemical Society 129*(3), 506-507.

(32) Xu, J.; Bartels, J. W.; Bohnsack, D. A.; Tseng, T.-C.; Mackay, M. E.; Wooley, K. L. (2008) Hierarchical Inorganic-Organic Nanocomposites Possessing Amphiphilic and Morphological Complexities: Influence of Nanofiller Dispersion on Mechanical Performance. *Advanced Functional Materials 18*(18), 2733-2744.

(33) Brown, G. O.; Bergquist, C.; Ferm, P.; Wooley, K. L. (2005) Unusual, Promoted Release of Guests from Amphiphilic Crosslinked Polymer Networks. *J. Am. Chem. Soc. 127*, 11238-11239.

(34) Pound, G.; Aguesse, F.; McLeary, J. B.; Lange, R. F. M.; Klumperman, B. (2007) Xanthate-mediated copolymerization of vinyl monomers for Amphiphilic and double-hydrophilic block copolymers with poly(ethylene glycol). *Macromolecules 40*(25), 8861-8871.

(35) Pound, G.; McLeary, J. B.; McKenzie, J. M.; Lange, R. F. M.; Klumperman, B. (2006) In-situ NMR spectroscopy for probing the efficiency of RAFT/MADIX agents. *Macromolecules 39*(23), 7796-7797.

(36) Baldoli, C.; Oldani, C.; Maiorana, S.; Ferruti, P.; Ranucci, E.; Bencini, M.; Contini, A. (2008) Functionalization and molecular dynamics study of carboxy-terminated poly(1-vinylpyrrolidin-2-one): A potential soluble carrier of biomolecules. *Journal of Polymer Science Part A-Polymer Chemistry 46*(5), 1683-1698.

(37) Cheng, C.; Qi, K.; Germack, D. S.; Khoshdel, E.; Wooley, K. L. (2007) Synthesis of core-crosslinked nanoparticles with controlled cylindrical shape and narrowly-dispersed size via core-shell brush block copolymer templates. *Advanced Materials 19*(19), 2830-+.

(38) Devasia, R.; Bindu, R. L.; Borsali, R.; Mougin, N.; Gnanou, Y. (2005) Controlled radical polymerization of N-vinylpyrrolidone by reversible addition-fragmentation chain transfer process. *Macromolecular Symposia 229*, 8-17.

(39) Hu, Z. Q.; Tao, M.; Zhang, Z. C. (2007) "Gradient" polymer prepared by complex-radical terpolymerization of styrene, maleic anhydride, and N-vinyl pyrrolidone via gamma ray irradiation by use of a RAFT method - 2. Used in dispersion polymerization of styrene as a stabilizer. *Colloids and Surfaces a-Physicochemical and Engineering Aspects 302*(1-3), 307-311.

(40) Benoit, D.; Harth, E.; Fox, P.; Waymouth, R. M.; Hawker, C. J. (2000) Accurate structural control and block formation in the living polymerization of 1,3-dienes by nitroxide-mediated procedures. *Macromolecules 33*(2), 363-370.

(41) Ruehl, J.; Nilsen, A.; Born, S.; Thoniyot, P.; Xu, L. P.; Chen, S. W.; Braslau, R. (2007) Nitroxide-mediated polymerization to form symmetrical ABA triblock copolymers from a bidirectional alkoxyamine initiator. *Polymer 48*(9), 2564-2571.

(42) Wegrzyn, J. K.; Stephan, T.; Lau, R.; Grubbs, R. B. (2005) Preparation of poly(ethylene oxide)-block-poly(isoprene) by nitroxide-mediated free radical polymerization from PEO macroinitiators. *Journal of Polymer Science Part A-Polymer Chemistry 43*(14), 2977-2984.

(43) Germack, D. S.; Harrisson, S.; Brown, G. O.; Wooley, K. L. (2006) Influence of the structure of nanoscopic building blocks on the assembly of micropatterned surfaces. *Journal of Polymer Science Part A-Polymer Chemistry 44*(17), 5218-5228.

(44) Germack, D. S.; Wooley, K. L. (2007) Isoprene polymerization via reversible addition fragmentation chain transfer polymerization. *Journal of Polymer Science Part A-Polymer Chemistry 45*(17), 4100-4108.

(45) Jitchum, V.; Perrier, S. (2007) Living radical polymerization of isoprene via the RAFT process. *Macromolecules 40*(5), 1408-1412.

(46) Ceylan, D.; Okay, O. (2007) Macroporous polyisobutylene gels: A novel tough organogel with superfast responsivity. *Macromolecules 40*(24), 8742-8749.

(47) Neumann, A. W.; Good, R. J. (1979) Techniques of measuring contact angles [in surface studies]. *Journal of Surface and Colloid Science 11*, 31-91.

(48) Otts, D. B.; Zhang, P.; Urban, M. W. (2002) *Langmuir 18*, 6473.

(49) Lai, J. T. (2000) S,S'-bis-(a,a'-disubstituted-a"-acetic acid)-trithiocarbonates and derivatives as initiator-chain transfer agent-terminators for controlled radical polymerizations and their manufacture. *U.S. Patent 6 596 899*.

(50) Lai, J. T.; Filla, D.; Shea, R. (2002) Functional Polymers from Novel Carboxyl-Terminated Trithiocarbonates as Highly Efficient RAFT Agents. *Macromolecules 35*, 6754-6756.

(51) Bouchekif, E.; Narain, R. (2007) Reversible addition-fragmentation chain transfer polymerization of N-isopropylacrylamide: A comparison between a conventional and a fast initiator. *Journal of Physical Chemistry B 111*(38), 11120-11126.

(52) Pound, G.; Eksteen, Z.; Pfukwa, R.; McKenzie, J. M.; Lange, R. F. M.; Klumperman, B. (2008) Unexpected reactions associated with the xanthate-mediated polymerization of N-vinylpyrrolidone. *Journal of Polymer Science Part A-Polymer Chemistry 46*(19), 6575-6593.

(53) Lin-Vein, D.; Colthup, N. B.; Fateley, W. G.; Grasselli, J. G. (1991) *The Handbook of Infrared and Raman Characteristics Frequencies of Organic Molecules*. Academic Press: San Diego, CA.

## Chapter 5

# Conclusions

Newer generations of anti-fouling materials that are rapidly crosslinkable, durable and commercially available polymer film analogs to HBFP-PEG were developed. The films were prepared from primarily commercially available, non-toxic reagents and were engineered to be crosslinked in such an efficient manner (room temperature curing, rapid time of cure with little to no impact on the film properties). The overall emphasis of this dissertation research was in the development of novel amphiphilic anti-fouling coatings having complex surface topography and compositional heterogeneity and a fundamental and thorough investigation of their mechanical/thermomechanical, surface and biofouling properties.

A series of Boltorn-PEG films were prepared by the thiol-ene photocrosslinking of Boltorn-ene and 4-armed PEG tetrathiol with PETMP, as was reported in Chapter 2. The main feed ingredient, Boltorn-ene, was easily prepared by the simple esterification of commercially available Boltorn H30™ polyol and 3-butenoic acid. IR spectroscopy was employed to monitor completion of the thiol-ene reaction, where it was found that near-complete crosslinking occurred above 0.75 eq SH/ene PETMP concentration. Thermomechanical analysis was performed on the film set, where it was observed that $T_g$ increased as a function of PEG wt%, a range of over 30+ degrees from 0 to 25 wt%. Tensile tests of films in both the dry and wet state revealed a dramatic increase in Young's modulus as a function of PETMP, reaching a peak at 0.75 eq SH/ene. The nanotopography of the films was analyzed using AFM and was supplemented with contact angle analysis, where increasing roughness occurred with increasing PEG wt%. A comprehensive anti-fouling study was performed against *Ulva* algae on Boltorn-

PEG films at constant 0.25 eq SH/ene PETMP concentration across a wide range of PEG wt% (0-35 wt%), where it was observed that spore settlement and growth was much lower when compared to commercial PDMSe coatings.

The investigation into using common trade monomers to create interesting and complex amphiphilic block copolymers, with which to form anti-fouling coatings, was investigated in Chapter 3. The preparation of non-toxic anti-fouling coatings that produced complex surface morphology, topography and composition dispersed on the nano- and microscopic size scales was generated by the preparation of a series of interesting and novel amphiphilic $PNVP_{120}$-*b*-$PIp_m$ copolymers. Controlled radical polymerization techniques were applied to the polymerization of common monomers to afford unique amphiphilic block copolymers, which served as the components for an attempted cheap production of these complex films. Different block sizes were investigated in order to achieve nanoscopically-resolved films having morphologically- and topographically-complex surface features. A variety of surface analysis methods were used to probe the heterogeneity, including methods such as XPS and AFM and IRIR imaging. The complex surface features could provide evidence as to which structure-property relationships are important in designing anti-fouling coatings, *i.e.* to what degree chemical composition plays *versus* that of morphological and topographical nano- or microscopic surface features in preventing adsorption and adhesion of proteins, marine organisms, *etc*.

Highly interesting, multi-functional, amphiphilic PEO-*b*-PIp block copolymers were prepared *via* RAFT polymerization, spurning investigating into the challenges that occurred during polymer purification. In Chapter 4, two RAFT-capable PEO macro-CTAs, having $M_n$ values of 2 and 5 kDa, were prepared and used for the polymerization of isoprene, affording

block copolymers of varied lengths and compositions. GPC analysis of the PEO macro-CTAs and block copolymers showed remaining unreacted PEO macro-CTA. Following analysis of the GPC chromatograms using mathematical deconvolution, the blocking efficiency was estimated to be around 50% for the 5 kDa PEO macro-CTA and 64% for the 2 kDa CTA. The resultant polymers were also investigated for their abilities to self assemble in both water and decane, and the resulting regular and inverse assemblies, respectively, were analyzed with DLS, AFM, and TEM to ascertain their dimensions and properties. Assembly of PEO-*b*-PIp block copolymers in aqueous solution resulted in uniform micelles of varying sizes while the assembly in hydrophobic, organic solvent resulted in the formation of heterogeneous morphologies, including large aggregates, cylindrical and spherical structures. Thiol-ene crosslinked films of PEO-*b*-PIp showed promise against fouling biomacromolecules in the form of fluorescently-tagged proteins, lipopolysaccarhides and lectin.

Additional work into both improving and fundamentally studying the mechanical properties of HBFP-PEG were studied as reported in the Appendices. In Appendix 1 it was shown that the mechanical properties of amphiphilic crosslinked HBFP-PEG45 networks can be improved by introducing nanoscopic fillers, including SWNTs and $SiO_2$ nanoparticles. Each nanofiller was incorporated into the polymer networks non-covalently and was also engineered through chemical functionalization to perform as phase-designated reinforcing functional materials. SWNT-*g*-PEG and $SiO_2$-*g*-HBFP were designed to (1) improve the dispersion of fillers, nanotubes or spherical nanoparticles, in the amphiphilic matrices, (2) enhance the non-covalent interactions between the nanofillers and the polymers, and more importantly, (3) maintain reactive functionalities to be further covalently integrated into the complex networks.

Significantly greater reinforcement was achieved by covalent incorporation of SWNT-*g*-PEG into HBFP-PEG, than was observed for the physical doping method, whereas higher moduli were measured for nanocomposites physically doped with $SiO_2$ nanoparticles than for nanocomposites containing $SiO_2$-*g*-HBFP designed for covalent incorporation.

The internal chemical environment within HBFP-PEG polymer networks was probed using solid-state NMR studies, reported in Appendix 2. The results have provided unambiguous determination of the molecular-level structural reorganizations that lead to unique macroscopic mechanical properties for amphiphilic crosslinked networks of HBFP and PEG, wherein wetted HBFP-PEG networks with sub-45 wt% PEG showed stiffening as a result of rearrangement, proving the mechanism postulated in previous publications, whereas networks with greater than 55 wt% PEG showed properties similar to common hydrogel materials (that is, swelling of the matrix with a loss in modulus).

The applications of these materials towards preparing readily crosslinked commercial film coatings can be realized by undertaking a series of follow up experiments which are currently ongoing. Experiments into improving and investigating the adhesion of the thiol-ene coatings onto glass and eventually metal substrates is needed for end-use applicability. Additional investigation into the low VOC crosslinking of the films using natural sunlight can help provide impetus for using the films in an environmental and cost-efficient manner. Improvements into tuning the Young's modulus of the Boltorn-PEG films, perhaps involving the inclusion of silane components, could also be useful for improving latent non-fouling ability. Varying the type and MW of the PEG's in all of the polymer film compositions would lead to a better understanding of structure-property relationships, perhaps emulating the success of the properties discovered in the investigation of HBFP-PEG as seen in the Appendices.

An interesting series of crosslinked polymer film analogs were synthesized and crosslinked using commercially available or easily prepared non-toxic polymer components coupled with rapid crosslinking methods for ultimate use for marine anti-fouling applications. The overall impact of this work is not immediately realized, as many properties and functionalities still need fine tuning and improvement, but it can be seen that this work was striving towards providing the next generation of advanced materials in area or marine anti-fouling coatings, as well as answering many fundamental questions that occurred along the way.

# Appendix 1

## Hierarchical Inorganic-Organic Nanocomposites Possessing Amphiphilic and Morphological Complexities: Influence of nanofiller dispersion on mechanical performance

[Portions of this work have been published previously as Jinqi Xu, Jeremy W. Bartels, David A. Bohnsack, Tzu-Chia Tseng, Michael E. Mackay and Karen L. Wooley, *Advanced Functional Materials*, **2008**, *18*, 2733-2744]

**Abstract**

Novel nanocomposites possessing ternary compositions and complex morphologies have been prepared from amphiphilic crosslinked hyperbranched fluoropolymer-poly(ethylene glycol) (HBFP-PEG) in the presence of pristine and chemically-functionalized nanoscopic fillers, single-walled carbon nanotubes (SWNTs) and silica nanoparticles ($SiO_2$). Both SWNTs and $SiO_2$ were engineered specifically to become phase-designated reinforcing functional materials, SWNT-*g*-PEG and $SiO_2$-*g*-HBFP, which (1) improved the dispersion of fillers, nanotubes or spherical nanoparticles, in the amphiphilic matrices, (2) enhanced the non-covalent interactions between nanofillers and polymers, and more importantly, (3) maintained reactive functionalities to be further covalently integrated into the complex networks. Tensile moduli ($E_{dry}$) for these as-prepared SWNT-containing composites increased by up to 430% relative to the unfilled material, while those incorporated with $SiO_2$ had a 420% increase of $E_{dry}$. After swelling in water, the water absorption within the micro- and nano-channels of PEG-rich domains rigidified or softened the entire crosslinked network, as determined by the amount of PEG.

## Introduction

Over the past decade, amphiphilic chemically-crosslinked networks, comprised of co-continuous hydrophobic and hydrophilic phases, have been studied actively with designs for their broad application as biomedical devices, or their use in various other industries.(1, 2) Unlike typical hydrogels,(3-5) these complex crosslinked networks undergo morphological isomerization upon changes between organic and aqueous media, and have been described as being 'smart' by Erdodi and Kennedy.(1) This distinct phenomenon leads to reorganization of two phase-incompatible components on the surface as well as in the interior domains, and further transformations, to afford many unique materials properties, such as mechanical behavior,(6) morphological variability,(7, 8) sub-surface compartmentalizations and membrane performance,(9, 10) surface anti-biofouling,(10-12) and bio-capability.(13, 14) Moreover, such properties can be expanded with the variety and attributes of chemical compositions that polymers possess and the complexity and control of architectures that polymers provide,(15) making it feasible to fabricate these amphiphilic crosslinked networks into intelligent devices for many fields, including the marine coatings industry.(7, 11) It is challenging to devise efficient, environmentally-benign, and universally-applicable anti-fouling and fouling-release coatings to prevent biofouling (*i.e.*, inhibit adhesion and promote detachment) on the surfaces of ships and underwater structures.(16, 17) Historically, the application of traditional biocidal antifouling paints containing tributylytin (TBT) or copper compounds has exerted severe effects on marine lifeforms.(16-18) Recent efforts toward non-toxic, anti-biofouling coatings have focused primarily on fluoropolymers and silicone elastomers,(16, 17, 19) since these two polymers feature low critical surface energy, good chemical stability, and interesting mechanical properties.

Several studies have found that bioadhesion behaviors can be correlated with surface and bulk properties, including the critical surface energy,(16, 19) elastic modulus,(20, 21) thickness,(22) and surface wettability,(23) roughness(24) and reconstruction.(11, 25, 26)

Our strategy to develop novel, non-toxic anti-fouling materials utilizes amphiphilic crosslinked networks, which has relied upon chemically-crosslinked hyperbranched fluoropolymer-poly(ethylene glycol) (HBFP-PEG) materials (Scheme A1-1). This system was designed to provide complex surface topographies, morphologies, and compositions over nanoscopic and microscopic dimensions.(6, 7, 9, 11, 27) The ability of this material to inhibit protein adsorption and marine organism settlement has proven to be exceptional;(11) results that were attributed to intrinsic properties of both fluoropolymer and PEG, but also from surface features derived from the complex network and its surface reconstruction under water.(7) In addition to remarkable surface characteristics, coatings for marine application must be mechanically robust. Interestingly, our recent studies(6) on a series of HBFP-PEG crosslinked systems with varying ratios of hydrophobic HBFP/hydrophilic PEG showed that these materials exhibit unusual mechanical performance. The crosslinked networks, unlike hydrogels, became rigidified upon swelling with water (*ca*. 10-50 × enhancement of the elastic moduli, in comparison to the samples when dry) when PEG was the minority phase, whereas, when PEG was the majority component, they behaved as hydrogels, experiencing tensile modulus reductions upon water swelling.(6)

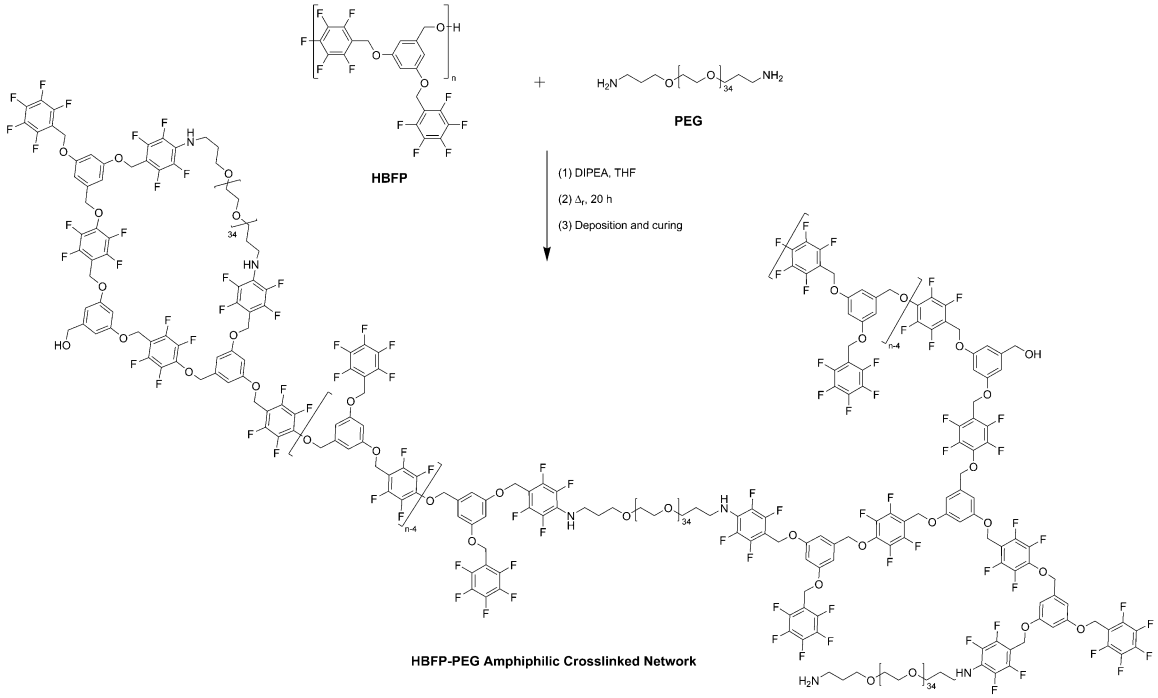


**Scheme A1-1.** Preparation of HBFP-PEG amphiphilic crosslinked networks.

In order to further improve mechanical performance of these amphiphilic crosslinked networks without impairing the anti-fouling performance, two types of exceptional nanoscopic fillers, one-dimensional single-walled carbon nanotubes and zero-dimensional silica nanoparticles, were chosen in our studies, since it has been shown in recent literature that a small amount of incorporation of these materials can improve bulk mechanical properties remarkably. These two well-studied nanofillers were chosen based upon their different compositions and aspect ratios, together with their abilities to undergo surface modification reactions and their demonstrated abilities to enhance the mechanical properties of polymer matrices. Research has shown that SWNTs have great potential as reinforcement fillers because of their exceptional mechanical, thermal, and electronic properties.(28-35) For instance, the tensile modulus of an isolated SWNT is up to 1 TPa, its tensile strength is 50-150 GPa, and its strain at fracture is only 5-10%.(34, 36-38) However, pristine SWNTs with large aspect ratios prefer to form aggregates, due to the strong, intrinsic van der Waals

interactions among nanotubes, and are insoluble in organic solvents or water. Uniform dispersion of SWNTs within polymer matrices,(29, 32, 33) is critical to improve the mechanical performance of the polymers, through the formation of nanocomposites.(28, 30, 31) Recently, many examples(39-45) have been used to show that chemical functionalization of carbon nanotubes (CNTs), to introduce small groups or polymer chains that were compatible with the polymer matrix, was one of most effective methods for improving dispersion. Such modification not only overcame the dispersion problem, but also introduced covalent and/or strong non-covalent interactions (such as hydrogen bonding, π-π interactions, or ionic interactions) between carbon nanotubes and their surrounding polymers. As a result, the load transfer from the matrix to the nanotubes was enhanced, while the occurrences of nanotubes pulling out from the matrix (rather than fracturing) and slippage among nanotubes were suppressed.(46-48) Similarly, amorphous $SiO_2$ nanoparticles with large surface areas and high surface energies form agglomerates readily.(49-51) The presence of many hydroxyl groups on their surfaces provides numerous methods to perform further chemical modification,(28, 31, 49-51) including sol-gel processing and *in situ* polymerization. Improved dispersion of $SiO_2$ nanoparticles in various polymer matrices and optimization of $SiO_2$/polymer interfaces to maximize stress transfer have led to excellent mechanical performance of many $SiO_2$-containing polymer nanocomposites.(52-56)

Physical and covalent incorporation of SWNTs and $SiO_2$ nanoparticles into matrices comprised of both HBFP and PEG was explored as a means to prepare four different types of amphiphilic ternary nanocomposites, for investigation of their mechanical properties. The HBFP-PEG crosslinked network has been known to be an intricate system with the presence of phase segregation, since HBFP is hydrophobic

and amorphous while PEG is hydrophilic and semi-crystalline. Previous studies(7, 11) demonstrated that HBFP-PEG45 (containing 45 wt% PEG), the most effective coating composition against protein adsorption and marine organism settlement, coincidently possessed the most complex, nanoscopically-resolved features on its surfaces. Therefore, we have focused upon HBFP-PEG45 in our current efforts. Herein, two strategies, physical doping and covalent incorporation, have been employed to introduce 'phase-designated' SWNTs and $SiO_2$ nanoparticles into HBFP-PEG45. The nanoscopic filler-to-polymer *vs*. filler-to-filler interactions determine the location and dispersion of any nanofiller, *e.g.* SWNTs or $SiO_2$ nanoparticles integrated within crosslinked polymer networks, which then determine the overall properties of the nanocomposites. In the present study, we have engineered SWNTs with diamine-terminated PEGs through amidation (SWNT-*g*-PEG), while $SiO_2$ nanoparticles were grafted with HBFP *via in situ* polymerization ($SiO_2$-*g*-HBFP). Given that SWNT-*g*-PEG is hydrophilic and $SiO_2$-*g*-HBFP is hydrophobic, the surfaces of these polymer-modified nanofillers were engineered to be structurally and morphologically equivalent with one specific phase of HBFP-PEG45, and also equipped for covalent integration into the network, providing an optimized nanofiller-polymer interface. The mechanical properties of four types of nanocomposites, as prepared in the dry state and after swelling in water, were investigated. HBFP-PEG45/SWNTs and HBFP-PEG45/$SiO_2$ were prepared *via* physical doping, and HBFP-PEG45-SWNT-*g*-PEG and HBFP-PEG45-$SiO_2$-*g*-HBFP through covalent integration of SWNT-*g*-PEG and $SiO_2$-*g*-HBFP, respectively, each with HBFP and PEG. Through this systematic study, we show that improved dispersion of nanoscopic reinforcing fillers within the complex amphiphilic crosslinked network could be achieved by using the covalent incorporation method. However, the

mechanical properties, especially the elastic moduli (*E*), of as-prepared nanocomposites containing SWNTs or $SiO_2$ nanoparticles were greatly improved by either preparation method. In addition, water-swollen nanocomposites, like the original HBFP-PEG systems,(6) exhibited atypical mechanical performance, rigidifying or softening, depending upon the amount of PEG.

**Experimental**

*Materials*: SWNTs (prepared *via* Chemical Vapor Deposition method, diameter = 1.1 nm, length = 0.5-100 μm, 90+%), bis(3-aminopropyl) terminated PEG ($M_n$ = 1,600 Da, $DP_n$ = 34), *N*,*N*-diisopropylethylamine (DIPEA, 99+%), and sodium (30 wt% dispersion in toluene, <0.1 mm particle size) were purchased from Aldrich Chemical Co. (Milwaukee, WI) and used as received. Pentafluorophenyltriethoxysilane was from Gelest, Inc. (Morrisville, PA). Hyperbranched fluoropolymer ($M_n$ = 9,000 Da, $M_w/M_n$ = 2.5) and 3,5-bis[(pentafluoro-benzyl)oxy]benzyl alcohol ($A_2B$ monomer for HBFP) were synthesized according to a procedure reported previously.(57) Silica nanoparticles (average particle size: 10 nm, surface area: ~ 640 $m^2/g$; 99.5% purity) were acquired from Nanostructured & Amorphous Materials, Inc. (Houston, TX). Prior to use, toluene and THF were distilled from Na/benzophenone.

*Characterization*: Infrared spectra were acquired on a Perkin-Elmer Spectrum BX FT-IR instrument using KBr pellets. $^1H$ and $^{19}F$ NMR spectra were recorded on a Varian 300 spectrometer interfaced to a UNIX computer using Mercury software. $^1H$ NMR spectra were acquired at 300 MHz, using the solvent proton signal as internal reference. $^{19}F$ NMR spectra were acquired at 282.2 MHz, using TFA as an external reference. Optical microscopy was performed on an Olympus IX-70 inverted

microscope (Olympus Corp., Tokyo, Japan) under bright-field conditions, and images were collected with an Olympus model C-5060 digital camera. SEM was performed using a Hitachi S-4500 field-emission scanning electron microscope. Samples were coated with gold. TEM cross-sections were prepared by using cryo-microtome (CRX, Power Tome XL, RMC, Boeckeler Instruments, Tucson, Arizona) at -60 °C. The sections were picked up on formvar-coated nickel grids and then imaged with a JEOL 100CX transmission electron microscope. TGA was conducted on a Mettler-Toledo TGA/SDTA851$^e$ instrument under a $N_2$ flow of 50 mL/min. DSC was performed on a Mettler-Toledo instrument equipped with DSC822$^e$ module, calibrated with an indium standard. Heating and cooling rates of 10 °C/min were employed. Melting temperatures ($T_m$) were recorded as the peak point of a melting endotherm, upon the first heating scan, and the glass transition temperatures ($T_g$) were determined as the midpoint of the inflection tangent, upon the third or subsequent heating scan using the STAR$^e$ SW 7.01 software.

*Functionalization of SWNTs*: Following the reported procedures,(58-60) the as-received pristine SWNTs (150 mg) were sonicated for 2-3 h at *ca*. 40 °C in aqueous nitric acid solution (3 M), then heated at reflux for 2-3 d. After the mixture was allowed to cool to room temperature (rt), it was diluted with DI water, and then the resulting SWNTs were collected by membrane filtration (0.22 μm pore size), washed (DI water 5×), and dried under vacuum. Typically, acid-treated SWNTs (40 mg) and diamine-terminated PEGs (650 mg) were stirred at 140 °C under nitrogen for 2-4 d, followed by addition of THF (*ca*. 20 mL) and 1 h sonication. The reaction mixture was then transferred to a pre-soaked dialysis tube (MWCO: *ca*. 12,000-14,000 Da) and dialyzed against THF for 4-5 d. After vigorous centrifugation to

remove insoluble SWNT solids, a dark-colored solution was acquired and then dried *in vacuo* to obtain SWNT-*g*-PEG.

*Grafting Polymerization of HBFP onto $SiO_2$ Nanoparticles*: $SiO_2$ nanoparticles were first surface functionalized with pentafluorophenyl groups. A sample of pristine $SiO_2$ nanoparticles (2.0 g) was preheated at 150 °C under vacuum for several hours to remove possible water adsorbed on their surfaces, followed by addition of anhydrous toluene (35 mL) under $N_2$. After 15 min sonication, pentafluorophenyltriethoxysilane (1.4 mL) was added to the $SiO_2$ dispersion in toluene. After solvent removal *via* centrifugation, these $SiO_2$ nanoparticles were then cured at 170 °C overnight under vacuum. Pentafluorophenyl-functionalized $SiO_2$ (PFP-$SiO_2$, 2.2 g) contained 3.4 wt% of pentafluorophenyl groups based upon TGA analysis. After a pre-treatment (3 h vacuum at 100 °C), PFP-$SiO_2$ (0.35 g) was mixed with 3,5-bis[(pentafluorobenzyl)oxy]benzyl alcohol (1.94 g) and anhydrous THF (20 mL) under $N_2$ at rt, followed by sonication and the addition of sodium (1.51 mL, 30 wt% suspension in toluene) to begin the polymerization.(57) The reaction mixture was maintained at reflux for 3-4 d. Additional aliquots of sodium were added after 1 and 3 d. The reaction mixture was then allowed to cool to rt and the polymerization was quenched by precipitation into a dilute $NaHCO_3$ aqueous solution. Upon isolation by centrifugation, the solid mixture was dissolved in $CH_2Cl_2$ and then centrifuged to separate the HBFP-grafted silica nanoparticles ($SiO_2$-*g*-HBFP) from the unbound HBFP polymer. After excessive $CH_2Cl_2$ washing (>5×, monitoring the filtrate by IR until no free HBFP was observed), neat $SiO_2$-*g*-HBFP (1.30 g, 57% yield) was obtained and dried under vacuum overnight. In addition, a control experiment on the generation of HBFP was conducted in the presence of pristine $SiO_2$ nanoparticles, which indicated that ≤ 5% unbound HBFP remained as a contaminant.

*Preparation of HBFP-PEG45/SWNTs and HBFP-PEG45/$SiO_2$ Nanocomposites*: A pre-gel solution of amphiphilic HBFP-PEG45 was prepared before the introduction of unfunctionalized nanoscopic fillers and formation of free-standing nanocomposite films.(27) Typically, HBFP (2.0 g, 4.16 mmol of pentafluorophenyl groups), diamine-terminated PEG (45 wt%, 1.64 g, 2.01 mmol of amino groups) and DIPEA (0.54 g, 4.16 mmol) were dissolved in anhydrous THF (50 mL). The solution was heated at reflux for 20 h under nitrogen to provide the pre-gel HBFP-PEG45 mixture, which remained clear and was later mixed with varied amounts of SWNTs or $SiO_2$ nanoparticles. Following a standard protocol,(6) microscope glass slides (Fisher Scientific, 75 mm × 25 mm × 1 mm) were surface functionalized with trimethylsilyl groups to afford a hydrophobic surface. Viscous pre-gel solutions of HBFP-PEG45 with doped nanoscopic fillers, after sonication, were cast onto trimethylsilyl-functionalized glass slides *via* drop deposition and were allowed to dry for several hours under ambient conditions. After these slides were cured at 100-110 °C under nitrogen for 2 h, the bubble-free, free-standing nanocomposite films, HBFP-PEG45/SWNTs and HBFP-PEG45/$SiO_2$, were obtained by razor-peeling from the glass surfaces. Their thicknesses ranged from 200 to 500 μm as measured by a digital micrometer.

*Preparation of HBFP-PEG45-SWNT-g-PEG and HBFP-PEG45-$SiO_2$-g-HBFP Nanocomposites:* Similar procedures as above were performed. The mixture of pre-gel HBFP-PEG45-SWNT-*g*-PEG was obtained after the 20-h-reflux procedure upon a reaction mixture in THF containing HBFP (2.0 g, 4.16 mmol of pentafluorophenyl groups), diamine-terminated PEG (45 wt%, 1.64 g, 2.01 mmol of amino groups), DIPEA (0.54 g, 4.16 mmol), and varied amounts of SWNT-*g*-PEG. In contrast, the pre-gel mixture of HBFP-PEG45-$SiO_2$-*g*-HBFP was prepared from the

mixture of diamine-terminated PEGs (45 wt%, 1.64 g, 2.01 mmol of amino groups), DIPEA (0.54 g, 4.16 mmol) and varied amounts of HBFP and $SiO_2$-*g*-HBFP, in which the total mass of HBFP added and HBFP contributed from $SiO_2$-*g*-HBFP remained constant at 2.0 g (4.16 mmol of pentafluorophenyl groups). These viscous, clear pre-gel solutions, after sonication, were then cast onto trimethylsilyl-functionalized glass slides *via* drop deposition and cured as described above. The thicknesses of these nanocomposite films, HBFP-PEG45-SWNT-*g*-PEG and HBFP-PEG45-$SiO_2$-*g*-HBFP, also ranged from 200 to 500 μm.

*Tensile Measurements on Dry and Swollen HBFP-PEG45 Nanocomposites:* Tensile measurements, based upon a test method adapted from ASTM D882-95a, were conducted using a Rheometrics Solids Analyzer, RSA III (TA Instruments, New Castle, DE), at 22 °C. The speed of testing was 2.54 mm/min and the initial grip separation was 10 mm. For each sample: (1) at least five dry specimens (dimensions: 22 mm × 6 mm × 0.2-0.5 mm) were tested; (2) two or three specimens were swollen in DI water for > 5 min and then tested after re-measuring their swollen cross-sectional areas (*i.e.*, width and thickness; employed in the calculation of tensile modulus). Due to slack in the film being taken up at the start of the test, a considerable toeing region was observed for many samples. This was corrected for by extrapolating the linear regime of the stress-strain response to zero stress, which was defined as the zero strain origin. For the dry samples, the tensile modulus ($E_{dry}$, MPa) was calculated as the slope of the initial linear (Hookean) portion of the stress-strain curve, and the ultimate tensile strength ($\sigma_{UTS}$, MPa) and strain to failure ($\varepsilon_f$, %) were also recorded. For the swollen films, the time needed (*ca*. 1-2 minutes) to complete the re-measurement of swollen cross section area and affix the samples to the

instrument for evaluation introduced uncertainties in the measured quantities at higher strain values, such that only the tensile modulus ($E_{wet}$, MPa) data are reported.

## Results and Discussion

### Functionalization of SWNTs with PEG (SWNT-*g*-PEG)

To prepare the SWNTs for compatibility with the hydrophilic, PEG-rich phases of the HBFP-PEG nanocomposites, functionalization of carbon nanotubes with diamine-terminated PEGs was performed (Scheme A1-2a). Pristine SWNTs were partially oxidized upon strong acid treatment, introducing carboxylic acid groups mainly on the ends of the nanotubes and also on defect sites along the nanotubes.(61) Thermal reactions of the carboxylic acid-functionalized carbon nanotubes with diamine-terminated PEGs then afforded SWNT-*g*-PEG through amidation.(58-60) The covalent attachment of PEG to SWNTs was supported by IR analyses, by the appearance of amide C=O stretching at 1663 $cm^{-1}$ in SWNT-*g*-PEG (Figure A1-3b) and coincident disappearance of the C=O stretching band of carboxylic acids at 1720 $cm^{-1}$ in acid-treated SWNTs (Figure A1-3a). In addition, the strong peak at 1113 $cm^{-1}$ (C-O stretching) and broad band centered at 2890 $cm^{-1}$ (C-H stretching) (Figure A1-3b) confirmed the presence of PEG. However, other structures, *via* acid-amine zwitterionic interactions(60) or non-covalent physical adsorption of the diamine-terminated PEG upon the SWNTs,(62) could also be partially responsible for the SWNT-*g*-PEG conjugate. Thermogravimetric analysis (TGA, Figure A1-1) indicated that SWNT-*g*-PEG contained *ca*. 5 wt% SWNTs. As expected,

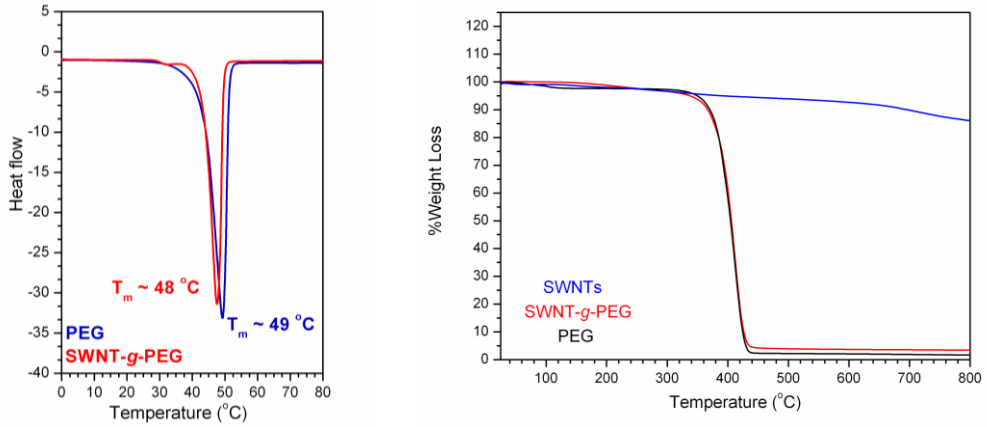


**Figure A1-1.** DSC curves (left) of diamine-terminated PEGs and SWNT-*g*-PEG and TGA mass loss curves (right) of SWNTs, SWNT-*g*-PEG and diamine-terminated PEGs.

SWNT-*g*-PEG was soluble in tetrahydrofuran (THF), dichloromethane, water, and other common solvents, remaining as stable dispersions for months. $^{1}$H NMR spectroscopy in $CDCl_3$ (Figure A1-2) observed the characteristic broad peak of the methylene protons of

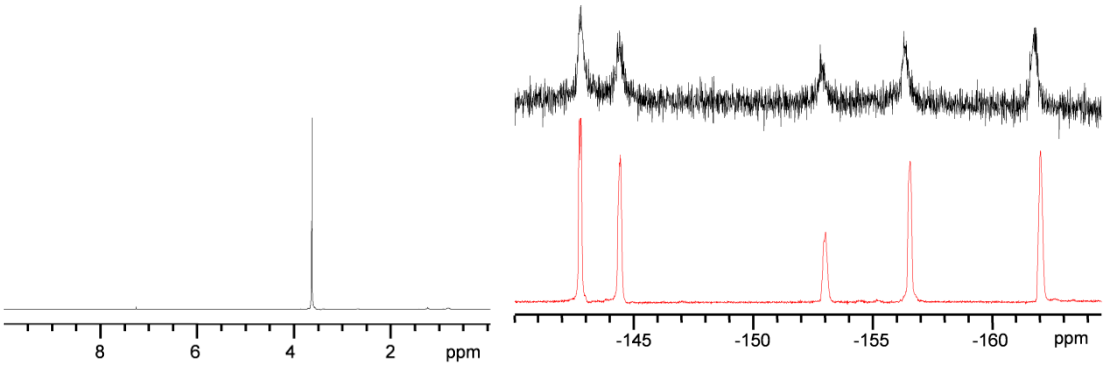


**Figure A1-2.** Solution-state $^{1}$H NMR spectrum (left, 300 MHz, $CDCl_3$) of SWNT-*g*-PEG and solution-state $^{19}$F NMR spectrum (right, 282.2 MHz, $CDCl_3$) of HBFP (red line) and $SiO_2$-*g*-HBFP (black line).

the PEG chains, a fraction of whose motions were slowed by close proximity to the neighboring carbon nanotubes.(59)

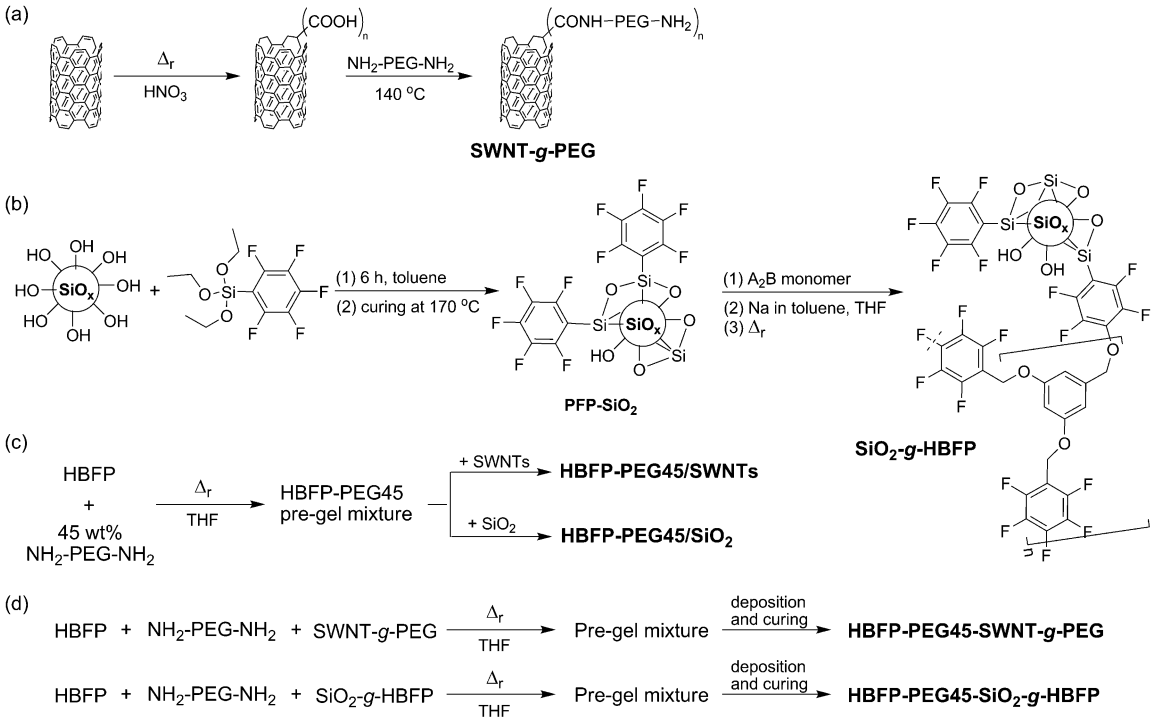


**Scheme A1-2.** Functionalization of nanoscopic fillers: (a) SWNTs with diamine-terminated PEGs and (b) $SiO_2$ nanoparticles grafted with HBFP; Preparation of nanocomposite films: (c) with physically doped fillers, HBFP-PEG45/SWNTs and HBFP-PEG45/$SiO_2$, and (d) with functionalized fillers *in situ*, HBFP-PEG45-SWNT-*g*-PEG and HBFP-PEG45-$SiO_2$-*g*-HBFP.

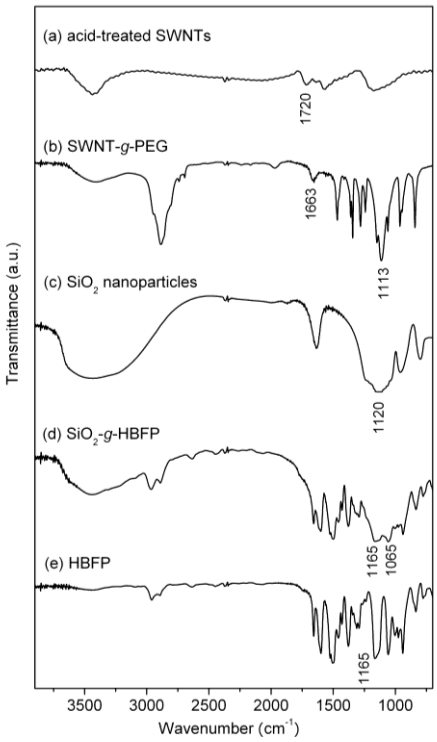


**Figure A1-3.** FTIR spectra of (a) acid-treated SWNTs, (b) SWNT-*g*-PEG, (c) pristine $SiO_2$ nanoparticles, (d) $SiO_2$-*g*-HBFP, and (e) HBFP.

### $SiO_2$ Nanoparticles Grafted with HBFP

The surface chemistry of the $SiO_2$ nanoparticles was modified to provide fluoroaromatic groups for partitioning within the hydrophobic, HBFP-rich domains, and covalent integration into the polymer matrix. Pristine $SiO_2$ nanoparticles were first modified with the functionalized silane coupling agent, pentafluorophenyltriethoxysilane, to introduce pentafluorophenyl groups (PFP) onto the surface, which later were involved in the growth of HBFP (Scheme A1-2b). The amount of PFP within these PFP-functionalized $SiO_2$ nanoparticles (PFP-$SiO_2$) was determined to be *ca*. 3.4 wt%, *i.e.*, approximately 63 PFP groups per $SiO_2$ particle (*ca*. 4 % consumption of hydroxyl groups available on the $SiO_2$ nanoparticle surface),

based upon TGA analysis (Figure A1-4). Adapted from procedures reported previously,(57)

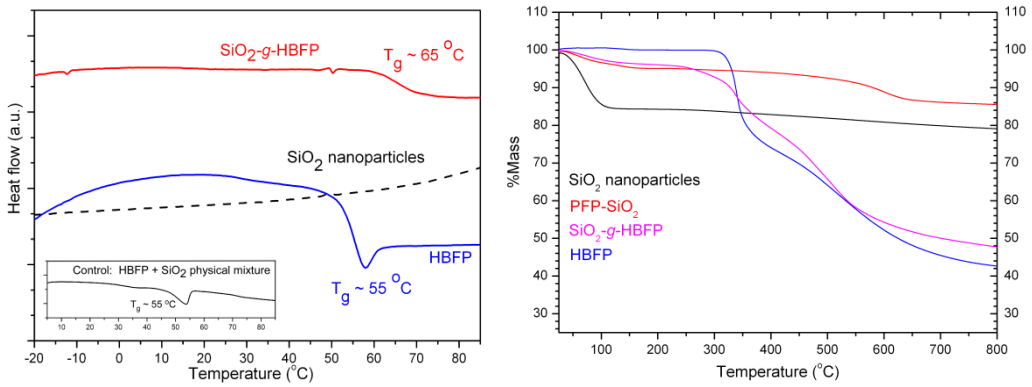


**Figure A1-4**. DSC curves (left) of $SiO_2$ nanoparticles, HBFP and $SiO_2$-*g*-HBFP as well as a physical mixture of $SiO_2$ nanoparticles and HBFP (inset), and TGA mass loss curves (right) of $SiO_2$ nanoparticles, PFP-$SiO_2$, $SiO_2$-*g*-HBFP and HBFP.

the $A_2B$ monomer for HBFP, 3,5-bis[(pentafluorobenzyl)oxy]benzyl alcohol, was polymerized in the presence of PFP-$SiO_2$ in THF *via* direct condensation, facilitated by the addition of fine sodium metal. This procedure allowed for grafting of the growing HBFP units onto the silica nanoparticles and also continued propagation from the nanoparticle surfaces, to give a combination of "grafting-onto" and "grafting-from" hyperbranched polymer brush growth upon the inorganic nanoparticulate substrates. After the polymerization was quenched, exhaustive washing and centrifugation removed unbound HBFP and afforded HBFP-grafted $SiO_2$ nanoparticles ($SiO_2$-*g*-HBFP). Characterization by gel permeation chromatography (GPC) determined that unbound HBFP had a number average molecular weight ($M_n$) of 2,700 Da with a relatively broad molecular weight distribution ($M_w/M_n$ = 2.5); the HBFP of $SiO_2$-*g*-HBFP was assumed to possess similar $M_n$ and $M_w/M_n$.

IR and NMR spectroscopy observed characteristic data for both the $SiO_2$ nanoparticles and the HBFP in samples of $SiO_2$-*g*-HBFP. The spectrum of $SiO_2$-*g*-

HBFP (Figure A1-3d) exhibits the characteristic C-F stretching at 1165 $cm^{-1}$ as does HBFP (Figure A1-3e), and also contains the anti-symmetric stretching of Si-O-Si at 1065 $cm^{-1}$, which is similar to that of pristine $SiO_2$ at 1120 $cm^{-1}$ (Figure A1-3c). Moreover, for $SiO_2$-*g*-HBFP particles, the C-C stretching modes of phenyl groups were present within the 1450-1650 $cm^{-1}$ range while the C-H stretching was observed from 2830-3100 $cm^{-1}$. In addition, $SiO_2$-*g*-HBFP particles gave a similar $^{19}F$ NMR spectrum as that observed for the unbound HBFP (Figure A1-2). The existence of a peak at -153 ppm, from the labile *para*-fluorine of the pentafluorophenyl groups,(57) indicated that $SiO_2$-*g*-HBFP retained the reactive sites that are capable of undergoing nucleophilic substitution with amine groups of PEG, to allow for covalent integration into the HBFP-PEG crosslinked networks.

Although the IR and NMR spectroscopy data could not confirm covalent coupling between the $SiO_2$ nanoparticles and HBFP, interestingly, the glass transition temperature ($T_g$) of HBFP was raised to *ca*. 65 °C in $SiO_2$-*g*-HBFP, 10 °C higher than that of HBFP or a physical mixture of HBFP and pristine $SiO_2$ nanoparticles (Figure A1-4), demonstrating the influence of covalently-incorporated silica on the mobility of the surrounding polymers. Moreover, the fact that the entire $SiO_2$-*g*-HBFP sample was able to be dispersed into THF, chloroform and dichloromethane provided further evidence for the covalent coupling. A high weight percentage of silica nanoparticles, 25.4 wt%, was found in $SiO_2$-*g*-HBFP, as observed by TGA (Figure A1-4). As shown in Figure A1-5a, PFP-functionalized silica nanoparticles still tended to form agglomerates, since they retain the high surface area and surface energy as those of pristine $SiO_2$. Such aggregations were partially disassembled to improve dispersion of $SiO_2$ *via* the grafting of HBFP. In this case, discrete HBFP-coated $SiO_2$ nanoparticles were visible (Figure A1-5b). Control experiments, involving the

polymerization of the $A_2B$ monomer in the presence of pristine $SiO_2$ nanoparticles, followed by the typical washing protocols, indicated that ≤ 5% unbound HBFP remains as a contaminant. However, this contaminant is not viewed as a liability, as the ultimate incorporation of these $SiO_2$-*g*-HBFP into the HBFP-PEG matrices involves the addition of HBFP.

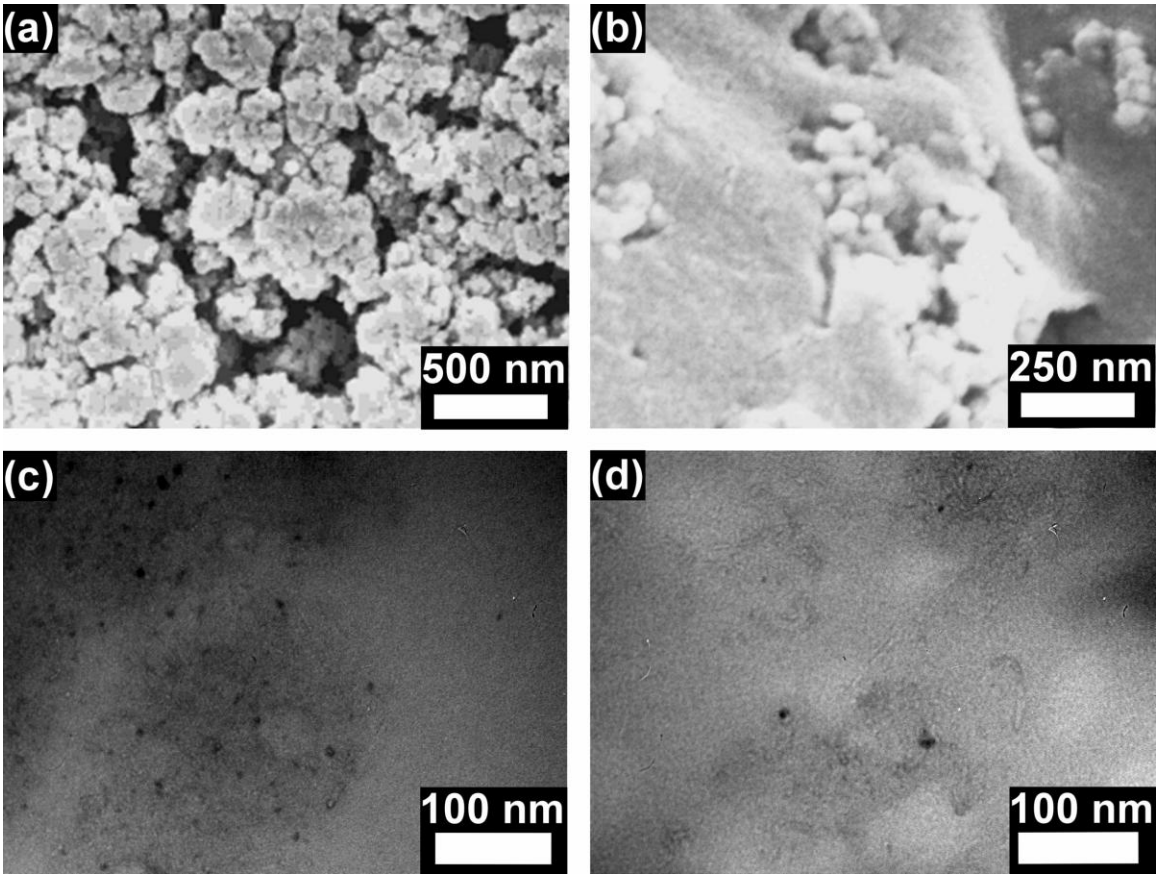


**Figure A1-5.** Typical SEM micrographs of (a) PFP-$SiO_2$ nanoparticles and (b) $SiO_2$-*g*-HBFP; TEM cross-sectional micrographs of cryo-microtomed samples of (c) HBFP-PEG45/SWNTs with 0.25 wt% physical doping and (d) HBFP-PEG45-SWNT-*g*-PEG with 0.25 wt% covalent incorporation.

**Preparation of HBFP-PEG45 Nanocomposite Films**

The formation of amphiphilic HBFP-PEG45 crosslinked networks involved the preparation of a pre-gel mixture of HBFP and diamine-terminated PEGs, by

heating the polymer reagents in THF at reflux for 20 h, followed by drop deposition and curing at 110 °C for 2 h.(7, 27) HBFP-PEG45 nanocomposites with physically doped nanofillers, HBFP-PEG45/SWNTs and HBFP-PEG45/$SiO_2$, were prepared through the mixing (sonication) of varying amounts of nanofillers with the pre-gel mixture (Scheme A1-2c), while those with covalent integration of modified nanofillers, HBFP-PEG45-SWNT-*g*-PEG and HBFP-PEG45-$SiO_2$-*g*-HBFP were from the pre-gel mixture of HBFP, diamine-terminated PEGs, and controlled amounts of the functionalized fillers, SWNT-*g*-PEG or $SiO_2$-*g*-HBFP (Scheme A1-2d).

TEM images of HBEP-PEG nanocomposites containing 0.25 wt% SWNTs (Figure A1-5c and A1-5d) indicate the uneven distribution of carbon nanotubes in these networks, with better dispersion occurring for the SWNTs that had undergone PEG grafting and covalent incorporation into the crosslinked polymer networks. Optical microscopy was performed as well (Figure A1-6b), which showed that the physical dispersion of pristine SWNTs in the amphiphilic HBFP-PEG network was

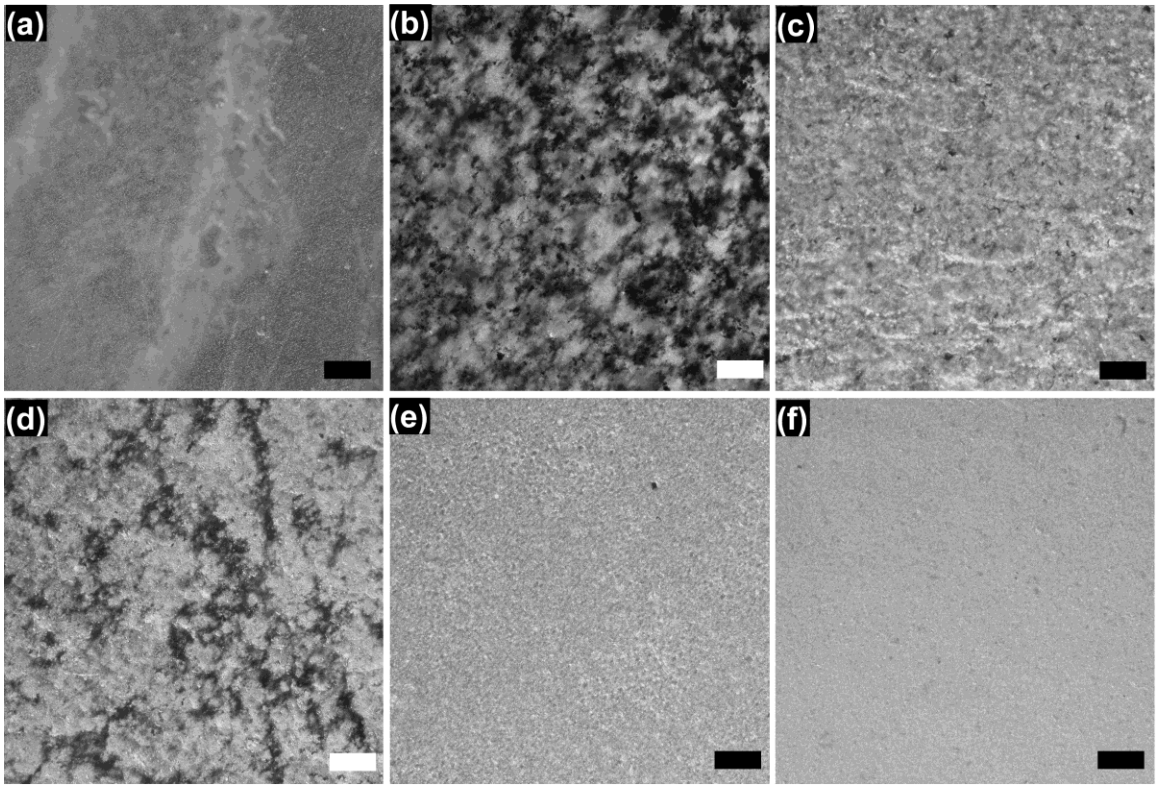


**Figure A1-6.** Optical micrographs of (a) HBFP-PEG45, (b) HBFP-PEG45/SWNTs with 0.25 wt% physical doping, (c) HBFP-PEG45-SWNT-*g*-PEG with 0.25 wt% covalent incorporation, (d) HBFP-PEG45-SWNT-*g*-PEG with 0.5 wt% covalent incorporation, (e) HBFP-PEG45/$SiO_2$ with 5 wt% physical doping, and (f) HBFP-PEG45-$SiO_2$-*g*-HBFP with 5 wt% covalent incorporation; Scale Bar: 100 μm.

poor. As expected, carbon nanotube aggregates were formed throughout the entire network, even when the doping amount was the lowest, 0.25 wt%. In contrast, HBFP-PEG45-SWNT-*g*-PEG films with ≤ 0.25 wt% covalent incorporation exhibited no noticeable conglomerates on the micrometer scale (Figure A1-6c), however, aggregation emerged and became prevailing with further addition of SWNT-*g*-PEG to higher wt% loadings (Figure A1-6d). For nanocomposites prepared from HBFP-PEG45 with silica nanoparticles, the agglomeration of $SiO_2$ certainly existed in the matrix, even though $SiO_2$ particles were chemically grafted with HBFP as noted by

SEM (Figure A1-5b). These differences are correlated with the mechanical performance of the nanocomposites (*vide infra*).

**Mechanical Properties of HBFP-PEG45/SWNTs and HBFP-PEG45-SWNT-*g*-PEG**

The tensile properties of the nanocomposites were determined as dry films (as prepared) and wet (after swelling in water). Typical stress-strain curves before and after water swelling are shown in Figure A1-7. These remarkable changes suggest that the mechanical performance of these nanocomposites were dependent upon the type and amount of nanofiller, and the incorporation strategy used, as well as the absence or presence of water.

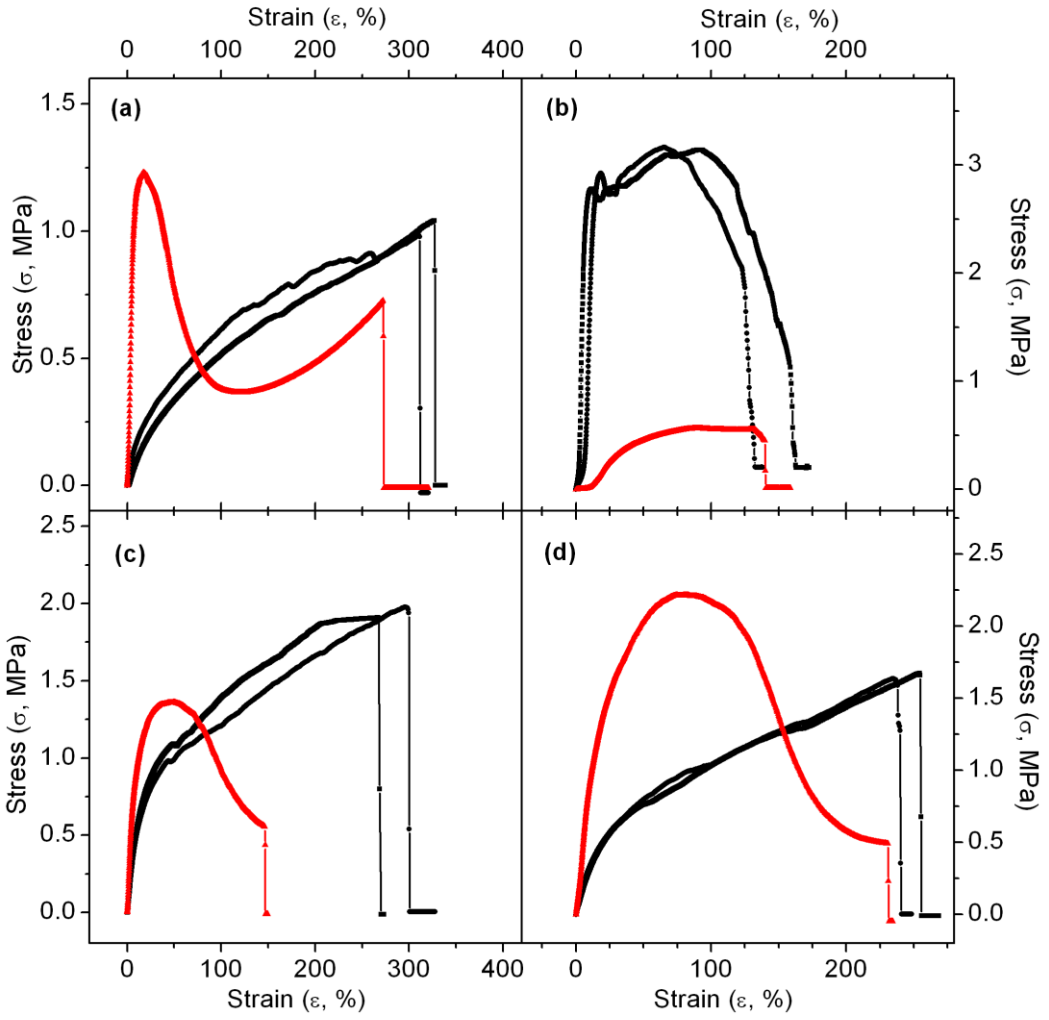


**Figure A1-7.** Typical stress-strain curves of (a) HBFP-PEG45/SWNTs with 2.5 wt% physical doping, (b) HBFP-PEG45-SWNT-*g*-PEG with 0.5 wt% covalent incorporation, (c) HBFP-PEG45/$SiO_2$ with 1.0 wt% physical doping, and (d) HBFP-PEG45-$SiO_2$-*g*-HBFP with 1.0 wt% covalent incorporation, as-prepared (■ and ●) and after swelling in water (▲).

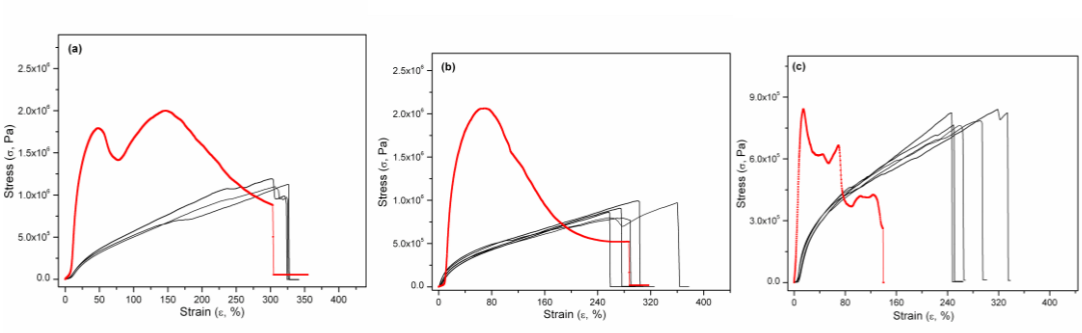


**Figure A1-8**. Typical stress-strain curves of HBFP-PEG45/SWNTs nanocomposite films containing (left) 0.25 wt% SWNTs, (center) 0. 5 wt% SWNTs and (right) 1.0 wt% SWNTs as the speed of testing was 2.54 mm/min. Black curves were obtained from films as prepared and red ones were from those after swelling in DI water for > 5 minutes.

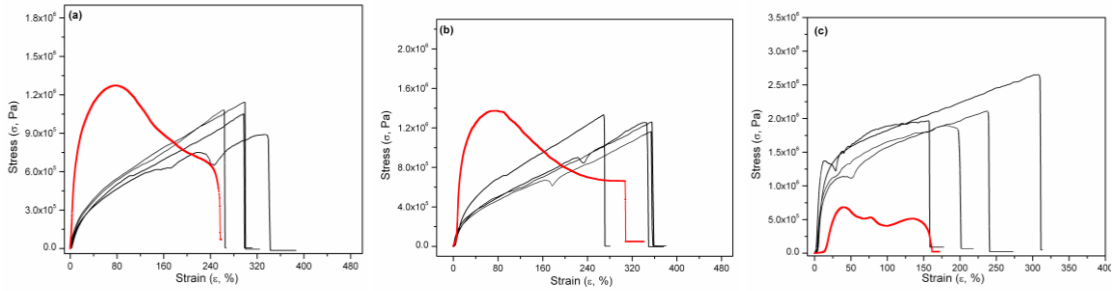


**Figure A1-9**. Typical stress-strain curves of HBFP-PEG45-SWNT-*g*-PEG nanocomposite films containing (left) 0.05 wt% SWNTs, (center) 0.1 wt% SWNTs and (right) 0.25 wt% SWNTs as the speed of testing was 2.54 mm/min. Black curves were obtained from films as prepared and red ones were from those after swelling in DI water for > 5 minutes.

*Before Swelling in Water*

Uniform dispersion of nanofillers within polymer matrices and proper engineering of the nanofiller/polymer interfacial regions are indispensable to

maximize the load transfer from the polymer to the nanofillers, resulting in the expected superior mechanical performance.(46-48) Consistent with the occurrence of SWNT aggregation, the tensile properties of as-prepared HBFP-PEG45/SWNTs nanocomposites exhibited none to moderate improvement over the control sample, HBFP-PEG45 (Table A1-1), with increasing SWNT loadings. For instance, there was little change in elastic modulus ($E_{dry}$) when the doping amount of pristine SWNTs was 0.25 wt%. The highest extent of physical doping, 2.5 wt% SWNTs, did lead to a modest 77% increase of $E_{dry}$. In addition, the ultimate tensile strength ($\sigma_{UTS}$) and the strain-to-failure ($\varepsilon_f$) values of HBFP-PEG/SWNTs were approximately 1.0 MPa and 300%, respectively, nearly equivalent to those of HBFP-PEG45. Such mechanical performance was foreseen because the main interplay between SWNTs and the amphiphilic network was based upon weak van der Waals interactions. Furthermore, the existence of SWNT bundles reduces the interfacial contact area between the nanotubes and polymer matrix, and also encourages slippage among SWNTs during tensile stretching. As a consequence, the stress transfer from the crosslinked HBFP-PEG amphiphilic network to SWNTs was limited.

**Table A1-1.** Summary of mechanical properties of HBFP-PEG45/SWNTs and HBFP-PEG45-SWNT-*g*-PEG nanocomposites containing varying amounts of carbon nanotubes fillers before and after water swelling.

| | | | Before swelling in water | | | | |
|---|---|---|---|---|---|---|---|
| Films | SWNTs [wt%] | PEG [wt%] [a] | Ultimate tensile strength [$\sigma_{UTS}$, MPa] | Failure strain [$\varepsilon_f$, %] | $E_{dry}$ [MPa] | $E_{wet}$ [MPa] [b] | $E_{wet}/E_{dry}$ |
| HBFP-PEG45 [c] | 0 | 45 | 0.985 ± 0.057 | 300 ± 60 | 1.44 ± 0.24 | 13.0 ± 2.5 | 9.0 |
| HBFP-PEG45 /SWNTs | 0.25 | 45 | 1.03 ± 0.07 | 320 ± 20 | 1.15 ± 0.15 | 13.7 ± 2.4 | 12 |
| | 0.5 | 45 | 0.880 ± 0.091 | 280 ± 50 | 2.12 ± 0.33 | 14.9 ± 1.0 | 7.1 |
| | 1.0 | 45 | 0.806 ± 0.033 | 270 ± 30 | 2.10 ± 0.45 | 11.0 ± 2.4 | 5.3 |
| | 2.5 | 45 | 1.07 ± 0.14 | 300 ± 30 | 2.55 ± 0.52 | 18.8 ± 2.4 | 7.4 |
| HBFP-PEG45-SWNT-*g*-PEG | 0.05 | 46 | 1.05 ± 0.10 | 300 ± 30 | 2.11 ± 0.35 | 11.6 ± 1.7 | 5.5 |
| | 0.1 | 47.5 | 1.36 ± 0.19 | 310 ± 40 | 3.62 ± 0.63 | 12.5 ± 2.0 | 3.5 |
| | 0.25 | 51 | 2.33 ± 0.42 | 240 ± 50 | 20.5 ± 4.0 [d] | 5.32 ± 0.60 | 0.26 |
| | 0.5 | 58 | 3.20 ± 0.11 | 80 ± 15 | 63.4 ± 10 [d] | 2.52 ± 0.52 | 0.04 |

[a] It was the total wt% of the diamine-terminated PEGs added and the PEG amount (calculated upon TGA analyses) from the SWNT-*g*-PEG introduced. [b] After swelling in DI water for > 5 min. [c] Previously reported.(6) [d] $E_{dry}$ of HBFP-PEG55 was 11.9 MPa.(6)

Since the crystalline polymer domains participate in the reinforcement of the network, it is important to understand the influence of carbon nanotubes on the crystallization process. It is known that CNTs can act as nucleating agents for several semi-crystalline polymers,(41, 47) including PEG.(45, 63, 64) However, many factors can alter the crystallization, including the interactions of the pristine or functionalized CNTs with their adjacent polymer chains, the thermal history of nanocomposites, and the amount of CNTs introduced.(45, 63, 64) For instance, fluorinated SWNTs exerted little changes on the crystallinity of PEG with up to 4 wt% loading.(45, 63, 64) As for HBFP-PEG, the properties of the phase segregated domains of semi-crystalline, hydrophilic PEG have been shown to be controlled partially through the curing process, which was performed at 110 °C, a temperature

that is significantly higher than the $T_g$ of HBFP and the $T_m$ of PEG.(7, 11, 27) The molten diamine-terminated PEGs reacted efficiently with HBFP to form the HBFP-PEG crosslinked amphiphilic network, resulting in suppression but not disappearance of crystallinity. Certainly, one-dimensional SWNTs could affect the formation of such complex networks to some degree. DSC studies (Figure A1-10a-d) indicated that the latent heats of fusion of HBFP-PEG45/SWNTs with a physical doping of 0.25 to 2.5 wt% were within *ca*. 28 to 31 J/g, similar to that of HBFP-PEG45. Meanwhile, the $T_m$ values for the PEG phases within these nanocomposites were lowered by *ca*. 2-5 °C, in comparison to that of HBFP-PEG45 (*ca*. 49 °C). Since there was no apparent increase in the degree of PEG crystallinity, the moderate improvements in $E_{dry}$ observed for HBFP-PEG45/SWNTs are attributed mainly to the reinforcing effect of CNTs.

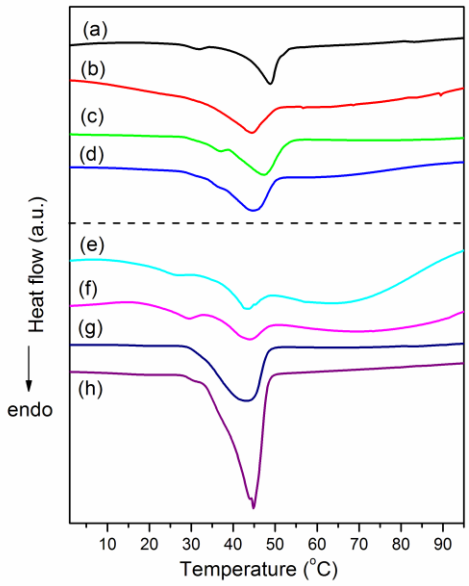


**Figure A1-10.** DSC curves of (a) HBFP-PEG45 and nanocomposites containing SWNTs: (b) HBFP-PEG45/SWNTs with 0.25 wt% physical doping, (c) HBFP-PEG45/SWNTs with 1.0 wt% physical doping, (d) HBFP-PEG45/SWNTs with 2.5

wt% physical doping, (e) HBFP-PEG45-SWNT-*g*-PEG with 0.05 wt% covalent incorporation, (f) HBFP-PEG45-SWNT-*g*-PEG with 0.1 wt% covalent incorporation, (g) HBFP-PEG45-SWNT-*g*-PEG with 0.25 wt% covalent incorporation and (h) HBFP-PEG45-SWNT-*g*-PEG with 0.5 wt% covalent incorporation.

The moduli of SWNT-containing nanocomposites increased significantly when SWNTs were covalently integrated into the HBFP-PEG45 network (Table A1-1, Figure A1-11b). HBFP-PEG45-SWNT-*g*-PEG nanocomposites with 0.05 wt% and 0.1 wt% covalent incorporation of PEG-functionalized SWNTs exhibited 47% and 150% increase in $E_{dry}$, respectively, over HBFP-PEG45; much better than observed for any of the physically incorporated HBFP-PEG45/SWNTs, even with 2.5 wt% doping. It is important to note that the actual amounts of PEG present in such covalently-integrated nanocomposites were higher than 45 wt%, due to contributions introduced from SWNT-*g*-PEG (Table A1-1). In fact, the actual amounts of PEG in the two nanocomposites containing 0.05 wt% and 0.1 wt% functionalized SWNTs were only slightly higher than 45 wt%. However, DSC studies (Figure A1-10e-f) demonstrated that their latent heats of fusion were approximately 16 J/g, much lower than HBFP-PEG45, and they possessed two melting transitions of PEG crystallites at *ca.* 30 °C and 44 °C. Clearly, the influence exerted by the PEG-coated SWNTs during the phase segregation and curing processes improved the dispersion of carbon nanotubes in the network (Figure A1-6b-c). Therefore, it is reasonable to conclude that the high $E_{dry}$ values are due to the optimized contact areas and numerous interactions between SWNTs and the polymer matrices, including weak van der Waals interactions and stronger interactions, such as covalent attachment, mechanical interlocking, and hydrogen bonding.(40, 43, 46)

An even more significant effect was observed at higher loadings of SWNT-*g*-PEG. HBFP-PEG45-SWNT-*g*-PEG with 0.25 wt% and 0.50 wt% covalent incorporation contained actual amounts of PEG in excess of 50 wt% (Table A1-1, Figure A1-11c). DSC studies (Figure A1-10g-h) also showed much higher latent heats of fusion (> 40 J/g) than observed for HBFP-PEG45. Therefore, $E_{dry}$ increased for HBFP-PEG45-SWNT-*g*-PEG with 0.25 wt% and 0.5 wt % covalent incorporation (51 wt% and 58 wt% actual PEG, respectively) by 73% and 430%, respectively, in comparison to HBFP-PEG55 (55 wt% PEG), whose $E_{dry}$ was 11.6 MPa.(6) As anticipated, $\sigma_{UTS}$ was also improved while $\varepsilon_f$ decreased. Attempts to prepare nanocomposites with higher loadings of SWNT-*g*-PEG (≥ 1 wt%) resulted in brittle films that could not be handled without damaging the sample prior to evaluation, presumably due to the overwhelming relative amount of PEG, which prevented complete crosslinking throughout an established matrix. The existence of even 0.25-0.5 wt% of SWNT-*g*-PEG could induce the aggregation of SWNTs as shown in Figure A1-6d, but it also positively affected the crystallization of PEG. Therefore, besides enhanced molecular interfacial interactions (*vide supra*), increased degrees of PEG crystallites could also contribute to the large improvement in tensile modulus for these two HBFP-PEG45-SWNT-*g*-PEG samples having higher SWNT loadings.

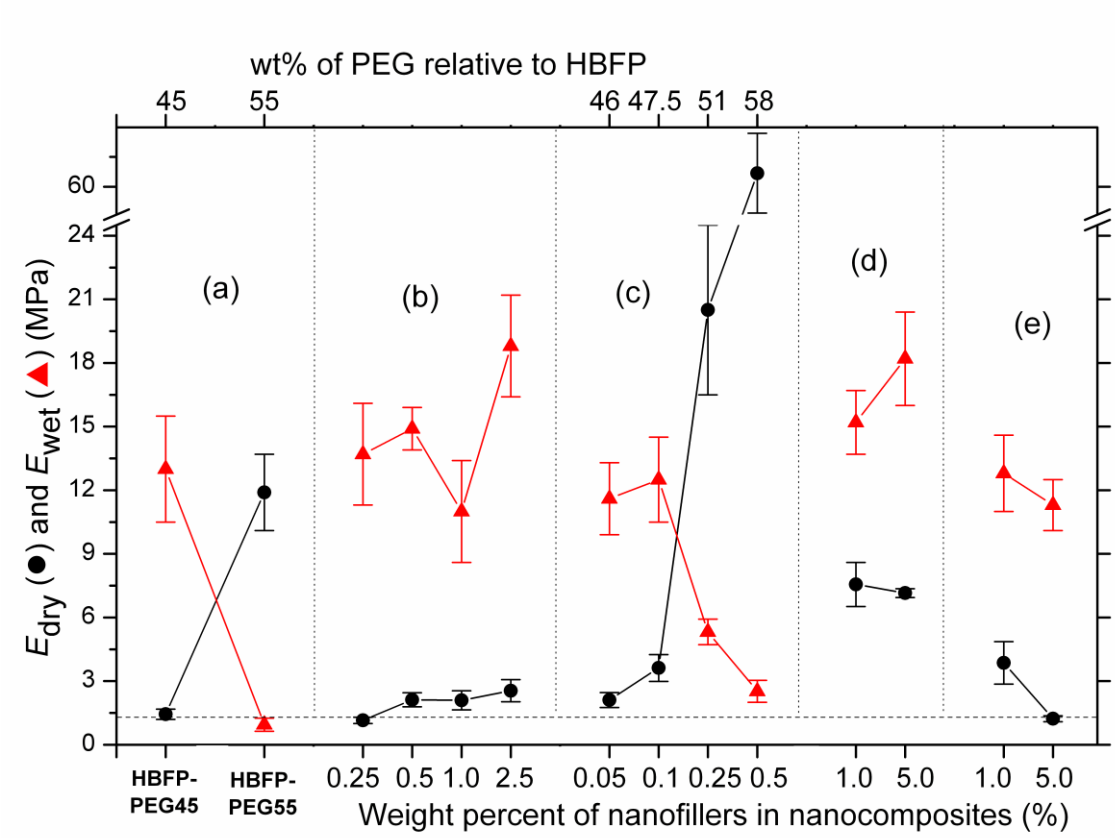


**Figure A1-11.** Direct comparison of elastic moduli of (a) HBFP-PEG45 and HBFP-PEG55,(6) (b) HBFP-PEG45/SWNTs, (c) HBFP-PEG45-SWNT-*g*-PEG, (d) HBFP-PEG45/$SiO_2$, and (e) HBFP-PEG45-$SiO_2$-*g*-HBFP as prepared (●) and after swelling in water (▲).

*After Swelling in Water*

It was suggested previously that water swelling in the PEG-rich domains of the HBFP-PEG networks can play contrasting roles which are dependent upon the amount of PEG introduced, relative to the HBFP.(6) Water swelling resulted in opposing effects, either rigidification or softening of the networks, with the crossover point being at *ca*. 50 wt% of PEG. HBFP-PEG45/SWNTs with varying amounts of physical doping and HBFP-PEG45-SWNT-*g*-PEG with 0.05 wt% and 0.1 wt% covalent incorporation exhibited $E_{wet}$ values, 11.0 to 18.8 MPa, similar to that of

HBFP-PEG45 after swelling in water, as expected, since these nanocomposites contained around 45 wt% of PEG (Table A1-1, Figure A1-11a-c). Their ratio of $E_{wet}$ to $E_{dry}$ was > 3, and even up to 12, an extraordinary enhancement. The current hypothesis is that water swelling in the micro- and nano-channels of crystalline PEG-rich phases led to the disappearance of PEG crystallites, but such swollen domains remained within the network and deformed the amorphous HBFP-rich regions, rigidifying the whole network.(6) For HBFP-PEG45-SWNT-*g*-PEG with 0.25 wt% and 0.5 wt% covalent incorporation, their $E_{wet}$ values were 5.32 MPa and 2.52 MPa, respectively, much lower than their $E_{dry}$ values (Table A1-1, Figure A1-11c). Like HBFP-PEG55 (Figure A1-11a) and HBFP-PEG63,(6) water swelling in the PEG-rich domains simply softened the whole network (as water swelling does with hydrogels(3-5)) when PEG existed as the major and dominant phase.

**Mechanical Properties of HBFP-PEG45/$SiO_2$ and HBFP-PEG45-$SiO_2$-*g*-HBFP**

*Before Swelling in Water*

Differing from pristine SWNTs, silica nanoparticles dispersed in the HBFP-PEG45 network can interact strongly with the polymer matrices, *i.e.*, with the PEG-rich regions through H-bonding.(65, 66) The presence of such strong non-covalent interactions is capable of intensifying the load transfer from the polymer to its neighboring $SiO_2$, as can be seen in typical stress-strain curves in Figure A1-12. As anticipated, $E_{dry}$ increased around 400-420%

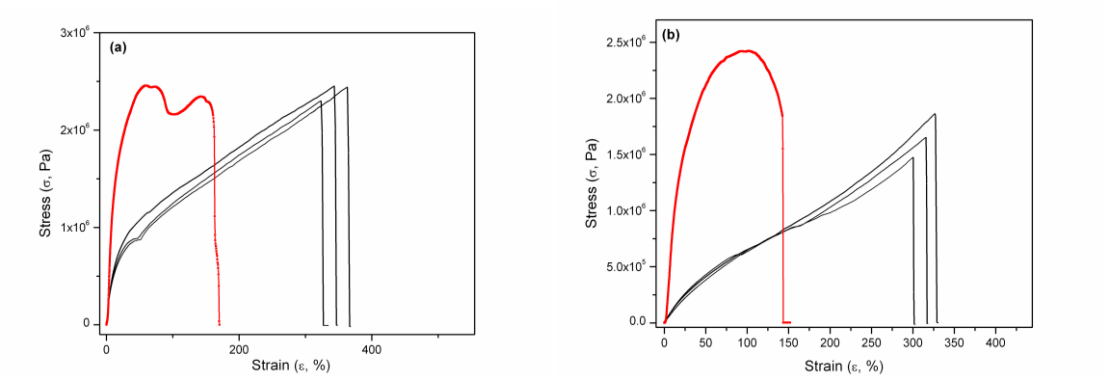


**Figure A1-12.** Typical stress-strain curves of (a) HBFP-PEG45/$SiO_2$ nanocomposite films containing 5 wt% physical doping and (b) HBFP-PEG45-$SiO_2$-*g*-HBFP nanocomposite films containing 5 wt% covalent incorporation as the speed of testing was 2.54 mm/min. Black curves were obtained from films as prepared and red ones were from those after swelling in DI water for > 5 minutes.

for HBFP-PEG45/$SiO_2$ with 1 or 5 wt% physical doping, compared to HBFP-PEG45 (Table A1-2, Figure A1-11d). Meanwhile, $\sigma_{UTS}$ became higher while $\varepsilon_f$ remained the same (within experimental error). The occurrence of inevitable agglomeration of pristine $SiO_2$ in the network probably contributes to the little variation between the 1 wt% and 5 wt% doping. In addition, the crystallization of PEG was affected slightly under the low loading levels (Figure A1-13b-c). Both nanocomposites showed smaller latent heats of fusion (*ca*. 20 J/g) than HBFP-PEG45, since the strong interactions between $SiO_2$ and its nearby PEG chains can restrict the mobility of these chains and the formation of PEG crystallites.(65, 66)

Through the grafting strategy, the surface features of $SiO_2$ nanoparticles were altered with the intention to transform them to present hydrophobic surfaces. Surprisingly, HBFP-PEG45-$SiO_2$-*g*-HBFP nanocomposites, where $SiO_2$-*g*-HBFP was similar to the hydrophobic HBFP-rich phases and covalently integrated into the entire network, exhibited poorer mechanical properties than those observed for HBFP-

PEG45/$SiO_2$ (Table A1-2, Figure A1-11e), although there was still improvement over HBFP-PEG45 at 1 wt% loading. $E_{dry}$ for HBFP-PEG45-$SiO_2$-*g*-HBFP with 1 wt% loading improved 170% over HBFP-PEG45, however, when the loading was 5 wt% there was no statistical difference in comparison to the $E_{dry}$ for HBFP-PEG45. DSC studies showed decreased crystallinity in these $SiO_2$-*g*-HBFP-containing systems (Figure A1-13d-e). Further studies are required to determine the structure-property relationships for these materials, including whether the $SiO_2$-*g*-HBFP nanoparticles present an incompletely-coated, amphiphilic surface that influences the regions within HBFP-PEG to which the nanofillers partition.

**Table A1-2.** Summary of mechanical properties of HBFP-PEG45/$SiO_2$ and HBFP-PEG-$SiO_2$-*g*-HBFP nanocomposites containing varying amounts of nanoscopic silica particles before and after water swelling.

| | | | Before swelling in water | | | | |
|---|---|---|---|---|---|---|---|
| Samples | $SiO_2$ [wt%] | PEG [wt%] | Ultimate tensile strength [$\sigma_{UTS}$, MPa] | Failure strain [$\varepsilon_f$, %] | $E_{dry}$ [Mpa] | $E_{wet}$ [MPa] [a] | $E_{wet}/E_{dry}$ |
| HBFP-PEG45 [b] | 0 | 45 | 0.985 ± 0.057 | 300 ± 60 | 1.44 ± 0.24 | 13.0 ± 2.5 | 9.0 |
| HBFP-PEG45 /$SiO_2$ | 1.0 | 45 | 1.86 ± 0.14 | 260 ± 40 | 7.56 ± 1.04 | 15.2 ± 1.5 | 2.0 |
| | 5.0 | 45 | 2.41 ± 0.10 | 340 ± 30 | 7.15 ± 0.21 | 18.2 ± 2.2 | 2.6 |
| HBFP-PEG45-$SiO_2$-*g*-HBFP | 1.0 | 45 | 1.47 ± 0.29 | 250 ± 30 | 3.86 ± 1.00 | 12.8 ± 1.8 | 3.3 |
| | 5.0 | 45 | 1.67 ± 0.16 | 320 ± 20 | 1.23 ± 0.14 | 11.3 ± 1.2 | 9.2 |

[a] After swelling in DI water for > 5 min. [b] Previously reported.(6)

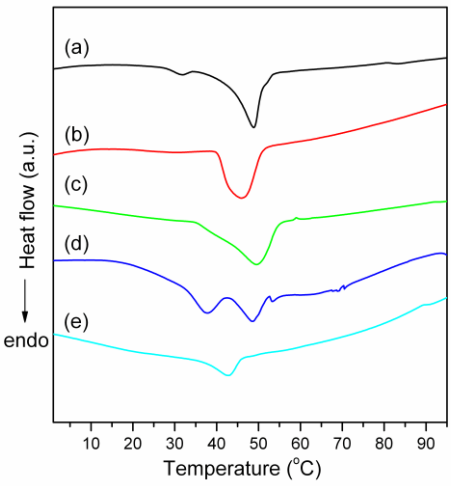


**Figure A1-13.** DSC curves of HBFP-PEG45 (a) and nanocomposites containing $SiO_2$ nanoparticles: (b) HBFP-PEG45/$SiO_2$ with 1.0 wt% physical doping, (c) HBFP-PEG45/$SiO_2$ with 5.0 wt% physical doping, (d) HBFP-PEG45-$SiO_2$-*g*-HBFP with 1.0 wt% covalent incorporation, and (e) HBFP-PEG45-$SiO_2$-*g*-HBFP with 5.0 wt% covalent incorporation.

*After Swelling in Water*

The $SiO_2$-containing HBFP-PEG nanocomposite samples contained PEG as a minority phase, giving what is now characterized as the standard behavior of an increased modulus after water swelling. As shown in Table A1-2 and Figure A1-11d-e, the four $SiO_2$ nanocomposites exhibited similar $E_{wet}$ values, 11.3 to 18.2 MPa, since the amount of PEG relative to HBFP was 45 wt%.

**Conclusions**

In summary, we have demonstrated that the mechanical properties of amphiphilic crosslinked HBFP-PEG45 networks can be improved by introducing nanoscopic fillers, including SWNTs and $SiO_2$ nanoparticles. Each nanofiller was

incorporated into the polymer networks non-covalently and was also engineered through chemical functionalization to perform as phase-designated reinforcing functional materials. SWNT-*g*-PEG and $SiO_2$-*g*-HBFP were designed to (1) improve the dispersion of fillers, nanotubes or spherical nanoparticles, in the amphiphilic matrices, (2) enhance the non-covalent interactions between the nanofillers and the polymers, and more importantly, (3) maintain reactive functionalities to be further covalently integrated into the complex networks.

Significantly greater reinforcement was achieved by covalent incorporation of SWNT-*g*-PEG into HBFP-PEG, than was observed for the physical doping method. The covalent incorporation of PEG-functionalized SWNTs at 0.5 wt% of loading into HBFP-PEG45 gave a 430 % increase of elastic modulus as prepared, which exceeded the 77% increase in $E_{dry}$ for the physically-doped material, even at 2.5 wt% loading. The improved mechanical properties can be attributed to improved dispersion of SWNTs upon PEG grafting onto SWNTs and their covalent integration into the HBFP-PEG, in comparison to the physical doping of pristine SWNTs into HBFP-PEG. In addition, the existence of PEG crystallites is critical to the mechanical performance of SWNT-containing nanocomposites as prepared. It is clear that one-dimensional SWNTs, when functionalized with PEG, affected the crystallization of PEG. Such influence is expected to be generally applicable to other semi-crytalline polymers, broadening and fortifying the application of target polymer-functionalized SWNTs within matrices of multiple polymer components. As expected, swelling with water rigidified the amphiphilic crosslinked networks when PEG was the minor phase, whereas it softened the nanocomposites when the amount of PEG increased to become the major component.

For the samples loaded physically and covalently with silica nanoparticles, surprising results were obtained. Higher moduli were measured for nanocomposites doped with $SiO_2$ nanoparticles than for nanocomposites containing $SiO_2$-*g*-HBFP designed for covalent incorporation. The physically-incorporated $SiO_2$ nanoparticles gave greater than 400% increase in $E_{dry}$ at loadings of 1-5 wt%. In contrast, the modulus decreased with increased loading of $SiO_2$-*g*-HBFP, providing no difference from neat HBFP-PEG45 when the loading was 5 wt%. The strong non-covalent interactions between hydroxyl groups on the surfaces of silica nanoparticles and PEG chains could make the load transfer more effective, explaining the significant moduli increases with HBFP-PEG45/$SiO_2$. Meanwhile, $SiO_2$-*g*-HBFP is expected to have many of those hydrophilic surface sites buried beneath the HBFP coating, which would reduce the polar, hydrophilic and hydrogen-bonding interactions and may place these nanofillers into different domains or interfaces within HBFP-PEG.

Our studies suggest that control of the location and dispersion of the nanofiller is a prerequisite to improving the mechanical performance of polymers, especially those with complex network structures. At this point, we have investigated two types of nanofillers of differing compositions, shapes and surface chemistries. It is interesting that the main correlation that can be drawn is that those nanofillers having a hydrophilic surface, capable of favorable interactions with and crystallization of the PEG-rich phases within HBFP-PEG complex networks, provide significant increases in modulus, when the samples were analyzed as prepared, in the dry state. Furthermore, even in the presence of the nanofillers, swelling of micro- and nanochannels of PEG-rich domains gave the most dramatic modulus increases, but these effects gave end results that are similar to HBFP-PEG45, having no nanofiller present. Further studies are needed to probe the exact structural details that lead to the

observed properties, which will then allow for new directions to be followed that may produce materials that can take advantage of both the influences of water and nanofillers.

**References**


(1) Erdodi, G.; Kennedy, J. P. (2006) Amphiphilic conetworks: Definition, synthesis, applications. *Prog. Polym. Sci. 31*(1), 1-18.

(2) Patrickios, C. S.; Georgiou, T. K. (2003) Covalent amphiphilic polymer networks. *Curr. Opin. Colloid Interface Sci. 8*(1), 76-85.

(3) Peppas, N. A.; Hilt, J. Z.; Khademhosseini, A.; Langer, R. (2006) Hydrogels in biology and medicine: From molecular principles to bionanotechnology. *Adv. Mater. 18*(11), 1345-1360.

(4) Langer, R.; Tirrell, D. A. (2004) Designing materials for biology and medicine. *Nature 428*(6982), 487-492.

(5) Drury, J. L.; Mooney, D. J. (2003) Hydrogels for tissue engineering: scaffold design variables and applications. *Biomaterials 24*(24), 4337-4351.

(6) Xu, J.; Bohnsack, D. A.; Mackay, M. E.; Wooley, K. L. (2007) Unusual Mechanical Performance of Amphiphilic Crosslinked Polymer Networks. *J. Am. Chem. Soc. 129*(3), 506-507.

(7) Gudipati, C. S.; Greenlief, C. M.; Johnson, J. A.; Prayongpan, P.; Wooley, K. L. (2004) Hyperbranched fluoropolymer and linear poly(ethylene glycol) based amphiphilic crosslinked networks as efficient antifouling coatings: An insight into the surface compositions, topographies, and morphologies. *J. Polym. Sci., Part A: Polym. Chem. 42*(24), 6193-6208.

(8) Isayeva, I. S.; Kasibhatla, B. T.; Rosenthal, K. S.; Kennedy, J. P. (2003) Characterization and performance of membranes designed for macroencapsulation/implantation of pancreatic islet cells. *Biomaterials 24*(20), 3483-3491.

(9) Brown, G. O.; Bergquist, C.; Ferm, P.; Wooley, K. L. (2005) Unusual, Promoted Release of Guests from Amphiphilic Cross-Linked Polymer Networks. *J. Am. Chem. Soc. 127*(32), 11238-11239.

(10) Nicolson, P. C.; Vogt, J. (2001) Soft contact lens polymers: an evolution. *Biomaterials 22*(24), 3273-3283.

(11) Gudipati, C. S.; Finlay, J. A.; Callow, J. A.; Callow, M. E.; Wooley, K. L. (2005) The Antifouling and Fouling-Release Performance of Hyperbranched Fluoropolymer (HBFP)-Poly(ethylene glycol) (PEG) Composite Coatings Evaluated by Adsorption of Biomacromolecules and the Green Fouling Alga Ulva. *Langmuir 21*(7), 3044-3053.

(12) Haigh, R.; Fullwood, N.; Rimmer, S. (2002) Synthesis and properties of amphiphilic networks 2: a differential scanning calorimetric study of poly(dodecyl methacrylate-stat-2,3 propandiol-1-methacrylate-stat-ethandiol dimethacrylate) networks and adhesion and spreading of dermal fibroblasts on these materials. *Biomaterials 23*(16), 3509-3516.

(13) Barakat, I.; Dubois, P.; Grandfils, C.; Jerome, R. (1999) Macromolecular engineering of polylactones and polylactides. XXV. Synthesis and characterization of bioerodible amphiphilic networks and their use as controlled drug delivery systems. *J. Polym. Sci., Part A: Polym. Chem. 37*(14), 2401-2411.

(14) Bruns, N.; Tiller, J. C. (2005) Amphiphilic network as nanoreactor for enzymes in organic solvents. *Nano Lett. 5*(1), 45-48.

(15) George, O. (2004) *Principles of Polymerization* 4th ed.; John Wiley & Sons: Hoboken, NJ.

(16) Anderson, C.; Atlar, M.; Callow, M. E.; Candries, M.; Milne, A.; Townsin, R. L. (2003) The development of foul-release coatings for seagoing vessels. *J. Mar. Des. Oper.* (B4), 11-23.

(17) Brady, R., Jr. (2000) Clean hulls without poisons: devising and testing nontoxic marine coatings. *J. Coatings Tech. 72*(900), 44-56.

(18) Champ, M. A. (2000) A review of organotin regulatory strategies, pending actions, related costs and benefits. *Sci. Total Environ. 258*(1-2), 21-71.

(19) Brady, R. F. (1999) Properties which influence marine fouling resistance in polymers containing silicon and fluorine. *Prog. Org. Coatings 35*(1-4), 31-35.

(20) Berglin, M.; Loenn, N.; Gatenholm, P. (2003) Coating modulus and barnacle bioadhesion. *Biofouling 19*(Suppl.), 63-69.

(21) Brady, R. F. (2001) A fracture mechanical analysis of fouling release from nontoxic antifouling coatings. *Prog. Org. Coatings 43*(1-3), 188-192.

(22) Wendt, D. E.; Kowalke, G. L.; Kim, J.; Singer, I. L. (2006) Factors that influence elastomeric coating performance: the effect of coating thickness on basal plate morphology, growth and critical removal stress of the barnacle Balanus amphitrite. *Biofouling 22*(1/2), 1-9.

(23) Carman, M.; Estes, T.; Feinberg, A.; Schumacher, J.; Wilkerson, W.; Wilson, L.; Callow, M.; Callow, J.; Brennan, A. (2006) Engineered antifouling microtopographies - correlating wettability with cell attachment. *Biofouling 22*(1/2), 11-21.

(24) Hoipkemeier-Wilson, L.; Schumacher, J.; Carman, M.; Gibson, A.; Feinberg, A.; Callow, M.; Finlay, J.; Callow, J.; Brennan, A. (2004) Antifouling potential of lubricious, micro-engineered, PDMS elastomers against zoospores of the green fouling alga Ulva (Enteromorpha). *Biofouling 20*(1), 53-63.

(25) Yarbrough, J. C.; Rolland, J. P.; DeSimone, J. M.; Callow, M. E.; Finlay, J. A.; Callow, J. A. (2006) Contact Angle Analysis, Surface Dynamics, and Biofouling Characteristics of Cross-Linkable, Random Perfluoropolyether-Based Graft Terpolymers. *Macromolecules 39*(7), 2521-2528.

(26) Krishnan, S.; Ayothi, R.; Hexemer, A.; Finlay, J. A.; Sohn, K. E.; Perry, R.; Ober, C. K.; Kramer, E. J.; Callow, M. E.; Callow, J. A.; Fischer, D. A. (2006) Anti-Biofouling Properties of Comblike Block Copolymers with Amphiphilic Side Chains. *Langmuir 22*(11), 5075-5086.

(27) Gan, D.; Mueller, A.; Wooley, K. L. (2003) Amphiphilic and hydrophobic surface patterns generated from hyperbranched fluoropolymer/linear polymer networks: Minimally adhesive coatings via the crosslinking of hyperbranched fluoropolymers. *J. Polym. Sci., Part A: Polym. Chem. 41*(22), 3531-3540.

(28) Vaia, R. A.; Maguire, J. F. (2007) Polymer Nanocomposites with Prescribed Morphology: Going beyond Nanoparticle-Filled Polymers. *Chem. Mater. 19*(11), 2736-2751.

(29) Tasis, D.; Tagmatarchis, N.; Bianco, A.; Prato, M. (2006) Chemistry of Carbon Nanotubes. *Chem. Rev. 106*(3), 1105-1136.

(30) Moniruzzaman, M.; Winey, K. I. (2006) Polymer Nanocomposites Containing Carbon Nanotubes. *Macromolecules 39*(16), 5194-5205.

(31) Mark, J. E. (2006) Some Novel Polymeric Nanocomposites. *Acc. Chem. Res. 39*(12), 881-888.

(32) Sun, Y. P.; Fu, K.; Lin, Y.; Huang, W. (2002) Functionalized Carbon Nanotubes: Properties and Applications. *Acc. Chem. Res. 35*(12), 1096-1104.

(33) Niyogi, S.; Hamon, M. A.; Hu, H.; Zhao, B.; Bhowmik, P.; Sen, R.; Itkis, M. E.; Haddon, R. C. (2002) Chemistry of Single-Walled Carbon Nanotubes. *Acc. Chem. Res. 35*(12), 1105-1113.

(34) Dresselhaus, M.; Dresselhaus, G.; Avouris, P. (2001) *Carbon Nanotubes: Synthesis, Properties and Applications*. Springer-Verlag: Berlin.

(35) Ajayan, P. M.; Zhou, O. Z. (2001) Applications of carbon nanotubes. *Top. Appl. Phys. 80*, 391-425

(36) Wong, E. W.; Sheehan, P. E.; Lieber, C. M. (1997) Nanobeam mechanics: Elasticity, strength, and toughness of nanorods and nanotubes. *Science 277*(5334), 1971-1975.

(37) Yu, M. F.; Lourie, O.; Dyer, M. J.; Moloni, K.; Kelly, T. F.; Ruoff, R. S. (2000) Strength and breaking mechanism of multiwalled carbon nanotubes under tensile load. *Science 287*(5453), 637-640.

(38) Walters, D. A.; Ericson, L. M.; Casavant, M. J.; Liu, J.; Colbert, D. T.; Smith, K. A.; Smalley, R. E. (1999) Elastic strain of freely suspended single-wall carbon nanotube ropes. *Appl. Phys. Lett. 74*(25), 3803-3805.

(39) Shofner, M. L.; Khabashesku, V. N.; Barrera, E. V. (2006) Processing and mechanical properties of fluorinated single-wall carbon nanotube-polyethylene composites. *Chem. Mater. 18*(4), 906-913.

(40) Chen, J.; Ramasubramaniam, R.; Xue, C.; Liu, H. (2006) A versatile, molecular engineering approach to simultaneously enhanced, multifunctional carbon-nanotube-polymer composites. *Adv. Funct. Mater. 16*(1), 114-119.

(41) Liu, L. Q.; Barber, A. H.; Nuriel, S.; Wagner, H. D. (2005) Mechanical properties of functionalized single-walled carbon-nanotube/poly(vinyl alcohol) nanocomposites. *Adv. Funct. Mater. 15*(6), 975-980.

(42) Gao, J.; Itkis, M. E.; Yu, A.; Bekyarova, E.; Zhao, B.; Haddon, R. C. (2005) Continuous Spinning of a Single-Walled Carbon Nanotube-Nylon Composite Fiber. *J. Am. Chem. Soc. 127*(11), 3847-3854.

(43) Zhu, J.; Peng, H. Q.; Rodriguez-Macias, F.; Margrave, J. L.; Khabashesku, V. N.; Imam, A. M.; Lozano, K.; Barrera, E. V. (2004) Reinforcing epoxy polymer composites through covalent integration of functionalized nanotubes. *Adv. Funct. Mater. 14*(7), 643-648.

(44) Sen, R.; Zhao, B.; Perea, D.; Itkis, M. E.; Hu, H.; Love, J.; Bekyarova, E.; Haddon, R. C. (2004) Preparation of single-walled carbon nanotube reinforced polystyrene and polyurethane nanofibers and membranes by electrospinning. *Nano Lett. 4*(3), 459-464.

(45) Geng, H. Z.; Rosen, R.; Zheng, B.; Shimoda, H.; Fleming, L.; Liu, J.; Zhou, O. (2002) Fabrication and properties of composites of poly(ethylene oxide) and functionalized carbon nanotubes. *Adv. Mater. 14*(19), 1387-1390.

(46) Barber, A. H.; Cohen, S. R.; Eitan, A.; Schadler, L. S.; Wagner, H. D. (2006) Fracture transitions at a carbon-nanotube/polymer interface. *Adv. Mater. 18*(1), 83-87.

(47) Cadek, M.; Coleman, J. N.; Ryan, K. P.; Nicolosi, V.; Bister, G.; Fonseca, A.; Nagy, J. B.; Szostak, K.; Beguin, F.; Blau, W. J. (2004) Reinforcement of polymers with carbon nanotubes: The role of nanotube surface area. *Nano Lett. 4*(2), 353-356.

(48) Ajayan, P. M.; Schadler, L. S.; Giannaris, C.; Rubio, A. (2000) Single-walled carbon nanotube-polymer composites: Strength and weakness. *Adv. Mater. 12*(10), 750-753.

(49) Sanchez, C.; Laine, R. M.; Yang, S.; Brinker, C. J. (2002) *Organic/Inorganic Hybrid Materials* Materials Research Society Warrendale, PA, Vol. 726.

(50) Sayari, A.; Hamoudi, S. (2001) Periodic Mesoporous Silica-Based Organic-Inorganic Nanocomposite Materials. *Chem. Mater. 13*(10), 3151-3168.

(51) Hjelm, R. J.; Nakatani, A. I.; Gerspacher, M.; Krishnamoorti, R. (2001) *Filled and Nanocomposite Polymer Materials*. Materials Research Society: Warrendale, PA, Vol. 661.

(52) Zhou, H. J.; Rong, M. Z.; Zhang, M. Q.; Ruan, W. H.; Friedrich, K. (2007) Role of reactive compatibilization in preparation of nanosilica/polypropylene composites. *Polym. Eng. Sci. 47*(4), 499-509.

(53) Hong, R. Y.; Fu, H. P.; Zhang, Y. J.; Liu, L.; Wang, J.; Li, H. Z.; Zheng, Y. (2007) Surface-modified silica nanoparticles for reinforcement of PMMA. *J. Appl. Polym. Sci. 105*(4), 2176-2184.

(54) Yang, F.; Nelson, G. L. (2004) PMMA/silica nanocomposite studies: Synthesis and properties. *J. Appl. Polym. Sci. 91*(6), 3844-3850.

(55) Wu, W.; Wagner, M. H.; Xu, Z. D. (2003) Surface treatment mechanism of nano-SiO2 and the properties of PP/nano-SiO2 composite materials. *Colloid Polym. Sci. 281*(6), 550-555.

(56) Hajji, P.; David, L.; Gerard, J. F.; Pascault, J. P.; Vigier, G. (1999) Synthesis, structure, and morphology of polymer-silica hybrid nanocomposites based on hydroxyethyl methacrylate. *J. Polym. Sci., Part B: Polym. Phys. 37*(22), 3172-3187.

(57) Mueller, A.; Kowalewski, T.; Wooley, K. L. (1998) Synthesis, Characterization, and Derivatization of Hyperbranched Polyfluorinated Polymers. *Macromolecules 31*(3), 776-786.

(58) Ramanathan, T.; Fisher, F. T.; Ruoff, R. S.; Brinson, L. C. (2005) Amino-functionalized carbon nanotubes for binding to polymers and biological systems. *Chem. Mater. 17*(6), 1290-1295.

(59) Huang, W. J.; Fernando, S.; Allard, L. F.; Sun, Y. P. (2003) Solubilization of single-walled carbon nanotubes with diamine-terminated oligomeric poly(ethylene glycol) in different functionalization reactions. *Nano Lett. 3*(4), 565-568.

(60) Chen, J.; Rao, A. M.; Lyuksyutov, S.; Itkis, M. E.; Hamon, M. A.; Hu, H.; Cohn, R. W.; Eklund, P. C.; Colbert, D. T.; Smalley, R. E.; Haddon, R. C. (2001) Dissolution of full-length single-walled carbon nanotubes. *J. Phys. Chem. B 105*(13), 2525-2528.

(61) Liu, J.; Rinzler, A. G.; Dai, H. J.; Hafner, J. H.; Bradley, R. K.; Boul, P. J.; Lu, A.; Iverson, T.; Shelimov, K.; Huffman, C. B.; Rodriguez-Macias, F.; Shon, Y. S.; Lee, T. R.; Colbert, D. T.; Smalley, R. E. (1998) Fullerene pipes. *Science 280*(5367), 1253-1256.

(62) Chattopadhyay, D.; Galeska, L.; Papadimitrakopoulos, F. (2003) A route for bulk separation of semiconducting from metallic single-wall carbon nanotubes. *J. Am. Chem. Soc. 125*(11), 3370-3375.

(63) Yang, B. X.; Shi, J. H.; Pramoda, K. P.; Goh, S. H. (2007) Enhancement of stiffness, strength, ductility and toughness of poly(ethylene oxide) using phenoxy-grafted multiwalled carbon nanotubes. *Nanotechnology 18*(12).

(64) Vaisman, L.; Marom, G.; Wagner, H. D. (2006) Dispersions of surface-modified carbon nanotubes in water-soluble and water-insoluble polymers. *Adv. Funct. Mater. 16*(3), 357-363.

(65) Sur, G. S.; Sun, H. L.; Lee, T. J.; Lyu, S. G.; Mark, J. E. (2003) Composites prepared by penetrating poly(ethylene oxide) chains into mesoporous silica. *Colloid Polym. Sci. 281*(11), 1040-1045.

(66) Ding, J.; Maitra, P.; Wunder, S. L. (2003) Characterization of the interaction of poly(ethylene oxide) with nanosize fumed silica: Surface effects on crystallization. *J. Polym. Sci., Part B: Polym. Phys. 41*(17), 1978-1993.

# Appendix 2

# Solid-state NMR investigations of the unusual effects resulting from the nanoconfinement of water within amphiphilic crosslinked polymer networks

[Portions of this work have been published previously as Ryutaro Ohashi, Jeremy W. Bartels, Jinqi Xu, Karen L. Wooley, and Jacob Schaefer *Advanced Functional Materials*, **2009**, *19*(21), 3404-3410]

## Abstract

Two types of solid-state $^{19}F$ NMR experiments were used to characterize phase-separated hyperbranched fluoropolymer-poly(ethylene glycol) (HBFP-PEG) crosslinked networks. Mobile (soft) domains were detected in the HBFP phase by a rotor-synchronized Hahn echo under magic-angle spinning conditions, and rigid (hard) domains by a solid echo with no magic-angle spinning. The mobility of chains was detected in the PEG phase by $^{1}H\rightarrow^{13}C$ cross-polarization transfers with $^{1}H$ spin-lock filters with and without magic-angle spinning. The interface between HBFP and PEG phases was detected by a third experiment, which utilized a $^{19}F\rightarrow^{1}H$-(spin diffusion)-$^{1}H\rightarrow^{13}C$ double transfer with $^{13}C$ solid-echo detection. The results of these experiments show that composition-dependent PEG inclusions in the HBFP glass rigidify on hydration, consistent with an increase in macroscopic tensile strength.

## Introduction

The combination of dissimilar polymer components to effect microscopic phase segregation is a simple process, whereby the polymers order themselves and produce well-defined nanoscopic features.(1-3) Such processes have led to materials having feature sizes below those accessed lithographically for use in microelectronics devices.(4) For many applications, however, the interest is merely in the hybridization of incompatible polymer materials to produce domains of nanoscopic size. These materials possess distinctive compositions and properties, even in the absence of high degrees of order. Of particular interest are mixing of cationic *vs*. anionic polyelectrolytes,(5) or hydrophilic *vs*. hydrophobic polymers,(6, 7) to achieve interpenetrating, self-assembled polymer networks that have utility for tissue-engineering scaffolds,(8) complex delivery vessels,(9) membranes,(10) and non-toxic anti-biofouling coatings.(11)

Distinguishing features of amphiphilic crosslinked networks arise from the properties of the individual hydrophobic and hydrophilic polymer components, which can be trapped kinetically by subsequent covalent crosslinking between the dissimilar regimes. These materials(12) have many desirable features including unique swelling properties(13-16) important for anti-fouling coatings for the marine environment,(17) and inhibition of biomolecule adsorption or promotion of release(18) for use as potential pharmaceutical or biomedical devices. Such systems can be prepared readily, but often pose unique challenges in the characterization of their heterogeneous structures and morphologies. Surface analyses have observed compositional heterogeneity(19) and complex topographies(20) for amphiphilic crosslinked networks. SANS,(21) X-ray,(22) TEM,(23) and EPR(24) studies have confirmed the extension of the morphological heterogeneity in addition to nano- and microphase segregation throughout the bulk of such materials.

Crosslinking of a hyperbranched fluoropolymer (HBFP, $M_n$ = 9000 Da) by bis(3-amino-propyl)-terminated poly(ethylene glycol) (PEG, $M_n$ = 1600 Da) creates a complex amphiphilic network (Figure A2-1).(20) The hyperbranched architecture of HBFP introduces n + 1 pentafluorophenyl groups, where n is the degree of polymerization. Each pentafluorophenyl group is capable of undergoing reaction with an amino terminus of the di-functional linear PEG to produce a crosslinked network, containing intermolecular crosslinks, intramolecular loops, or attached PEGs that retain a free amino terminus (Figure A2-1). Because of the coincident phase segregation and covalent crosslinking, domains that are rich in hydrophobic HBFP or hydrophilic PEG are generated, which are connected by an amphiphilic interface. The composition of such crosslinked networks is altered according to the stoichiometry of the HBFP and PEG employed during their preparation. These materials were found to have unique properties that were hypothesized to result from nanoscopic channels and confinement of guest molecules.(23, 25) Interestingly, when PEG was the minor component, swelling with water gave a ten-fold increase in modulus, relative to the dry state, whereas when PEG was the major component, the materials behaved as ordinary hydrogels, exhibiting a ten-fold reduction in modulus upon the introduction of water.(25) Trapping of water within PEG-rich nanochannels was invoked to explain the unusual increase in modulus for samples having less than 50 wt% PEG.

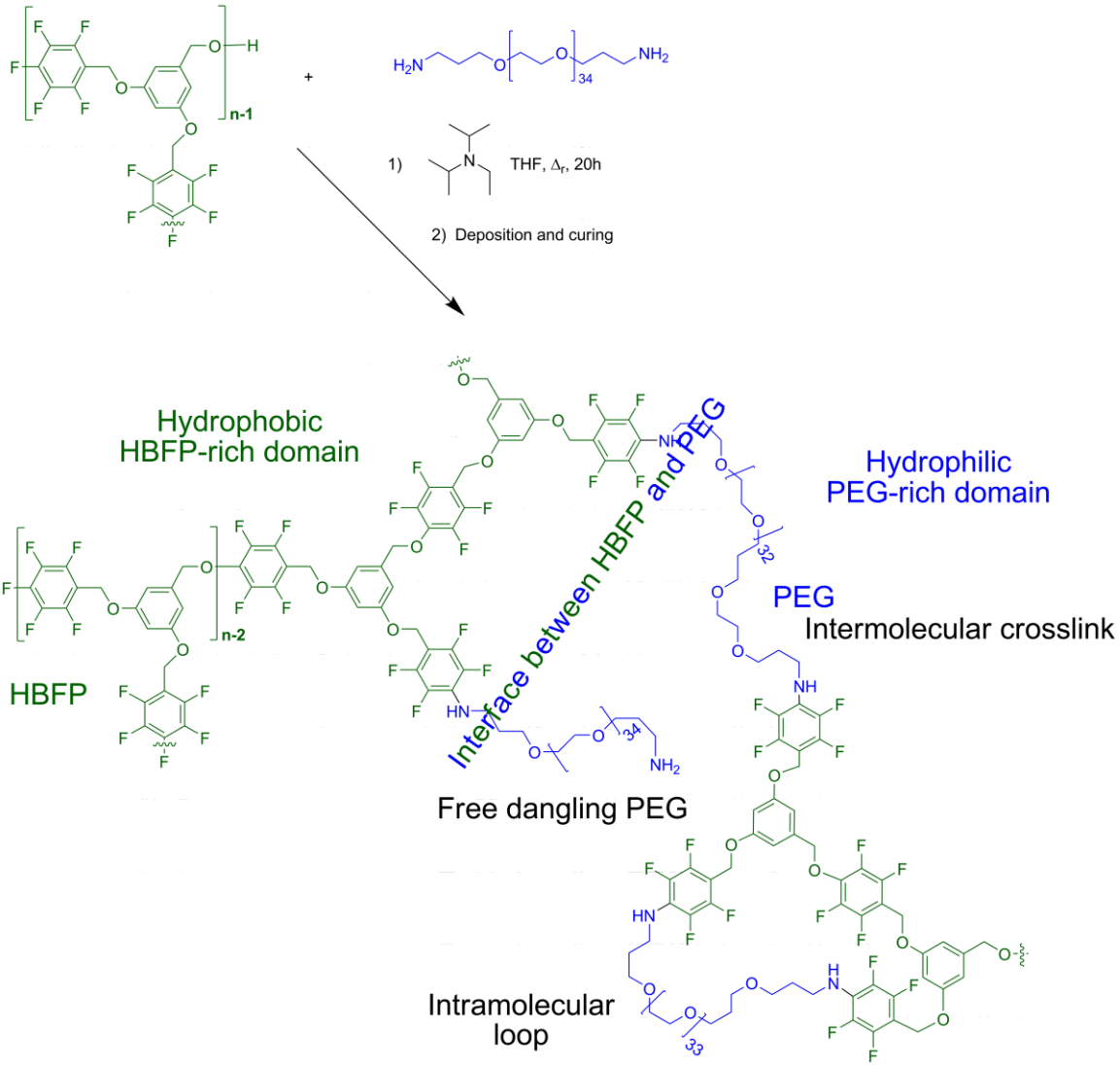


**Figure A2-1.** The crosslinking reaction between HBFP (green) and diamino PEG (blue), produces an amphiphilic HBFP-PEG crosslinked network, illustrated with the various structural elements and the resulting chemical environments.

In an effort to find molecular-level evidence for this behavior, solid-state NMR studies were undertaken to investigate the chemical and physical environment within these complex networks at compositions just below and above 50 wt% PEG, each with and without the addition of water. Two networks were investigated, HBFP-PEG45 and HBFP-PEG55, having 45 and 55 wt% PEG, respectively. Solid-state NMR was used to probe those domains and the interfacial contact areas between them using $^{19}F$ (HBFP)

and $^{13}C$ (PEG) at natural abundance. The results of these experiments show that when PEG is the minor component, and the interfacial PEG regions of HBFP-PEG networks become swollen with water, the interface is constrained and rigidified. In contrast, when PEG is the major component, swelling with water provides greater mobility throughout the matrix, giving rise to hydrogel-like characteristics.

**Experimental**

*Materials.* Tetrahydrofuran (Aldrich, HPLC grade inhibitor free), N,N-diisopropylethylamine (Aldrich, 99 % +), chlorotrimethylsilane (Aldrich, 99 % +), poly(ethylene glycol) bis (3-aminopropyl) terminated ($M_n$ = 1600 Da, $DP_n$ = 34, Aldrich) and sodium (30 wt% dispersion in toluene, <0.1 mm particle size) were used as received. Prior to use, toluene and THF were distilled from Na/benzophenone. The hyperbranched fluoropolymer (HBFP, $M_n$ = 9,000 Da, $M_w/M_n$ = 2.5) was synthesized according to a previously reported procedure (20, 26).

*Procedure for the preparation of hyperbranched fluoropolymer with bis(3-aminopropyl) terminated poly(ethylene glycol), HBFP-PEG45.* Mixtures of HBFP (2.0 g, 4.2 mmol of pentafluorophenyl groups), diamine-terminated PEG (45 wt%, 1.64 g, 2.01 mmol of amino groups) and DIPEA (0.54 g, 4.2 mmol) were dissolved in anhydrous THF (50 mL). The solution was heated at reflux for 20 h under nitrogen to provide the pre-gel HBFP-PEG45 mixture, then cast onto trimethylsilyl-functionalized glass slides *via* drop deposition. The slides were allowed to dry for several hours under ambient conditions, and were then cured at 110 °C under nitrogen for 2 h, producing bubble-free, free-standing films that could be easily removed from the glass substrate with a razor blade and cut into pieces for mechanical properties testing (Table A2-1) and evaluation by solid-state NMR.

**Table A2-1**. Summary of data for HBFP-PEG45 and HBFP-PEG55 amphiphilic networks [a] before and after water swelling.(25)

| Films | PEG wt % | Ultimate tensile strength [$\sigma_{UTS}$, MP | Failure strai [$\varepsilon_f$, %] | $E_{dry}$ [MPA] | $E_{wet}$ [MP/ [b] | Swelling % ba on mass [b] | Swelling % based volume [b] |
|---|---|---|---|---|---|---|---|
| **HBFP-PEG45** | 45 | 0.985 ± 0.057 | 30 ± 60 | 1.44 ± 0.24 | 13.0 ± 2. | 85 | 100 |
| **HBFP-PEG55** | 55 | 1.29 ± 0.22 | 13 ± 20 | 11.9 ± 1.8 | 0.95 ± 0. | 112 | 125 |

[a] Tensile measurements were performed on a RSA III instrument under ambient conditions. [b] After swelling in water for 5 min.

*Solid-State NMR Spectrometer*. Experiments were performed at 12 T using a four-frequency transmission-line probe(27) having a 12-mm long, 6-mm inner-diameter analytical coil, and a Chemagnetics/Varian ceramic spinning module. Samples were spun using a thin-wall Chemagnetics/Varian (Fort Collins, CO/Palo Alto, CA) 5-mm outer-diameter zirconia rotor at 6250 Hz, with the speed under active control and maintained to within ±2 Hz. A Tecmag Apollo console (Houston, TX) controlled the spectrometer. A 2-kW American Microwave Technology power amplifier was used to produce radio-frequency pulses for $^{13}C$ (125 MHz). The $^{1}H$ (500 MHz) and $^{19}F$ (470 MHz) radio-frequency pulses were generated by 2-kW Creative Electronics tube amplifiers driven by 50-W American Microwave Technology power amplifiers. All final-stage amplifiers were under active control(28). The π-pulse lengths were 7 μs for $^{13}C$ and 5 μs for $^{1}H$ and $^{19}F$.

Hydrated samples were sealed in rotors using gaskets cut from a 1/16-inch thick sheet of silicone rubber, cooled by liquid nitrogen, and inserted cold on both sides of friction-fit boron nitride spacers that positioned the sample in the center of the analytical coil (Figure A2-2). With this arrangement, a hydrated sample, approximately 50% by weight water, could be spun at 6 kHz for two months with a weight loss of less than 1%.

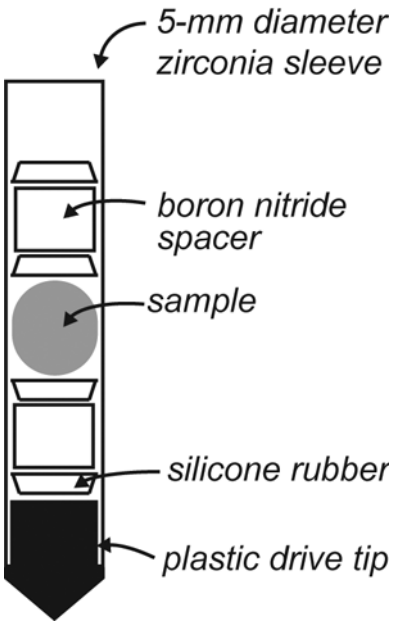


**Figure A2-2**. Rotor configuration for magic-angle spinning of hydrated HBFP-PEG samples. Wet samples were spun for two months with less than 1% weight loss.

*Pulse Sequences.* The pulse sequence and phase table for the $^{19}F$ solid-echo experiment ($90^{o}_{x}$-$\tau$-$90^{o}_{y}$-$\tau$, with $\tau$ = 13.5 μs) are shown in Figure A2-3. A split $180^{o}$ pulse preceding the solid-echo sequence and synchronized with the acquisition phase resulted in flat baselines over 150 kHz and a null signal from an empty rotor.

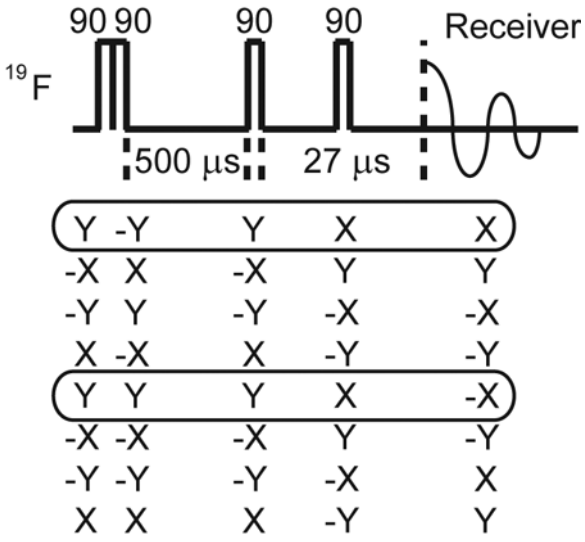


**Figure A2-3.** Pulse sequence and phase routing for the $^{19}F$ solid-echo experiment. The split $180^{o}$ pulse preceding the $90^{o}$-$\tau$-$90^{o}$ suppresses baseline artifacts.

The pulse sequence for FHHC $^{13}C$ NMR with solid-echo detection is shown in Figure A2-4. The acquisition phase followed the spin-temperature alternation of the initial $^{19}F$ spin lock. The $^{1}H$ spin-lock spin temperature of the second cross-polarization was not alternated. Thus, $^{13}C$ signals arising from the protons of the PEG domains exactly cancelled. The HH spin diffusion period was 50 ms, selected by optimizing the final $^{13}C$ signal intensity for both wet samples. The refocusing time, $\tau$, for $^{19}F$ and $^{13}C$ solid-echo experiments was 13.5 μs (which includes half the width of the refocusing 90$^{o}$ pulse). The second half of the sequence of Figure A2-4 (no $^{19}F$ channel) was used for solid-echo $^{13}C$ experiments with no spin-diffusion filtering.

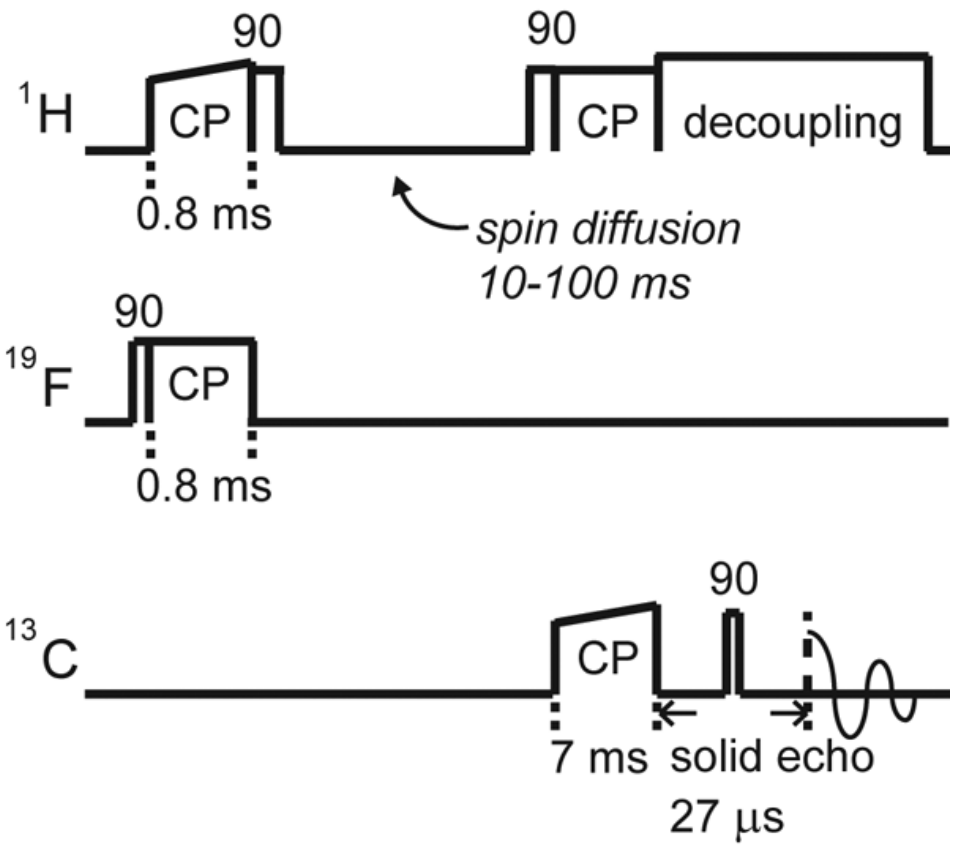


**Figure A2-4.** Pulse sequence for characterization of the HBFP-PEG interface. Magnetization originates with $^{19}F$ in the HBFP domain and is transferred to protons using a $^{19}F \rightarrow {}^{1}H$ ramped cross-polarization transfer, followed first by $^{1}H$-$^{1}H$ spin diffusion of z-stored magnetization, and then by a $^{1}H \rightarrow {}^{13}C$ ramped cross-polarization transfer, all under

magic-angle spinning. Detection of the PEG-domain $^{13}C$ signal is by solid echo. The sign of the observed $^{13}C$ signal follows the spin-temperature alternation of the $^{19}F$ spin lock. The sign of the $^{1}H$ spin-lock temperature is not alternated; that is, PEG-phase $^{13}C$ signals from the second cross-polarization transfer are cancelled.

The refocusing time for all rotor-synchronized magic-angle spinning Hahn-echo experiments was $T_r$=160 μs, corresponding to a 6250-Hz spinning speed. Ramped cross-polarization transfers were made in 7 ms for HC, and 0.8 ms for HF and FH. The $^{13}C$ radiofrequency carrier was on resonance for the PEG signal. Proton dipolar decoupling was 100 kHz during data acquisition. A sequence recycle time of 6 s was used for cross-polarization, Hahn-echo, and solid-echo experiments for fully relaxed spectra.

**Results and discussion**

*Fluorine-19 NMR.*

Two types of solid-state $^{19}F$ NMR experiments were used to characterize the HBFP domains of the phase-separated HBFP-PEG block copolymers. Mobile (soft) domains were detected by a rotor-synchronized Hahn echo under magic-angle spinning conditions,(29) and rigid (hard) domains by a solid echo with no magic-angle spinning (Figure A2-4, experimental section).(30) The spectra of dry HBFP-PEG45 and HBFP-PEG55 are similar to one another (Figure A2-5, top), and to HBFP homopolymer (Figure A2-6). All three materials are predominantly solid-like. Based on microscopy to determine which of the two components in the copolymers is the continuous phase,(23) the NMR results suggest that HBFP-PEG45 can be described as a low-$T_g$ HBFP glass with PEG inclusions, whereas HBFP-PEG55 is more like a PEG glass with a constrained-rubber HBFP filler. The latter has the greater tensile modulus in the dry state,(25, 31) which is hypothesized as being due to crystalline PEG-rich domains in the dry samples.

These materials exhibited melting transitions at 47-48 $^{o}$C, as measured by differential scanning calorimetry.

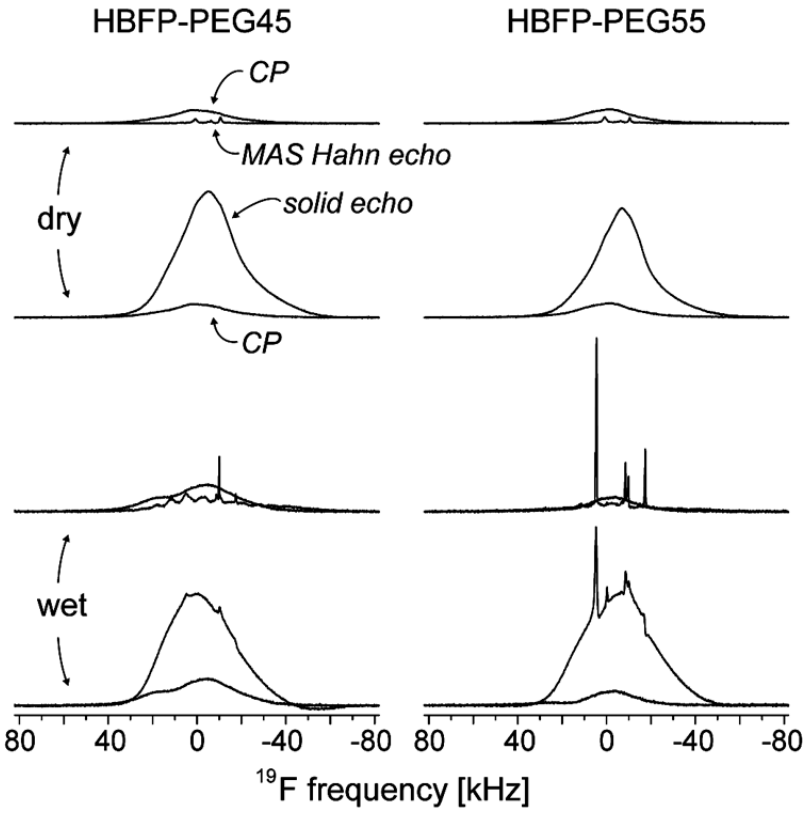


**Figure A2-5.** Solid-state $^{19}$F NMR spectra of HBFP-PEG45 (left) and HBFP-PEG55 (right) dry (top two rows) and hydrated to approximately 50% water by weight (bottom two rows). Each of the eight panels makes a comparison of a $^{1}$H→$^{19}$F ramped cross-polarization (CP) spectrum obtained without magic-angle spinning, to either a $90^{o}_{x}$-τ-$180^{o}_{y}$-τ rotor-synchronized Hahn echo (τ = 160 μs) obtained with spinning (rows 1 and 3), or a $90^{o}_{x}$-τ-$90^{o}_{y}$-τ solid echo (τ = 13.5 μs) obtained without spinning (rows 2 and 4). The CP spectra were also detected by solid echo. All of the spectra arise exclusively from HBFP. The spectra were obtained by the accumulation of 4096 scans, are scaled by sample weight, and are referenced to the $^{19}$F resonance of solid D-[3-$^{19}F_1$]alanine.

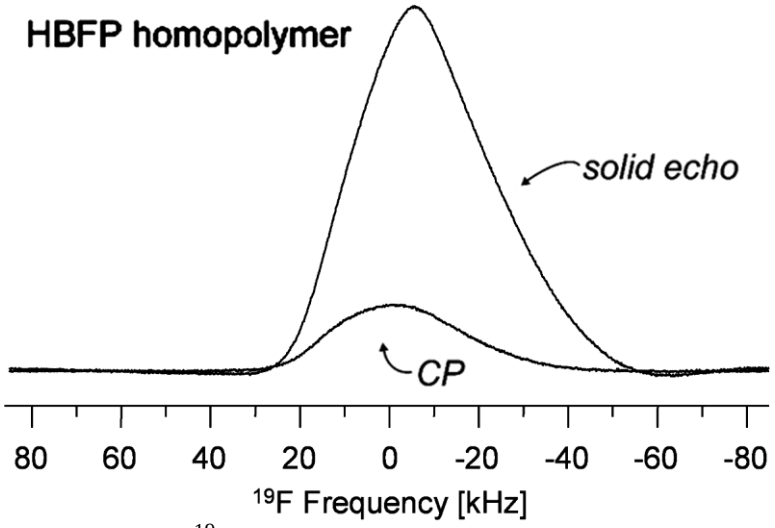


**Figure A2-6.** $^{19}F$ solid echo (top) and CP (bottom) NMR spectra of HBFP homopolymer. The CP transfer was made from protons in 0.8 ms. Both spectra are the result of the ammumulation of 4096 scans without magic angle spinning.

The HBFP domains (and presumably the interface between HBFP and PEG domains) were detected by a third $^{19}F$ NMR experiment, which utilized a $^{1}H \rightarrow ^{19}F$ cross-polarization (CP) transfer. In each repeat unit of HFBP, there are 9 protons and 9 fluorines. However, the protons are clustered in or near the central protonated ring of the repeat unit (Figure A2-1). Most of the fluorines are therefore more than 5 Å from a proton. This geometry, combined with significant local motion about HBFP mainchain oxygen linkages, means that the $^{1}H \rightarrow ^{19}F$ CP transfer results in a much smaller $^{19}F$ signal than does a direct-excitation experiment (Figure A2-5, CP *vs* solid echo, top left).

While the CP signal for dry HBFP-PEG55 is indistinguishable from that for dry HBFP-PEG45 (Figure A2-5, top two rows), the CP, Hahn echo, and solid echo $^{19}F$ NMR spectra of wet HBFP-PEG55 and HBFP-PEG45 are markedly dissimilar (Figure A2-5, bottom two rows). Although both materials are still predominantly solid-like, the increased narrow-line Hahn-echo signals for HBFP-PEG55 relative to that for HBFP-PEG45 indicates an increased concentration of mobile domains for wet HBFP-PEG55.

By contrast, the increased $^{19}F$ CP intensity for wet HBFP-PEG45 relative to that for HBFP-PEG55 (wet or dry) shows an increased proton-fluorine contact for HBFP-PEG45. This means a stronger coupling for the same number of spins, or the same coupling for more spins, resulting from a reduction in local motion or tighter chain packing. We describe either of these situations as rigidification.

*Carbon-13 NMR.*

Abundant protons in the PEG domains means that the $^{1}H \rightarrow ^{13}C$ CP spectra of the copolymers are dominated by the PEG oxygenated methylene carbons at 70-72 ppm(32) (Figure A2-7, top). This shift is an exclusive PEG signature (Figure A2-8). The $^{13}C$ signal is detected both as a Hahn echo (black) or a solid echo (red) (Figure A2-7). For the latter, the phase of the $90^{o}$ pulse matched the phase of the carbon spin lock, which for isolated natural-abundance $^{13}C$ results in a standard full-size signal (*vide infra.*).

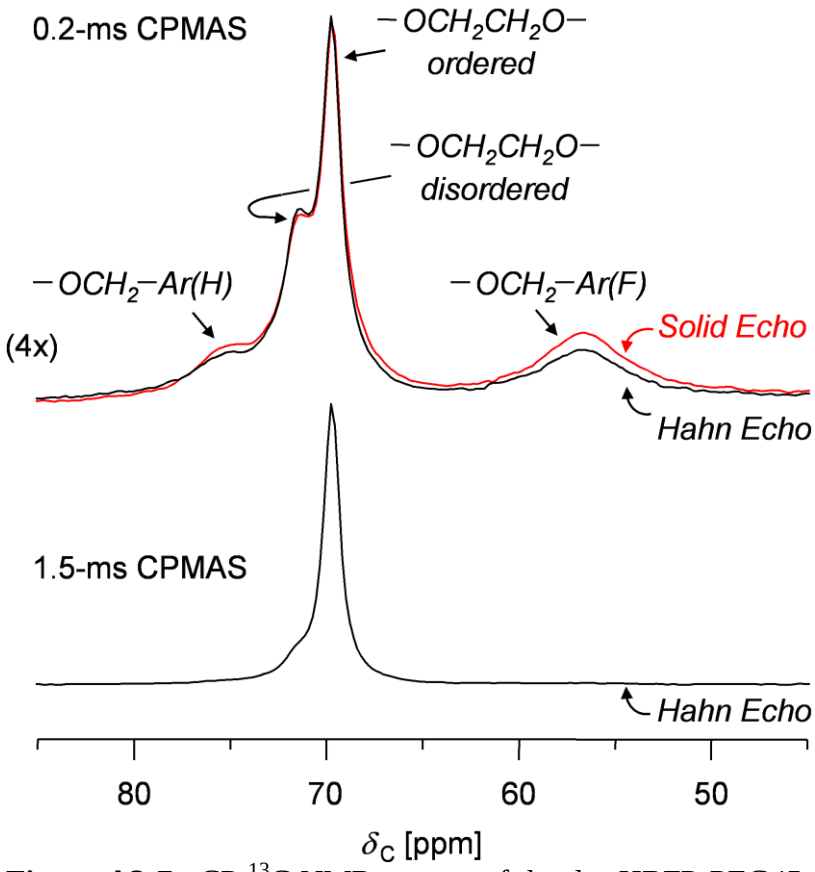


**Figure A2-7.** CP $^{13}$C NMR spectra of the dry HBFP-PEG45 copolymer obtained with a 0.2-ms $^{1}$H→$^{13}$C ramped cross-polarization transfer (top) and detected by a Hahn echo (black) or solid echo (red), or with a 1.5-ms transfer and detected by a Hahn echo (bottom). Only the regions between 45 and 85 ppm are shown. The chemical shifts of the oxygenated methylene carbons in the PEG domains are between those in the HBFP domains. The low-field 72-ppm PEG signal and the HBFP oxygenated methylene-carbon signals are associated with a short $T_{1\rho}$(H). The $^{13}$C radiofrequency carrier was centered on the PEG signals. The spectra were obtained with magic-angle spinning and proton decoupling and are the result of the accumulation of 16384 scans.

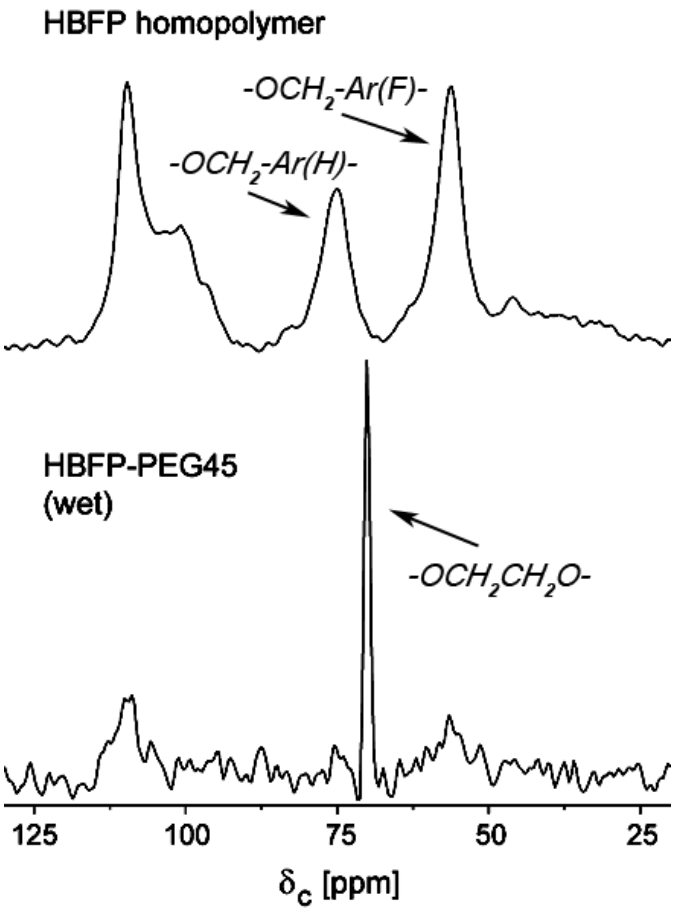


**Figure A2-8.** CP $^{13}C$ NMR spectra of HBFP homopolymer (top) and hydrated HBFP-PEG45 block copolymer (bottom). Only the regions between 25 and 125 ppm are shown. The spectra were obtained using a $^{1}H \rightarrow ^{13}C$ ramped cross-polarization transfer and detection by a solid echo with magic-angle spinning. The spectra were obtained by the accumulation of 32768 scans. The 70-ppm chemical shift of the ordered oxygenated methylene carbons in the PEG domain is between the shifts of the oxygenated methylene carbons in the HBFP domain.

The 72-ppm low-field PEG peak is due to chains with gauche defects and has an extremely short $T_{1\rho}(H)$.(32) The 70-ppm high-field peak is due to chains with an all-*trans* conformation, some of which are in crystallites in dry HBFP-PEG. The $T_{1\rho}(H)$ associated with the high-field peak is longer than that for the low-field peak, consistent with less mobility for the more ordered chains. Thus, with an increase in the length of

the CP transfer time, the intensity of the low-field peak decreases relative to the 70-ppm high field peak (Figure A2-7, bottom).

Hydration of HBFP-PEG55 has little effect on the 7-ms $T_{1\rho}$(H)-filtered 70-ppm $^{13}C$ CP peak (the 72-ppm peak has been totally removed by the filter), whereas hydration of HBFP-PEG45 results in more than a doubling of the solid-echo signal intensity (Figure A2-9). This result suggests a relative increase in the $T_{1\rho}$(H) of the more ordered PEG components(33) for wet HBFP-PEG45, which can only occur by an increase in constraints; that is, a decrease in mobility. An increase in mobility would make the 70-ppm high-field peak more like the 72-ppm low-field peak with its very short $T_{1\rho}$(H). Hydration of HBFP-PEG45 also increases the $T_{1\rho}$(H) of the HBFP domains so that $^{13}C$ signals pass the 7-ms $T_{1\rho}$(H) filter of the CP transfer (Figure A2-10, top). The increase in $T_{1\rho}$(H) means an increase in constraints (decrease in mobility), consistent with the increase in $^{19}F$-$^{1}H$ contact observed in the short $^{1}H \rightarrow ^{19}F$ CP transfer of Figure A2-5 (bottom, left).

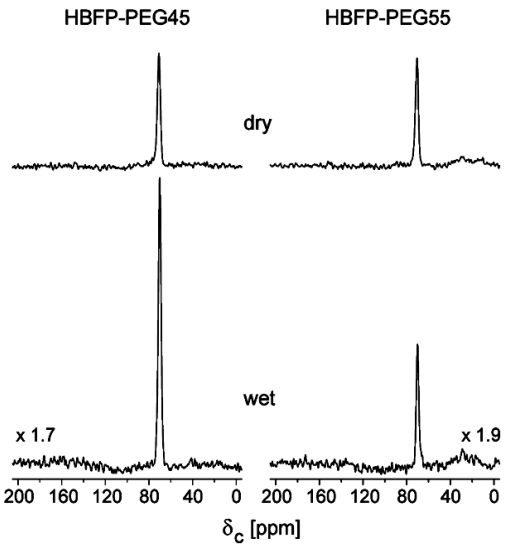


**Figure A2-9**. CP $^{13}C$ NMR spectra of HBFP-PEG45 (left) and HBFP-PEG55 (right) dry (top) and hydrated (bottom). The spectra were obtained using a 7-ms $^{1}H \rightarrow ^{13}C$ ramped cross-polarization transfer without magic-angle spinning and were detected by a solid echo with 100-kHz proton decoupling. Only the high-field 70-ppm PEG signal is observed. Protonated aromatic-carbon signals from the wet HBFP domains are too broad to detect in the absence of spinning. The spectra were obtained by the accumulation of 4096 scans, are scaled by sample weight (scale factors inset), and are referenced to external TMS.

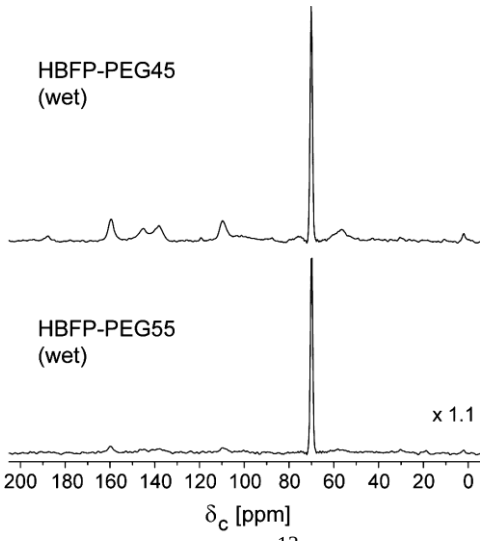


**Figure A2-10.** CP $^{13}C$ NMR spectra of HBFP-PEG45 hydrated copolymer (top) and HBFP-PEG55 hydrated copolymer (bottom). The spectra were obtained using a 7-ms $^{1}H \rightarrow ^{13}C$ ramped cross-polarization transfer and detection by a rotor-synchronized Hahn echo with magic-angle spinning. The spectra were the result of the accumulation of 8192 scans. Only the high-field 70-ppm PEG signal is observed. The $T_{1\rho}(H)$ of the HBFP domains on HBFP-PEG45 has been increased by PEG hydration and HBFP $^{13}C$ signals pass the 7-ms $T_{1\rho}(H)$ filter.

The same increase in $T_{1\rho}(H)$-filtered $^{13}C$ CP solid-echo intensity on hydration is observed when a PEG $^{13}C$ signal is directly linked by an FHHC experiment to $^{19}F$ in an adjacent HBFP domain (Figure A2-11). This experiment (Figure A2-4) starts with a magnetization transfer from fluorines to protons in HBFP followed by storage along the static field for a mixing time of 50 ms. Magnetization transfer between protons during mixing to diffusing water is impossible because of the inherently weak coupling to mobile species. The relatively low H spin density in HFBP and the HFBP interface means that in 50 ms, HH spin diffusion cannot extend much beyond the HBFP domains.(34) We estimate the spin-diffusion range by $\sqrt{(Dt_m)}$, where

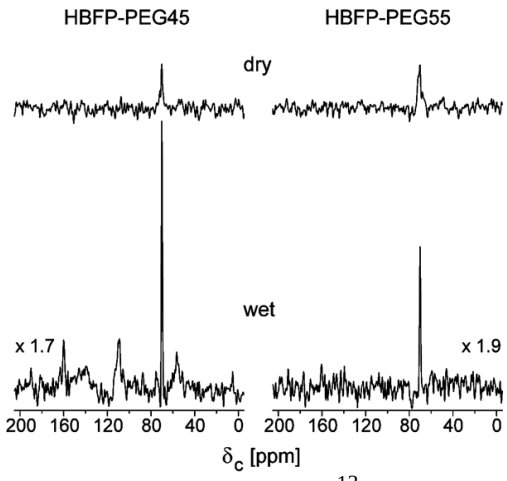


**Figure A2-11.** FHHC $^{13}C$ NMR spectra of HBFP-PEG45 (left) and HBFP-PEG55 (right) dry (top) and hydrated (bottom). The spectra were obtained using a 0.8-ms $^{19}F \rightarrow {}^{1}H$ ramped cross-polarization transfer, followed first by $^{1}H$-$^{1}H$ spin diffusion of z-stored magnetization for 50 ms, and then by a 7-ms $^{1}H \rightarrow {}^{13}C$ ramped cross-polarization transfer (see Figure A2-4), all with magic-angle spinning. Magic-angle spinning eliminated shift anisotropy and reduced the linewidths of both wet and dry samples relative to those observed without spinning (see Figure A2-9). The sign of the observed $^{13}C$ signal followed the spin-temperature alternation of the $^{19}F$ spin lock; that is, PEG-phase $^{13}C$ signals from the second cross-polarization transfer were cancelled. The spectra were detected by solid echo with magic-angle spinning and resulted from the accumulation of 32768 scans, scaled by sample weight (scale factors inset), and referenced to external TMS.

$D \approx 10^{-12}$ cm$^2$/s(35) and $t_m$ = 50 ms, a distance of approximately 20 Å. We take this distance of approximately 10-15 covalent bonds as the extent of the interface. The final $^{1}H \rightarrow {}^{13}C$ transfer is to a locally ordered PEG carbon (as determined by chemical shift), which is necessarily in the interfacial region and so adjacent to a HBFP lattice. This signal was zero when the initial $^{19}F$ spin-temperature alternation was suppressed. That is,

there is no contribution to the signals of Figure A2-11 from the PEG domains. The protons making the transfer to the 70-ppm $^{13}$Cs are in the interface.

*Carbon-13 Solid Echos.*

The use of the term "solid echo" is unconventional for $^{13}$C experiments at natural abundance. What we mean by this usage is that the phase of the $^{13}$C 90$^{o}$ pulse is the same as the phase of the $^{13}$C spin lock during the cross-polarization transfer. Thus, the 90$^{o}$ pulse is along the direction of the $^{13}$C magnetization. For an isolated carbon, the pulse has no effect, and a full-size signal is observed. However, for $^{13}$Cs that are part of homogeneous dipolar interactions,(26) the $^{13}$C signal detected as a solid echo could be larger than a standard Hahn echo. The increase in intensity for the solid-echo (red) relative to Hahn-echo (black) HBFP peaks in Figure A2-7 may be due to such refocusing, or to the shorter evolution time of the solid-echo experiment, and poor refocusing due to slow internal motions in the Hahn-echo experiment. In any event, our motivation for the solid-echo $^{13}$C detection for HBFP-PEG copolymers was simply to ensure detection of PEG $^{13}$Cs at the interface that might have partial homogeneous coupling to immobile $^{19}$Fs, while avoiding possible interferences from simultaneous $^{19}$F and $^{1}$H decoupling.

*Hydration and Domain Rigidification.*

The observed increased intensity for the HBFP-PEG45 $^{13}$C PEG 70-ppm signal on hydration (Figure A2-9, left) means an increase in $T_{1\rho}$(H) and therefore rigidification of locally ordered PEG chains within the PEG phase. If hydration of these chains had resulted in more mobility, $T_{1\rho}$(H) would have decreased and the 70-ppm signal would not have passed the 7-ms spin-lock filter. The increase in $T_{1\rho}$(H) (Figure A2-10) and $^{19}$F-$^{1}$H contact (Figure A2-5, CP, bottom left) show a similar rigidification within the HBFP phase on hydration. With both HBFP and PEG phases constrained, the rigidification of the interface of HBFP-PEG45 on hydration (Figure A2-11, left) is not a surprise. The

lack of a similar increase in signal intensity for HBFP-PEG55 on hydration (Figure A2-9, right) agrees with the absence of rigidification on swelling of the majority PEG component.

*Hydration and Mechanical Properties.*

The hydration effects on PEG domains and interfaces are consistent with the increase in tensile modulus for HBFP-PEG45 and decrease in tensile modulus for HBFP-PEG55. We believe that HBFP-PEG55 with its PEG continuous phase becomes more like a PEG hydrogel with a mobile HBFP filler on hydration. HBFP-PEG45 by contrast remains a HBFP glass although now with water-swollen PEG inclusions and its tensile modulus accordingly increases on swelling by water. Both of these comparisons are consistent with an increased segregation of PEG to the solid-water interface and a roughening of the PEG-domain surface for HBFP-PEG45. Thus, varying the amount of PEG in an amphiphilic crosslinked film alters the properties from a material with discrete, constrained regions of HBFP with swollen inclusions of PEG and superior mechanical properties, to one with localized HBFP inside a PEG hydrogel and inferior mechanical properties.(25, 31)

**Conclusions**

Solid-state NMR studies have provided unambiguous determination of the molecular-level structural reorganizations that lead to unique macroscopic mechanical properties for amphiphilic crosslinked networks of HBFP and PEG. Insights into the internal chemical environment within these polymers are expected to lead to their development as complex functional materials for broad utility, from membranes for fuel cells, to substrates for tissue engineering, to robust antifouling coatings for biomedical

and marine applications. Gradient forms of these materials are also being designed as interesting transitional biomaterials and antifouling surfaces.

**References**


(1) Bates, F. S.; Fredrickson, G. H. (1999) Block copolymers - Designer soft materials. *Phys. Today 52*(2), 32-38.

(2) Tang, C.; Lennon, E. M.; Fredrickson, G. H.; Kramer, E. J.; Hawker, C. J. (2008) Evolution of Block Copolymer Lithography to Highly Ordered Square Arrays *Science 322*, 429-432.

(3) Tang, C. B.; Bang, J.; Stein, G. E.; Fredrickson, G. H.; Hawker, C. J.; Kramer, E. J.; Sprung, M.; Wang, J. (2008) Square packing and structural arrangement of ABC triblock copolymer spheres in thin films. *Macromolecules 41*(12), 4328-4339.

(4) Hawker, C. J.; Russell, T. P. (2005) Block copolymer lithography: Merging "bottom-up" with "top-down" processes. *MRS Bull. 30*(12), 952-966.

(5) Frisch, H. L. (1985) Interpenetrating polymer networks. *British Polymer Journal 17*(2), 149-153.

(6) Muller, M.; Binder, K. (1998) Wetting and capillary condensation in symmetric polymer blends: A comparison between Monte Carlo simulations and self-consistent field calculations. *Macromolecules 31*(23), 8323-8346.

(7) Rogovina, L. Z.; Dembo, A. T.; Sharma, P. R. S.; Frisch, H. L.; Schulz, M. (2000) Swollen interpenetrating polymer networks. *Polymer 41*(8), 2893-2898.

(8) Behravesh, E.; Jo, S.; Zygourakis, K.; Mikos, A. G. (2002) Synthesis of in situ cross-linkable macroporous biodegradable poly(propylene fumarate-co-ethylene glycol) hydrogels. *Biomacromolecules 3*(2), 374-381.

(9) Zhu, C.; Hard, C.; Lin, C. P.; Gitsov, I. (2005) Novel materials for bioanalytical and biomedical applications: Environmental response and binding/release capabilities of amphiphilic hydrogels shape-persistent dendritic junctions. *Journal of Polymer Science Part A-Polymer Chemistry 43*(18), 4017-4029.

(10) Olson, D. A.; Chen, L.; Hillmyer, M. A. (2008) Templating Nanoporous Polymers with Ordered Block Copolymers. *Chem. Mater. 20*, 869-890.

(11) Gudipati, C. S.; Finlay, J. A.; Callow, J. A.; Callow, M. E.; Wooley, K. L. (2005) The antifouling and fouling-release perfomance of hyperbranched fluoropolymer (HBFP)-poly(ethylene glycol) (PEG) composite coatings evaluated by adsorption of biomacromolecules and the green fouling alga Ulva. *Langmuir 21*(7), 3044-3053.

(12) Gitsov, I.; Zhu, C. (2003) Novel functionally grafted pseudo-semi-interpenetrating networks constructed by reactive linear-dendritic copolymers. *Journal of the American Chemical Society 125*(37), 11228-11234.

(13) Doura, M.; Naka, Y.; Aota, H.; Matsumoto, A. (2003) Novel amphiphilic network polymers consisting of polar, short primary polymer chains and nonpolar, long cross-link units obtained by free-radical cross-linking monomethacrylate/dimethacrylate copolymerizations. *Macromolecules 36*(22), 8477-8482.

(14) Erdodi, G.; Kennedy, J. P. (2005) Ideal tetrafunctional amphiphilic PEG/PDMS conetworks by a dual-purpose extender/crosslinker. I. Synthesis. *Journal of Polymer Science Part A-Polymer Chemistry 43*(20), 4953-4964.

(15) Erdodi, G.; Kennedy, J. P. (2005) Ideal tetrafunctional amphiphilic PEG/PDMS conetworks by a dual-purpose extender/crosslinker. II. Characterization and

properties of water-swollen membranes. *Journal of Polymer Science Part A-Polymer Chemistry 43*(20), 4965-4971.

(16) Isayeva, I. S.; Yankovski, S. A.; Kennedy, J. P. (2002) Novel amphiphilic membranes of poly(N,N-dimethyl acrylamide) crosslinked with octa-methacrylate-telechelic polyisobutylene stars. *Polymer Bulletin 48*(6), 475-482.

(17) Bronich, T. K.; Vinogradov, S. V.; Kabanov, A. V. (2001) Interaction of nanosized copolymer networks with oppositely charged amphiphilic molecules. *Nano Letters 1*(10), 535-540.

(18) Achilleos, D. S.; Georgiou, T. K.; Patrickios, C. S. (2006) Amphiphilic model conetworks based on cross-linked star copolymers of benzyl methacrylate and 2-(dimethylamino)ethyl methacrylate: Synthesis, characterization, and DNA adsorption studies. *Biomacromolecules 7*(12), 3396-3405.

(19) Powell, K. T.; Cheng, C.; Wooley, K. L.; Singh, A.; Urban, M. W. (2006) Complex amphiphilic networks derived from diamine-terminated poly(ethylene glycol) and benzylic chloride-functionalized hyperbranched fluoropolymers. *Journal of Polymer Science Part A-Polymer Chemistry 44*(16), 4782-4794.

(20) Gudipati, C. S.; Greenlief, C. M.; Johnson, J. A.; Prayongpan, P.; Wooley, K. L. (2004) Hyperbranched fluoropolymer and linear poly(ethylene glycol) based Amphiphilic crosslinked networks as efficient antifouling coatings: An insight into the surface compositions, topographies, and morphologies. *Journal of Polymer Science Part A-Polymer Chemistry 42*(24), 6193-6208.

(21) Vamvakaki, M.; Patrickios, C. S.; Lindner, P.; Gradzielski, M. (2007) Amphiphilic networks based on cross-linked star polymers: A small-angle neutron scattering study. *Langmuir 23*(21), 10433-10437.

(22) Sun, P. C.; Dang, Q. Q.; Li, B. H.; Chen, T. H.; Wang, Y. N.; Lin, H.; Jin, Q. H.; Ding, D. T.; Shi, A. C. (2005) Mobility, miscibility, and microdomain structure in nanostructured thermoset blends of epoxy resin and amphiphilic poly(ethylene oxide)-block-poly(propylene oxide)-block-poly(ethylene oxide) triblock copolymers characterized by solid-state NMR. *Macromolecules 38*(13), 5654-5667.

(23) Brown, G. O.; Bergquist, C.; Ferm, P.; Wooley, K. L. (2005) Unusual, promoted release of guests from amphiphilic cross-linked polymer networks. *Journal of the American Chemical Society 127*(32), 11238-11239.

(24) Junk, M. J. N.; Jonas, U.; Hinderberger, D. (2008) EPR Spectroscopy Reveals Nanoinhomogeneities in the Structure and Reactivity of Thermoresponsive Hydrogels. *Small 4*(9), 1485-1493.

(25) Xu, J.; Bohnsack, D. A.; Mackay, M. E.; Wooley, K. L. (2007) Unusual mechanical performance of amphiphilic crosslinked polymer networks. *Journal of the American Chemical Society 129*(3), 506-507.

(26) Mehring, M.; Sinning, G. Z.; Pines, A. (1976) NMR line broadening in solids by slowing down of spin fluctuations *Physik B 23*, 73-76.

(27) Schaefer, J.; McKay, R. A. Multi-tuned single coil transmission line probe for nuclear magnetic resonance spectrometer. 5,861,748, (1999).

(28) Stueber, D.; Mehta, A. K.; Chen, Z.; Wooley, K. L. (2006) Local Order in Polycarbonate Glasses by $^{13}C\{^{19}F\}$ Rotational-Echo Double-Resonance NMR. *J. Polym. Sci., Part B: Polym. Phys. 44*, 2760-2775.

(29) Schaefer, J.; Garbow, J. R.; Stejskal, E. O.; Lefelar, J. A. (1987) Plasticization of poly(butyral-covinyl alcohol). *Macromolecules 20*, 1271-1278.

(30) Powles, J. G.; Mansfield, P. (1962) Double-Pulse Nuclear-Resonance Transients in Solids. *Phys. Lett. 2*, 58.

(31) Xu, J.; Bartels, J. W.; Bohnsack, D. A.; Tseng, T.-C.; Mackay, M. E.; Wooley, K. L. (2008) Hierarchical Inorganic-Organic Nanocomposites Possessing Amphiphilic and Morphological Complexities: Influence of Nanofiller Dispersion on Mechanical Performance. *Advanced Functional Materials 18*(18), 2733-2744.

(32) Schmidt-Rohr, K.; Spiess, H. W. (1994) *Multidimensional Solid-State NMR and Polymers*. Academic Press, New York: p 264-267.

(33) Harris, D. J.; Bonagamba, T. J.; Hong, M.; K., S.-R. (2005) Two-dimensional solid-state NMR studies of crystalline poly(ethylene oxide): Conformations and chemical shifts. *Polymer Bulletin 46*, 11737-11743.

(34) Afeworki, M.; Schaefer, J. (1992) Mechanism of DNP-Enhanced Polarization Transfer across the Interface of Polycarbonate/Polystyrene Heterogeneous Blends. *Macromolecules 25*, 4092-4096.

(35) van der Wel, P. C. A.; Hu, K.-N.; Lewandowski, J.; Griffin, R. G. (2006) High Frequency Dynamic Nuclear Polarization in MAS Spectra of Amyloid Peptides - GNNQQNY Nanocrystals. *J. Am. Chem. Soc. 128*, 10840-10846.